Transitions and bistability of thermal convection between differentially rotating spherical shells

a thesis presented for the degree of

Doctor of Philosophy of Imperial College London

and the

Diploma of Imperial College

by

Paul M. Mannix

Department of Mathematics

Imperial College

180 Queen's Gate, London SW7 2BZ

November 2019

Declaration of originality

I certify that the contents of this thesis, and the research if refers to, are the product my work. Any ideas or quotations from other peoples work are fully acknowledged in accordance with the standard referencing practices of the discipline.

Copyright

The copyright of this thesis rests with the author. Unless otherwise indicated, its contents are licensed under a Creative Commons Attribution-Non Commercial 4.0 International Licence (CC BY-NC).

Under this licence, you may copy and redistribute the material in any medium or format. You may also create and distribute modified versions of the work. This is on the condition that: you credit the author and do not use it, or any derivative works, for a commercial purpose.

When reusing or sharing this work, ensure you make the licence terms clear to others by naming the licence and linking to the licence text. Where a work has been adapted, you should indicate that the work has been changed and describe those changes.

Please seek permission from the copyright holder for uses of this work that are not included in this licence or permitted under UK Copyright Law.

Thesis advisor: Professor A.J. Mestel Paul M. Mannix

Transitions and bistability of thermal convection between differentially rotating spherical shells

Abstract

This thesis investigates the motion of heated fluid between two differentially rotating spherical shells. Although the motion is simple for weak heating and differential rotation, it transitions to more complicated states as both increase. Heating a quiescent fluid from below gives rise to cellular convective motion as the temperature gradient becomes sufficiently steep. Typically this transition increases heat transfer. Differentially rotating spherical shells also generate a state of cellular motion, which in this case transports angular momentum. When both effects are present, it is often assumed the fluid chooses an optimal configuration which maximises the transfer of angular momentum and heat. Depending on how the equilibrium is reached however, this maximisation may not always be achieved, with two different stable equilibria often found to co-exist for the same heating and rotation strengths. We want to understand why the fluid motion in a spherical shell is bistable, and how this scenario might arise. We find that bistability in the non-rotating problem depends largely on the shell separation, and when differential rotation is introduced, on the relative strength of heating to rotation. In both cases the strength of thermal plume boundary layers appears to play a key role. We find that for differentially rotating problem, the transition between solutions can occur either due to the destabilisation of an equatorial plume by buoyancy forces, or alternatively a polar plume by Ekman pumping. Our results demonstrate that although bistability in this system cannot be simply explained by the flow maximising its torque or heat transfer, the polar and equatorial regions are of particular significance. As bistability is a ubiquitous feature of many fluid systems, particularly those for which the transport of heat and angular momentum is important, it's hoped that this

study can provide valuable insights and help towards the understanding of such behaviour.

To my family.

Acknowledgments

Without my sister's reasoned advice and encouragement, I would never have come to study at Imperial. For much of the decision to undertake a Masters and subsequently a PhD at Imperial, experiences which I greatly value despite the difficulties encountered I owe her greatly.

For having the patience and time to deal with a engineering student, whose background in applied mathematics was far from proficient, I owe many thanks to my supervisor Jonathan Mestel. Similarly for all his encouragement, support, generosity at giving his time and the clarity of thought he provided throughout my PhD I am equally indebted.

I would also like to acknowledge the help of my office mates, fellow fluids CDT students, my second supervisor Dr. Jennifer Tweedy and the CDT administrator Clodagh Li.

To my family and to Luiza for all their eternal support and encouragement.

List of figures

1.1 *Schematic of Enceladus' interior structure and rapidly rotating convection in a spherical shell.* 3

1.2 *Hysteresis phenomena in a model of thermal convection and differential rotation.* 4

1.3 *Schematic of the anticipated fluid-flow in a spherical annulus due to differential rotation or thermal convection.* 5

2.1 *The fluid domain is a closed annular region between two concentric spheres, each with constant surface temperatures.* 15

3.1 *Dependence of the characteristic equation's roots of* (3.17) *with mode number* ℓ. 29

3.2 *Neutral stability curves* $\mathrm{Ra_c}(d)\, d^3$ *for stress-free and no-slip boundary conditions.* 30

3.3 *Eigenfunctions* $\psi(r)$ & $T(r)$ *of the marginally stable state.* 31

3.4 *Neutral stability curves* $\mathrm{Ra}(d)$ *of modes* $\ell = 1 \to 4$. 32

3.5 *Variation of the equation coefficients with Pr for modes* $\ell = 2, 3$. . . . 40

3.6 *Bifurcation loci of the* $\ell = 2, 3$ *mode interaction for Pr* $= 10$. 41

3.7 *Bifurcation diagrams of the mode interaction* $\ell = 2, 3$ *for* $\delta = -0.2, 0.2$. 41

3.8 *Phase-plane diagrams* (A, B) *describing the* even-odd *interaction for mode numbers* $\ell = 2, 3$ *and Pr* $= 10$. 43

3.9 *Prandtl number dependency of coefficients for the* $\ell = 3, 4$ *interaction.* 44

3.10 *Bifurcation loci for the* odd-even *mode interactions with Pr* $= 10$. . . 44

3.11 *Variation of the amplitude equation coefficients with Pr for* $\ell = 1, 2$. . 45

3.12 *Variation of the amplitude equation coefficients with Pr for modes* $\ell = 2, 4$. 45

3.13 *Bifurcation loci of the* even-even *interactions* $\ell = 2, 4$ & $\ell = 4, 6$ *with* $Pr = 10$. 46

3.14 *Phase-plane diagrams* (A, B) *describing the* even-even *interaction for mode numbers* $\ell = 2, 4$ *and* $Pr = 10$. 47

3.15 *Numerical solutions* $\psi(r, \theta)$ *in the neighbourhood of the* $\ell = 2, 3$ *degenerate point (*$d_c = 1.9883, \mathrm{Ra}_c = 857.53$*) for* $Pr = 1$. 49

3.16 *Numerical solutions* $\psi(r, \theta)$ *in the neighbourhood of the* $\ell = 3, 4$ *degenerate point (*$d_c = 1.2291, \mathrm{Ra}_c = 2381.1$*) with* $Pr = 1$. 50

3.17 *Symmetric solutions* $\psi(r, \theta)$ *near the* $\ell = 2, 4$ *degenerate point (*$d_c = 1.5807, \mathrm{Ra}_c = 1515.399$*) for* $Pr = 10$. 51

3.18 *DNS oscillation signature for the periodic solutions near the* even-even *and* odd-odd *degeneracies with* $Pr = 0.05$. 52

3.19 *Stability and convective heat transfer* Nu *of the even* u_r^-, u_r^+ *and mixed* $1 - cell$ *solutions at* $Pr = 0.05, d = 3$. 54

3.20 *Steady states showing the vorticity* $D^2\psi$ *and temperature field* T *of the even and mixed solutions at* $Pr = 0.05, d = 3$. 55

3.21 *Bifurcation diagram indicating both the stability and convective heat transfer of the even* u_r^-, u_r^+ *and mixed* $1 - cell$ *solutions at* $Pr = 10, d = 3$. 56

3.22 *Steady states of the vorticity* $D^2\psi$ *and temperature field* T *of the even and mixed solutions at* $Pr = 10, d = 3$. 58

3.23 *Thermal boundary layer profiles of the even and mixed solutions at* $Pr = 10, d = 3$. 58

4.1 *Decoupled steady state solutions of the differential rotation and thermal convection (*$Pr = 10$*) problems illustrating similar spatial solutions.* 61

4.2 *Bifurcation of the conductive state to even thermal convection for different* Re_1 *and* Pr. 67

4.3 *Transition between the rotating branch* u_r^+ *and the convection branch* u_r^- *for* $(Ra - Ra_c)/Ra_c = 0.5$. 68

4.4 *Steady equilibrium solutions for* $Re_1 = 1$, $(Ra - Ra_c)/Ra_c = 0.5$ *demonstrating different coupling regimes at high and low* Pr. 69

4.5 *Bifurcation diagram of odd mode thermal convection for different Pr at* $d = 1.5$. 70

4.6 *Hysteresis between the convecting 3-cell flow and the rotating 2-cell flow for* $(Ra - Ra_c)/Ra_c = 0.2$. 70

4.7 *Mixed/odd equilibrium solutions for* $Re_1 = 1$, $(Ra - Ra_c)/Ra_c = 0.25$ *demonstrating different coupling regimes at high and low* Pr. 71

4.8 *Bifurcation loci illustrating the stable solutions in* Re_1, Ra *space for* $d = 3, Pr = 10$. 76

4.9 *Bifurcation diagram, showing the sequence of transitions as* Ra *is varied with fixed* $Re_1 = 5$, *plus the equilibrium solution* $\boldsymbol{X}_{PF}$ *and leading eigenvector* $\boldsymbol{q}_{PF}$. 78

4.10 *Bifurcation diagram, showing the sequence of transitions as* Ra *is varied with fixed* $Re_1 = 5$, *plus the equilibrium solution* $\boldsymbol{X}_{SN}$ *and leading eigenvector* $\boldsymbol{q}_{SN}$. 79

4.11 *Schematic of the anticipated fluid-flow due to Ekman pumping in the pole regions.* 80

4.12 *Temperature, radial velocity* u_r *and polar velocity* u_θ *profiles of the 1-cell solution for* $Re_1 = 33$. 81

4.13 *Bifurcation diagram showing the* u_r^- *solution branch for different* Re_1, *with the steady solution* $\boldsymbol{X}_{SN2}$ *and its leading eigenvector* $\boldsymbol{q}_{SN2}$ *at the saddle node* $SN2$. 81

4.14 *Latitudinally averaged* $\overline{T(r,\theta)}$ *and centreline* $T(r = 1+d/2, \theta)$ *profiles of the* u_r^+ *and 1-cell solutions for* $Re_1 = 33$. 82

4.15 *Energy spectrum of the steady solution vectors at* $Re = 50$ *using a resolution of* $Nr = 50$ *Chebyshev and* $N_\theta = 60$ *Legendre polynomials.* 83

4.16 *Bifurcation diagram, showing the sequence of transitions to time dependent states at* $Re_1 = 40$, *plus the equilibrium solution* $\boldsymbol{X}_{H_{\ell 2}}$ *and its leading eigenvector* $\boldsymbol{q}_{H_{\ell 2}}$. 84

4.17 *Bifurcation diagram, showing the sequence of transitions to time dependent states at* $Re_1 = 40$, *plus the equilibrium solution* $\boldsymbol{X}_{H_{\ell 1}}$ *and its leading eigenvector* $\boldsymbol{q}_{H_{\ell 1}}$. 86

4.18 *Transition from the 2-cell* u_r^+ *to the 1-cell solution for* $Re_1 = 40, Ra = 2.2 \times 10^4$. 87

4.19 *Snapshots of the temperature field demonstrating the time-periodic oscillation of the equatorial jet for* $Re_1 = 40, Ra = 2.2 \times 10^4$. 88

4.20 *Snapshots of the temperature field demonstrating the time-periodic oscillation of the polar plume for* $Re_1 = 5, Ra = 8 \times 10^3$. 89

4.21 *Snapshots of the temperature field demonstrating the time-periodic oscillation of the deflected polar plume for* $Re_1 = 30, Ra = 1.8 \times 10^4$. 90

4.22 *Plots of the norm of the stream-function* $||\psi||$ *against its rate of change* $||\dot{\psi}||$ *for the 2-cell solution* $u_r^+(t)$ *at* $Re_1 = 40$. 91

4.23 *Plots of the norm of the stream-function* $||\psi||$ *against its rate of change* $||\dot{\psi}||$ *for the 1-cell solution 1-cell(t) at* $Re_1 = 40$. 91

5.1 *Stability of the axisymmetric 2-cell solution* u_r^+ *for* $d = 3$*, shown in terms of the growth rate* $\Re(\lambda)$ *as* Ra *and* Re_1 *Pr are varied.* 99

5.2 *Stability of the axisymmetric 4-cell solution* u_r^+ *for* $d = 1$*, shown in terms of the growth rate* $\Re(\lambda)$ *as* Ra *and* Re_1 *Pr are varied.* 99

5.3 *Stability of the asymmetric 3-cell solution for* $d = 1.5$*, shown in terms of the growth rate* $\Re(\lambda)$ *as* Ra *and* Re_1 *Pr are varied.* 100

C.1 *Convergence of the vorticity* ξ *and temperature field* T *converge to their true solution as the grid-size* N_r *is increased.* 123

C.2 *Convergence of the specific angular momentum* Ω *and stream function fields* ψ *converge to their true solution as the grid-size* N_r *is increased.* 123

D.1 *Convergence of the steady-state solver to the known solution for Pr* $= 0.1, 1, 10$ *as measured using the* L^2 *norm.* 137

List of tables

3.1 *Comparison of DNS $(A, B)_{num}$ and weakly nonlinear $(A, B)_{wkly}$ solutions for the modes $\ell = 2, 3$.* 49

3.2 *Comparison of DNS and weakly non-linear solutions for the modes $\ell = 3, 4$.* 50

3.3 *Comparison of numerical and weakly non-linear solutions for the modes $\ell = 2, 4$.* 51

5.1 *Three-dimensional stability at large Pr of axisymmetric solutions to azimuthal perturbations of wavenumber m at each $(\ell, \ell+1)$ degeneracy.* 97

5.2 *Three-dimensional stability at large Pr of axisymmetric solutions to azimuthal perturbations of wavenumber m at each $(\ell, \ell+2)$ degeneracy.* 98

C.1 *Set of grid-sizes chosen for code validation.* 122

Contents

1 Introduction **1**

1.1 Motivation for studying a model of differentially rotation convection in a spherical shell 1

1.2 Description of the physical processes considered in this model 5

1.3 Previous work on thermal convection and differentially rotating spherical shells 7

1.4 Outline and approach taken in this thesis 10

2 Mathematical Model **13**

2.1 General equations of motion 13

2.2 Thermally convective spherical Couette flow 15

2.2.1 Axisymmetric formulation 16

2.2.2 Base states 18

2.3 Numerical methods 19

2.3.1 Steady-state solving 21

2.3.2 Linear stability 21

2.3.3 Time-stepping 21

2.3.4 Pseudo arc-length continuation 22

2.4 Model summary 23

3 Mode interactions in thermal convection **25**

3.1 Linear theory 27

3.2 Weakly nonlinear theory 32

3.2.1 Odd-odd mode interactions 33

3.2.2 Even-even & even-odd mode interactions 35
3.3 Analysis of amplitude equations 39
3.3.1 Neighbouring mode interactions 39
3.3.2 Non-neighbouring mode interactions 46
3.4 Comparison of weakly nonlinear theory with DNS 48
3.4.1 Neighbouring mode interactions 48
3.4.2 Non-neighbouring mode interactions 51
3.5 Transition to time-dependent convection 53
3.5.1 Bifurcation sequence for moderate Ra at low Pr 54
3.5.2 Bifurcation sequence for moderate Ra at high Pr . . . 56

4 Thermally convective spherical Couette flow 60
4.1 Model equations and solution regimes 60
4.1.1 Decoupled steady solutions 61
4.1.2 Role of Prandtl number 62
4.2 Primary bifurcations 65
4.2.1 Even solutions $d = 3$ 66
4.2.2 Odd solutions $d = 1.5$ 68
4.2.3 Symmetries 71
4.3 Numerical continuation of 1-parameter bifurcations 72
4.4 Flow transitions at large Ra, Re_1 75
4.4.1 Steady bifurcations 77
4.4.2 Stability of thermal boundary layers 82
4.4.3 Transition to time-dependence 82

5 Non-axisymmetric stability analysis 92
5.1 Thermal convection 96
5.1.1 Odd-even & even-odd interactions 97

5.1.2 Even-even interactions 98
5.2 Thermal convection with weak differential rotation 98
5.2.1 Symmetric even solutions 98
5.2.2 Asymmetric mixed solutions 100

6 Conclusion **102**
6.1 Further work 104

Appendix A Self adjointness of the operator $\mathcal{L}$ **105**

Appendix B Computation of amplitude equation coefficients **107**
B.1 Simplification of $\mathcal{O}(\epsilon^2)$ terms 107
B.2 Simplification of $\mathcal{O}(\epsilon^3)$ terms 115

Appendix C Axisymmetric finite-difference code **119**
C.1 Code validation 121

Appendix D Axisymmetric spectral code **124**
D.1 Finite difference method 126
D.1.1 Linear terms 126
D.1.2 Non-linear terms 129
D.2 Pseudo-spectral method 131
D.2.1 Linear terms 132
D.2.2 Non-linear terms 133
D.3 Galerkin projection 135
D.4 Validation of numerical code 136

Appendix E 3D stability numerical solution method **138**

1

Introduction

Motivated by the recent discovery that the *icy* moons of Jupiter and Saturn have subsurface oceans, this thesis investigates the motion of a rotating hot fluid between two spherical shells with self-gravitation. The main question which we attempt to answer is: Why the fluid motion in a spherical shell can have two different states for the same heating and rotation rate? To motivate this question we first give a brief overview of the astrophysical problem.

1.1 Motivation for studying a model of differentially rotation convection in a spherical shell

When considering the interior of a planet or satellite such as Earth or its moon, we typically picture a hot inner core which radiates heat. We assume that this heat, along with solar radiation prevents the planet from freezing over. Unlike Earth's moon however, many of Jupiter's and Saturn's moons are not internally heated, nor do they receive large amounts of radiation from the sun. Yet, successive missions have found that these planets have complex thermal behaviours (Nimmo & Pappalardo 2016). During the Galileo and Voyager missions, Jupiter's closest moon Io, was found to be extremely geologically active (Peale *et al.* 1979, Peale 2003), while its largest moon Ganymede was found to have a low moment of inertia suggesting the presence of multiple subsurface oceans (Schubert *et al.* 1981). Incidentally Ganymede also harbours a weak magnetic field (Saur *et al.* 2015), the only moon to do so. More recently the Cassini mission observed the outer surface

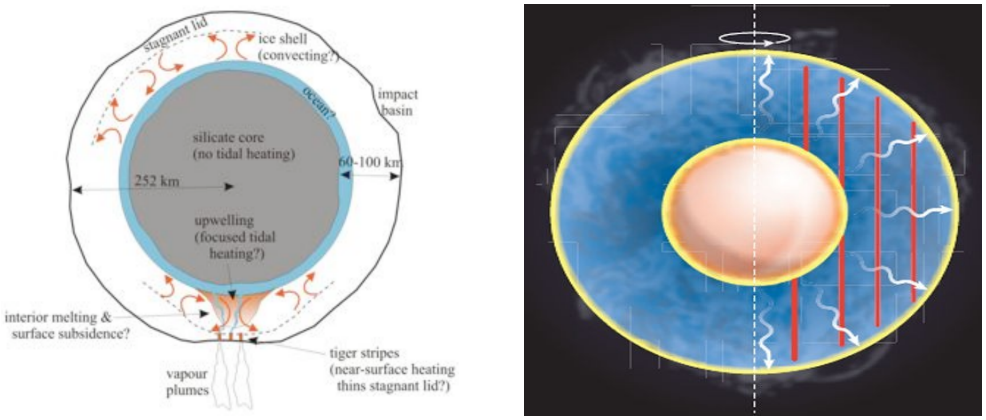
of Saturn's moon Enceladus *oscillating*, and during a subsequent flyby photographed and *sniffed* the emission of hydrogen and ice-crystals from Enceladus' south pole (Hansen *et al.* 2006, Spencer *et al.* 2006, Howett *et al.* 2011). Collectively these observations pose the following puzzle: If these moons are not heated internally, and their thermal history does not explain their current state, how is Io so geologically active? And how does Ganymede and Enceladus maintain their subsurface oceans from freezing?

Groups of Jupiter's and Saturn's moons orbit their parent planet eccentrically, but unlike Earth's moon which has evolved to become tidally locked, these moons maintain their eccentricity due to orbital resonances (Nimmo & Pappalardo 2016). As a consequence they also experience tidal forces which vary throughout their orbit. These forces exert stresses which result in plastic deformations of these moon's solid interiors, a process that dissipates energy, typically in the form of heat. The significance of this process was used by Peale *et al.* (1979) to successfully explain the source of Io's high degree of geological activity.

This idea is however more challenging to apply and less significant in determining the current state of Europa and Enceladus, as both moons have differentiated interiors consisting of solid and liquid layers. A schematic of Enceladus' proposed interior structure is shown in frame (a) of figure 1.1. It is inevitable that stresses applied to the moon will exhibit a different response within each layer, but as the layers couple with one-another their non-linear interactions must also be accounted for. A simple energy balance for Enceladus indicates however, that any heating due to tidal forces even when combined with optimistic estimates of the internal heat production cannot balance the heat lost from its outer shell (Tyler 2008).

The resolution of this puzzling behaviour, particularly in the case of Enceladus, appears to rely on the fluid motion in its subsurface ocean (Tyler 2008). In addition to tidal forces heating the moon's solid interior, they also cause its outer ice shell to oscillate back and forth (also termed *libration*) driving fluid motion in the oceans (cf. frame (a) of figure 1.1). Experiments and theoretical studies of libration driven flows in spherical shells, show that even when weakly forced, these flows become turbulent (Noir *et al.* 2009, 2012). It is suggested the fluid motion within these subsurface oceans is so vigorous that it dissipates energy, and that when accounted for, this energy dissipation may help balance the energy losses from the moon's surface (Tyler 2008, Wilson & Kerswell 2018).

To apply this idea however, requires an understanding of the ocean's general behaviour and how energy dissipation within the ocean depends on external forcing such as the libration amplitude or the core's radial heat flux. Experimentally, the measurement of energy dissipation is an extremely challenging task (Noir *et al.* 2012), as are numerical simulations due to the large range of relevant length-scales demanding resolution (Wilson & Kerswell 2018). In addition these investigations have not considered thermal effects, as to do so requires a zero gravity environment. While this is easily achieved in numerical



(a) Proposed interior structure for Saturn's moon Enceladus (Spencer *et al.* 2009).

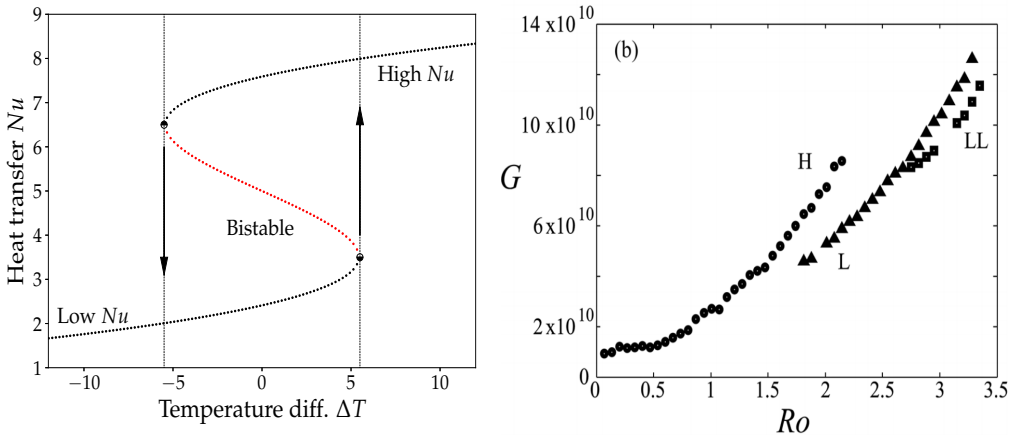
(b) Rapidly rotating convection between hot and cold spheres (Read 2009).

Figure 1.1: The moons of Saturn and Jupiter are believed to have subsurface oceans which lie beneath an icy outer shell. This is indicated for Saturn's moon Enceladus in frame (a). Plastic deformations cause *some* tidal heating in the moon's solid interior, while the outer ice shell rotates differentially to the core driving fluid motion. An interesting feature of this moon is that it emits vapour plumes from its south pole. (b) Convective heat transfer directed radially outwards is indicated by white arrows. The tendency of rotation to stabilise fluid motion by arranging it in concentric layers is shown in red.

experiments, it demands yet higher resolution.

An additional complication which arises in studying these systems is that there are often two or more equally favourable equilibria, such that only the system's history can determine its preferred state (figure 1.2). Although this behaviour is difficult to observe, it is believed to be of importance in the convective zone of stars where differential rotation is present Gastine *et al.* (2013). This phenomenon is also demonstrated in laboratory experiments of the turbulent flow between two rotating spheres allowing for differential rotation (Zimmerman *et al.* 2011), and in experiments of the turbulent flow in a cylindrical container, driven by counter rotating discs at its ends (Ravelet *et al.* 2004). Notably in each case, the fluid does not necessarily choose the state which minimises the driving torque required (cf. frame (b) of figure 1.2). Similarly in experiments of turbulent convection, where the mean circulation of convection cells abruptly switches direction (Sreenivasan *et al.* 2002), or in numerical experiments of geostrophic turbulence where the transition to a state with a different number of vortices occurs (Favier *et al.* 2019), bistability is also observed.

While the mechanisms leading to bistability are often well understood in simpler models governed by a small number of ordinary differential equations (ODEs), it is more complicated for partial differential equations (PDEs), particularly those which model fluid flows due to their high dimensionality, and yet more complex for turbulent flows which are ulti-



(a) Varying ΔT switches the system between two different states, but returning to the lower state we must decrease ΔT more than it was increased.

(b) Torque G vs. Ro the differential rotation strength (Zimmerman *et al.* 2011). When $2 \leq Ro \leq 2.25$ the system can occupy a high H or low L torque state.

Figure 1.2: Varying a control parameter, the systems in frames (a) and (b) transition between different equilibrium states upon reaching bifurcation points indicated by black circles. A parameter window exists for which these states are also bistable, such that only the history of the system determines the state it chooses. (a) As ΔT is varied in a model of convection, the convective heat transfer of each state can be simultaneously low or high. (b) Experiments of rapidly co-rotating spheres allowing for the inner sphere to rotate faster showed that the system does not evolve to minimise the torque (Zimmerman *et al.* 2011).

mately of the most relevance (Shtern & Hussain 1999, Simitev & Busse 2009). All scenarios are however extremely challenging to understand in the case of a non-autonomous system (Langa *et al.* 2002), where the system parameters or other effects such as the rotation rate (Noir *et al.* 2012) depend on time. The decrease in Ganymede's orbital eccentricity, which is linked to a reduction in the moon's tidal heating (Showman & Malhotra 1997) constitutes an example of this behaviour. We believe that it is crucial for many physical systems to try and understand the origin of bistability, and in the context of astrophysics particularly for those in which the transport of heat and angular momentum is important. Before outlining the approach undertaken in this thesis, the relevant physical processes are first described.

1.2 Description of the physical processes considered in this model

In a spherical shell geometry we consider differential rotation and thermal convection as shown in figure 1.3, where the fluid motion arising from these effects is also indicated. We allow the inner and outer spheres to rotate differentially $\omega_1 \neq \omega_2$ as shown in frame (a), and for thermal convection by keeping the inner sphere hotter than the outer $(T_1 - T_2) > 0$ as per frames (b),(c). Unless otherwise stated we assume a viscous fluid of low thermal diffusivity such that the Prandtl number $Pr = \nu/\kappa \gg 1$, where ν is the kinematic viscosity and κ the thermal diffusivity. This implies that thermal convection will be more significant than conduction, and that the velocity field will dictate the temperature field except in regions where thermal gradients are sufficiently large so that thermal diffusion can act. This regime is chosen on the basis that seawater has $Pr \geq 10$.

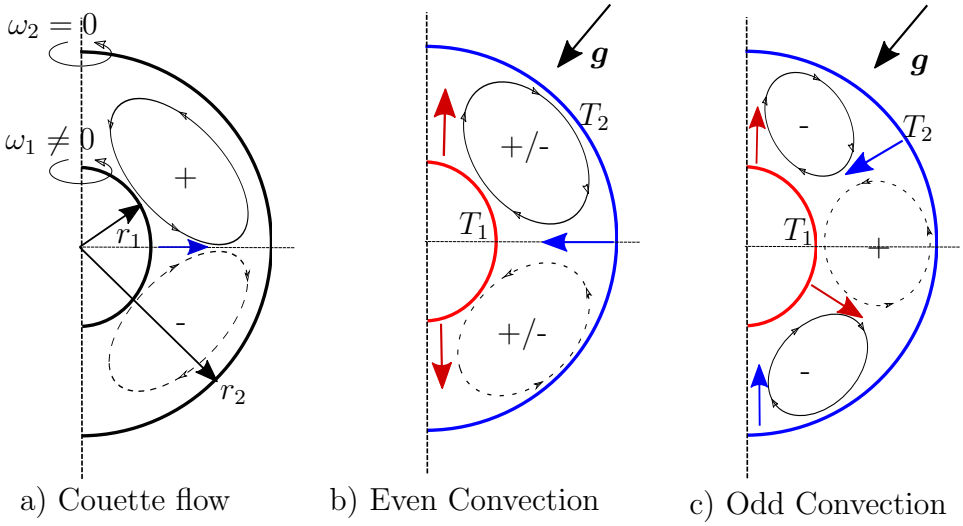


Figure 1.3: Schematic of the anticipated fluid-flow in a spherical annulus due to differential rotation (shear) or a destabilising thermal gradient (buoyancy). (a) Inner sphere rotation establishes a cellular pattern of fluid motion, originating from the need to transport high angular momentum fluid outwards at the equator, where the sphere's velocity is greatest. (b),(c) Thermal convection can establish even or odd cellular patterns depending on the annulus width. These cells transport lighter hot fluid outwards and draw cooler fluid inwards.

In frame (a) of figure 1.3, the flow configuration also referred to as spherical Couette flow is shown. Differential rotation of the spheres ($\omega_1 \neq \omega_2$) shears the flow imparting angular momentum to the fluid. As the annular domain is closed the fluid is forced to recirculate so that for small rotation rates, as characterised by the inner sphere Reynolds number $Re_1 = \omega_1 r_1^2/\nu$, the resulting imbalance generates a large scale flow containing

2-cells. These cells tend to localise about the equator where the velocity is greatest. A radial inflow or outflow is established at the equator in the direction of decreasing angular momentum. In frame (a) this is an equatorial outflow as $\omega_1 > \omega_2$. Provided the separation between is $d = (r_2 - r_1)/r_1 \leq 0.335$, 2-cells occupy the annulus (Junk & Egbers 2000).

In frames (b),(c) of figure 1.3 the behaviour of thermal convection is shown schematically. When the temperature gradient across the annulus as characterised by the Rayleigh number Ra (the ratio of buoyancy to viscous forces) becomes sufficiently steep a cellular flow succeeds the conductive state. In this convecting state hotter fluid with a lower density rises while colder heavier fluid sinks under the action of gravity. Theoretically, this behavioural tendency was first outlined by Rayleigh (1916) who demonstrated that a fluid layer heated from below becomes unstable to 2D rolls with a definite horizontal wavenumber. Similarly in a spherical shell, a different number of cells will occupy the annulus depending on the separation d between the spheres. This is shown schematically in frames (b) and (c) of figures 1.3 where an even 2-cell and odd 3-cell flow are depicted. Distinct from spherical Couette-flow, thermal convection can establish either an equatorial inflow or outflow. In addition, the cellular convecting state arises from a thermal instability while in spherical Couette-flow it is present for all $Re_1 \neq 0$.

It was indicated in frame (b) of figure 1.1, that astrophysical studies of rotating convection focus on the case of rapid co-rotation where the dominant physical balances are between the Coriolis and buoyancy forces. In this regime rotation tends to stabilise the flow such that it arranges itself in concentric layers of fluid known as Taylor columns (Proudman & Lamb 1916). Typically one takes into account these leading order effects first, and subsequently higher order effects such as differential rotation are considered. Although we allow for the possibility of both spheres rapidly co-rotating with differential rotation imposed, which is the most relevant configuration for the moons of Jupiter and Saturn (Wilson & Kerswell 2018), we do not consider this case. Instead we keep the outer sphere stationary throughout this thesis and rotate the inner sphere only ($\omega_1 \neq 0, \omega_2 = 0$).

This configuration is chosen with the purpose of understanding, how the flow facilitates the transport of angular momentum and heat, as the strength of the temperature gradient Ra and differential rotation Re_1 increase. According to the Rayleigh criterion (Taylor 1923) rotating the inner sphere (or counter rotating the spheres) presents the least stable configuration. Therefore we anticipate that the flow is more likely to transition to a more complicated state for smaller Ra, Re_1 when $Re_2 = 0$. It is also argued by Zimmerman *et al.* (2011) that bistability is associated with the breakdown or resilience of zonal flows such as jets and plumes. These flow features are easily accessible in the configuration considered. In addition many studies have focused on case of rapid rotation (Zhang & Liao 2017) but few have looked at the problem when only one of the spheres is rotated. This makes it possible to demonstrate new findings that are hopefully of general relevance. Finally from a numerical point of view, to study rapidly rotation convection allowing for

differential rotation is a numerically challenging task (Heimpel & Aurnou 2012).

In addition to rapid rotation, we omit numerous other potentially relevant physical effects. It is possible that the moon's subsurface oceans are saline (Spencer *et al.* 2006), have a temperature dependent viscosity (Travnikov *et al.* 2017) or that the ice shell has a varying topography (Rovira-Navarro *et al.* 2019). The model we investigate is nevertheless still highly complex, and the approach we adopt therefore is to consider its simplest aspects first, and subsequently increase its complexity.

1.3 Previous work on thermal convection and differentially rotating spherical shells

Motivated by convective processes in the Earth's mantle and the pattern forming nature of the problem, thermal convection in a spherical shell has received considerable attention. Similarly the spherical Couette problem which is closely related to the flow between cylinders (Taylor Couette-flow) has a long history of both experimental and numerical investigation. The combined problem however has comparatively few previous studies.

Thermal Convection in a spherical shell

The linearised stability of thermal convection in a spherical shell was first considered by Chandrasekhar (1961) and in a more complete manner by Joseph & Carmi (1966) using an energy method. Both identified the stability threshold for convective motion and remarked upon the significance of the purely conductive thermal base state and functional form of gravity chosen. However neither work made evident the Prandtl number dependence, nor addressed the $2\ell + 1$ fold degeneracy of the linear problem to establish the preferred solution at onset. Throughout this thesis we define ℓ, m to be the degree and order of the spherical harmonic Y_ℓ^m.

Ignoring the radial structure, Busse (1975) and Busse & Riahi (1982) tackled the problem of degenerate mode selection, revealing the potential for numerous patterns or solutions. Applying bifurcation theory and group theoretical methods, Chossat (1978) performed a detailed analysis of the non-rotating and slowly rotating problem, focusing in particular on the spectral properties of the linearised governing equations. Evoking these results he described the possible solutions for a single, even spherical harmonic $Y_{\ell=2}^m$, and identified stable axisymmetric solutions which bifurcate supercritically. Approaching the problem in a similar manner Friedrich & Haken (1986) studied the interaction of modes $\ell = 1, 2$ near onset to identify concretely the presence of complicated time-dependent behaviour. The most recent work in this direction has been undertaken by Matthews (2003), who considered the existence and stability of patterns of even ℓ on a sphere's surface, indicating a

preference for icosahedral patterns. While Beltrame & Chossat (2015) who were concerned primarily with the configuration of the GeoFlow experimental apparatus (Futterer *et al.* 2010), applied a centre manifold reduction to derive a reduced order model for the set of spherical harmonics of degrees $\ell = 3, 4$.

Young (1974) conducted the first numerical study of 3D spherical convection including azimuthal dependence using a Galerkin projection, but was restricted to hemispheres. With limited computational resources he focused on particular cases, but nonetheless demonstrated a strong dependence on the Prandtl number, shell separation and initial conditions chosen. Notably he found stable time-periodic solutions for particular parameter values. The majority of subsequent studies were motivated by the Earth's core and therefore focused on in the infinite Prandtl number case. The axisymmetric problem and its stability to 3D perturbations has been investigated by Zebib *et al.* (1980, 1983), while Bercovici *et al.* (1989), King *et al.* (2010) studied the fully 3D case.

Recent numerical work is motivated by the GeoFlow experiment (Futterer *et al.* 2010), a spherical fluid annulus in which gravity is modelled by a radial electrostatic potential. Studies by Feudel *et al.* (2011) and Li *et al.* (2005) highlight the multiplicity of solutions that can be obtained in this system, while Travnikov *et al.* (2017) studied the influence of variable viscosity on the cellular pattern selected near the onset of convective motions. In addition he provided a comparison of results obtained numerically, with those of the GeoFlow experiment.

The most recent and comprehensive numerical work is that of Gastine *et al.* (2015), which considered Ra up to 10^9. For fixed $Pr = 1$, they considered a variety of gravity models and shell separations to determine their effect on the asymmetry between the inner and outer boundary layers. They demonstrated that in wide shells the boundary layer asymmetry is largest, but that it reduces with the separation. The scaling dependence on Ra of the convective heat transfer Nu and convective Reynolds number, which differ from other geometries were also computed.

Additional reviews of thermal convection in planar geometries are given by Gettling (1998), (Bodenschatz *et al.* 2000) for low Prandtl numbers and (Moore & Weiss 1973) for larger Prandtl numbers.

Spherical Couette-flow

Following initial analytical studies by Munson & Joseph (1971a,b), the problem was investigated experimentally by Wimmer (1976, 1981), who identified the possibility of solutions with 2 (as per frame (a) of figure 1.3), 4 and 6 cells. By identifying two of these equilibria for the same parameter values, the study confirmed that the governing system of equations has non-unique solutions. Critically, the work also emphasised the combined importance

of initial conditions and accelerations (recipes) to correctly approach different solutions. Later experimental work which focused on the transition between flows, also reported that the equilibria could be equatorially asymmetric (Bühler 1990).

The sequence of possible states adopted as Re_1 increases, and the transitions which occur between these states was investigated numerically by Marcus & Tuckerman (1987a,b) for $d = 0.18$. Using numerical continuation Mamun & Tuckerman (1995) also confirmed the experimental findings of (Bühler 1990) numerically, and outlined the sequence of bifurcations by which an equatorially asymmetric state originates.

Considering wider shell separations it was established by (Junk & Egbers 2000) that for $d \geq 0.335$, only the 2-cell flow persists as Re_1 is increased. Computing the stability of the axisymmetric state to non-axisymmetric disturbances for various d, Hollerbach *et al.* (2006) demonstrated the narrow gap case remains axisymmetric for a larger range of Re_1 and subsequently transitions directly to a turbulent state. In contrast, for wider gaps the 2-cell state transitions to a 3D state with azimuthally travelling waves for lower Re_1, which in turn transitions to a turbulent state.

Although we do not consider the effect of weak differential rotation in a rapidly co-rotating system, it is also worth mentioning the behaviour anticipated in this configuration. This problem has been investigated theoretically by Proudman (1956), who showed that outside the inner sphere's tangent cylinder Taylor columns persist, and that cellular motions are typically confined to higher latitudes within the inner sphere's tangent cylinder. These regions are typically separated by a free shear layer also termed the Stewartson layer. The stability of this layer has been considered numerically by Hollerbach *et al.* (2006) and more recently in experiments by Hoff & Harlander (2019).

Thermal convection with differential rotation in a spherical shell

Four works have studied the composite effects of differential rotation and thermal convection in spheres. The studies of Yanase *et al.* (1995) and Araki *et al.* (1996) allow for rotation of the inner sphere with fixed $Pr = 7$ and separation $d = 0.45$. Assuming the system is azimuthally axisymmetric and by (restrictively) enforcing equatorial symmetry they consider even solutions only. Numerically solving for steady state solutions Yanase *et al.* (1995) identified multiple solution branches for the same parameter values, while Araki *et al.* (1996) associated the imperfect pitchfork bifurcation encountered with the asymmetry introduced by differential rotation. Loukopoulos (2004) also studied the axisymmetric system numerically, but allowed for equatorial asymmetry in contrast to Yanase *et al.* (1995) and Araki *et al.* (1996). Varying Ra, while keeping $Pr = 1, d = 0.18$ and Re_1 fixed, asymmetric solutions and the transitions towards a solution state with a

progressively larger number of Taylor vortices was reported.

Recently Inagaki *et al.* (2019) considered the fully 3D problem with fixed $Pr = 1$ and the separation $d = 1$. Numerically they showed that for small Re_1, the Ra at which the onset of 3D convection occurs increases with Re_1, while for large $Re_1 \approxeq 500$ it is reduced. In addition they showed that increasing Re_1 for fixed Ra, the flow transitions to a non-axisymmetric state, but that the resulting transition does not necessarily increase the torque or heat transfer. Their (Re_1, Ra) stability diagram (although constructed in an imprecise fashion) indicates that the axisymmetric 2-cell solution is preferred for a large range of parameter space.

1.4 Outline and approach taken in this thesis

This thesis is structured as follows. In chapter 2 we start by outlining our assumptions and the equations governing the 3D flow. Making the additional assumption of azimuthal axisymmetry, we also outline their axisymmetric formulation, the case on which we focus predominantly in this thesis. Rather than proceeding to study the combined effect of thermal convection and differential rotation, we first study the convection problem in chapter 3. Having developed an understanding for this aspect of the problem, we then introduce differential rotation in chapter 4. Finally in chapter 5 non-axisymmetric effects are considered. Throughout this thesis linear and weakly nonlinear theory are used in tandem with numerical methods to inform and help understand the physical mechanisms responsible for transitions between solution states, such as those outlined in figure 1.2.

Thermal convection problem

To this end we begin by studying the linear convection problem in section 3.1 for which the eigenfunctions are found analytically and the dependence of the Rayleigh number Ra on the separation d is outlined. By solving the linear problem, we also indicate how the number of convection cells depends on the shell separation d, and that for certain critical points or values of d and Ra two cellular patterns can simultaneously become unstable. Using the sensitivity of these points to parameter changes, we employ weakly nonlinear theory in section 3.2 to derive a set of ODEs which describe the amplitude of each convection pattern. This allows us to study the simplest non-linearity possible, involving only two coupled modes and serves to demonstrate how the geometry influences the dynamics and possible solutions of this thermal convection problem.

In section 3.3 the parameter dependent coefficients which arise in these ODEs are determined. Numerical continuation is then used to outline the possible solutions of these ODEs including the presence of bistable solutions. The analytical predictions made using these

equations are then verified against those predicted by DNS in section 3.4, where we also relate the structure of the ODEs to the time dependent behaviour computed using DNS. Guided by the ODE model, we then use numerical continuation to study the behaviour of convection at large Ra in section 3.5. Focusing in particular on how the heat transfer and stability of different bistable solutions compares. We numerically demonstrate the relevance of thermal boundary layers, at both the sphere walls and poles in determining the preferred solution.

Thermal convection problem with differential rotation

In section 4.1 we present the solutions of the full problem. Firstly when there is only rotation and subsequently when their is only thermal convection. This serves to demonstrate the similarity of the spatial solutions for each problem at small Re_1, Ra (as illustrated schematically in figure 1.3). Weakly nonlinear theory is then used to obtain a variation of the ODEs derived in chapter 3. In turn the solutions of these ODEs are used to provide a starting point for numerical continuation. In section 4.2 we demonstrate how the transition to convection is modified by rotation, and how the Prandtl number determines whether the transition from an even to an odd number of cells (cf. figure 1.3) exhibits hysteresis.

Using the transitions points or bifurcation points identified in this small parameter regime we then perform 2-parameter continuation in section 4.3. This allows us to efficiently outline all possible solutions in Re_1, Ra space and to understand the physical mechanisms underlying the transition between solutions states akin to those depicted in figure 1.2. By using the eigenfunctions and solutions computed exactly at these bifurcation points, we demonstrate that the solution favoured by strong rotation is destabilised by a disturbance localised at the equator, and similarly that the solution favoured by strong thermal convection is destabilised by a disturbance localised at poles.

3D stability of axisymmetric solutions

To validate our restriction to axisymmetry in chapters 3,4 we then compute the stability of axisymmetric states to non-axisymmetric disturbances. In section 5.1 we show that although axisymmetric solutions of the thermal convection problem are unstable for small Ra, they are stable for moderate Ra. In section 5.2 it is shown that allowing for weak differential rotation, an axisymmetric solution of the thermal convection problem, although unstable for $Re_1 = 0$ is stabilised as Re_1 increases.

Finally in chapter 6 we conclude by summarising the main results of this thesis and outline

possible directions for future work.

Publications

The content of chapter 3 is largely based on the following publication:

Mannix P. & Mestel J. (2019) Weakly nonlinear mode interaction in spherical Rayleigh-Bénard convection, Journal of Fluid Mechanics, Vol 874, DOI: https://doi.org/10.1017/jfm.2019.440

2

Mathematical Model

In this section we outline the assumptions and derive the system of equations describing the physical model considered in this thesis. Subsequently we outline the model geometry, boundary conditions and non-dimensional parameters.

2.1 General equations of motion

Denoting the position vector by $\boldsymbol{r}$ and time by t, the variables $\boldsymbol{u} = \boldsymbol{u}(\boldsymbol{r}, t), \rho = \rho(\boldsymbol{r}, t), p = p(\boldsymbol{r}, t)$ are the fluid velocity, density and pressure respectively and ∇ is the gradient operator. The motion of a weakly-compressible Newtonian fluid in a stationary frame of reference is described by

$$\frac{D\boldsymbol{u}}{Dt} = -\frac{1}{\rho_0}\nabla p + \frac{\rho \boldsymbol{g}}{\rho_0} + \nu \nabla^2 \boldsymbol{u} \tag{2.1a}$$

$$\frac{DT}{Dt} = \kappa \nabla^2 T, \tag{2.1b}$$

$$\nabla \cdot \boldsymbol{u} = 0, \tag{2.1c}$$

$$\rho = \rho(p, T), \tag{2.1d}$$

where constants ν, κ are the kinematic viscosity and thermal diffusivity respectively. The terms on the right hand side of (2.1a) starting with ∇p account for non-local hydrostatic forces, $\rho \boldsymbol{g}$ gravitational forces and $\nu \nabla^2 \boldsymbol{u}$ non-conservative frictional forces. The material

derivative given by

$$\frac{D}{Dt} = \frac{\partial}{\partial t} + \boldsymbol{u} \cdot \nabla, \tag{2.2}$$

accounts for the rate of change that a fluid element experiences as it is moves with the flow. The partial derivative $\partial/\partial t$ is the rate of change at a fixed point in space, while the term $\boldsymbol{u} \cdot \nabla$ describes advection and accounts for accelerations due to spatial gradients in the flow.

We allow the fluid to be weakly-compressible by adopting the Boussinesq approximation, which assumes that density variations are of significance only in the buoyancy forces. Assuming that a judiciously chosen thermodynamic equilibrium (typically an average over the fluid layer depth) denoted by subscript zero exists, and that the density varies linearly about this thermodynamic equilibrium, (2.1d) is expanded to yield

$$\rho = \rho_o + (\partial_T \rho)_0 \delta T + (\partial_p \rho)_0 \delta p + \mathcal{O}(\delta T^2, \delta p^2). \tag{2.3}$$

Assuming that temperature fluctuations δT are small, and that $|\boldsymbol{u}|$ is much smaller than the speed of sound that pressure fluctuations δp can also be neglected. Taking the thermal expansion to be a constant $\hat{\beta}$ we can write

$$\rho = \rho_o(1 + \hat{\beta}\delta T). \tag{2.4}$$

This assumption remains valid provided the quantity $|\hat{\beta}\delta T|$ and temperature gradients over the fluid layer remain small (Gough 1969). Its validity in the context of astrophysical fluid dynamics where magnetic buoyancy may also be of significance is discussed by (Spiegel & Weiss 1982).

In all subsequent sections in thesis we will assume equations (2.1) hold and consider these only. It is noted however that our assumption of a Newtonian fluid applies only when ν does not depend on strain, as distinct from viscoelastic fluids such as cornstarch or ice where ν is typically a nonlinear function of strain. In addition while (2.1c) applies in all scenarios where the effect of acoustic motions is small, and variations in density due to temperature are small. The relation (2.1d) applies only for fluids of a single species and requires modification for multi-species fluids such as saline oceans and thermohaline convection in stars (Turner 1974). We now proceed by outlining the system geometry and boundary conditions for this model.

2.2 Thermally convective spherical Couette flow

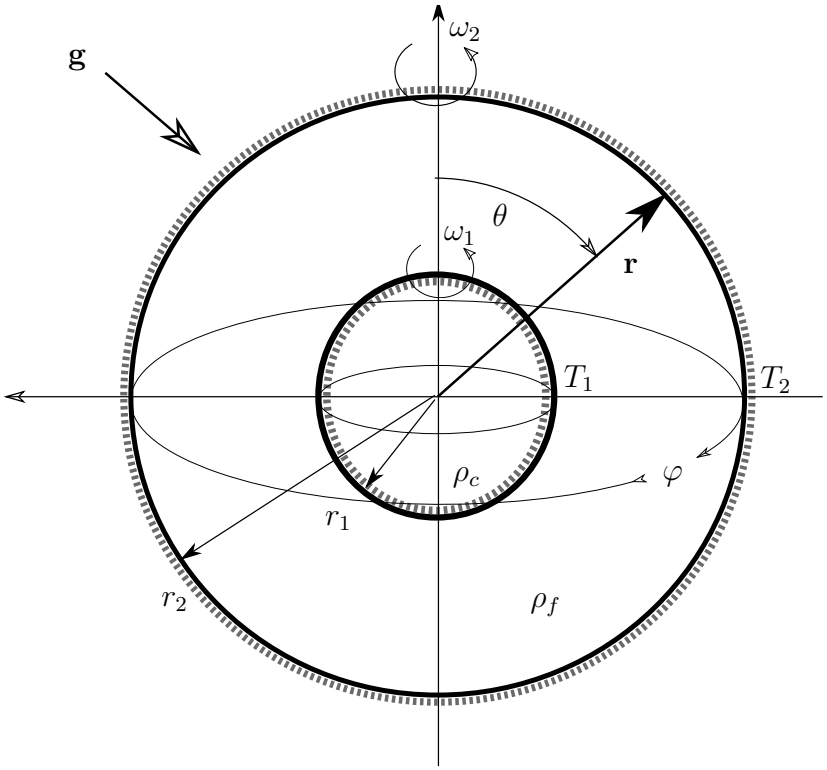


Figure 2.1: The fluid domain is a closed annular region between two concentric spheres, of radii r_1, r_2. Each sphere maintains a constant surface temperature T_1, T_2, rotating with an angular velocities ω_1, ω_2 respectively and gravity $\boldsymbol{g}$ acts radially inward. The inner core has a density ρ_c and the fluid annulus ρ_f.

As shown in figure 2.1, we consider convection in a spherical annulus of separation $r_2 - r_1$ allowing for differential rotation of the spheres' $\omega_1 \neq \omega_2$. Constant temperatures T_1, T_2 are prescribed at the spheres' boundaries, with difference $\Delta T = T_1 - T_2 > 0$.

We assume a Boussinesq fluid with density ρ_f that varies linearly with temperature fluctuations according to the relation

$$\rho = \rho_f[1 + \hat{\beta}(T_0(r) - T(r, \theta, t))], \tag{2.5}$$

where the thermal expansion coefficient $\hat{\beta}$ is small and $T_0(r)$ is the conductive base state.

The spherically symmetric gravity field is expressed as

$$\mathbf{g} = -g_0 g(r)\boldsymbol{r} = -g_0[(1-\eta)\frac{r_1^2}{r^3} + \eta\frac{1}{r_1}]\boldsymbol{r}, \quad \eta = \frac{\rho_f}{\rho_c}, \tag{2.6}$$

where gravity is normalised such that at the inner sphere surface $g(r_1) = 1$, and g_0 is the acceleration due to gravity on the inner sphere's surface. Throughout this thesis we consider the case $\eta = 0$, corresponding to an inner core density much greater than that of the outer fluid. The motivation for this choice is outlined in chapter 3.

Choosing the length scale r_1, thermal diffusion time scale r_1^2/κ and ΔT as the temperature scale, non-dimensionally equations (2.1) may be written

$$\frac{1}{Pr}\left(\frac{D\boldsymbol{u}}{Dt} + \nabla p\right) = \mathrm{Ra}\, g(r)\boldsymbol{r}T + \boldsymbol{\nabla}^2\boldsymbol{u}, \tag{2.7a}$$

$$\frac{\partial T}{\partial t} + \boldsymbol{u}\cdot\nabla T = \nabla^2 T, \qquad \boldsymbol{\nabla}\cdot\boldsymbol{u} = 0, \tag{2.7b}$$

where p contains pressure and gradient like terms. In addition we specify no-slip boundary conditions for $\boldsymbol{u}$ and assume perfectly conducting spherical shells for T at the spheres' walls.

$$\begin{aligned} &\boldsymbol{u}(r=1,\theta,\varphi) = Re_1 Pr\sin\theta\,\hat{\boldsymbol{\varphi}}, \quad \boldsymbol{u}(r=1+d,\theta,\varphi) = Re_2 Pr\sin\theta\hat{\boldsymbol{\varphi}}, \\ &T(r=1,\theta,\varphi) = 1, \quad T(r=1+d,\theta,\varphi) = 0. \end{aligned} \tag{2.8}$$

For reference, it is convenient to define the following parameters

$$\left.\begin{array}{lll} Pr & = \nu/\kappa & \\ \mathrm{Ra} & = \frac{g_0\beta\Delta T r_1^3}{\nu\kappa} & \\ \mathrm{d} & = \frac{r_2-r_1}{r_1} & \\ Re_1 & = \frac{\omega_1 r_1^2}{\nu} & \\ Re_2 & = \frac{\omega_2 r_2^2}{\nu} & \end{array}\right\} \begin{array}{r} \text{Prandtl Number} \\ \text{Rayleigh Number} \\ \text{Annulus Width} \\ \text{Inner Reynolds Number} \\ \text{Outer Reynolds Number} \end{array} \tag{2.9}$$

2.2.1 Axisymmetric formulation

Throughout this thesis we concentrate primarily on the axisymmetric system which is now outlined. While this reduced system assumes that all longitudinal variations $\partial/\partial\varphi = 0$, we do not however discount the possibility of 3D motions. The approach we adopt rather

is to solve for axisymmetric solutions of (2.7) and subsequently compute their stability to 3D perturbations. In this manner we verify if a given axisymmetric solution represents a stable 3D state.

The motivation for this approach is twofold. Firstly on physical grounds, experiments show that spherical Couette flow is axisymmetric for moderate inner sphere Reynolds numbers $Re_1 \neq 0, Re_2 = 0$ (**?**Hollerbach *et al.* 2006). While spherical shell convection is typically 3D for $Pr \ll 1$, in the limit $Pr \to \infty$ numerical computations show that axisymmetric solutions are stable for wide separations $d \geq 0.5$ (Zebib *et al.* 1980, 1983). Secondly in the interest of simplicity, the axisymmetric case is easier to treat both analytically and numerically, and represents an appropriate starting point from which valuable insights can be obtained.

The axisymmetric flow $\boldsymbol{u}$ is described by a stream-function $\psi(r,\theta,t)$ and specific angular momentum $\Omega(r,\theta,t)$

$$\boldsymbol{u} = \nabla \times \big(0, 0, \frac{\psi}{r\sin\theta}\big) + \big(0, 0, \frac{\Omega}{r\sin\theta}\big) = \left(\frac{1}{r^2\sin\theta}\frac{\partial\psi}{\partial\theta}, \frac{-1}{r\sin\theta}\frac{\partial\psi}{\partial r}, \frac{\Omega}{r\sin\theta}\right), \tag{2.10}$$

for which the vorticity vector $\boldsymbol{\omega}$ can be expressed as

$$\boldsymbol{\omega} = \nabla\times\boldsymbol{u} = \left(\frac{1}{r^2\sin\theta}\frac{\partial\Omega}{\partial\theta}, \frac{-1}{r\sin\theta}\frac{\partial\Omega}{\partial r}, \frac{-D^2\psi}{r\sin\theta}\right), \quad \text{where} \quad D^2 = \frac{\partial^2}{\partial r^2} + \frac{\sin\theta}{r^2}\frac{\partial}{\partial\theta}\left(\frac{1}{\sin\theta}\frac{\partial}{\partial\theta}\right). \tag{2.11}$$

Substituting (2.10) into (2.7) we obtain the following system, for which the flow is completely described by its azimuthal vorticity ω_φ, temperature T and specific angular momentum Ω

$$\frac{\partial D^2\psi}{\partial t} + \mathcal{J}(\psi,\psi) + N_1(\Omega,\Omega) = Pr\left(\mathrm{Ra}\, g(r) r\frac{\partial T}{\partial\theta}\sin\theta + D^2D^2\psi\right), \tag{2.12a}$$

$$\frac{\partial T}{\partial t} + J(\psi,T) = \nabla^2 T, \tag{2.12b}$$

$$\frac{\partial\Omega}{\partial t} + J(\psi,\Omega) = PrD^2\Omega, \tag{2.12c}$$

where

$$J(f,g) = \frac{1}{r^2\sin\theta}\frac{\partial(f,g)}{\partial(\theta,r)}, \quad \mathcal{J}(f,g) = \sin\theta\frac{\partial(f, D^2g/(r^2\sin^2\theta))}{\partial(\theta,r)}, \tag{2.13}$$

and

$$N_1(f,g) = \frac{2f}{r^2\sin\theta}\big(\cot\theta\frac{\partial g}{\partial r} - \frac{1}{r}\frac{\partial g}{\partial\theta}\big). \tag{2.14}$$

In this framework the no-slip and perfect conductor boundary conditions become

$$\begin{aligned}
&\psi(r,\theta) = \psi_r(r,\theta) = 0, \quad \text{for } r = 1, 1+d \\
&T(1,\theta) = 1, \quad T(1+d,\theta) = 0, \\
&\Omega(1,\theta) = Re_1\, Pr \sin^2\theta, \quad \Omega(1+d,\theta) = Re_2\, Pr \sin^2\theta.
\end{aligned} \tag{2.15}$$

In addition the following symmetry conditions must be enforced at the symmetry axis

$$\psi(r,\theta) = \Omega(r,\theta) = T_\theta(r,\theta) = 0, \quad \text{for} \quad \theta = 0, \pi, \tag{2.16}$$

By choosing the polar basis functions to be the Legendre $P_\ell(\cos\theta)$ polynomials for T and the Gegenbauer polynomials $G_\ell(\theta) = \sin\theta\partial_\theta P_\ell(\cos\theta)$ for ψ, Ω, these conditions are naturally enforced.

2.2.2 Base states

In the model system we consider (2.12), fluid motion can be maintained either by a sufficiently large thermal gradient when $Ra \geq Ra_c$, the threshold at which the thermal conduction states is destabilized and thermal convection ensues, or by differential rotation (wall shear) for $Re_{1,2} \neq 0$. These forcings correspond to the two solution regimes of (2.12) whose base states we now outline.

When $Re_1 = Re_2 = 0$ we obtain the thermal convection problem. In this case the temperature equation admits the purely conductive base state $T_0(r)$ which is obtained by solving $\nabla^2 T = 0$ with boundary conditions (2.15). This yields

$$\frac{dT_0}{dr} = \frac{A_T}{r^2}, \quad T_0 = -A_T/r + B_T, \quad A_T = \frac{1+d}{-d}, \quad B_T = \frac{1}{-d}, \tag{2.17}$$

implying that temperature gradients are greatest near the inner sphere's surface.

For $Ra = 0$ and $Re_1 \ll 1, Re_2 \ll 1$ equations (2.12) admit a Stokes solution $\Omega_0(r,\theta)$ which is obtained by solving $D^2\Omega = 0$ with boundary conditions (2.15) giving

$$\begin{aligned}
\Omega &= PrRe_1\Omega_0(r,\theta) + \mathcal{O}(PrRe_1^3) = PrRe_1\big(\tilde{a}\, r^2 + \frac{\tilde{b}}{r}\big)G_1(\theta) + \mathcal{O}(PrRe_1^3), \\
\psi &= PrRe_1^2\psi_0(r,\theta) + \mathcal{O}(PrRe_1^4) = PrRe_1^2 f(r)G_2(\theta) + \mathcal{O}(PrRe_1^4),
\end{aligned} \tag{2.18}$$

where

$$\tilde{a} = -\left(\frac{Re_2/Re_1(1+d) - 1}{(1+d)^3 - 1}\right), \quad \tilde{b} = \frac{-(1+d)\big((1+d)^2 - Re_2/Re_1\big)}{(1+d)^3 - 1}, \tag{2.19}$$

and $f(r)$ is a known quintic polynomial (Munson & Joseph 1971b,a). Notably this basic state is not a simple function of a single spatial variable but instead depends on both r & θ. This leads to a cellular background flow $\psi(r,\theta)$ for all non-zero Re_1, Re_2, excluding the case of solid body rotation when $\omega_1 = \omega_2$.

It is because this cellular flow always exists for non-zero rotation, rather than arising from an instability that makes the analysis of this convection problem non-standard. The expansion (2.18) in the small Re_1 regime has been shown by Munson & Joseph (1971b) to accurately represent the non-linear solution of equation (2.12) for $Ra = 0, Re_1 \leq 1$. To study (2.12) outside this regime however demands the use of numerical methods.

2.3 Numerical methods

In this section the numerical methods used to solve for steady-states, time-evolution and to determine the linear stability of a general 2D steady-state are outlined. We adopt the vector notation

$$\boldsymbol{X} = \begin{pmatrix} \psi & T & \Omega \end{pmatrix}^T \tag{2.20}$$

to describe an axisymmetric state such that in matrix form the equations are

$$\mathcal{M}\frac{\partial \boldsymbol{X}}{\partial t} = \boldsymbol{\mathcal{F}}(\boldsymbol{X}, \boldsymbol{\mu}) \equiv \boldsymbol{\mathcal{N}}(\boldsymbol{X}, \boldsymbol{X}) + \mathcal{L}\boldsymbol{X} + \boldsymbol{F}, \quad \text{where} \quad \boldsymbol{\mu} = (Pr, \mathrm{Ra}, Re_1, Re_2). \tag{2.21}$$

The vector $\boldsymbol{F}$ and matrix operator $\mathcal{L}$ contain terms resulting from the transformation

$$\tilde{\psi} = \psi(r,\theta,t), \quad \tilde{T} = T(r,\theta,t) + T_0(r), \quad \tilde{\Omega} = \Omega(r,\theta,t) + Pr\, Re_1 \Omega_0(r,\theta), \tag{2.22}$$

used to enforce that in (2.21) $\boldsymbol{X}$ must satisfy homogeneous boundary conditions only where the functions T_0, Ω_0 are given by (2.17),(2.18). The 3×3 matrices $\mathcal{M}, \mathcal{L}$ are linear differential operators of the form

$$\mathcal{M} = \begin{pmatrix} D^2 & 0 & 0 \\ 0 & \mathbb{I} & 0 \\ 0 & 0 & \mathbb{I} \end{pmatrix}, \quad \mathcal{L} = \begin{pmatrix} Pr\, D^2 D^2 & Pr\,\mathrm{Ra}\, g(r) r \sin\theta \frac{\partial}{\partial\theta} & \mathcal{N}(\Omega_0) \\ \frac{-T_0'(r)}{r^2\sin\theta}\frac{\partial}{\partial\theta} & \nabla^2 & 0 \\ -\frac{1}{r^2\sin\theta}\frac{\partial(\ ,\Omega_0)}{\partial(\theta,r)} & 0 & Pr\, D^2 \end{pmatrix}, \tag{2.23}$$

and the vector $\boldsymbol{F}$ is given by

$$\boldsymbol{F} = \begin{pmatrix} -2\,Pr^2\left(\frac{\tilde{a}\tilde{b}}{r^2} + \frac{\tilde{b}^2}{r^5}\right)G_2(\theta) \\ 0 \\ 0 \end{pmatrix}, \tag{2.24}$$

where $\tilde{a}, \tilde{b}$ are as defined in (2.19), and the operator $\mathcal{N}(\Omega_0)$ is given by

$$\mathcal{N}(\Omega_0)\Omega = -\frac{2\Omega}{r^2 \sin\theta}\left(\cot\theta \frac{\partial \Omega_0}{\partial r} - \frac{1}{r}\frac{\partial \Omega_0}{\partial \theta} \right) - \frac{2\Omega_0}{r^2 \sin\theta}\left(\cot\theta \frac{\partial \Omega}{\partial r} - \frac{1}{r}\frac{\partial \Omega}{\partial \theta} \right). \tag{2.25}$$

The nonlinear term is given by the vector

$$\boldsymbol{\mathcal{N}}(\boldsymbol{X}, \boldsymbol{X}) = \begin{pmatrix} -\sin\theta \frac{\partial(\psi, D^2\psi/(r^2\sin^2\theta))}{\partial(\theta, r)} - \frac{2\Omega}{r^2\sin\theta}\left(\cot\theta \frac{\partial \Omega}{\partial r} - \frac{1}{r}\frac{\partial \Omega}{\partial \theta} \right) \\ -\frac{1}{r^2\sin\theta}\frac{\partial(\psi, T)}{\partial(\theta, r)} \\ -\frac{1}{r^2\sin\theta}\frac{\partial(\psi, \Omega)}{\partial(\theta, r)} \end{pmatrix}. \tag{2.26}$$

To solve (2.21) numerically we must use a discrete representation of the vector $\boldsymbol{X}$ and define the associated differentiation matrices. We employ two different methods. A finite difference stencil in both spatial directions (restricted to perform time-stepping only) which is outlined in appendix C, and a Galerkin-Legendre projection in θ combined with a Chebyshev psuedo-spectral method in r which is outlined in appendix D. In addition to satisfying the polar boundary conditions exactly, the spectral method is chosen on the basis that wide shells (the case on which we will focus) tend to concentrate energy amongst lower mode numbers thus reducing the necessary vector dimensions. Given that the numerical complexity of computing non-linear terms scales as $\mathcal{O}(N^3)$ for Galerkin projection methods, where N is taken to be the vector dimension, it is unsuitable for thin layers requiring even moderately large N. The convergence of each code's discrete representation as N increases is verified by computing numerical approximations of a known solution, and where possible demonstrating that it also agrees with asymptotic scaling relations. This is outlined in appendices C,D.

The motivation for developing two distinct codes stems from the restrictions associated with finite difference methods, in particular their ability to accurately resolve the fine scales which typically emerge in the near wall boundary layer regions (Trefethen 2000). This is overcome by use of spectral methods, which concentrate resolution in the near wall region(s) to circumvent this difficulty. While spectral methods are numerically more intensive, they typically achieve better resolution to that of finite difference methods with comparably lower storage. This property is particularly desirable for the numerical implementation of continuation methods, where the dimension of augmented systems is typically multiples of the solution vector (Kuznetsov 2004). Nevertheless as finite difference methods are relatively simple to implement, they provide a comparison for other codes developed. In this thesis the results obtained by each code are compared so that should a spurious solution arise from numerical artefacts it can be detected.

Using the discrete spectral formulation of (2.21) outlined in appendix D the following routines are implemented.

2.3.1 Steady-state solving

Steady-states are solved by Newton iteration, where Stokes preconditioning has been implemented following Mamun & Tuckerman (1995) to accommodate the large range of eigenvalues associated with the linear operator $\mathcal{L}$. The solution is updated according to

$$\boldsymbol{\mathcal{F}}(\boldsymbol{X}^n) + \mathcal{DF}_{\boldsymbol{X}^n}(\boldsymbol{X}^{n+1} - \boldsymbol{X}^n) = 0, \tag{2.27}$$

where $\boldsymbol{\mathcal{F}}$ and $\mathcal{DF}$ correspond to the right hand side of (2.21) and its linearisation both multiplied by the pre-conditioner $\mathcal{L}^{-1}$. The solution of (2.27) which requires the inverse of the Jacobian is obtained using an iterative matrix-free method.

2.3.2 Linear stability

The linear stability of a steady state is determined by computing its leading eigenvalues and eigenvectors. To identify the presence and/or proximity of a change in the solution, we look for regions in the parameter space where the real part of the leading eigenvalue(s) pass through zero. These transitions correspond to a bifurcation of the given state. The steady state solution $\boldsymbol{X}_0$ and the perturbation denoted by prime are

$$\boldsymbol{X} = \boldsymbol{X}_0 + e^{\lambda t}\boldsymbol{X}', \quad \text{where} \quad \lambda \in \mathbb{C}, \quad \boldsymbol{X}' = \begin{pmatrix} \psi' & T' & \Omega' \end{pmatrix}^T. \tag{2.28}$$

It has been assumed that the unknown functions have an exponential time-dependence such that a linear eigenvalue problem is obtained. It should be noted that the eigenvalues of this problem only determine asymptotic stability.

$$\lambda \mathcal{M}\boldsymbol{X}' = \mathcal{L}\boldsymbol{X}' + \boldsymbol{\mathcal{N}}(\boldsymbol{X}_0, \boldsymbol{X}') + \boldsymbol{\mathcal{N}}(\boldsymbol{X}', \boldsymbol{X}_0) = \mathcal{DF}_{\boldsymbol{X}^0}\boldsymbol{X}'. \tag{2.29}$$

As the linearised matrix operator $\mathcal{DF}_{\boldsymbol{X}^0}$ given by 2.29 is generally non-normal, transient growth is possible and must be considered (Schmid 2007, Trefethen 2000). Eigenvalues λ are determined by solving the generalized eigenvalue problem using a LAPACK based routine.

2.3.3 Time-stepping

Time-stepping is carried out using an $\mathcal{O}(\Delta t^2)$ Adams-Bashforth scheme for nonlinear terms and a Crank-Nicolson algorithm for linear terms.

$$\mathcal{M}\frac{\boldsymbol{X}^{n+1}-\boldsymbol{X}^{n}}{\Delta t}=\frac{1}{2}\Big[3\boldsymbol{\mathcal{N}}(\boldsymbol{X}^{n},\boldsymbol{X}^{n})-\boldsymbol{\mathcal{N}}(\boldsymbol{X}^{n-1},\boldsymbol{X}^{n-1})\Big]+\frac{1}{2}\mathcal{L}\big(\boldsymbol{X}^{n+1}+\boldsymbol{X}^{n}\big)+\boldsymbol{F}. \quad (2.30)$$

This scheme is chosen for its low computational and storage costs as compared with alternative schemes that are $\mathcal{O}(\Delta t^2)$ accurate. When solving for time dependent states, the time step is typically set to be a sufficiently small fraction of the oscillation period and is reduced to ensure the persistence of observed behaviour. Further conditions for the numerical stability of time-stepping with finite-difference are outlined in appendices C.

2.3.4 Pseudo arc-length continuation

To follow different steady solution branches and investigate their parameter dependence we wish to solve the system

$$\boldsymbol{\mathcal{F}}(\boldsymbol{X},\mu)=0, \quad \text{where} \quad \mu\in[Pr,\mathrm{Ra},Re_1,Re_2], \quad (2.31)$$

and $\boldsymbol{X}$ is the solution vector. Typically, we want to vary a single parameter μ while leaving all remaining parameters fixed. While Newton's method provides the steady state solution, it relies on the Jacobian matrix $\mathcal{D}\mathcal{F}_{\boldsymbol{X}}$ which becomes singular near turning points. In order to follow solution branches around turning points we therefore use a psuedo-arclength method outlined by Chan (1984). Rather than performing continuation in μ, a new parameter s which approximates the arc-length parameter is introduced and we seek solutions of the augmented system.

$$\begin{aligned}\boldsymbol{\mathcal{F}}(\boldsymbol{X}(s),\mu(s))&=0,\\ p(\boldsymbol{X}(s),\mu(s),s)=\delta\dot{\boldsymbol{X}}_0^T\cdot(\boldsymbol{X}-\boldsymbol{X}_0)+(1-\delta)\dot{\mu}_0(\mu-\mu_0)-ds&=0,\end{aligned} \quad (2.32)$$

where $\dot{\boldsymbol{X}}$ and $\dot{\mu}$ denote derivatives with respect to s. Additionally, we impose the constraint

$$\delta||\dot{\boldsymbol{X}}(s)||^2+(1-\delta)|\dot{\mu}(s)|^2=1, \quad (2.33)$$

which approximates the arc-length condition. The second condition $p(\boldsymbol{X}(s),\mu(s),s)=0$, requires that the point $(\boldsymbol{X}(s),\mu(s))$ lies in a plane normal to the tangent. From the total derivative we obtain

$$d\boldsymbol{\mathcal{F}}=D\mathcal{F}_{\boldsymbol{X}}\dot{\boldsymbol{X}}+\boldsymbol{\mathcal{F}}_{\mu}\dot{\mu}=0. \quad (2.34)$$

Writing $\boldsymbol{\xi}=-\big(D\mathcal{F}_{\boldsymbol{X}}\big)^{-1}\boldsymbol{\mathcal{F}}_{\mu}$ and using constraint (2.33) we have

$$\dot{\boldsymbol{X}}=\dot{\mu}\boldsymbol{\xi}, \quad \dot{\mu}=\pm\frac{1}{\sqrt{1+\delta(||\boldsymbol{\xi}||^2-1)}}, \quad (2.35)$$

where the sign of $\dot{\mu}$ may be changed to enable following a new branch. Using these relations the continuation is performed by a combination of predictor and corrector steps. The predictor step yields

$$\begin{aligned} \boldsymbol{X}^{n+1}(s+\Delta s) &= \boldsymbol{X}^{n}(s) + \dot{\boldsymbol{X}}\Delta s, \\ \mu^{n+1}(s+\Delta s) &= \mu^{n}(s) + \dot{\mu}\Delta s, \end{aligned} \tag{2.36}$$

where Δs is chosen to be a small increment along the solution arc. The corrector step is obtained by writing the augmented system $\boldsymbol{G}$ and its state vector $\boldsymbol{Y}$ as

$$\boldsymbol{G} = \begin{pmatrix} \boldsymbol{\mathcal{F}} \\ p \end{pmatrix}, \quad \boldsymbol{Y} = \begin{pmatrix} \boldsymbol{X} \\ \mu \end{pmatrix}, \tag{2.37}$$

and Taylor expanding to obtain

$$\boldsymbol{G}(\boldsymbol{Y}^n + \Delta\boldsymbol{Y}) = \boldsymbol{G}(\boldsymbol{Y}^n) + \boldsymbol{G}_{\boldsymbol{Y}}(\boldsymbol{Y}^n)\Delta\boldsymbol{Y} + \mathcal{O}(|\Delta\boldsymbol{Y}^2|), \tag{2.38}$$

where the Jacobian matrix is

$$\boldsymbol{G}_{\boldsymbol{Y}} = \begin{pmatrix} D\mathcal{F}_{\boldsymbol{X}} & \boldsymbol{\mathcal{F}}_{\mu} \\ p_{\boldsymbol{X}} & p_{\mu} \end{pmatrix} = \begin{pmatrix} D\mathcal{F}_{\boldsymbol{X}} & \boldsymbol{\mathcal{F}}_{\mu} \\ \delta\dot{\boldsymbol{X}}_0^T & (1-\delta)\dot{\mu}_0 \end{pmatrix}. \tag{2.39}$$

At a fixed point the left hand side of (2.38) vanishes, so that the solution of the system can be corrected or updated by iterating $\boldsymbol{Y}^n$ according to

$$\boldsymbol{Y}^{n+1} = \boldsymbol{Y}^n - \boldsymbol{G}_{\boldsymbol{Y}}^{-1}\boldsymbol{G}(\boldsymbol{Y}^n). \tag{2.40}$$

Following Uecker *et al.* (2014) we have chosen to parametrise the arc length condition (2.33) using δ. This parameter may be adjusted to favour Newton searches in the $\boldsymbol{X}$ or μ directions and thus tune the continuation. Typically $\delta \in [0.05, 0.1]$ is found to be most suitable for computations.

2.4 Model summary

In this chapter we've derived the Oberbeck-Boussinesq equations and outlined the appropriate boundary conditions for thermal convection in a spherical shell allowing for differential rotation of the spheres. The axisymmetric formulation of the problem and the base states admitted by the equations have also been described. Two different numeri-

cal discretisations for the treatment of these equations have also been outlined. In the subsequent chapters we consider two scenarios: thermal convection in a spherical shell without rotation and subsequently the same problem but now allowing for rotation. This order is chosen so that we start by considering the simplest model system which retains essential features of the full system, thus allowing us to increase the complexity of the system gradually.

3

Mode interactions in thermal convection

The equations describing axisymmetric Rayliegh-Bénard convection in a spherical annulus are given by

$$Pr^{-1}\left(\frac{\partial D^2\psi}{\partial t}+\sin\theta\,\frac{\partial(\psi,D^2\psi/r^2\sin^2\theta)}{\partial(\theta,r)}\right)=\mathrm{Ra}\,g(r)r\frac{\partial T}{\partial\theta}\sin\theta+D^2D^2\psi, \tag{3.1a}$$

$$\frac{\partial T}{\partial t}+\frac{1}{r^2\sin\theta}\frac{\partial(\psi,T)}{\partial(\theta,r)}=\nabla^2T, \tag{3.1b}$$

such that the flow is completely described by the azimuthal vorticity and temperature equations. As per (2.7) the inner sphere radius r_1 , and thermal diffusion timescale r_1^2/κ, have been chosen to make the equations non-dimensional. We would like to emphasise that by defining the flow in terms of a stream-function, we are restricting the system to axisymmetric solutions only. Non-axisymmetric effects are considered in chapter 5.

In this section we consider both no-slip and stress-free boundary conditions for the fluid velocity at the spherical walls, the assumption of perfectly conducting spheres is retained. For the case of no-slip at the boundaries

$$\left.\begin{aligned}&\psi(r,\theta)=\tfrac{\partial}{\partial r}\psi(r,\theta)=0,\quad \text{for } r=1,1+d\\&T(1,\theta)=1,\quad T(1+d,\theta)=0,\end{aligned}\right\}\quad\text{Case A} \tag{3.2}$$

or alternatively when both spheres have stress-free boundaries

$$\left.\begin{aligned}&\psi(r,\theta)=0=\tfrac{\partial}{\partial r}\left(\tfrac{1}{r^2}\tfrac{\partial}{\partial r}\psi(r,\theta)\right),\quad \text{for } r=1,1+d\\&T(1,\theta)=1,\quad T(1+d,\theta)=0.\end{aligned}\right\}\quad\text{Case B} \tag{3.3}$$

Unfortunately, neither of these boundary conditions nor any of their combinations gives a *nice* set of eigenfunctions. Hence there is no advantage in choosing stress free boundary conditions as is often the case in planar domains. As previously outlined the symmetry conditions (2.16) must also be enforced at the symmetry axis.

Given the equations (3.1) and the boundary conditions (3.2) we aim to answer the following questions in this chapter. What types of solutions does this system of equations possess? How do the Prandtl number, geometry and buoyancy forces influence the convective state in these solutions? How is the temperature field distorted for different Pr? And ultimately what determines the preferred state of convective motion in the presence of multiple solutions?

Depending on Pr the convective state described by (3.1b) is characterised by three regimes (Moore & Weiss 1973). For $Pr \gg 1$ and moderate Ra the flow is viscous such that, the advection term in the vorticity equation can be neglected. In this regime the dominant

transport terms are in the temperature equation. For $Pr \ll 1$ and moderate to large Ra advection of vorticity becomes significant however and one should adopt the rescaling

$$\tilde{\psi} = Pr^{-1}\psi, \quad \tilde{T} = Pr^{-1}T, \quad \tilde{t} = Pr\, t, \tag{3.4}$$

such that advective terms in the vorticity equation are dominant. Convective heat transfer is typically described by the Nusselt number

$$Nu = \frac{\int_\theta \frac{\partial T}{\partial r} \sin\theta d\theta}{\int_\theta \frac{\partial T_0}{\partial r} \sin\theta d\theta} \quad \text{for} \quad r = 1, 1+d, \tag{3.5}$$

an integral quantity (evaluated at the inner or outer sphere) which measures the total heat transfer to the conductive heat transfer. In a numerical study of 2D planar Boussinesq convection for both high and low Pr Moore & Weiss (1973) found that the convective heat transport measured in each of these regimes scales as $Nu \approxeq 2(Ra/Ra_c)^{1/3}$ and $Nu \approxeq 1.9(Ra/Ra_c)^{0.365}$ respectively.

In addition to these convective regimes present at moderate to large Ra, Moore & Weiss (1973) denote a third convective regime for small Ra where the convective heat transfer Nu increases sharply with Ra and the amplitudes of convective motions is small.

To address the questions outlined and to consider the three convective regimes highlighted by (Moore & Weiss 1973) we adopt the following approach. We first consider the linear problem followed by the small Ra regime using weakly nonlinear theory. In doing so we elucidate the dependence of convective motion on the shell separation d and highlight geometric effects present in a spherical shell domain. Subsequently the behaviour at larger Ra is considered using numerical continuation and stability analysis. Using this approach the bifurcation sequence leading to time-dependent behaviour is first outlined for low $Pr \ll 1$. Subsequently the bifurcation sequence and scaling of Nu with Ra are outlined for $Pr \gg 1$. Finally we comment on the role of thermal boundary layers asymmetries in determining the preferred solution.

3.1 Linear theory

We substitute $T(r,\theta,t) = T_0(r) + \tilde{T}(r,\theta,t)/r$ where $T_0(r)$ is the conductive base state (2.17) which is spherically symmetric. Dropping the tildes the governing equations can be written

$$Pr^{-1}\left(\frac{\partial D^2\psi}{\partial t} + J_\psi(\psi,\psi)\right) = \mathrm{Ra}\, g(r)\frac{\partial T}{\partial \theta}\sin\theta + D^2D^2\psi, \tag{3.6a}$$

$$\frac{\partial T}{\partial t} + J_T(\psi,T) = \widehat{D}^2 T - \frac{1}{\sin\theta}\frac{\partial \psi}{\partial \theta}\frac{T_0'}{r}, \tag{3.6b}$$

where

$$\widehat{D}^2 f = r\nabla^2(f/r), \quad J_\psi(f,g) = \sin\theta \frac{\partial(f, D^2 g/(r^2\sin^2\theta))}{\partial(\theta, r)}, \quad J_T(f,g) = \frac{1}{r\sin\theta}\frac{\partial(f,g/r)}{\partial(\theta,r)}. \tag{3.7}$$

Their linearised form may be written as

$$\left(\frac{\partial}{\partial t}\mathcal{M} - \mathcal{L}\right)\boldsymbol{\phi}_1 = 0, \tag{3.8}$$

where

$$\boldsymbol{\phi}_1 = \begin{pmatrix}\psi_1 \\ T_1\end{pmatrix}, \quad \mathcal{M} = \begin{pmatrix} Pr^{-1}D^2 & 0 \\ 0 & 1\end{pmatrix}, \quad \mathcal{L} = \begin{pmatrix} D^2 D^2 & \mathrm{Ra}\, g(r)\sin\theta\frac{\partial}{\partial\theta} \\ \frac{-T_0'}{r\sin\theta}\frac{\partial}{\partial\theta} & \widehat{D}^2\end{pmatrix}. \tag{3.9}$$

It is shown in appendix A, that operators $\mathcal{M}$ and $\mathcal{L}$ are self-adjoint with respect to a weighted inner product and boundary conditions (3.2) provided the condition

$$\frac{d}{dr}\left(\frac{g(r)r}{T_0'}\right) = 0 \tag{3.10}$$

is satisfied (Joseph & Carmi 1966). This implies the temperature gradient and gravity fields (2.6) must have the same radial variation. Assuming a dense core so that $\eta = 0$ we obtain

$$g(r) = r^{-3}, \quad T_0'/r = A_T/r^3. \tag{3.11}$$

We concentrate on this mathematically convenient self-adjoint case as it provides semi-explicit solutions to (3.8). Physically it corresponds to a very dense core underlying a light fluid layer (Schubert *et al.* 1981). Satisfying (3.10) guarantees the absence of oscillatory motions at the onset of linear instability. Separable solutions ψ_1, T_1 then take the form

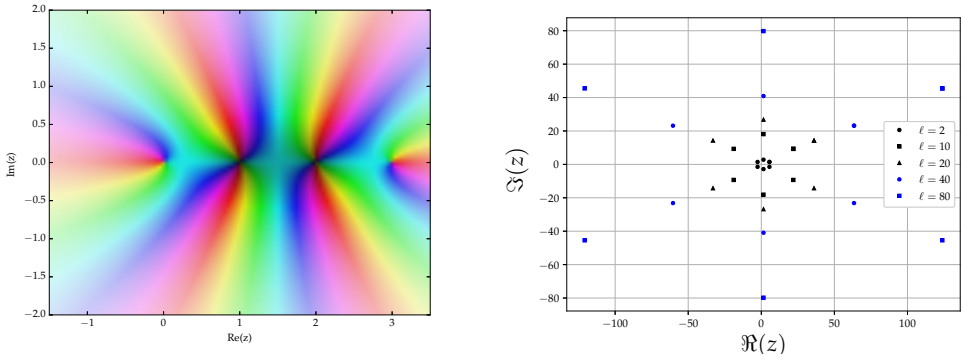
$$\psi_1^\ell = \psi_\ell(r)G_\ell(\theta)e^{\lambda t}, \qquad T_1^\ell = T_\ell(r)P_l(\cos\theta)e^{\lambda t}, \quad \lambda\in\mathbb{R}, \tag{3.12}$$

for a prescribed mode ℓ. Provided (3.10) holds, the system is neutrally stable $\lambda = 0$ for a critical Rayleigh number $\mathrm{Ra_c}$ so that the governing equations may be reduced to the 6^{th} order ODE

$$D_\ell^2\big(g(r)^{-1}D_\ell^2 D_\ell^2\psi_\ell(r)\big) - \mathrm{Ra_c}\, l(l+1)T_0'/r\,\psi_\ell(r) = 0, \quad D_\ell^2 = \frac{\partial^2}{\partial r^2} - \frac{l(l+1)}{r^2}, \tag{3.13}$$

with no-slip boundary conditions

$$\psi_\ell(r) = \psi_\ell'(r) = 0, \quad D_\ell^2 D_\ell^2\psi_\ell(r) = 0, \quad \text{for} \quad r = 1, 1+d. \tag{3.14}$$



(a) $\{z_i\}$ for $\ell = 0$. **(b)** $\{z_i\}$ for $\ell = 2 \to 80$.

Figure 3.1: Dependence of the roots of (3.17) with mode number ℓ. In each frame the plots show the roots of the neutrally stable eigenmode evaluated at the critical Rayleigh number Ra_c for fixed separation d. In frame (b) the modulus of the roots is observed to scale like $|z_i| \sim \ell$ for large ℓ.

It should be noted that (3.13) implies the stability threshold is independent of Pr, so that the Prandtl number only affects the nonlinear problem. The form and solution of (3.13) in terms of spherical Bessel functions for the special case $g(r) = 1, T_0'/r = 1$ was initially determined by Chandrasekhar (1961). In our case, substituting (3.11) one obtains the equation

$$D_\ell^2\left(r^3 D_\ell^2 D_\ell^2 \psi_\ell(r)\right) + \frac{C\psi_\ell(r)}{r^3} = 0, \quad C = -\mathrm{Ra_c}\, l(l+1) A_T, \tag{3.15}$$

whose solutions for a given polar mode ℓ, take the form of complex polynomials

$$\psi_\ell(r) = \sum_{i=1}^{6} E_i r^{z_i} + c.c., \quad \text{where} \quad z_i, E_i \in \mathbb{C}. \tag{3.16}$$

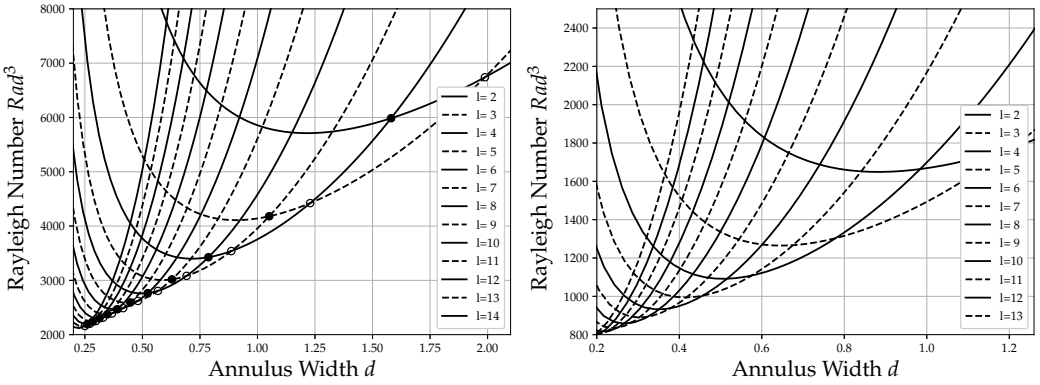
Substituting (3.16) into (3.15) an implicit expression for the roots z_i as function of $\mathrm{Ra_c}$ is obtained

$$[(z-1)(z-2) - \ell(\ell+1)][(z-2)(z-3) - \ell(\ell+1)][z(z-1) - \ell(\ell+1)] + C = 0. \tag{3.17}$$

This polynomial is symmetric under the transformations $z \mapsto 3 - z$ and $z + 1.5 \mapsto z - 1.5$, and its roots are complex conjugate pairs expressible in terms of real constants a, b, c

$$z_1 = a \pm \mathrm{ib}, \quad z_2 = (3 - \mathrm{a}) \pm \mathrm{ib}, \quad z_3 = 1.5 \pm \mathrm{ic}. \tag{3.18}$$

The dependence of z_i with ℓ is considered in figure 3.1 frame (b) where the modulus of the roots is observed to scale like $|z_i| \sim \ell$ for large ℓ.



(a) No-slip boundaries **(b)** Stress free boundaries

Figure 3.2: Neutral stability curves $\mathrm{Ra_c}(d)\, d^3$ where the rightmost mode of each figure is $\ell = 2$. Select degenerate points are indicated by hollow dots if neighbouring, and solid black dots if non-neighbouring. These solutions have previously been obtained numerically for both density ratios $(\eta = 1, \eta = 0)$ by Araki *et al.* (1994) and by Chossat (1978).

The boundary conditions (3.14) are now imposed to obtain a set of linear homogeneous equations for the coefficients E_i of the form

$$\mathsf{M}_\ell(\mathrm{Ra_c}, d) \begin{pmatrix} E_1 \\ \vdots \\ E_6 \end{pmatrix} = 0, \tag{3.19}$$

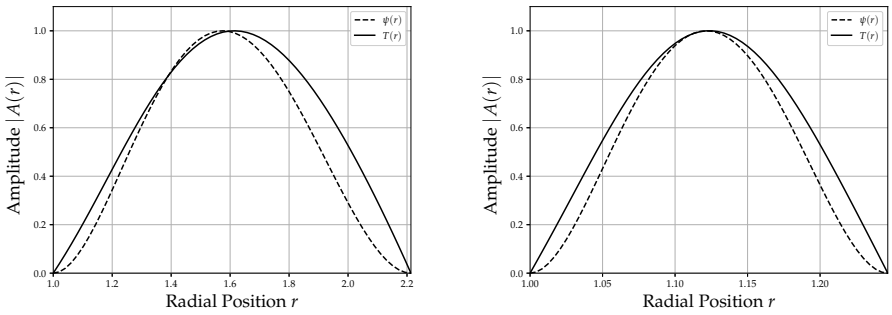
where M_ℓ is a 6×6 matrix depending on $\mathrm{Ra_c}, d$ and the complex roots z_i. Non-trivial solutions of the linear problem with the required boundary conditions are determined by solving the system

$$\Re\big(det(\mathsf{M}_\ell(\mathrm{Ra_c}, d))\big) = 0, \quad \Im\big(det(\mathsf{M}_\ell(\mathrm{Ra_c}, d))\big) = 0, \tag{3.20}$$

numerically for each ℓ, and for a range of $(\mathrm{Ra_c}, d)$ to determine the neutral curves (figure 3.2). Arbitrarily setting $E_1 = 1 + \mathrm{i}$, the remaining amplitudes are determined.

$$\begin{aligned} \psi_1^\ell(r,\theta) &= G_\ell(\theta)\frac{1}{2}\sum_{i=1}^{6}\left(E_i r^{z_i} + \bar{E}_i r^{\bar{z}_i}\right), \quad z_i, E_i \in \mathbb{C}, \\ T_1^\ell(r,\theta) &= P_\ell(\cos\theta)\frac{1}{2}\sum_{i=1}^{6}\left(F_i r^{z_i - 1} + \bar{F}_i r^{\bar{z}_i - 1}\right), \quad z_i, F_i \in \mathbb{C}. \end{aligned} \tag{3.21}$$

In planar convection where d represents the separation of hot and cold plates $\mathrm{Ra_c}(d)d^3$



(a) Mode $\ell = 2,\ d = 1.2.$ **(b)** Mode $\ell = 12,\ d = 0.246.$

Figure 3.3: Eigenfunctions $\psi(r)$ & $T(r)$ of the marginally stable state. As $d \to 0$ symmetry about the annulus centreline $r = 1 + d/2$ is approached.

shares a common minimum for all mode numbers. In a spherical fluid annulus this is evidently not the case, a physical difference which may be understood by considering the volume of fluid being heated relative to the heating element's surface area (*inner sphere*). For $d \ll 1$ these are almost coincident, but as $d \to \infty$ the inner sphere becomes in effect a point source, as observed in figures 3.2. The symmetry about the annulus centreline ($r = (r_1 + r_2)/2$) is also broken (figure 3.3), with the effect of replacing the sinusoidal eigenfunctions of planar geometries, by functions exhibiting a radial oscillatory decay

$$\psi(r) \sim r^{x+\mathrm{iy}} \sim r^x e^{\mathrm{iy}\log(\mathrm{r})}, \quad x, y \in \mathbb{R}. \tag{3.22}$$

This makes the annular domain $\mathbb{Z}_2$ symmetric rather than $\mathbb{D}_2 = \mathbb{Z}_2 \times \mathbb{Z}_2$ symmetric and alters the form of the amplitude equations derived in section 3.2.

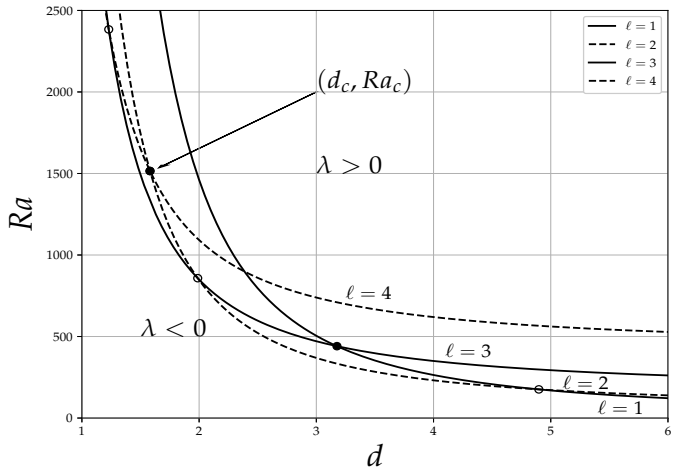


Figure 3.4: Neutral stability curves $\mathrm{Ra}(d)$. Hollow dots indicate degenerate points where two modes $(\ell, \ell+1)$ simultaneously become unstable, while solid black dots indicate the even degenerate point $(2,4)$ unstable to the odd $\ell = 3$ mode and the odd degenerate point $(1,3)$ unstable to the even $\ell = 2$ mode.

3.2 Weakly nonlinear theory

The linear theory of section 3.1 demonstrated that there exist neutral curves for each mode ℓ. These curves correspond to a stability boundary $\lambda = 0$, at which transition from the stable $\lambda < 0$ *conductive* regime to the unstable $\lambda > 0$ *convective* regime occurs, as shown in figure 3.4. Previously $\mathrm{Ra}\, d^3$ *vs.* d was plotted for comparison with the planar case, but now we plot Ra *vs.* d as Ra is the natural control parameter in (3.6). One can see from the curves for various modes, that there are special values of the control parameter $\mathrm{Ra_c}$ and geometry d_c where two modes $(\ell, n = \ell + 1, 2, ..)$ lose their stability simultaneously, marked by dots in figure 3.4.

These are termed *degenerate points*. Linear theory fails to establish the preferred neutral mode so that (3.8) may be solved by any solution of the form

$$\boldsymbol{\phi}_1 = A(\tilde{t})\boldsymbol{\phi}_1^{\ell} + B(\tilde{t})\boldsymbol{\phi}_1^{n}, \quad A, B \in \mathbb{R}. \tag{3.23}$$

where

$$\boldsymbol{\phi}_1^{\ell} = \begin{pmatrix} \psi_1^{\ell}(r,\theta) \\ T_1^{\ell}(r,\theta) \end{pmatrix}, \quad \boldsymbol{\phi}_1^{n} = \begin{pmatrix} \psi_1^{n}(r,\theta) \\ T_1^{n}(r,\theta) \end{pmatrix} \tag{3.24}$$

and the amplitudes $A(\tilde{t}), B(\tilde{t})$ are functions of an appropriately chosen slow timescale $\tilde{t}$. In this section, we concentrate on the dynamics in the vicinity of such points; deriving a set of coupled ordinary differential equations to describe the time evolution of the convective

amplitudes A, B. Physically this aims to understand how patterns of convection cells interact and are affected by changes in the annulus width d, buoyancy forcing Ra and Prandtl number Pr.

As the eigenfunctions are either symmetric or antisymmetric (within the interval $[0, \pi]$), all possible interactions are summarised by four cases. If mode-numbers (ℓ, n) are both even, their interaction is termed *even-even* while if (ℓ, n) are odd and even their interaction is termed *odd-even* or *even-odd*. In both scenarios the amplitude equations contain quadratic terms and are resonant. Finally if (ℓ, n) are both odd, their interaction is termed *odd-odd*. This case is the simplest and is studied first, as no quadratic terms appear. While applicable at all degenerate points, higher interactions such as $(\ell = 2, n = 11)$ are unstable to a large number of intermediate modes and so are less relevant (figure 3.2).

3.2.1 Odd-odd mode interactions

Following Kidachi (1982) we introduce a small parameter ϵ and define the appropriate scalings for the *odd-odd* interaction as

$$\boldsymbol{\phi} = \epsilon\boldsymbol{\phi}_1 + \epsilon^2\boldsymbol{\phi}_2 + \epsilon^3\boldsymbol{\phi}_3, \tag{3.25}$$

with the slow timescale $\tau_1 = \epsilon^2 t$ so that

$$\frac{\partial}{\partial t} = \epsilon^2 \frac{\partial}{\partial \tau_1}, \tag{3.26}$$

while the Rayleigh number and annulus width scale as

$$\frac{\mathrm{Ra} - \mathrm{Ra_c}}{\mathrm{Ra_c}} = \mu\epsilon^2, \qquad d - d_c = \delta\epsilon^2. \tag{3.27}$$

The effect of varying the outer sphere radius is to modify the radial boundary conditions from $\mathcal{O}(\epsilon^3)$. Expanding $\psi(r, \theta, t)$ and $T(r, \theta, t)$ about $r = 1 + d_c$ one obtains

$$\begin{aligned}
\psi(1+d,\theta,t) &= \epsilon\psi_1 + \epsilon^2\psi_2 + \epsilon^3\left(\psi_3 + \delta\psi_1'\right) + \mathcal{O}(\epsilon^4) = 0,\\
\psi'(1+d,\theta,t) &= \epsilon\psi_1' + \epsilon^2\psi_2' + \epsilon^3\left(\psi_3' + \delta\psi_1''\right) + \mathcal{O}(\epsilon^4) = 0,\\
T(1+d,\theta,t) &= \epsilon T_1 + \epsilon^2 T_2 + \epsilon^3\left(T_3 + \delta T_1'\right) + \mathcal{O}(\epsilon^4) = 0,
\end{aligned} \tag{3.28}$$

where all terms on the right hand side are evaluated at $r = 1 + d_c$. Substituting these scaled expressions into (3.6b) we obtain order by order

$\mathcal{O}(\epsilon)$:

$$\mathcal{L}\boldsymbol{\phi}_1 = 0, \tag{3.29}$$

$\mathcal{O}(\epsilon^2)$:

$$\mathcal{L}\boldsymbol{\phi}_2 = N_2(\boldsymbol{\phi}_1, \boldsymbol{\phi}_1) \equiv \begin{pmatrix} Pr^{-1} J_\psi(\psi_1, \psi_1) \\ J_T(\psi_1, T_1) \end{pmatrix}, \tag{3.30}$$

where $\mathcal{L}$ is given by (3.9) with homogeneous boundary conditions. At order $\mathcal{O}(\epsilon^3)$

$$\mathcal{L}\boldsymbol{\phi}_3 = N_3(\boldsymbol{\phi}_1, \boldsymbol{\phi}_2) \equiv \begin{pmatrix} -\mu \,\mathrm{Ra_c}\, g(r) \frac{\partial T_1}{\partial \theta} \sin\theta + Pr^{-1}\left(J_\psi(\psi_1, \psi_2) + J_\psi(\psi_2, \psi_1) + \frac{\partial D^2 \psi_1}{\partial \tau_1} \right) \\ J_T(\psi_1, T_2) + J_T(\psi_2, T_1) + \frac{\partial T_1}{\partial \tau_1} \end{pmatrix}, \tag{3.31a}$$

$$\begin{aligned} &\psi_3 = 0, \qquad \psi_3' = 0, \qquad\quad T_3 = 0, \qquad\quad \text{at} \quad r = 1, \\ &\psi_3 = 0, \qquad \psi_3' = -\delta\psi_1'', \qquad T_3 = -\delta T_1', \qquad \text{at} \quad r = 1 + d_c. \end{aligned} \tag{3.31b}$$

Solving (3.29) recovers the solution for $\boldsymbol{\phi}_1$, which is just the expression (3.23). Inserting $\boldsymbol{\phi}_1$ into (3.30) leads to a linear inhomogeneous problem for $\boldsymbol{\phi}_2$. By *Fredholm's alternative*, a solution exists if and only if the conditions

$$\langle \boldsymbol{\phi}_1^\ell, N_2(\boldsymbol{\phi}_1, \boldsymbol{\phi}_1) \rangle = 0, \quad \text{and} \quad \langle \boldsymbol{\phi}_1^n, N_2(\boldsymbol{\phi}_1, \boldsymbol{\phi}_1) \rangle = 0, \tag{3.32}$$

are satisfied. As $\mathcal{L}$ is formally self-adjoint, the adjoint eigenfunctions $\boldsymbol{\phi}_1^\ell, \boldsymbol{\phi}_1^n$ are the same as the original ones (cf. Appendix A). Having satisfied these conditions, a general solution for $\boldsymbol{\phi}_2$ containing terms proportional to A^2, AB, B^2 is obtained. Inserting expressions for $\boldsymbol{\phi}_1, \boldsymbol{\phi}_2$ into (3.31a), a further solvability condition constraining the amplitudes A, B is encountered. The boundary conditions (3.31b) at this order are however inhomogeneous, so that the previously defined inner product must be modified to include terms proportional to $\delta A, \delta B$. Imposing the first solvability condition for the ℓ-harmonic gives

$$\langle \boldsymbol{\phi}_1^\ell, \mathcal{L}\boldsymbol{\phi}_3 \rangle = \langle \boldsymbol{\phi}_1^\ell, N_3(\boldsymbol{\phi}_1, \boldsymbol{\phi}_2) \rangle = \langle \mathcal{L}\boldsymbol{\phi}_1^\ell, \boldsymbol{\phi}_3 \rangle + \text{boundary terms}. \tag{3.33}$$

Integrating by parts and substituting for (3.31b) the form of these additional terms non-zero at $r = 1 + d_c$ are determined

$$\langle \boldsymbol{\phi}_1^\ell, \mathcal{L}\boldsymbol{\phi}_3 \rangle = \langle \mathcal{L}\boldsymbol{\phi}_1^\ell, \boldsymbol{\phi}_3 \rangle + \delta A \left\{ \int_\theta \left(\frac{\partial T_1^\ell}{\partial r} \right)^2 \sin\theta d\theta - \frac{A_T}{\mathrm{Ra_c}} \int_\theta \left(\frac{\partial^2 \psi_1^\ell}{\partial r^2} \right)^2 \frac{d\theta}{\sin\theta} \right\}, \tag{3.34}$$

where ψ_1^ℓ , T_1^ℓ are as defined in (3.12). An equivalent procedure is adopted to impose solvability for the n-harmonic, giving terms proportional to δB. Together with the conditions imposed for (3.31a) the following coupled equations are obtained

$$\left.\begin{aligned} a_0\frac{\partial A}{\partial \tau_1} &= \mu_1 A - \left(d_{11}A^2B + d_{12}AB^2 + d_{13}A^3 + d_{14}B^3\right), \\ b_0\frac{\partial B}{\partial \tau_1} &= \mu_2 B - \left(d_{21}A^2B + d_{22}AB^2 + d_{23}A^3 + d_{24}B^3\right), \\ \text{where} \qquad \mu_1 &= a_1\mu + a_2\delta, \quad \mu_2 = b_1\mu + b_2\delta, \end{aligned}\right\} \begin{aligned} &A \sim \ell \quad odd \\ &B \sim n > \ell \quad odd \end{aligned} \tag{3.35}$$

and $\mathcal{O}(1)$ parameters μ & δ as in (3.27) represent the distance from a degenerate bifurcation point $(d_c, \mathrm{Ra_c})$, for example the intersection of neutral curves $\ell = 1, n = 3$ as shown in figure 3.4. These parameters may be positive or negative, so that both geometry changes and buoyancy forces may excite convective motion. All coefficients $a_i, b_i, d_{ij} \in \mathbb{R}^+$ are found to be non-zero, highlighting that there are no pure mode solutions $(A, 0)$ or $(0, B)$. The computation of coefficients is outlined in appendix B, for algebraic convenience their sign is not prescribed. However, given that the interaction of odd modes explicitly excites intermediate even modes unstable in the vicinity of the bifurcation point, the relevance of (3.35) for the fully nonlinear problem is diminished. For this reason it is not considered further.

3.2.2 Even-even & even-odd mode interactions

We now consider the interaction of neighbouring and non-neighbouring even modes, as both cases contain quadratic terms at $\mathcal{O}(\epsilon^2)$. Following Proctor & Jones (1988) we adopt an expansion of the type (3.25), but now choose the slow timescale $\tau_1 = \epsilon t$ and scale the control parameters as

$$(\mathrm{Ra} - \mathrm{Ra_c})/\mathrm{Ra_c} = \mu\epsilon, \qquad d - d_c = \delta\epsilon. \tag{3.36}$$

Note that these scalings do modify (3.30) and (3.31a), but for brevity the changes are not outlined. Proceeding in a manner identical to the *odd-odd* case, $\boldsymbol{\phi}_1$ may be expressed as per (3.23). Inserting $\boldsymbol{\phi}_1$ into the non-linear terms in (3.30), terms proportional to $P_\ell(\cos\theta), G_\ell(\theta), P_n(\cos\theta), G_n(\theta)$ are encountered. It is the presence of these resonant terms at $\mathcal{O}(\epsilon^2)$ that motivates the alternate timescale and parameter scalings chosen. Imposing the inner products

$$\langle \boldsymbol{\phi}_1^\ell, N_2(\boldsymbol{\phi}_1, \boldsymbol{\phi}_1)\rangle = 0, \quad \text{and} \quad \langle \boldsymbol{\phi}_1^n, N_2(\boldsymbol{\phi}_1, \boldsymbol{\phi}_1)\rangle = 0, \tag{3.37}$$

the second-order amplitude equations may be determined. They are of the form

$$a)\quad \left.\begin{aligned} a_0\frac{\partial A}{\partial \tau_1} &= \mu_1 A + cA^2 - \alpha B^2, \\ b_0\frac{\partial B}{\partial \tau_1} &= \mu_2 B + \alpha AB, \end{aligned}\right\} \begin{aligned} &A \sim \ell \quad even \\ &B \sim n > \ell \quad odd \end{aligned} \tag{3.38}$$

$$b)\quad \left.\begin{aligned} a_0\frac{\partial A}{\partial \tau_1} &= \mu_1 A - \alpha AB, \\ b_0\frac{\partial B}{\partial \tau_1} &= \mu_2 B + \alpha A^2 + cB^2, \end{aligned}\right\} \begin{aligned} &A \sim \ell \quad odd \\ &B \sim n > \ell \quad even \end{aligned} \tag{3.39}$$

for the interaction of neighbouring modes, while for non-neighbouring even modes

$$c)\quad \left.\begin{aligned} a_0\frac{\partial A}{\partial \tau_1} &= \mu_1 A + cA^2 - \alpha AB - \beta B^2, \\ b_0\frac{\partial B}{\partial \tau_1} &= \mu_2 B + \alpha A^2 + \beta AB + cB^2, \end{aligned}\right\} \begin{aligned} &A \sim \ell \quad even \\ &B \sim n > \ell \quad even \end{aligned} \tag{3.40}$$

$$\text{where} \qquad \mu_1 = a_1\mu + a_2\delta, \quad \mu_2 = b_1\mu + b_2\delta, \quad \text{with} \quad a_i, b_i, \alpha, \beta \in \mathbb{R}^+. \tag{3.41}$$

and boundary terms $\sim \delta$ have been included as previously by modifying the inner product. It has been proven by Chossat (2001) that when $\mathcal{L}$ is self-adjoint, as is the case in this paper, the coefficient $c = 0$. When condition (3.10) is not satisfied however the even mode solution is found to bifurcate subcritically (Beltrame & Chossat 2015). Alternatively it may be seen that the even mode subspace $(0, B)$, must be invariant under the map $(0, B) \to (0, -B)$ (Hoyle 2006). While it seems consistent to stop at $\mathcal{O}(\epsilon^2)$, the quadratic nonlinearities do not lead to finite amplitudes at large times. As was demonstrated for the planar case by Proctor & Jones (1988), multiplying the first and second line of equations (3.38) to (3.40) by A & B respectively, and adding one obtains

$$\frac{1}{2}\frac{\partial}{\partial \tau_1}(a_0A^2 + b_0B^2) = \mu_1 A^2 + \mu_2 B^2, \tag{3.42}$$

so that if both μ_1 and μ_2 are positive the amplitudes tend to infinity. This is resolved through a regularization of the equations at $\mathcal{O}(\epsilon^3)$, even though these terms are an order ϵ smaller. Gathering terms proportional to modes ℓ, n we must obtain particular integrals for the expression

$$\mathcal{L}\boldsymbol{\phi}_2 = N_2^R(\boldsymbol{\phi}_1, \boldsymbol{\phi}_1) + N_2^N(\boldsymbol{\phi}_1, \boldsymbol{\phi}_1), \tag{3.43}$$

where N_2^R is the resonant part of the inhomogeneous terms whose components are of the form

$$\dot{A}\boldsymbol{\phi}_1^\ell + \dot{B}\boldsymbol{\phi}_1^n + \mu A\boldsymbol{\phi}_1^\ell + \mu B\boldsymbol{\phi}_1^n + A^2\boldsymbol{\phi}_1^n + AB(\boldsymbol{\phi}_1^\ell + \boldsymbol{\phi}_1^n) + B^2\boldsymbol{\phi}_1^\ell, \tag{3.44}$$

and N_2^N contains the non-resonant terms orthogonal to $\boldsymbol{\phi}_1$. Overdot notation is now used to indicate the time derivative. The non-resonant terms may be easily solved for but the resonant terms demand special treatment. The method of solution is to find a particular integral denoted by superscript p of (3.43) and then add terms of the form

$$\boldsymbol{\phi}_2 = \begin{pmatrix} \psi_2^p \\ T_2^p \end{pmatrix} + \sum_{k=0}^{2n+1} \sum_{j=1}^{6} \begin{pmatrix} E_{kj} r^{z_{kj}-1} G_k(\theta) \\ F_{kj} r^{z_{kj}-2} P_k(\cos\theta) \end{pmatrix} + c.c, \tag{3.45}$$

where the exponents z_{kj} are determined by solving (3.17) for each mode k. For each k the 6 coefficients E_{kj}, F_{kj} must be chosen to satisfy the 6 boundary conditions at second order (3.30). Application of these gives rise to a matrix equation of the form

$$\mathsf{M}_{ij}\boldsymbol{x_j} = \mathsf{b}_{ij}\boldsymbol{\chi_j}, \tag{3.46}$$

where $\boldsymbol{x}$ is an array of coefficients, matrices M, b have size 6×6, 6×7 and

$$\boldsymbol{\chi} = \begin{pmatrix} \dot{A}, & \dot{B}, & \mu A, & \mu B, & A^2, & AB, & B^2 \end{pmatrix}^T. \tag{3.47}$$

While this system may be solved easily for $k \neq \ell, n$, for $k = \ell, n$ the matrix M is singular, $\mathsf{M}\boldsymbol{x}_0 = 0 = \bar{\boldsymbol{y}}_0^T \mathsf{M}$. Applying a solvability condition, we remove the resonant component of each column b_i of b,

$$\mathsf{b}_i = \mathsf{b}_i - \langle \bar{\boldsymbol{y}}_0, \mathsf{b}_i \rangle \boldsymbol{x}_0, \quad \text{where} \quad \langle \bar{\boldsymbol{y}}_0, \boldsymbol{x}_0 \rangle = 1. \tag{3.48}$$

The solution space is then restricted by solving the invertible *bordered system* (Kuznetsov 2004).

$$\begin{pmatrix} \mathsf{M} & \boldsymbol{x}_0 \\ \bar{\boldsymbol{y}}_0^T & 0 \end{pmatrix} \begin{pmatrix} \boldsymbol{x} \\ \sigma \end{pmatrix} = \begin{pmatrix} \mathsf{b}\boldsymbol{\chi} \\ 0 \end{pmatrix}, \quad \text{where} \quad \sigma \in \mathbb{R}. \tag{3.49}$$

Having satisfied the boundary conditions, the last step in calculating $\boldsymbol{\phi}_2$ is to add suitable multiples of $\boldsymbol{\phi}_1^\ell, \boldsymbol{\phi}_1^n$ so that the orthogonality conditions

$$\langle \boldsymbol{\phi}_1^\ell, \boldsymbol{\phi}_2 \rangle = 0, \quad \text{and} \quad \langle \boldsymbol{\phi}_1^n, \boldsymbol{\phi}_2 \rangle = 0, \tag{3.50}$$

are satisfied. Substituting solutions $\boldsymbol{\phi}_1, \boldsymbol{\phi}_2$ into (3.31a), and taking the appropriate inner product we obtain the following equations. Describing the *even-odd* interaction

$$\left.\begin{aligned} \tilde{a}_0\dot{A} &= \tilde{\mu}_1 A - \tilde{\alpha}_3 B^2 + \epsilon\{\tilde{e}_{11}A\dot{A} + \tilde{e}_{14}B\dot{B} + \tilde{d}_{12}AB^2 + \tilde{d}_{13}A^3\}, \\ \tilde{b}_0\dot{B} &= \tilde{\mu}_2 B + \tilde{\beta}_2 AB + \epsilon\{\tilde{e}_{22}A\dot{B} + \tilde{e}_{23}B\dot{A} + \tilde{d}_{21}A^2B + \tilde{d}_{24}B^3\}, \end{aligned}\right\} \begin{aligned} &A \sim \ell \quad even \\ &B \sim n > \ell \quad odd \end{aligned} \tag{3.51}$$

where

$$\left.\begin{aligned}\tilde{\mu}_1 = a_1\mu + a_2\delta + \epsilon a_1\mu^2,\ \tilde{\mu}_2 = b_1\mu + b_2\delta + \epsilon b_1\mu^2,\ \tilde{\alpha}_3 = \alpha_3 + \epsilon\mu\alpha_{13},\\ \tilde{\beta}_2 = \beta_2 + \epsilon\mu\beta_{12},\ \tilde{a}_0 = a_0 + \epsilon\mu a_0,\ \tilde{b}_0 = b_0 + \epsilon\mu b_0,\end{aligned}\right\} \tag{3.52}$$

and for the alternate *odd-even* case one obtains

$$\left.\begin{aligned}\tilde{a}_0\dot{A} = \tilde{\mu}_1 A - \tilde{\alpha}_2 AB + \epsilon\{\tilde{e}_{12}A\dot{B} + \tilde{e}_{13}B\dot{A} + \tilde{d}_{12}AB^2 + \tilde{d}_{13}A^3\},\\ \tilde{b}_0\dot{B} = \tilde{\mu}_2 B + \tilde{\beta}_1 A^2 + \epsilon\{\tilde{e}_{21}A\dot{A} + \tilde{e}_{24}B\dot{B} + \tilde{d}_{21}A^2B + \tilde{d}_{24}B^3\},\end{aligned}\right\} \begin{aligned} A &\sim \ell \quad odd\\ B &\sim n > \ell \quad even\end{aligned} \tag{3.53}$$

where

$$\left.\begin{aligned}\tilde{\mu}_1 = a_1\mu + a_2\delta + \epsilon a_1\mu^2,\ \tilde{\mu}_2 = b_1\mu + b_2\delta + \epsilon b_1\mu^2,\ \tilde{\alpha}_2 = \alpha_2 + \epsilon\mu\alpha_{12},\\ \tilde{\beta}_2 = \beta_2 + \epsilon\mu\beta_{11},\ \tilde{a}_0 = a_0 + \epsilon\mu a_0,\ \tilde{b}_0 = b_0 + \epsilon\mu b_0.\end{aligned}\right\} \tag{3.54}$$

For the *even-even* case of two non-neighbouring modes

$$\left.\begin{aligned}\tilde{a}_0\dot{A} = \tilde{\mu}_1 A - \tilde{\alpha}_2 AB - \tilde{\alpha}_3 B^2 + \epsilon\{\tilde{e}_{11}A\dot{A} + \tilde{e}_{12}A\dot{B} + \tilde{e}_{13}B\dot{A} + \tilde{e}_{14}B\dot{B}\\ + \tilde{d}_{11}A^2B + \tilde{d}_{12}AB^2 + \tilde{d}_{13}A^3 + \tilde{d}_{14}B^3\},\\ \tilde{b}_0\dot{B} = \tilde{\mu}_2 B + \tilde{\beta}_1 A^2 + \tilde{\beta}_2 AB + \epsilon\{\tilde{e}_{21}A\dot{A} + \tilde{e}_{22}A\dot{B} + \tilde{e}_{23}B\dot{A} + \tilde{e}_{24}B\dot{B}\\ + \tilde{d}_{21}A^2B + \tilde{d}_{22}AB^2 + \tilde{d}_{23}A^3 + \tilde{d}_{24}B^3\},\end{aligned}\right\} \begin{aligned} A &\sim \ell \quad even\\ B &\sim n > \ell \quad even\end{aligned} \tag{3.55}$$

$$\text{where} \qquad \left.\begin{aligned}\tilde{\mu}_1 = a_1\mu + a_2\delta + \epsilon a_1\mu^2,\ \tilde{\mu}_2 = b_1\mu + b_2\delta + \epsilon b_1\mu^2, \tilde{\alpha}_2 = \alpha_2 + \epsilon\mu\alpha_{12},\\ \tilde{\alpha}_3 = \alpha_3 + \epsilon\mu\alpha_{13},\ \tilde{\beta}_1 = \beta_1 + \epsilon\mu\beta_{11},\ \tilde{\beta}_2 = \beta_2 + \epsilon\mu\beta_{12},\\ \tilde{a}_0 = a_0 + \epsilon\mu a_0,\ \tilde{b}_0 = b_0 + \epsilon\mu b_0.\end{aligned}\right\} \tag{3.56}$$

and terms proportional to coefficients $\tilde{e}_{ij}$ may be simplified using the appropriate second order equation (3.38) to (3.40) for each case. The computation of coefficients is outlined in appendix B, for algebraic convenience their sign is not prescribed.

Generalizations of equation (3.53) including non-axisymmetric effects, have previously been determined by Friedrich & Haken (1986) for the $\ell = 1, 2$ and by Beltrame & Chossat (2015) for the $\ell = 3, 4$ interactions. In this paper we focus rather on all axisymmetric interactions. This is justified by the tendency of axisymmetric poloidal flows to remain axisymmetric at large Pr. By computing the stability of solutions to non-axisymmetric disturbances in section 5.1 this claim is later clarified. When neighbouring modes are even and odd respectively we obtain (3.51), in which the role of quadratic terms are interchanged. Alternatively by choosing both modes to be even $(\ell, \ell \pm 2)$, equation (3.55) is obtained. The relevance of (3.55) may be queried as it fails to consider the influence of

the unstable intermediate modes $\ell \pm 1$ present at *even-even* degeneracies (figure 3.2). We argue, however, that as the nonlinear interaction of even modes excites even modes only, this equation remains valid in the absence of odd mode perturbations. This contrasts with the *odd-odd* interaction where even modes are explicitly excited. In section 5.1 we confirm the stability of such even solutions numerically at large Pr. Following an investigation of (3.55) in section 3.3 the motivations for its consideration are supported using DNS in section 3.4.

3.3 Analysis of amplitude equations

This section is divided between an analysis of neighbouring mode interactions $(\ell, \ell \pm 1)$, whose results are shown to compare directly with DNS, and an analysis of even non-neighbouring mode interactions $(\ell, \ell \pm 2)$ whose results compare with DNS in which odd modes are suppressed. By calculating the coefficients in (3.51) to (3.55) for $Pr \in [10^{-3}, 10^{3}]$ deemed sufficient to attain limiting behaviour, the effect of varying Pr in all (ℓ, n) degeneracies is clarified. Mapping solutions in terms of bifurcation parameters (δ, μ) regions of distinct convective behaviour for different Pr are demarcated. This approach aims to determine: How do the solutions obtained depend on system parameters? And which solutions are possible? In this section $\epsilon = 1$ is fixed, as our interest is in the form and stability of the solutions to (3.38) - (3.40) which do not dependent on its magnitude.

3.3.1 Neighbouring mode interactions

Even-odd $\ell < n$

The equations for *even-odd* interactions are

$$\left.\begin{aligned} \dot{A} &= \mu_1 A + \alpha_3 B^2 + d_{12} A B^2 + d_{13} A^3, \\ \dot{B} &= \mu_2 B + \beta_2 A B + d_{21} A^2 B + d_{24} B^3, \end{aligned}\right\} \begin{aligned} &A \sim \ell \quad even \\ &B \sim n > \ell \quad odd \end{aligned} \tag{3.57}$$

where

$$\mu_1 = a_1 \mu + a_2 \delta, \ \mu_2 = b_1 \mu + b_2 \delta \quad a_i, b_i \in \mathbb{R}^+. \tag{3.58}$$

The quadratic coefficients α_i, β_i in (3.57) have opposite signs, while the cubic coefficients d_{ij} are negative for all Pr as shown in figure 3.5. Subject to the coefficients outlined (3.57) have the fixed points

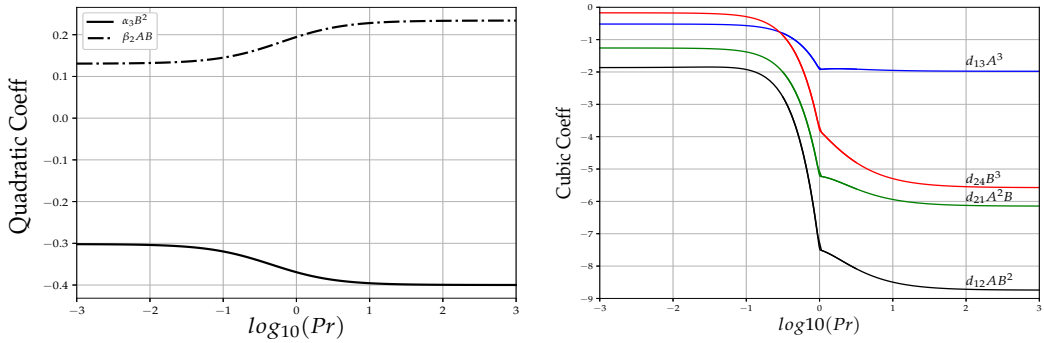


Figure 3.5: Variation of the equation coefficients with Pr for modes $\ell = 2, 3$. The kink obtained at $Pr = 1$ is a consequence of the rescaling (3.4). Quadratic coefficients increase or decrease to reach a limit as Pr varies about unity. Cubic coefficients demonstrate distinct limiting values for $Pr \to \infty$ and $Pr \to 0$. The magnitude of coefficients d_{13}, d_{24} pertaining to terms A^3 and B^3 respectively interchanges when $Pr \simeq 0.28$.

$$\begin{aligned} &A = 0,\ B = 0, && \text{Trivial Solution} \\ &A = \pm\sqrt{-\mu_1/d_{13}},\ B = 0, && \text{Pure Modes} \\ &(A_1, \pm B_1),\ (A_2, \pm B_2),\ (A_3, \pm B_3), && \text{Mixed Modes} \end{aligned} \tag{3.59}$$

highlighting that even modes are symmetric under the transform $(A, 0) \to (-A, 0)$ and mixed modes under the transform $(A, B) \to (A, -B)$. We also remark that for $d \ll 1$ the least stable modes are $\ell, n \gg 1$, so that the quadratic coefficients $\alpha_i, \beta_i \to 0$, behaviour concordant with regression towards a planar geometry. For $d \gg 1$, the degenerate points are spaced further apart, favouring smaller mode numbers for which fewer linearly unstable interactions occur (figure 3.2). It is for this reason lower mode numbers are used to demonstrate more general results.

Figure 3.6 shows the two parameter continuation of bifurcation points in (δ, μ) parameter space. All such calculations are performed with the numerical continuation software XPPAUT (Ermentrout 2002). The loci shown may be interpreted as a tracing of the different bifurcations points which emerge as the parameters (δ, μ) are varied from the degenerate point $(\delta, \mu) = (0, 0)$. These are used to demarcate the existence of stable pure modes in region 1, stable pure modes and unstable mixed modes in region 2, stable pure and mixed modes in region 3, stable mixed modes only in region 4, unstable pure modes and stable mixed modes in region 5, and finally a stable pure mode and stable mixed modes in region 6. Excluding region 3, all solutions emerge via pitchfork bifurcations from the trivial solution branch as shown in figure 3.7. This figure also shows that additional stable solutions emerge via secondary bifurcations in this region. Mixed mode solutions from region 4 and pure mode solutions from region 1 both remain stable if continued into region

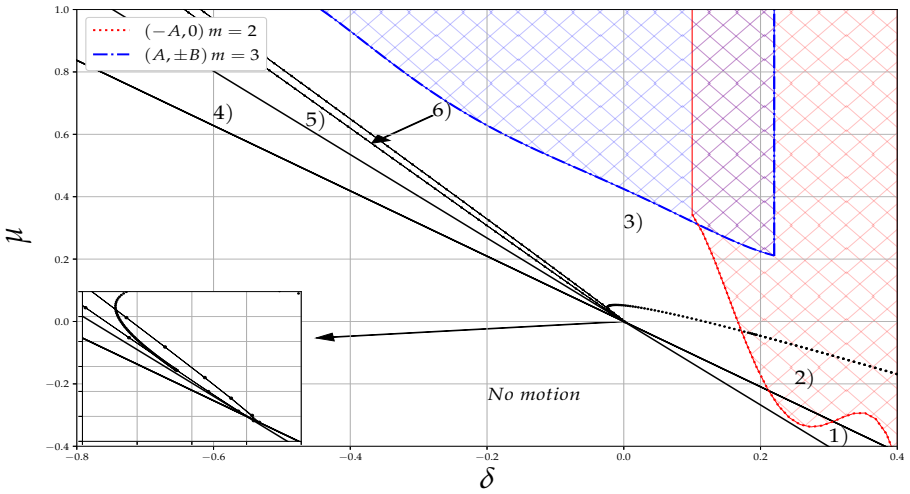
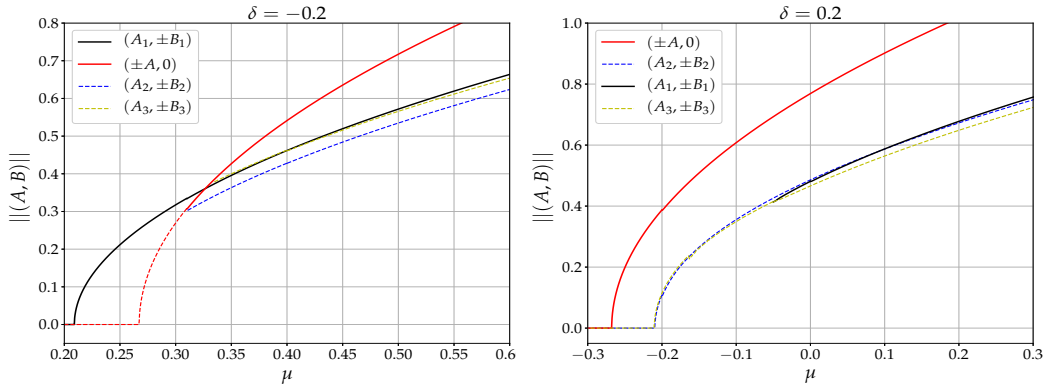


Figure 3.6: Bifurcation loci of the $\ell = 2,3$ mode interaction for $Pr = 10$. Solid lines $-$ denote a pitchfork and dotted $\cdots$ secondary bifurcations. Regions are: 1 stable pure $\ell = 2$ mode, 2 stable pure modes & unstable mixed modes, 3 stable pure $\ell = 2$ modes & stable mixed modes (*initial condition dependent*), 4 stable mixed modes, 5 stable mixed modes and unstable pure modes, and 6 a single stable pure mode and stable mixed modes. The 3D stability of axisymmetric solutions at large Pr is shown in colour inset. Within the red hatched region $(-A,0)$ is stable, but below loses stability to $m = 2$. Within the blue hatched region $(A,\pm B)$ is stable, but below loses stability to $m = 3$ (cf. section 5.1).



(a) $\delta = -0.2, Pr = 10.$ **(b)** $\delta = 0.2, Pr = 10.$

Figure 3.7: Bifurcation diagrams of the mode interaction $\ell = 2,3$. Frames (a) and (b) correspond to cross sections of figure 3.6 taken at $\delta = -0.2, 0.2$. Stable solutions are denoted by *solid lines*, unstable branches by *dashed lines*. (a) The stable mixed mode $(A_1,\pm B_1)$ and unstable pure mode $(\pm A,0)$ emerge via pitchfork bifurcations. The pure mode branch stabilises via two secondary bifurcations, giving rise to unstable mixed modes. (b) The stable pure mode $(\pm A,0)$ and ustable mixed modes emerge via pitchfork bifurcations. The mixed mode branch stabilises via a secondary bifurcation.

3. Within region 3, the transition between these states exhibits hysteresis and occurs via a saddle-node shown in frame 3 of figure 3.8. Notably, the equilibrium attained depends on the initial condition.

In region 4, only stable mixed modes exist for $\mu_1 < 0$, $\mu_2 > 0$, corresponding to a balance of linear and quadratic terms as is apparent by considering (3.57) without its cubic terms.

$$\left.\begin{aligned} 0 &= \mu_1 A + \alpha_3 B^2, \\ 0 &= (\mu_2 + \beta_2 A)B, \end{aligned}\right\} \begin{aligned} &A \sim \ell \quad even \\ &B \sim n > \ell \quad odd \end{aligned} \tag{3.60}$$

The fixed points are thus approximated by $B = \pm\sqrt{-(\mu_1\mu_2)/(\alpha_3\beta_2)}$ and $A = -\mu_2/\beta_2$ and the lower order equations hold in this scenario only. In the limit $Pr \to 0$, the odd B-mode dominates the mixed mode solutions as $|d_{24}| \ll |d_{13}|$, while for $Pr \to \infty$ both modes are of similar magnitude.

Odd-even $\ell < n$

This interaction is described by the equations

$$\left.\begin{aligned} \dot{A} &= \mu_1 A + \alpha_2 AB + d_{12} AB^2 + d_{13} A^3, \\ \dot{B} &= \mu_2 B + \beta_1 A^2 + d_{21} A^2 B + d_{24} B^3, \end{aligned}\right\} \begin{aligned} &A \sim \ell \quad odd \\ &B \sim n > \ell \quad even \end{aligned} \tag{3.61}$$

whose fixed points are as before with the modes reversed, so that pure $(0, \pm B)$ modes are now even. All cubic coefficients $d_{ij} < 0$ are negative, while the quadratic coefficients have opposite signs as shown in figure 3.9.

Figure 3.10 plots the bifurcation diagrams of the $(1, 2)$ and $(3, 4)$ mode interactions. The plot is akin to the Even-Odd interaction with the roles of the even and odd modes interchanged; in this case it is the odd A mode which excites the even B mode in the mixed mode solutions. A disparity in size between regions $1, 3, 4$ between the figures $(a), (b)$ highlights that the degeneracies of higher modes exhibit are more sensitive to changes in the annulus width. As the phase planes are qualitatively similar to the *even-odd* case (figure 3.8) they are not presented.

In both the neighbouring mode interactions presented, there are no pure odd mode solutions. In region 4 of figure 3.10 only mixed mode solutions exist where the even $(0, \pm B)$ modes are linearly unstable. This may be attributed to the self-interaction of odd or even modes generating even modes only

$$P_\ell^2(\cos\theta) = \sum_{k=0}^{\ell} c_{2k} P_{2k}(\cos\theta), \quad c_{2k} \in \mathbb{R}, \tag{3.62}$$

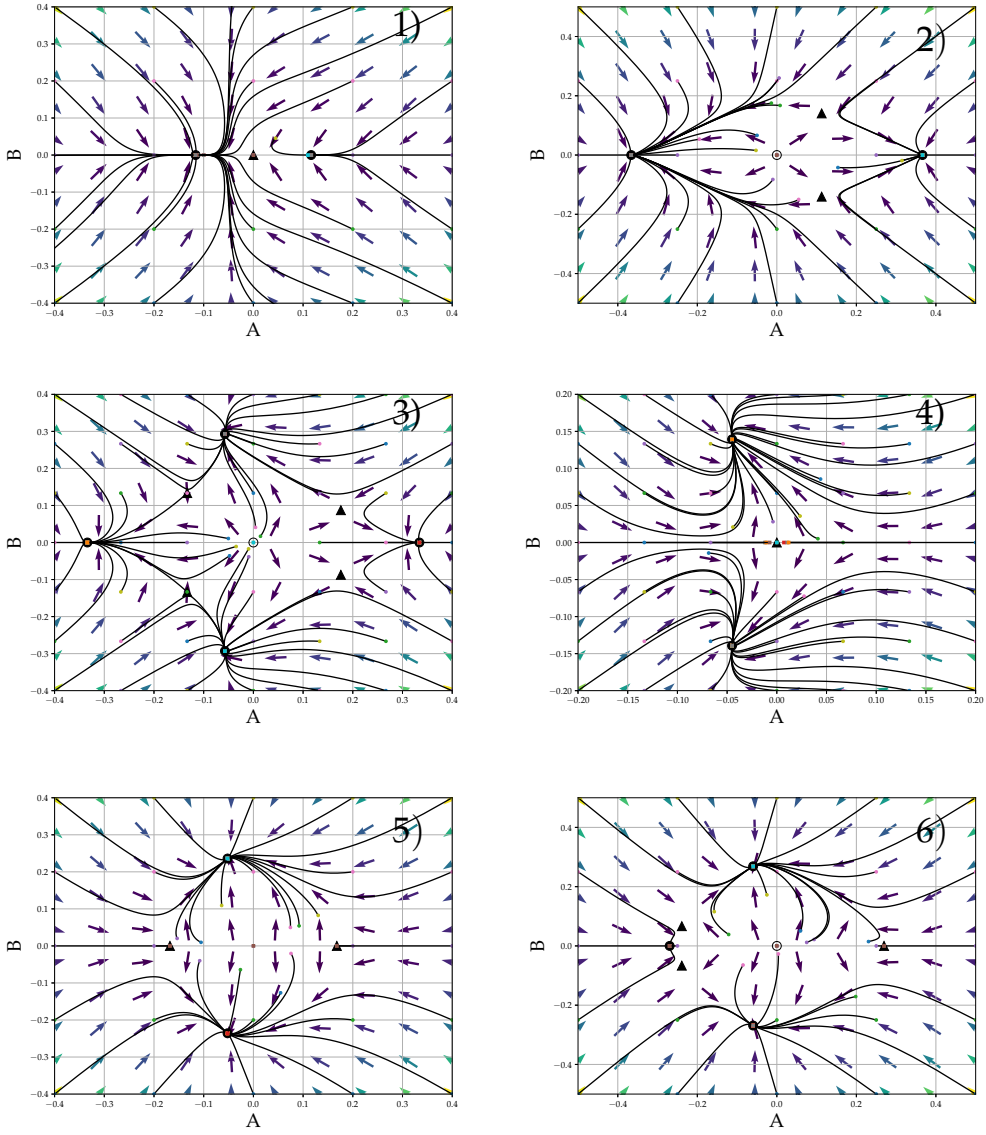


Figure 3.8: Phase-plane diagrams (A, B) describing the *even-odd* interaction for mode numbers $\ell = 2, 3$ and $Pr = 10$. Fixed points are denoted as: Stable node - •, Unstable node - ○, Saddle point - ▲. In regions: 1 only pure $(\pm A, 0)$ modes exist, 2 stable pure modes & unstable mixed modes $(A, \pm B)$, 3 stable pure modes & stable mixed modes (*initial condition dependent*), 4 stable mixed modes, 5 stable mixed modes & unstable pure modes, and 6 a single stable pure mode and stable mixed modes.

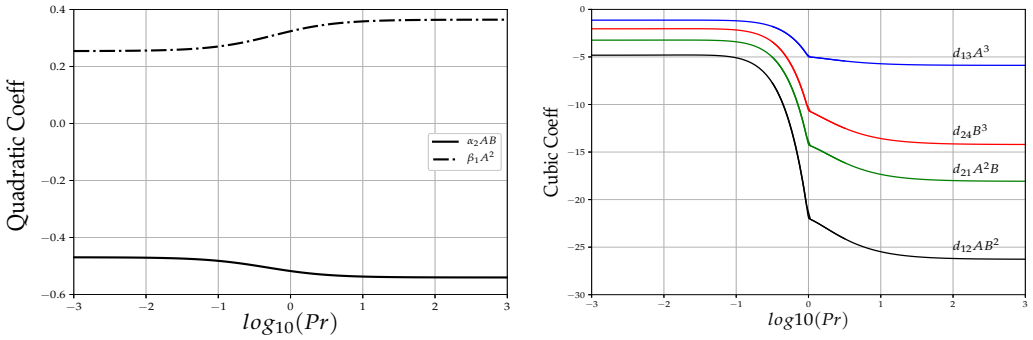
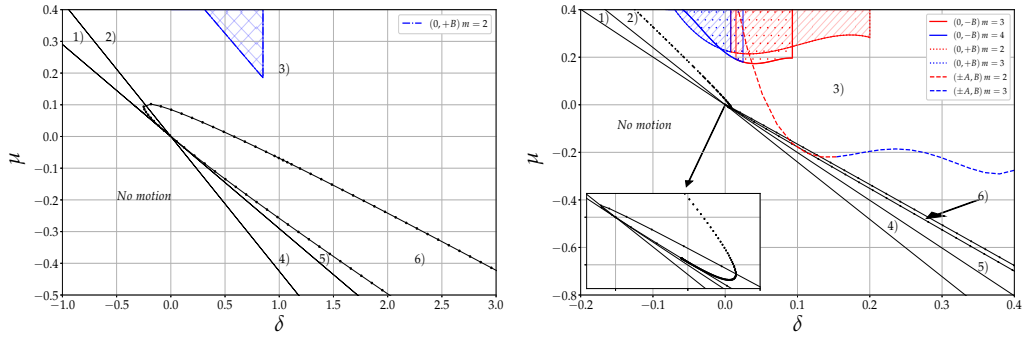


Figure 3.9: Prandtl number dependency of coefficients for the $\ell = 3, 4$ interaction. The kink obtained at $Pr = 1$ is a consequence of the rescaling (3.4). Distinct from the Even-Odd the relative size of cubic coefficients does not change in either limit of Pr. Quadratic coefficients are now smaller in magnitude relative to the cubic terms of the previous case for a wider annulus.



(a) Modes $\ell = 1, 2$ **(b)** Modes $\ell = 3, 4$

Figure 3.10: Bifurcation loci for the *odd-even* mode interactions with $Pr = 10$. Regions are: 1 stable pure $(0, \pm B)$ modes, 2 stable pure modes & unstable mixed modes, 3 stable pure modes & stable mixed modes $(\pm A, B)$ (*initial condition dependent*), 4 stable mixed modes, 5 stable mixed modes and unstable pure modes, and 6 a single stable pure mode and stable mixed modes. The 3D stability of axisymmetric solutions at large Pr is shown in colour inset (cf. section 5.1). (a) Within the blue hatched region $(0, +B)$ is stable, but below loses stability to $m = 2$. (b) Within the dotted region $(0, -B)$ is stable and in the dashed region $(0, +B)$ is stable. Within the unhatched region $(\pm A, B)$ is stable but below loses stability to $m = 2, 3$.

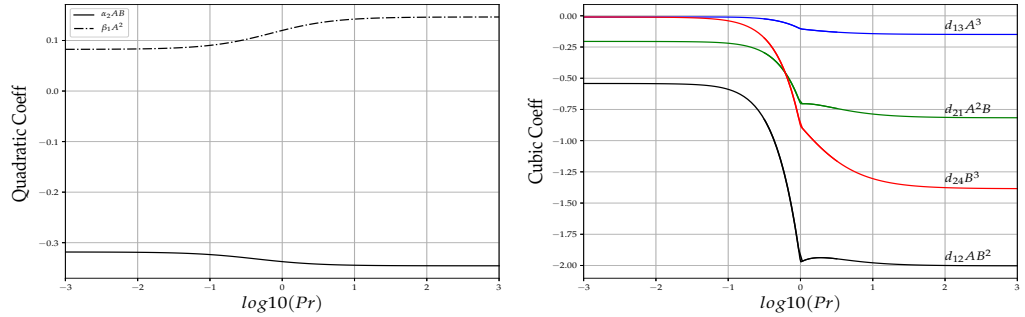


Figure 3.11: Variation of the amplitude equation coefficients with Pr for $\ell = 1, 2$. The kink obtained at $Pr = 1$ is a consequence of the rescaling (3.4). In the limit $Pr \to 0$ coefficients $d_{13} \ll 1$ and $d_{24} \ll 1$, while for large Pr the behaviour is akin to that of the $\ell = 3, 4$ case. Quadratic and cubic coefficients are of similar magnitude for this interaction.

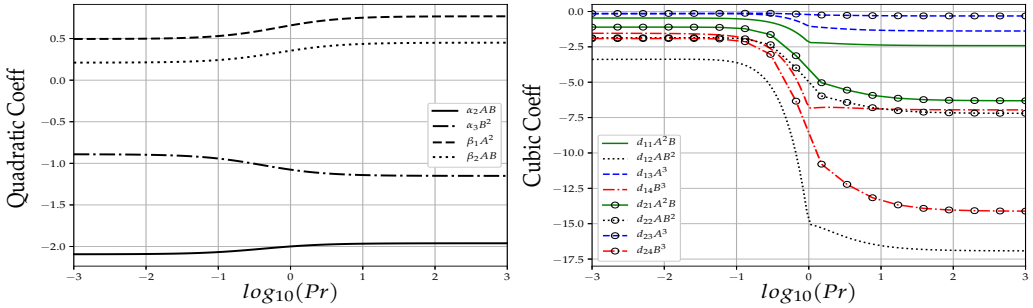
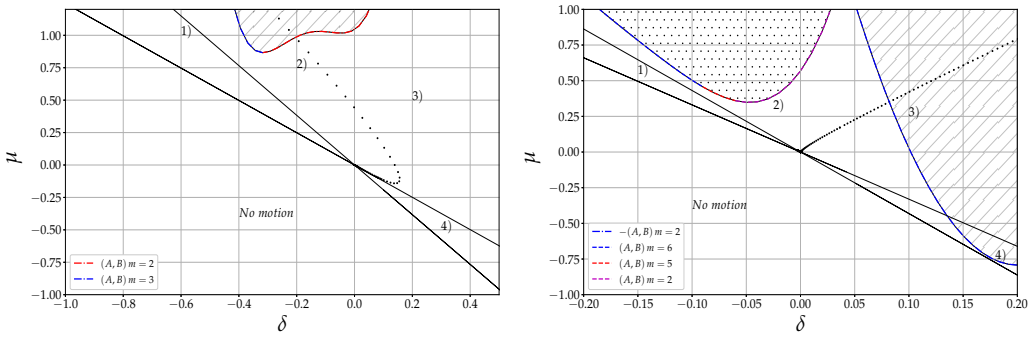


Figure 3.12: Variation of the amplitude equation coefficients with Pr for modes $\ell = 2, 4$. The kink obtained at $Pr = 1$ is a consequence of the rescaling (3.4). As $Pr \to 0$ coefficients of A^3 terms $d_{13} \ll 1$, $d_{23} \ll 1$, while coefficients d_{14}, d_{24} of B^3 terms are always larger in magnitude. This behaviour is akin to previous interactions where the higher mode dominates the saturation process.

implying that the saturation of odd modes does not decouple from even modes, a result stemming directly from the eigenfunctions. The $(1, 2)$ mode interaction is the lowest interaction possible, occurring for the annulus separation $d_c \approx 4.89$. Its coefficients shown in figure 3.11 demonstrate a particular behaviour in the limit $Pr \to 0$; where cubic coefficients $d_{13} \ll 1$ and $d_{24} \ll 1$ so that the quadratic and cross terms now dominate the saturation process.



(a) Modes $\ell = 2, 4$ **(b)** Modes $\ell = 4, 6$

Figure 3.13: Bifurcation loci of the *even-even* interactions $\ell = 2, 4$ & $\ell = 4, 6$ with $Pr = 10$. Region 1 contains two mixed modes $(A_1, +B_1), (A_2, -B_2)$, 2 two stable and unstable mixed modes, 3 a single stable fixed point, while 4 two stable spirals $(-A_1, B_1), (-A_2, B_2)$. The 3D stability of axisymmetric solutions at large *Pr* is shown in colour inset (cf. section 5.1). (a) Within the red hatched region (A, B) is stable, but below loses stability to $m = 2, 3$. (b) Within the densely hatched region (left) (A, B) is stable and in the lightly hatched region (right) $-(A, B)$ is stable. Below these regions the unstable azimuthal wavenumber m varies.

3.3.2 Non-neighbouring mode interactions

Even-even $(\ell, \ell \pm 2)$

This interaction is governed by the equations

$$\left.\begin{aligned}\dot{A} &= \mu_1 A + \alpha_2 AB + \alpha_3 B^2 + d_{11}A^2B + d_{12}AB^2 + d_{13}A^3 + d_{14}B^3,\\ \dot{B} &= \mu_2 B + \beta_1 A^2 + \beta_2 AB + d_{21}A^2B + d_{22}AB^2 + d_{23}A^3 + d_{24}B^3,\end{aligned}\right\} \begin{aligned} A &\sim \ell \quad even\\ B &\sim \ell \pm 2.\end{aligned} \tag{3.63}$$

The quadratic coefficients α_i, β_i have opposite signs, and the cubic coefficients remain negative as shown in figure 3.12, so that (3.63) may have mixed mode solutions only. In contrast to the neighbouring mode interactions no pure mode solutions exist, as (3.63) no longer has symmetry.

Figure 3.13 shows the bifurcation diagram and figure 3.14 the corresponding phase plane for the *even-even* mode interaction. The absence of symmetry in (3.63) results in two distinct fixed points in each region of 3.13. In region 4 where the ℓ mode dominates their are two stable spiral nodes. Transitioning to region 3 via a Hopf-bifurcation there is a single stable fixed point. Transitioning into into region 2 and subsequently region 1 where the $\ell + 2$ mode dominates, an additional stable fixed point appears.

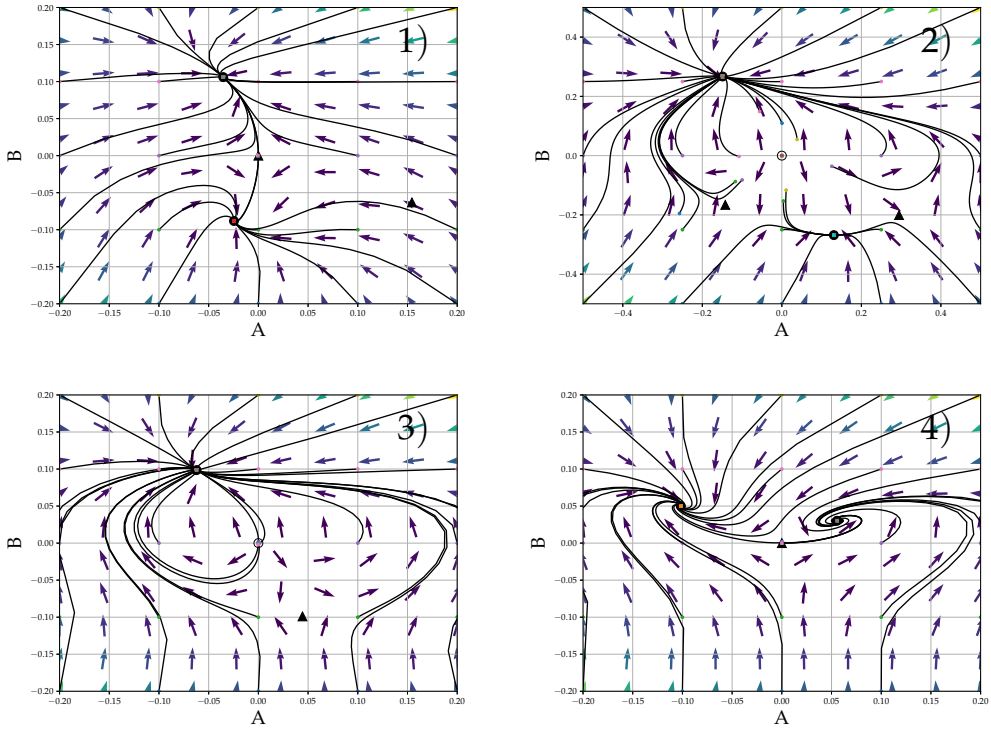


Figure 3.14: Phase-plane diagrams (A, B) describing the *even-even* interaction for mode numbers $\ell = 2, 4$ and $Pr = 10$. In regions: 1 mixed modes $(A_1, +B_1), (A_2, -B_2)$ exist, 2 two stable and unstable mixed modes, 3 a single stable mixed mode, while in region 4 two stable spiral nodes $(-A_1, B_1), (-A_2, B_2)$ are obtained.

3.4 Comparison of weakly nonlinear theory with DNS

Equations (3.51) - (3.55), derived using weakly nonlinear theory, apply rigorously only in an $\mathcal{O}(\epsilon)$ neighbourhood of the degenerate points (d_c, Ra_c) seen in figure 3.4. For this reason it is reasonable to question their validity in the context of the full problem. We validate previous results by performing DNS of the full equations (3.1). The numerical code used in this section uses a Galerkin-Legendre projection in θ and second order finite differences in r as outlined in appendix D. A minimum resolution of 15 polynomials in θ and 40 grid points in r was used in all computations. Specifying values of (d, Ra) a full numerical simulation is run, whose mode amplitudes are computed from the inner products

$$A_{num}(t) = \frac{\langle \boldsymbol{\psi}_{num}, \boldsymbol{\psi}_\ell \rangle}{\langle \boldsymbol{\psi}_\ell, \boldsymbol{\psi}_\ell \rangle}, \qquad B_{num}(t) = \frac{\langle \boldsymbol{\psi}_{num}, \boldsymbol{\psi}_n \rangle}{\langle \boldsymbol{\psi}_n, \boldsymbol{\psi}_n \rangle}, \quad \text{where} \quad \langle f, g \rangle = \int_r \int_\theta \frac{f\, g}{\sin\theta} dr d\theta. \tag{3.64}$$

Vectors $\boldsymbol{\psi}_\ell, \boldsymbol{\psi}_n$ are the eigenfunctions (3.16) evaluated at the grid points of the numerical finite difference solution $\boldsymbol{\psi}_{num}$. For comparison with weakly non-linear theory, values for μ, δ, ϵ are specified and the solution determined by solving the relevant amplitude equations. Setting $\mu = \pm 1$ we obtain

$$\epsilon = \frac{\mathrm{Ra} - \mathrm{Ra}_c}{\mathrm{Ra}_c}, \qquad \delta = \frac{d - d_c}{\epsilon}. \tag{3.65}$$

Simulating (3.51) – (3.55) with these values we obtain a solution (A, B), which is rescaled according to the original expansion (3.25). Amplitudes of the weakly nonlinear theory are obtained as

$$A_{wkly} = \epsilon A, \qquad B_{wkly} = \epsilon B. \tag{3.66}$$

3.4.1 Neighbouring mode interactions

The *even-odd* case is simulated for parameter values corresponding to regions 3 and 4 of figure 3.8 where both mixed and even solutions are found. This region is chosen in order to test the initial condition dependency predicted by theory. In the initial condition dependent region 3, even solutions are readily obtained from even initial conditions, as the linear stability of the even solutions tends to ensure that the solution remains even. Mixed solutions are not so easy to find, but can be located by continuation from the mixed solutions of region 4. The numerical values of each mode shown in table 3.1 confirm that odd modes maintain a larger amplitude in mixed mode solutions. Corresponding solutions of the flow field are shown in figure 3.15.

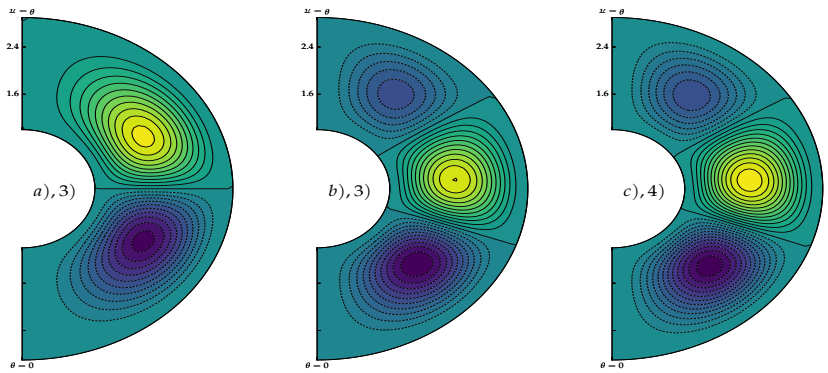


Figure 3.15: Numerical solutions $\psi(r,\theta)$ in the neighbourhood of the $\ell = 2,3$ degenerate point ($d_c = 1.9883, \mathrm{Ra}_c = 857.53$) for $Pr = 1$. (a) corresponds to region 3 of figure 3.8 for the $\ell = 2$ mode ($d_c, \mathrm{Ra} = 900.0$), (b) region 3 for the mixed ($d = 1.946, \mathrm{Ra} = 950.0$), (c) region 4 the mixed ($d = 1.9481, \mathrm{Ra} = 900.0$). The colour versions of this figure and those which follow may be viewed online.

Region	ϵ	(δ, μ)	$(A,B)_{wkly}$ $Pr = 1$	$(A,B)_{num}$	$(A,B)_{wkly}$ $Pr = 10$	$(A,B)_{num}$
3)	0.0495	0,1	(-0.2826,0.0)	(-0.3165,0.0)	(-0.3312,0.0)	(-0.3632,0.0)
3)	0.108	-0.4,1	(-0.0776, -0.2332)	(-0.1354,-0.2259)	(-0.0772, -0.2505)	(-0.1135, -0.2623)
4)	0.05	-0.8,1	(-0.0623, 0.0902)	(-0.0825,-0.1092)	(-0.0592, 0.1082)	(-0.0734,-0.1356)

Table 3.1: Comparison of DNS $(A,B)_{num}$ and weakly nonlinear $(A,B)_{wkly}$ solutions for the modes $\ell = 2,3$. The discrepancy between theory and simulation is attributed to the even $\ell = 4$ mode contribution, found to be non-negligible in DNS, particularly for the mixed solutions in region 3 where both modes are linearly unstable. The odd mode component of mixed solutions maintains a larger amplitude.

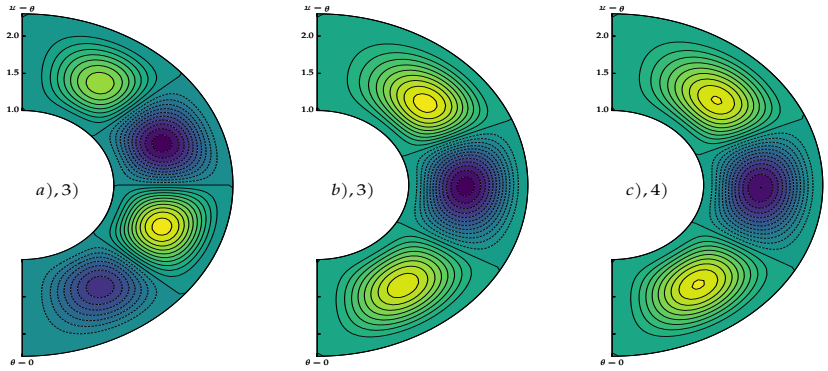


Figure 3.16: Numerical solutions $\psi(r,\theta)$ in the neighbourhood of the $\ell = 3,4$ degenerate point ($d_c = 1.2291, \mathrm{Ra}_c = 2381.1$) with $Pr = 1$. (a) corresponds to region 3 of figure 3.10 for the $n = 4$ mode ($d = 1.2291, \mathrm{Ra} = 2650.0$), (b) region 3 for the mixed ($d = 1.2674, \mathrm{Ra}_c$), (c) region 4 for the mixed ($d = 1.2674, \mathrm{Ra} = 2230.0$).

Region	ϵ	(δ, μ)	$(A,B)_{wkly}$ $Pr=1$	$(A,B)_{num}$	$(A,B)_{wkly}$ $Pr=10$	$(A,B)_{num}$
3)	0.1125	0,1	(0.0,-0.3208)	(0.0,-0.3508)	(0.0,-0.3474)	(0.0,-0.3662)
3)	0.05	0.766,0	(-0.3755, 0.0358)	(-0.3665,0.0549)	(-0.4202 0.0323)	(-0.4079,0.0518)
4)	0.05	0.7,-1.27	(-0.1675, 0.0265)	(-0.1705,0.0262)	(-0.1916, 0.0241)	(-0.1879,0.024)

Table 3.2: Comparison of DNS and weakly non-linear solutions for the modes $\ell = 3,4$. The discrepancy between theory and simulation is attributed to the $\ell = 2$ mode contribution, found to be non-negligible in DNS, particularly for the mixed solutions in region 3 where both modes are linearly unstable. The odd mode component of mixed solutions maintains a larger amplitude.

A similar procedure is adopted for the *odd-even* case to simulate mixed solutions in region 3 of figure 3.10. Only in certain sections of region 3 are even solutions found to be stable to odd mode perturbations. In addition to finding solutions corresponding to figure 3.10, the ratio of mixed mode amplitudes also matches well for even solutions in region 3 and mixed solutions in region 4 (see tables 3.1,3.2). For mixed solutions in region 3, however, the contribution of modes $\ell = 2,4$ becomes non-negligible for the values of ϵ considered. The discrepancy between theory and DNS is attributed to the omission of these modes for the respective cases. Corresponding solutions of the flow field are shown in figure 3.16.

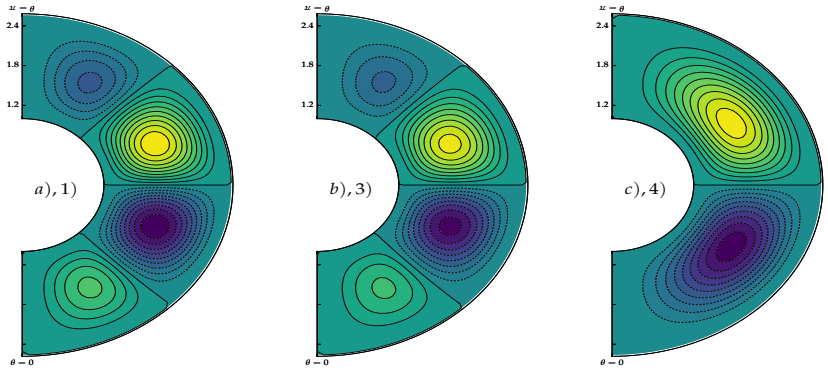


Figure 3.17: Symmetric solutions $\psi(r,\theta)$ near the $\ell = 2,4$ degenerate point ($d_c = 1.5807, \mathrm{Ra}_c = 1515.399$) for $Pr = 10$. (a) corresponds to region 1 of figure 3.13 with ($d = 1.5507, \mathrm{Ra} = 1591.392$), (b) region 3 for ($d_c, \mathrm{Ra} = 1591.392$), (c) region 4 for ($d = 1.6132, \mathrm{Ra} = 1480$). In frames a) and c) only modes $\ell = 4$ and $\ell = 2$ respectively are linearly unstable.

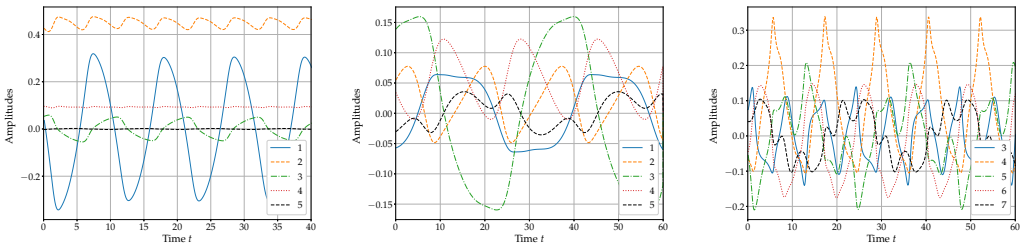
Region	ϵ	(δ, μ)	$(A,B)_{wkly}$ $Pr = 1$	$(A,B)_{num}$	$(A,B)_{wkly}$ $Pr = 10$	$(A,B)_{num}$
3)	0.05	-0.6,1	(-0.0817, 0.1454)	(-0.0806,0.1452)	(-0.0867, 0.1541)	(-0.0838,0.1544)
3)	0.05	0,1	(-0.1357, 0.2079)	(-0.1406,0.2135)	(-0.1458, 0.2196)	(-0.1486,0.2258)
4)	0.05	0.65,-0.47	(-0.1034, 0.1275)	(-0.1092,0.1246)	(-0.1212, 0.1339)	(-0.1272, 0.132)

Table 3.3: Comparison of numerical and weakly non-linear solutions for the modes $\ell = 2,4$. By removing all odd modes the dominance of the remaining modes is increased and an improved agreement between computation and theory is obtained.

3.4.2 Non-neighbouring mode interactions

The *even-even* interaction described by (3.55) may seem of limited relevance, as solutions obtained for small ϵ are necessarily unstable to odd mode perturbations. A rigorous reduced order model of this interaction point would therefore have to include the effect of unstable intermediate modes for example, the $\ell = 3$ mode in the ($\ell = 2,4$) case. However, when we compute the stability of saturated solutions for large ϵ in section 5.1, we find that some even solutions are in fact stable to odd perturbations. Such interactions are also thought to exhibit strong resonances and be of physical significance in mantle convection (Chossat & Stewart 1992). We compare DNS runs with and without screening of the odd modes to determine their validity for the fully nonlinear problem.

Unsurprisingly, the screened simulations (figure 3.17) near the $\ell = 2,4$ degenerate point are found to agree better with theory than those with odd modes. The numerical values



(a) $\ell = (1, 3),\ d = 3$ **(b)** $\ell = (2, 4),\ d = 1.5$ **(c)** $\ell = (4, 6),\ d = 0.78$

Figure 3.18: DNS oscillation signature for the periodic solutions near the *even-even* and *odd-odd* degeneracies with $Pr = 0.05$. Solutions are simulated at (a) $\mathrm{Ra}_c = 440.852, \epsilon = 5.85$, (b) $\mathrm{Ra}_c = 1515.41, \epsilon = 0.847$, (c) $\mathrm{Ra}_c = 3425.94, \epsilon = 0.4594$. Notably the Rayleigh number required to sustain oscillations increases as ℓ, n decrease. Even modes oscillate out of phase with equal period, while the odd mode oscillates with double the period of even modes. As the mode numbers increase additional modes contribute and the signal becomes increasingly modulated. Animations corresponding to each figure may be found online at https://doi.org/10.1017/jfm.2019.440.

are outlined in table 3.3. Given that the solution energy is quantised between fewer linearly unstable modes this improved agreement is anticipated.

For the same parameter values, unscreened simulations near the $\ell = 2, 4$ point lose stability to odd mode perturbations as expected, with significant components of modes $\ell = 1, 2, 3, 4$ remaining. Increasing the Rayleigh number beyond $Ra \cong 1.7 Ra_c$ (measured from the $\ell = 2, 4$ degenerate point), stable mixed time-periodic solutions emerge for low Pr. This is depicted in figure 3.18 where the amplitude of each mode is plotted as a function of time. Granted that no oscillatory solutions are found for two mode interactions we enquire: Why are odd mode components necessary to maintain a regular oscillation? and why is the oscillation period of odd modes approximately twice that of even modes? We stress that these time periodic solutions emerge for $\epsilon \sim \mathcal{O}(1),\ Pr \ll 1$ and are, strictly speaking, beyond the scope of weakly nonlinear theory. Nonetheless using the structure of (3.61) it is possible to explain their oscillation signature.

A distinctive feature of the time periodic solutions shown in figure 3.18 is that even and odd modes oscillate with approximately a $2:1$ frequency ratio. Also notable is that the time signature for smaller d becomes increasingly modulated when compared with that of lower mode numbers. Running DNS near each degeneracy with odd modes suppressed we find that the time-periodic solutions presented in figure 3.18 no longer persist. This suggests the bifurcation to time-periodic solutions at low Pr is an odd mode instability.

We attribute the $2:1$ resonance to a symmetry breaking Hopf bifurcation (as confirmed in section 3.5 using numerical continuation) whose weakly nonlinear behaviour may be described locally by a complex analogue of (3.61) (Proctor & Jones 1988). Writing (3.61)

in complex form

$$\left.\begin{aligned}\dot{A} &= \mu_1 A + \alpha_2 \bar{A} B + d_{12} A|B|^2 + d_{13} A|A|^2, \\ \dot{B} &= \mu_2 B + \beta_1 A^2 + d_{21}|A|^2 B + d_{24} B|B|^2,\end{aligned}\right\} \begin{array}{l} A \sim \ell \quad odd \\ B \sim n > \ell \quad even \end{array} \tag{3.67}$$

and subsituting the ansatz $A = ae^{i\omega_1 t}$, $B = be^{i\omega_2 t}$, one finds that the quadratic terms enforce the relation $2\omega_1 = \omega_2$. Thus by dictating the nonlinear terms permissible in (3.61) the eigenfunctions constrain the phase of even and odd modes in standing wave solutions. Near the $\ell = 1, 3$ degeneracy, the set of contributing modes is small so that few harmonics are generated. At higher degeneracies, more modes contribute generating additional harmonics which modulate the oscillation signature observed in figure 3.18.

3.5 Transition to time-dependent convection

A motivation for approaching this problem using weakly nonlinear theory was to gain a concise description of the flow's time-dependent behaviour, which typically emerges near onset for $Pr \ll 1$. An ODE model was thought to be useful, particularly for understanding the parameter dependence of any limit cycles which should emerge. This is in contrast to DNS where time dependence increases the numerical dimension of a solution, particularly for stiff systems or those with a ratio (or many ratios) of diffusive parameters analogous to the Pr. As evidenced in section 3.4 however, time dependent behaviour in 2D convection emerges only for larger values of $\epsilon \gg 1$ and is beyond the scope of weakly nonlinear theory. While time dependence is observed at onset for $\epsilon \ll 1$ in 3D system, the dimension of the reduced systems obtained at degenerate points $4(\ell + 1)$ is still large (Friedrich & Haken 1986, Beltrame & Chossat 2015).

In this section numerical computations (carried out with the pseudo-spectral code described in appendix D) are used to study the behaviour of steady and time-dependent convection at large Ra. Simulations use $Nr = 25 - 65$ Cheybshev collocation points radially and $N_\theta = 60$ Legendre polynomials in the polar direction. The separation is fixed at $d = 3$, a value chosen to facilitate numerical simulations. Near the onset of convection we find three possible solutions. An even 2-cell with rising plumes at the poles and sinking plumes at the equator denoted u_r^-, an even 2-cell with rising and sinking plumes in the opposite sense denoted u_r^+ and a mixed or odd 1-cell flow with one large rising plume. These flows are shown in figures 3.20 for $Pr = 0.05$ and figure 3.22 for $Pr = 10$.

Outlining the bifurcation sequence for $Pr = 0.05, 10$ we show how the time-dependent behaviour observed in section 3.4 emerges through a sequence of symmetry breaking bifurcations from the conductive state. By computing the latitudinally averaged temperature profile $\overline{T(r,\theta)}$, and convective heat transfer as measured by the Nusselt number Nu we also study the significance of the radially asymmetric thermal boundary layers which

emerge for $Pr \gg 1$. Finally we provide an additional validation for our numerical code by showing that the scaling $Nu \approxeq 0.122(Ra/Ra_c)^{0.2875}$ predicted by our code is in keeping with recent studies of 3D spherical shell convection (Gastine *et al.* 2015).

3.5.1 Bifurcation sequence for moderate Ra at low Pr

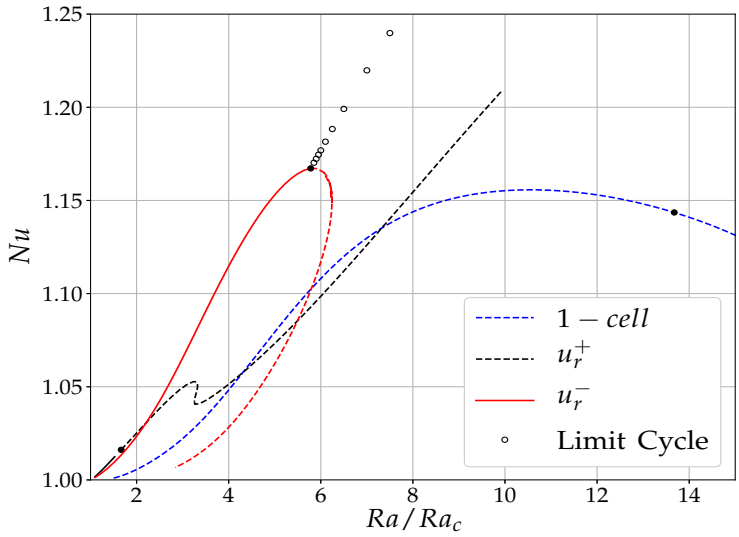
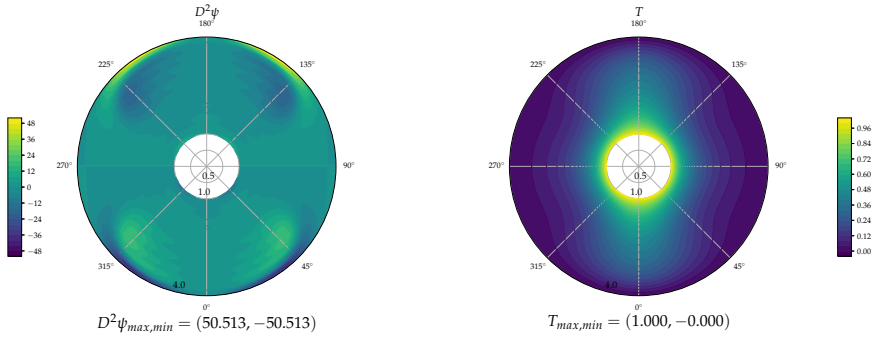


Figure 3.19: Time periodic solutions bifurcate from the even state in a symmetric Hopf bifurcation. Stability and convective heat transfer Nu of the even u_r^-, u_r^+ and mixed 1-cell solution states at $Pr = 0.05, d = 3$. Stable and unstable states are denoted by solid and dashed lines respectively with bifurcation points indicated by solid black dots.

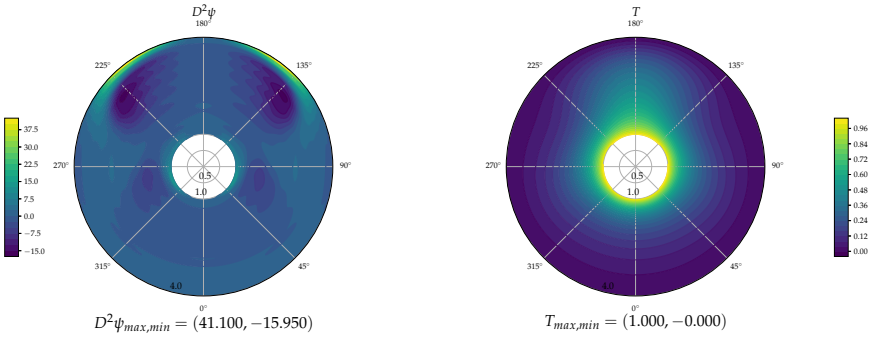
Figure 3.19 outlines the sequence of transitions by which time-dependent behaviour emerges for low Pr. The variation of Nu (the strength of convective heat transfer) with Ra/Ra_c is chosen to indicate the stability of solutions.

For small Ra/Ra_c both even solutions are stable, but as Ra/Ra_c increases only the u_r^- state represented by the solid red branch remains stable. This is despite the higher heat transfer of the u_r^+ solution state as compared with u_r^-. The temperature and vorticity fields of this solution are shown in frame (a) of figure 3.20. In this spatial solution the temperature field is weakly deformed from concentric circles, while the vorticity field attains a maximum at $\pm 45^o$ to the equator in each quadrant near the outer boundary.

Increasing Ra/Ra_c further leads to a symmetry breaking Hopf bifurcation where the even u_r^- state loses stability to an odd mode perturbation. This perturbation is found to be dominated by its $\ell = 1$ mode component. Time integration of the u_r^- state and this



(a) Even u_r^- state $Ra/Ra_c = 6.25$.



(b) Mixed 1-cell state $Ra/Ra_c = 4.9$.

Figure 3.20: Steady states of the vorticity $D^2\psi$ and temperature field T of the even and mixed solutions at $Pr = 0.05, d = 3$. (a) Symmetric even state with plumes directed along the poles, (b) Asymmetric mixed mode state with a single wide plume directed towards the pole.

perturbation results in periodic limit-cycle denoted by open circles in figure 3.19. The time-dependence of this flow at $Ra/Ra_c = 8$ for modes $\ell = 1 - 5$ is shown in figure 3.18. Accompanying animations of this solution are available in the supplementary material of Mannix & Mestel (2019). The animation shows the periodic growth and shrinking of each convection cell (ψ field) as they oscillate back and forth at the equator. Further increasing Ra it is found that this limit cycle undergoes period doubling bifurcations.

In addition to understanding the sequence of transitions leading to a time-dependent flow, it is also desirable to understand how the T field deforms with increasing Ra. To do so at low Pr where the temperature field largely dictates the velocity field makes it necessary to consider larger Ra than we have yet outlined. On the basis that low Pr convection is likely to be unstable to non-axisymmetric perturbations even for small Ra we do not investigate this case, but instead now consider large Pr flows to answer this question.

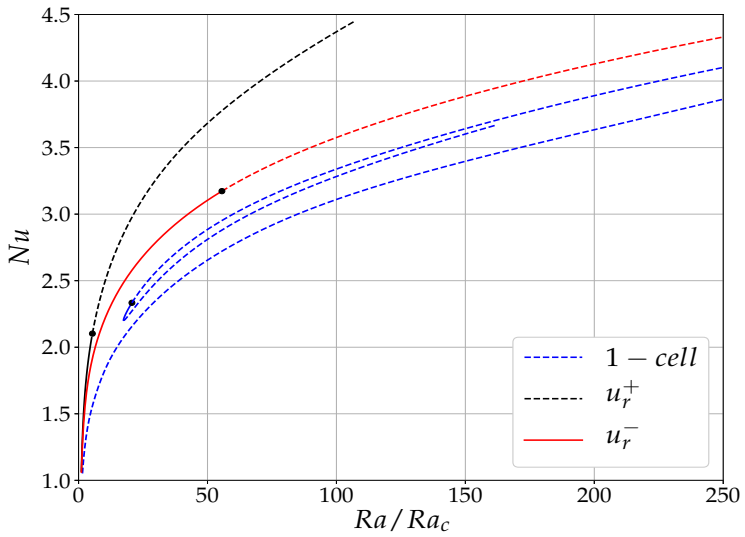


Figure 3.21: Bifurcation diagram indicating both the stability and convective heat transfer of the even u_r^-, u_r^+ and mixed 1-cell solutions at $Pr = 10, d = 3$. Stable and unstable states are denoted by solid and dashed lines respectively with bifurcation points indicated by solid dots.

3.5.2 Bifurcation sequence for moderate Ra at high Pr

Figure 3.21 outlines the sequence of transitions by which time-dependent behaviour emerges at high Pr. The branching structure for this case is notably less complex when compared with the $Pr \ll 1$ scenario. In addition all solutions are found to remain both steady and stable for much larger Ra.

For small Ra/Ra_c both even solutions are stable, but increasing Ra/Ra_c we find that only the u_r^- state indicated by the solid red branch remains stable. This behaviour was also observed at low Pr. The convective heat transfer achieved by both solutions in figure 3.21 shows that the u_r^- state despite being stable for larger Ra/Ra_c achieves a comparably lower Nu. The temperature and vorticity fields of this solution are shown in frame (a) of figure 3.22. The temperature field has rising plumes directed along the poles, which result from the fluid being heated as it passes near the hot inner sphere. The corresponding vorticity field attains its maxima at the sphere's boundaries and in the neighbourhood of the plumes where the thermal boundary layer is developed. Increasing Ra/Ra_c further causes the symmetric u_r^- state to lose stability and transition to a mixed state in a symmetry breaking bifurcation. This is indicated by a black dot on the red branch in figure 3.21.

A mixed solution state indicated by a solid blue line in figure 3.21 is also possible for a

narrow range of Ra/Ra_c. Decreasing Ra/Ra_c induces its transition back to the u_r^- state at the saddle-node, while increasing Ra/Ra_c results in a transition to a time-periodic state via the Hopf bifurcation denoted by a black dot. The temperature and vorticity fields of the stationary mixed solution are shown in frame (b) of figure 3.22. The time-periodic state which bifurcates from this stationary state is also found to have a similar spatial form. The temperature field has a single rising plume directed along the north pole and a weaker sinking plume of cold fluid near the south pole. As this flow is asymmetric a corresponding state with plumes arranged in the opposite sense also exists. This follows from the antisymmetry of odd numbered Legendre polynomials, and requires the consideration of non-axisymmetric effects to establish the preferred state. The corresponding vorticity field attains its maxima in the the sphere's upper half, in particular at the sphere's boundaries and in the neighbourhood of the plume where the thermal boundary layer is most developed. Notably this state in both its stationary and time-dependent forms is bistable with the even u_r^- state. This is despite its comparably lower heat transfer as indicated in figure 3.21.

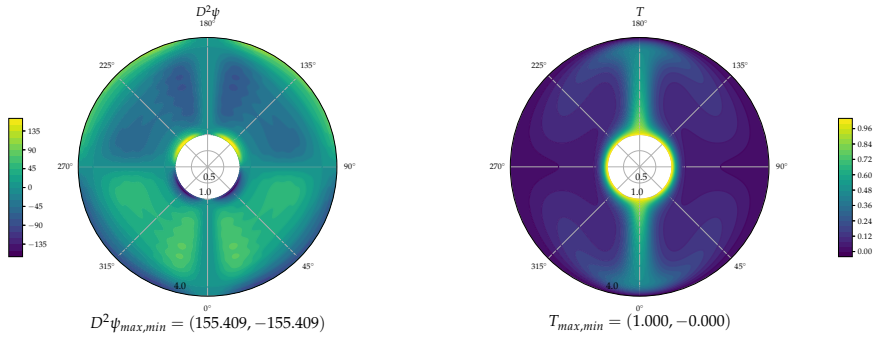
In order to obtain the asymptotic scalings of Nu with Ra for each flow, we have computed the Nusselt number of each state up to $Ra \approxeq 250 Ra_c$ as shown in figure 3.21. Considering the range $Ra/Ra_c \in [100, 250]$ or ($Ra \in [10^4, 10^5]$) of the mixed 1-cell and even u_r^- solutions we obtain the scalings

$$Nu \approxeq 0.112(Ra/Ra_c)^{0.309}, \qquad Nu \approxeq 0.125(Ra/Ra_c)^{0.2875}. \tag{3.68}$$

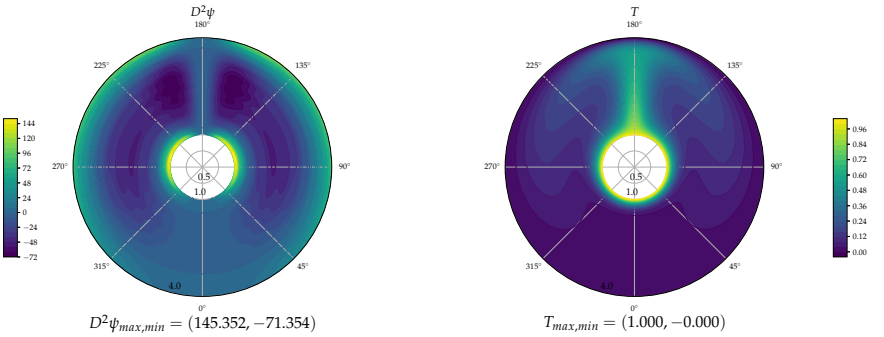
While the Nusselt number of the even state u_r^+ increases faster than these states, a clear asymptote is not apparent and for this reason it is not considered. These scalings appear consistent with those of Gastine *et al.* (2015) who obtained $Nu \approxeq 0.166(Ra/Ra_c)^{0.289}$ for DNS of 3D spherical shell convection for $Ra \in [10^3, 10^9]$. To compute this relation Gastine *et al.* (2015) used the mean exponent obtained over a range of Ra, but remarked that its value tended to be a slowly increasing function of Ra.

To provide a physical understanding for the differences which emerge in the scalings and stability of the flows obtained, we consider the thermal boundary layers which emerge at the sphere's surfaces and in the neighbourhood of the thermal plume(s). Consideration of these regions also highlights key differences between convection in a spherical shell geometry as compared with a rectangular plane layer.

Frame (a) of figure 3.23 shows the latitudinally averaged temperature profile of each solution considered in this section for $Ra/Ra_c \approxeq 100$. Each profile displays strong gradients near the inner and outer spheres, in addition to a core region where the temperature varies weakly with r. Excluding the u_r^+ profile which displays a higher temperature in its core region and larger gradients near the boundaries, all three remain qualitatively similar. That the temperature profiles with the larger near wall gradients should have

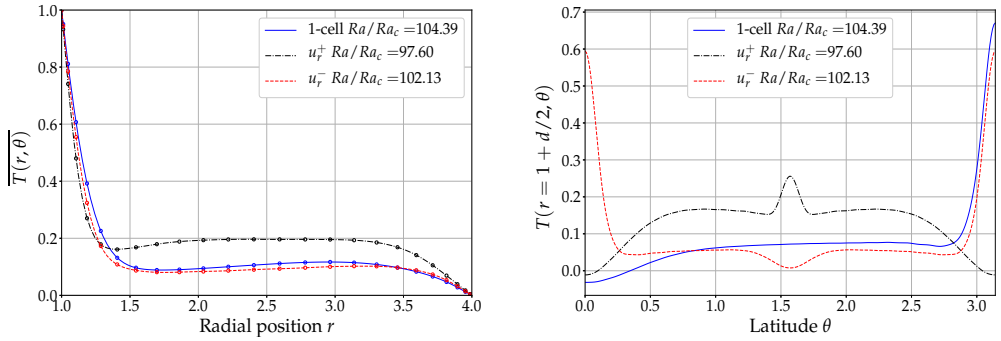


(a) Even u_r^- state $Ra/Ra_c = 30$.



(b) Mixed 1-cell state $Ra/Ra_c = 20$.

Figure 3.22: Steady states showing the vorticity $D^2\psi$ and temperature field T of the even and mixed solutions at $Pr = 10, d = 3$. (a) Symmetric even state with plumes directed along the poles, (b) Asymmetric mixed mode state with a single wide plume directed towards the pole.



(a) Latitudinally averaged T profile. **(b)** Annulus centreline T profile.

Figure 3.23: Thermal boundary layer profiles of the even and mixed solutions at $Pr = 10, d = 3$. (a) Latitudinally averaged profile showing the asymmetric inner and outer shell boundary layers, (b) Temperature profiles at the annulus centreline, demonstrating that the solutions with plumes rising at the poles have higher latitudinal gradients.

larger exponents in the scaling relation (3.68) also holds well with intuition. The radial asymmetry observed in these profiles is a consequence of the spherical shell geometry and radial gravity. Heat flux conservation requires a comparatively larger gradient at the inner sphere's surface to compensate for its lower surface area. Computations for a variety of separations by Gastine *et al.* (2015) indicate that as $d \to 0$, the latitudinally averaged temperature $\overline{T(r,\theta)}$ tends to become symmetric about the annulus centreline.

Frame (b) of figure 3.23 shows the temperature profile of each solution at the annulus centreline. The 1-cell flow whose plume is directed along the symmetry axis develops strong gradients near $\theta = \pi$. This is also the case for the u_r^- flow which develops strong gradients near $\theta = 0, \pi$ accompanied by weaker gradients at $\theta = \pi/2$, the location of its sinking plume as shown in figure 3.22. As was outlined in figure 3.21, both of these flows remain stable for large Ra despite their comparably lower heat transfer Nu. In contrast, the u_r^+ flow which has rising plumes at the equator but develops a comparably weaker boundary layers near $\theta = 0, \pi$ loses stability at small Ra

Collectively these observations suggest that for large Pr, it is the flows which achieve large gradients at both the sphere's boundaries and in their rising plumes that remain most stable. What remains surprising is that among the flows shown in this section, it is not necessarily those with the largest convective heat transfer Nu that are the most stable.

4

Thermally convective spherical Couette flow

4.1 Model equations and solution regimes

The equations describing axisymmetric Rayleigh-Bénard convection in a spherical annulus allowing for differential rotation are given by

$$\frac{\partial D^2\psi}{\partial t} + \mathcal{J}(\psi,\psi) + N_1(\Omega,\Omega) = Pr\left(\mathrm{Ra}\, g(r) r \frac{\partial T}{\partial \theta}\sin\theta + D^2 D^2 \psi\right), \tag{4.1a}$$

$$\frac{\partial T}{\partial t} + J(\psi,T) = \nabla^2 T, \tag{4.1b}$$

$$\frac{\partial \Omega}{\partial t} + J(\psi,\Omega) = Pr D^2\Omega, \tag{4.1c}$$

where

$$J(f,g) = \frac{1}{r^2\sin\theta}\frac{\partial(f,g)}{\partial(\theta,r)}, \quad \mathcal{J}(f,g) = \sin\theta\frac{\partial(f,D^2g/(r^2\sin^2\theta))}{\partial(\theta,r)}, \quad N_1(f,g) = \frac{2f}{r^2\sin\theta}\big(\cot\theta\frac{\partial g}{\partial r} - \frac{1}{r}\frac{\partial g}{\partial\theta}\big). \tag{4.2}$$

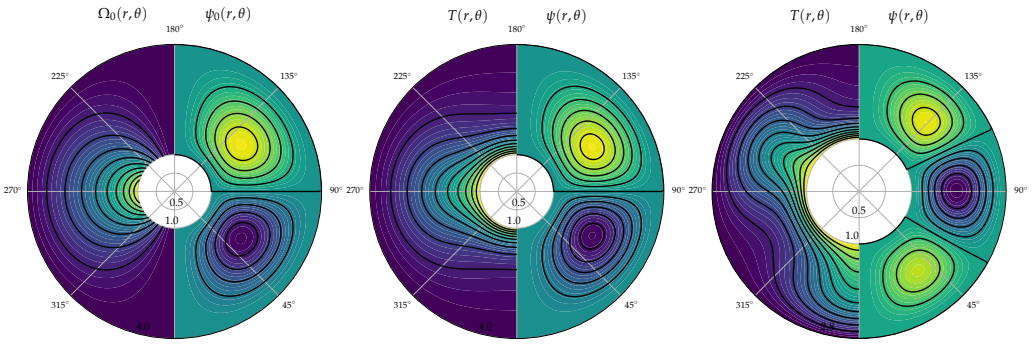
As per (2.7) the inner sphere radius r_1, and thermal diffusion timescale r_1^2/κ, have been chosen to make the equations non-dimensional. In this section we consider no-slip boundary conditions for the fluid velocity at the sphere walls, and make the assumption of

perfectly conducting spheres as per chapter 3. For the formulation 4.1 this gives

$$\begin{aligned}
&\psi(r,\theta) = \psi_r(r,\theta) = 0, \quad \text{for } r = 1, 1+d, \\
&T(1,\theta) = 1, \quad T(1+d,\theta) = 0, \\
&\Omega(1,\theta) = Re_1\, Pr \sin^2\theta, \quad \Omega(1+d,\theta) = Re_2\, Pr \sin^2\theta.
\end{aligned} \tag{4.3}$$

Although we allow for the possibility of outer sphere rotation we will fix $Re_2 = 0$. This choice is motivated by the assumption that inner sphere rotation presents a less stable configuration (following the Rayleigh criterion Taylor (1923)) leading transitions for smaller parameter values and reducing the number of parameters in this problem. The previously outlined symmetry conditions (2.16) must also be enforced at the symmetry axis. As per chapter 3, non-axisymmetric effects are considered later in chapter 5 to validate the assumption of axisymmetry.

4.1.1 Decoupled steady solutions



a) $\psi_{max,min} = (0.07, -0.07)$ b) $\psi_{max,min} = (2.72, -2.72)$ c) $\psi_{max,min} = (2.80, -3.93)$

Figure 4.1: Decoupled steady state solutions of the differential rotation and thermal convection ($Pr = 10$) problems illustrating similar spatial solutions. (a) Differential rotation (2.18) for $Re_1 = 1, d = 3, Ra = 0$. A 2-cell poloidal flow ψ_0 transports fluid near the inner sphere with high specific angular momentum (shown as yellow in the Ω_0 field) outwards. (b) 2-cell thermal convection $Re_1 = 0, d = 3, Ra = 740$, (c) 3-cell thermal convection $Re_1 = 0, d = 1.5, Ra = 2160$. Hot fluid near the inner sphere is convected outwards by a cellular flow ψ. For the convection problem $Ra \neq 0$, the number of cells as specified by the annulus width increases as d reduces.

As shown schematically in figure 1.3, fluid motion (vorticity) in this model can be maintained by two distinct processes: buoyancy forces which drive thermal convection when the conductive state becomes unstable, and differential rotation (wall shear) which drives a recirculating flow. Decoupled solutions of (4.1) for each process are shown in figure 4.1, where it is noteworthy that the contours of poloidal motion ψ in frames (a), (b) have a

similar spatial form. While a poloidal flow ψ_0 is generated for all $Re_1 \neq 0$, thermal convection arises from an instability of the conductive base state (2.17) when the Ra exceeds a critical Rayleigh number termed Ra_c. The solutions shown in frames (b), (c) are therefore simulated at a supercritical Rayleigh number $Ra > Ra_c$.

In the left half frame of figure 4.1 (a) the specific angular momentum field Ω_0 corresponding to the Stokes solution (2.18) for $Re_1 = 1$ is shown. In frames (b), (c) the temperature field T produced using DNS is shown. The corresponding poloidal flow field in terms of ψ is also shown in the right hand side of each frame. Focusing on frame (a) we see that the effect of inner sphere rotation is to generate a radial gradient of Ω that is strongest at the equator where the sphere's velocity is greatest. The fluid responds by generating a 2-cell poloidal flow ψ_0 which transports fluid near the inner sphere with high specific angular momentum Ω_0 outwards at the equator. In frames (b) and (c) an analogous situation arises, with hot fluid near the inner sphere convected outwards by a cellular poloidal flow ψ. Notably the number of cells is determined by the annulus width d, so that by reducing d in frame (c) the number of cells has increased. This contrasts with the behaviour of the flow shown in frame (a) where a 2-cell flow is generated independent of d provided Re_1 is not too large.

Given the equations (4.1) with boundary conditions (4.3) and the knowledge that the two physical mechanisms driving the fluid flow yield distinct solution regimes, we aim to answer the following questions in this chapter. In addition to the rotating and thermal convection solution regimes outlined, is there an intermediary regime where a mixed state exists? Or alternatively a regime where a transition between these states occurs? If so, how does the Prandtl number influence the solution state or transitions observed? And ultimately what determines the preferred state of convective motion in the presence of multiple solutions?

4.1.2 Role of Prandtl number

Before addressing these questions we briefly first describe the role of Pr. As Pr appears in the boundary conditions for (4.1) it is convenient to use the transformation

$$\psi = \tilde{\psi}(r,\theta,t), \quad T = T_0(r) + \tilde{T}(r,\theta,t), \quad \Omega = Re_1 Pr\ \Omega_0(r,\theta) + \tilde{\Omega}(r,\theta,t), \tag{4.4}$$

such that all tilde terms satisfy homogeneous boundary conditions. Substituting (4.4) into (4.1) and dropping the tilde terms this allows equations (4.1) to be expressed as

$$Pr^{-1}\left(\frac{\partial D^2\psi}{\partial t} + \mathcal{J}(\psi,\psi) + N_1(\Omega,\Omega)\right) = \mathrm{Ra}\, g(r) r \frac{\partial T}{\partial \theta}\sin\theta + D^2 D^2 \psi - Re_1\big(N_1(\Omega,\Omega_0) + N_1(\Omega_0,\Omega)\big) - Re_1^2\, Pr\, N_1(\Omega_0,\Omega_0), \tag{4.5a}$$

$$\frac{\partial T}{\partial t} + J(\psi, T) = -J(\psi, T_0) + \nabla^2 T, \tag{4.5b}$$

$$Pr^{-1}\left(\frac{\partial \Omega}{\partial t} + J(\psi, \Omega)\right) = -Re_1 J(\psi, \Omega_0) + D^2\Omega, \tag{4.5c}$$

where Re_1 now appears explicitly in the right hand side of (4.5a),(4.5c).

At small Pr viscous forces are weak and the effects of rotation will be felt only if $Re_1 Pr \sim \mathcal{O}(1)$. In the limit $Pr \to 0$ one must adopt the rescaling

$$\tilde{\psi} = Pr^{-1}\psi, \qquad \tilde{T} = Pr^{-1}T, \qquad \tilde{\Omega} = Pr^{-1}\Omega, \qquad \tilde{t} = Pr\, t, \tag{4.6}$$

as advection terms in both the vorticity and specific angular momentum equations are dominant with their gradients confined to a thin momentum boundary layer. As flows in this limit are likely to be both 3D and time-dependent we do not consider this limit. Furthermore in the subsurface oceans of Jupiter's moons and in the earth's outer core (applications which motivate this study) larger $Pr \in [0.1, 10]$ are more applicable (Aurnou *et al.* 2007, Noir *et al.* 2009).

In the large $Pr = \nu/\kappa$ regime, thermal diffusion $\kappa \ll 1$ is weak and we expect viscous effects to dominate in the fluid bulk such that the velocity field (driven by small Ra or Re_1) dictates the temperature field with $J(\psi, T) \approxeq 0$ (Batchelor 1956). Following Childress & Soward (1989) we anticipate that away from the boundaries and plumes the temperature takes a constant value. In their vicinity however, large temperature gradients develop as Ra increases, such that thermal diffusion although weak will become significant leading to the emergence of thermal boundary layers in which thermal diffusion and convection balance. Assuming a steady velocity field we require (in dimensional variables) that

$$\frac{u_\theta}{r}\frac{\partial T}{\partial \theta} \approxeq \kappa \frac{1}{r^2}\frac{\partial}{\partial r}\left(r^2 \frac{\partial T}{\partial r}\right), \tag{4.7}$$

inside the thermal boundary layers which develop near the spherical boundaries, while in the narrow thermal plumes we require

$$u_r \frac{\partial T}{\partial r} \approxeq \kappa \frac{1}{r^2 \sin\theta}\frac{\partial}{\partial \theta}\left(\sin\theta \frac{\partial T}{\partial \theta}\right). \tag{4.8}$$

Physically these relations state that the diffusion of temperature across the thermal boundary layer tends to increase its width, but is balanced by convection inside the layer which tends to reduce its width. For (4.7) convection is parallel to the sphere's boundaries while for (4.8) it radially outwards in rising a plume. While these balances are more easily understood for $Re_1 = 0$ where the cellular velocity field is less complex (Turcotte & Oxburgh

1967, Moore & Weiss 1973), understanding how they're influenced as $\boldsymbol{u}$ is determined more strongly by differential rotation or libration effects which give rise to strong zonal flows remains an important question.

Previous works demonstrate that the stability and form of convection in rotating spherical shells is highly Pr dependent and exhibits different regimes (Zhang & Liao 2017). For fast rotation rates and moderate Pr thermal Rossby waves in the form of spiralling columns are obtained while at low Pr these are equatorially attached waves. These differences largely reflect how the competition between buoyancy and Coriolis forces is altered.

In shear flows also driven by buoyancy as considered in this section, it is the competition between shear and thermal buoyancy which determines the flow's state. Such flows have been reviewed by Kelly (1994) and stability relations have been derived by H.W. Muller (1992), Müller *et al.* (1993) for planar Rayleigh-Bénard convection with a weak transverse shear flow. Neither of these works however considers variations of Pr despite its significant influence. Nevertheless its dependency is non-trivial, with studies of inclined layer convection for example Subramanian *et al.* (2016), showing that the while the onset of convection rolls is steady for $Pr \approxeq 1$ it is oscillatory for $Pr > 12.7$. Given that our problem also incorporates not only buoyancy but also aspects of shear flows and rotating flows, it is important to consider different Pr to help understand its role. As we later outline this leads to some technical challenges, in particular resolving the thermal boundary layers which emerge at high Pr.

To address the questions outlined and to consider the transitions between the convective and rotating regimes highlighted we adopt the following approach. We first consider the weakly nonlinear regime for $Re_1 \ll 1$ and $(Ra - Ra_c)/Ra_c \ll 1$ using numerical continuation for different Pr. This approach is guided by reduced order models which leverage the similar spatial form of the solutions shown in figure 4.1, and by the amplitude equations derived in chapter 3. In doing so we elucidate the dependence of flow transitions on the Pr and shell separation d. Using the insights and solutions obtained at these small parameter values, we subsequently investigate the behaviour of (4.5) at large Pr for varying Ra, Re_1. Rather than conducting exhaustive simulation for all values of Ra, Re_1, numerical continuation of the systems bifurcation points is used. By identifying the physical mechanisms that are the cause of each bifurcation, we can also understand how the dynamical properties of solutions to (4.5) change as we vary the parameter values. Finally we comment on the role of thermal boundary layers and symmetries in determining the preferred solution.

4.2 Primary bifurcations

In figure 3.2, it was shown that for combinations (d_c, Ra_c) the onset of convective motion is degenerate, with convection modes ℓ, n simultaneously losing stability. Using weakly nonlinear theory to derive amplitude equations valid near each degeneracy, the preferred mode of convection was established. Relying on the similar spatial form of solutions presented in figure 4.1, we now use (3.57) to describe the behaviour near the $\ell = 2, 3$ degeneracy, in the presence of weak rotation. This approach was also adopted by Araki *et al.* (1996) for a single mode, but not for degenerate points with a view to highlighting the effect of rotation on both even and mixed convection solutions.

Projecting the influence of *very weak* rotation $Re_1 \ll (Ra - Ra_c)/Ra_c \ll 1$ onto the $\ell = 2$ component of (3.57) yields

$$\left.\begin{aligned} \dot{A} &= a_0 Re_1^2 Pr + \mu_1 A + \alpha_3 B^2 + d_{12} A B^2 + d_{13} A^3, \\ \dot{B} &= \mu_2 B + \beta_2 A B + d_{21} A^2 B + d_{24} B^3, \end{aligned}\right\} \begin{aligned} &A \sim \ell = 2 \\ &B \sim n > \ell = 3 \end{aligned} \tag{4.9}$$

where

$$\mu_1 = a_1 \mu + a_2 \delta, \;\; \mu_2 = b_1 \mu + b_2 \delta \quad a_i, b_i \in \mathbb{R}^+. \tag{4.10}$$

The coefficients $\alpha_i, \beta_i, d_{ij} \in \mathbb{R}$ are as previous in figure 3.5 and $a_0 \in \mathbb{R}^+$ is determined from the inner product

$$a_0 = \int_r \int_\theta \left(\frac{A_T \psi_1^{\ell=2}}{Ra_c r^2 \sin^2\theta} N_1(\Omega_0, \Omega_0) \right) r^2 \sin\theta \, dr d\theta, \tag{4.11}$$

where ψ_1^ℓ is as defined in (3.12). Although (4.9) assumes that the degenerate point has not been significantly modified by the effect of rotation, and as such is valid only when $Re_1^2 Pr \ll (Ra - Ra_c)/Ra_c \ll 1$ it is nonetheless a useful guide.

Setting $\mu_1 > 0, \mu_2 < 0$ and $B = 0$ equation (4.9) reduces to

$$\dot{A} = a_0 Re_1^2 Pr + \mu_1 A + d_{13} A^3, \tag{4.12}$$

which applies in region 1 of figure 3.6 where only even convection is obtained. For non-zero rotation (4.12) the pitchfork bifurcation to even convection is thus split by a factor proportional to $Re_1^2 Pr$. It also suggests that solutions will be bistable but without hysteresis as variations in Re_1 are symmetric, such that (4.12) does not describe a cusp bifurcation (Lewis & Langford 2008, Kuznetsov 2004). Setting $\mu_1 < 0, \mu_2 > 0$ equation (4.9) reduces to

$$\dot{B} = (\mu_2 - \frac{\beta_2 a_0}{\mu_1} Re_1^2 Pr)B - \frac{\beta_2 \alpha_3}{\mu_1} B^3, \tag{4.13}$$

which applies in region 4 of figure 3.6 where only mixed convection is obtained. The fixed points of (4.13) are approximated by $A = -\mu_2/\beta_2$ and $B = \pm\sqrt{a_0 Re_1^2 Pr - (\mu_1\mu_2)/\beta_2}$, while the form of (4.13) suggests that the onset of odd convection is merely shifted by non-zero rotation.

To understand how differential rotation alters the cellular pattern selected by thermal convection we now consider two values of the annulus separation. The value $d = 3$ is chosen to ensure that thermal convection selects a 2-cell flow which exhibits dynamics described by (4.12) and conversely $d = 1.5$ is chosen so that an odd 3-cell flow is selected whose dynamics are described by (4.13). The choice of a wide annulus favouring low wave-numbers is also motivated by simplicity. Numerically fewer modes are required to resolve wider annuli and the presence of a similar spatial structure of the flows facilitates qualitative interpretations.

Using this setup we aim to understand how bifurcations from the conductive state to a state of thermal convection are altered by differential rotation. Is this scenario different for odd and even thermal convection (cf. frames (b),(c) of figure 4.1)? And how does each scenario depend on the Prandtl number Pr? In this section we now term solutions qualitatively similar to the left hand side of frame (a) of figure 4.1 *rotating solutions* and those qualitatively similar to (b), (c) *convective solutions*.

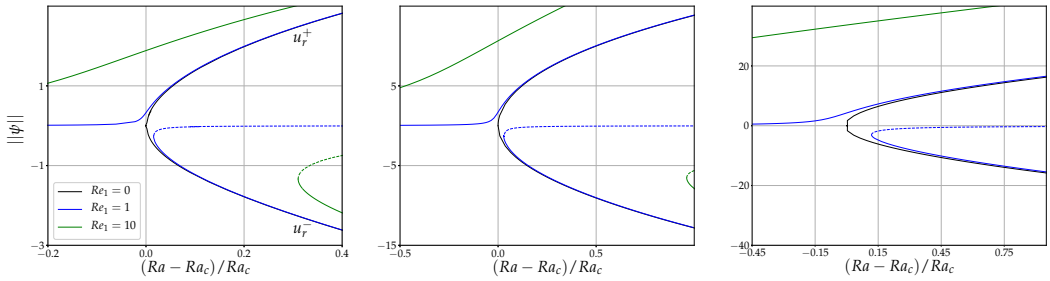
4.2.1 Even solutions $d = 3$

Figure 4.2 shows how the bifurcation of the conductive state to a state of even convection is altered by rotation of the inner sphere. In these bifurcation diagrams and those which follow the L2 norm of the stream function

$$||\psi|| = \text{sign}(u_r) \sum_{\ell=0}^{N_\theta} ||\psi_\ell||, \tag{4.14}$$

is used as a solution measure. In selected bifurcation diagrams $||\psi||$ is multiplied by the sign of the radial velocity u_r at the equator to demonstrate branching symmetry.

Solutions for different Re_1 are shown for three values of Pr in figure 4.2. When $Re_1 = 0$ the conductive basic state $T_0(r)$ loses stability at a critical Rayleigh number Ra_c through a pitchfork bifurcation. For $Re_1 \neq 0$ the pitchfork is split and becomes an imperfect pitchfork bifurcation as shown in figure 4.2. This structure follows from that predicted by (4.12). The branches with positive equatorial velocity u_r^+ resembling the rotating solution connect continuously to the conductive state, while those with negative velocity u_r^- resembling the



(a) $Pr = 0.1$ **(b)** $Pr = 1$ **(c)** $Pr = 10$

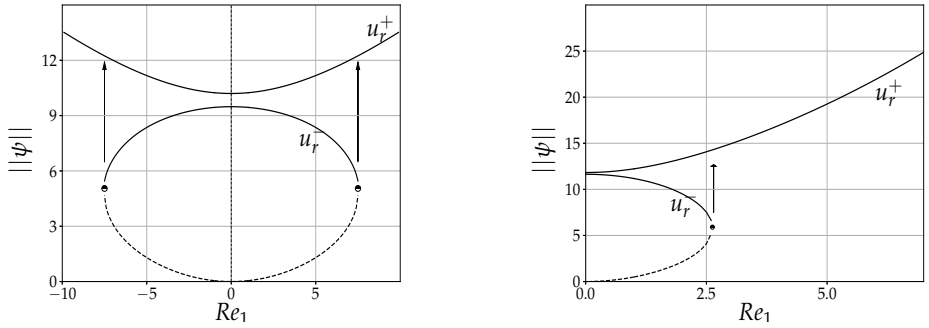
Figure 4.2: Splitting of the pitchfork bifurcation due to differential rotation is more pronounced for larger Pr. Bifurcation of the conductive state to even thermal convection for different Re_1 and Pr. Solid lines denote stable equilibria while dashed lines denote unstable equilibria. When $Re_1 \neq 0$ the symmetric pitchfork is split into two branches: a rotation dominated branch with positive radial velocity at the equator u_r^+ which emerges continuously from the conductive state and a convection dominated branch with negative radial velocity at the equator u_r^-.

convective solution emerge from a saddle-node bifurcation. The distance of this saddle node bifurcation from the point $(Ra_c, ||\psi|| = 0)$ is observed to increase with both Re_1 and Pr. For small Pr the pitchfork is slightly deformed while for larger Pr the role of rotation begins to dominate. Similarly for larger rotation rates $Re_1 = 10$ the bifurcation is further deformed as shown in figure 4.2 frame (c), such that the lower convection branches are longer found within the range investigated.

Fixing $(Ra - Ra_c)/Ra_c = 0.5$ and performing continuation in Re_1 we find that only the rotating branch persists for large Re_1 as shown in figure 4.3. Starting on the u_r^- branch and increasing Re_1 causes a transition to the u_r^+ branch, but decreasing Re_1 does not lead to the backwards transition. The system is bistable but not hysteretic. Comparing figures 4.3 (a) and (b) we observe that u_r^- persists for a larger interval of Re_1 when Pr is smaller. Similarly the amplitude of the rotating branch increases at a faster rate for large Pr.

Frames (a),(b) of figures 4.4 show the corresponding spatial solutions of the branches in bifurcation diagrams 4.2 at $Pr = 0.1, 10$. To illustrate the different coupling regimes present at high and low Pr we have shown solutions at $Pr = 0.1$ in the left hand frames and solutions at $Pr = 10$ in the right hand frames. The poloidal 2-cell flow ψ remains qualitatively consistent in all cases although its amplitude changes. Comparing the T, Ω fields for each case however the differences in these flows are made evident.

Considering the rotating branch u_r^+ shown in frame (a) of figure 4.4, we see that for $Pr = 0.1$ the contours of T are weakly deformed from concentric circles, but that gradients of Ω are strongly advected by the poloidal motion. Conversely we see that for $Pr = 10$ gradients of T are strongly advected. For the convecting branch u_r^- shown in frame (b)



(a) $Pr = 1$. **(b)** $Pr = 10$.

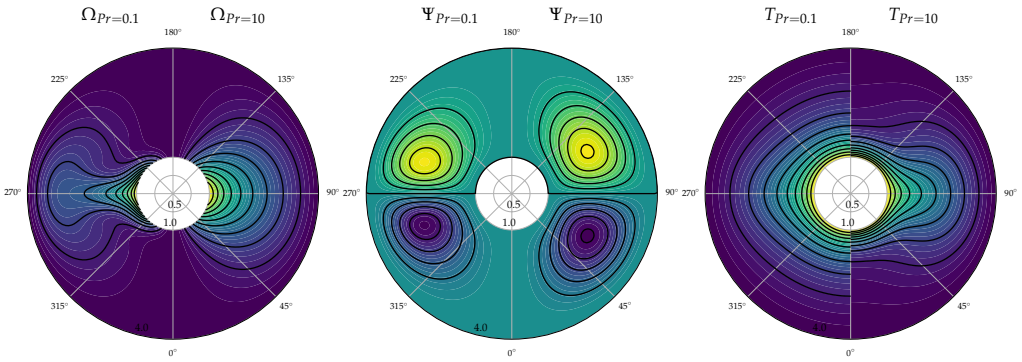
Figure 4.3: Symmetric solution states are bistable but do not exhibit hysteresis. Transition between the rotating branch u_r^+ and the convection branch u_r^- for $(Ra - Ra_c)/Ra_c = 0.5$. At $Re_1 = 0$ the u_r^+, u_r^- solution branches are approximately equal, but for sufficient Re_1 the u_r^- convection branch terminates in a saddle-node bifurcation and transitions to the rotating state. Frames (a),(b) are symmetric in Re_1, as rotation in both directions is equivalent when the outer sphere is fixed. For this reason only half the axis is shown in frame (b).

of figure 4.4 similar behaviour is observed, with gradients of T more strongly advected at $Pr = 10$ while gradients of Ω are more strongly advected at $Pr = 0.1$. A specific difference which emerges in this flow at $Pr = 0.1$ is that the poloidal motion, favoured by thermal convection, pushes fluid with greater specific angular moment to higher latitudes. This is shown in the right half of the Ω field in frame (b).

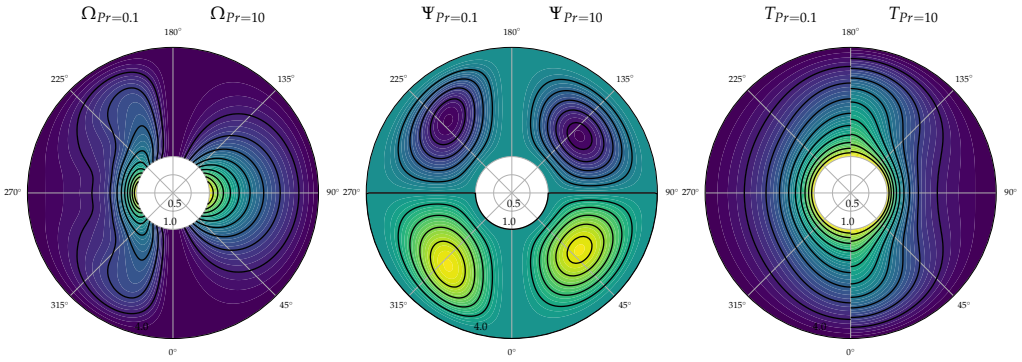
4.2.2 Odd solutions $d = 1.5$

Figure 4.5 shows how the bifurcation from a conductive state to a state of odd convective is modified by rotation of the inner sphere at different Pr. To examine this transition a preference for odd convection has been set by fixing $d = 1.5$. Branches with zero rotation are shown in black while those with $Re_1 = 1$ are shown in blue. Contrasting with the transitions observed for even solutions, the bifurcation to odd convection remains a pitchfork for $Re_1 \neq 0$ as follows from the asymmetry of odd numbered Legendre polynomials which constitute the polar eigenfunctions. Depending on the strength of rotation and Pr however, the location of the bifurcation point and whether the bifurcation is forward or backward changes. This structure follows from that predicted by (4.13).

For $Pr = 0.1, 1$ we observe that the odd convection branch shown in blue, bifurcates via a forward pitchfork almost coincidently with the black branch. In each case the rotating solution can be seen to persist as an unstable branch for values of Ra beyond this threshold. For $Pr = 10$ the 2-cell branch persists for a larger range of $(Ra - Ra_c)/Ra_c$ and transitions to a 3-cell solution at larger Ra via a subcritical pitchfork shown in frame (c) of figure 4.5.



(a) Rotation branch u_r^+, $Pr = 0.1$ left and $Pr = 10$ right.

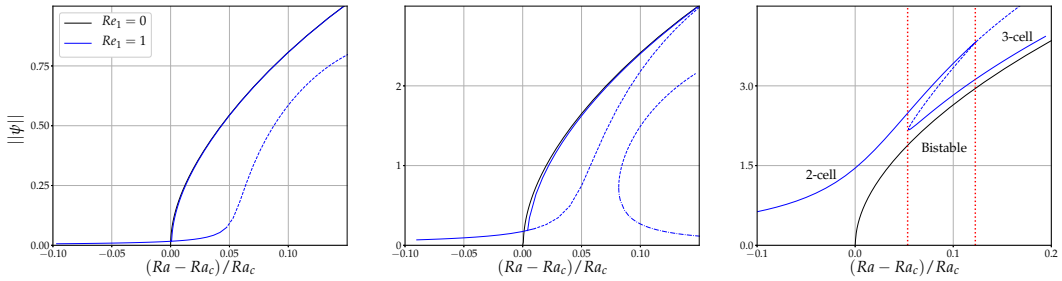


(b) Convection branch u_r^-, $Pr = 0.1$ left and $Pr = 10$ right.

Figure 4.4: Gradients of Ω are strongly advected by the poloidal flow for $Pr \ll 1$ and gradients of T for $Pr \gg 1$. Steady equilibrium solutions for $Re_1 = 1$, $(Ra - Ra_c)/Ra_c = 0.5$ demonstrating different coupling regimes at high and low Pr. Left frames show the $Pr = 0.1$ and right $Pr = 10$ solution. (a) Rotation branch u_r^+ , (b) Convection branch u_r^-.

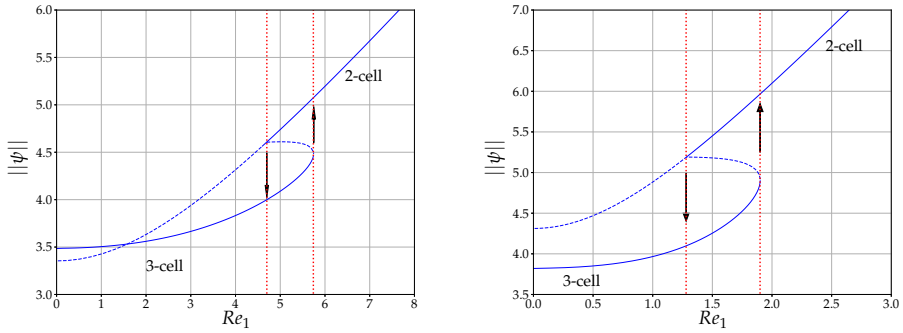
Notably the 2 and 3-cell solution states which are connected by an unstable branch are bistable within a range of $(Ra - Ra_c)/Ra_c$. Following this unstable branch backwards from the bifurcation point we find that the odd component of the solution increases until it gains a stable eigenvalue and stabilises at the saddle node. Fixing $(Ra - Ra_c)/Ra_c = 0.25$ and performing continuation in Re_1 we find that increasing Re_1 destabilises the 3-cell branch causing a transition to a 2-cell branch and that by decreasing Re_1 the reverse transition can take place also. This is distinct from the even case we previously considered where transitions between the convection state and the rotating state could be induced only by variations in Re_1 and were not hysteretic.

Figure 4.7 shows the corresponding spatial solutions for the bifurcation diagrams 4.5 and 4.6 at $Pr = 0.1, 10$. Despite variations in amplitude the 3-cell poloidal motion of both cases are in close resemblance, differences do however emerge in the Ω, T fields. For $Pr = 0.1$



(a) $Pr = 0.1$ **(b)** $Pr = 1$ **(c)** $Pr = 10$

Figure 4.5: Differential rotation causes the onset of odd convection to become subcritical for $Pr \gg 1$. Bifurcation diagram of odd mode thermal convection. In frames (a),(b) the forward pitchfork bifurcation is slightly perturbed to $Ra \geq Ra_c$, while in frame (c) the 2-cell branch dominates for a larger range of Ra and the pitchfork bifurcation to the 3-cell solution becomes subcritical or backwards. The hysteresis loop between the bistable 2 and 3-cell solution states is demarcated by dashed red lines.



(a) $Pr = 1.$ **(b)** $Pr = 10.$

Figure 4.6: Hysteresis between the convecting 3-cell flow and the rotating 2-cell flow for $(Ra - Ra_c)/Ra_c = 0.25$. (a) Increasing Re_1 causes the solution to jump from the convecting branch to the rotating branch, and similarly when decreasing Re_1 the rotating solution either persists unstably or returns to the convecting branch. (b) Increasing Re_1 causes the convecting branch to terminate in a saddle-node bifurcation and transition to a 2-cell rotating flow.

gradients in Ω are strongly advected by the poloidal flow, such that its profile becomes highly asymmetric. While at $Pr = 10$ it is gradients of T that are strongly advected resulting in the emergence of plumes.

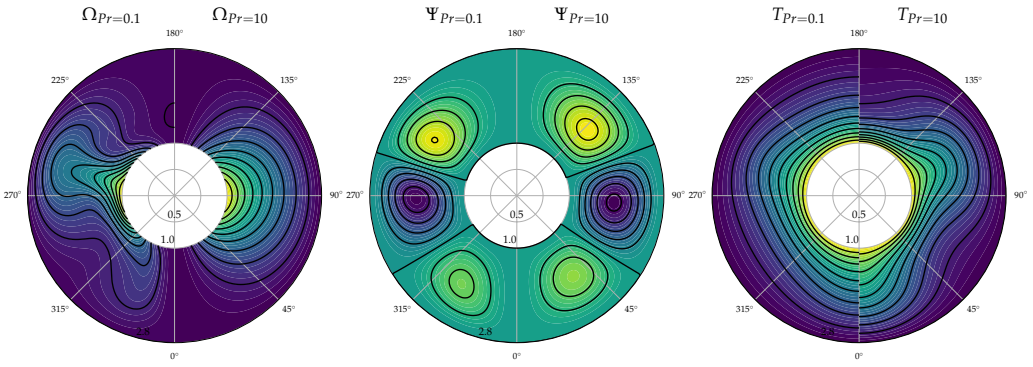


Figure 4.7: Mixed/odd equilibrium solutions for $Re_1 = 1$, $(Ra - Ra_c)/Ra_c = 0.25$ demonstrating different coupling regimes at high and low Pr. Left frames show the $Pr = 0.1$ solution and right $Pr = 10$. For $Pr = 0.1$ gradients of Ω are strongly advected by the poliodal flow, while at $Pr = 10$ it is gradients in the T field.

4.2.3 Symmetries

The bifurcations and spatial solutions presented demonstrate that equations (4.1) have two symmetries in addition to those imposed by axisymmetry, namely a reflection symmetry Γ about the equator and a sign change symmetry R_e of even convection solutions. The latter symmetry, which accounts for the pitchfork bifurcation observed for even modes, stems from the self-adjoint nature of the convection problem linearised about the conductive state (cf. 3.10). Following Araki *et al.* (1996) we define the equatorial reflection operator by

$$\Gamma \boldsymbol{X} = \begin{pmatrix} -\psi(r, \pi - \theta, t) \\ T(r, \pi - \theta, t) \\ -\Omega(r, \pi - \theta, t) \end{pmatrix}, \quad \text{where} \quad \boldsymbol{X} = \begin{pmatrix} \psi(r, \theta, t) \\ T(r, \theta, t) \\ \Omega(r, \theta, t) \end{pmatrix}. \tag{4.15}$$

Decomposing the solution into its symmetric even $\boldsymbol{X}_S$ and antisymmetic odd $\boldsymbol{X}_A$ components one obtains

$$\boldsymbol{X}_S = \frac{1}{2}(\boldsymbol{X} + \Gamma \boldsymbol{X}), \; \boldsymbol{X}_A = \frac{1}{2}(\boldsymbol{X} - \Gamma \boldsymbol{X}). \tag{4.16}$$

While the even component is a fixed point of the $\mathcal{Z}_2$ reflection symmetry operation $\Gamma(\boldsymbol{X}_S) = \boldsymbol{X}_S$ by operating on the odd component a second solution is obtained

$$\Gamma \boldsymbol{X}_A = \frac{1}{2}(\Gamma \boldsymbol{X} - \boldsymbol{X}) = -\boldsymbol{X}_A, \tag{4.17}$$

such that $\boldsymbol{X}$ acquiring an odd component corresponds to a symmetry breaking bifurcation. As shown by Golubitsky & Schaeffer (1985) this symmetry breaking will typically result

in a symmetric pitchfork bifurcation, or a symmetric Hopf bifurcation giving rise to a small amplitude periodic orbit. Numerically this symmetry can be exploited to reduce computational cost, in particular when detecting symmetry breaking bifurcations such as observed in the previous subsection. Writing (2.21) in terms of its symmetric and anti-symmetric components one obtains

$$\begin{aligned}\mathcal{M}\frac{\partial \boldsymbol{X}_S}{\partial t} &= \boldsymbol{\mathcal{F}}_s(\boldsymbol{X}_S, \boldsymbol{X}_A) \equiv \boldsymbol{\mathcal{N}}(\boldsymbol{X}_S, \boldsymbol{X}_S) + \boldsymbol{\mathcal{N}}(\boldsymbol{X}_A, \boldsymbol{X}_A) + \mathcal{L}\boldsymbol{X}_S + \boldsymbol{F}, \\ \mathcal{M}\frac{\partial \boldsymbol{X}_A}{\partial t} &= \mathcal{F}_A(\boldsymbol{X}_S)\boldsymbol{X}_A \equiv \boldsymbol{\mathcal{N}}(\boldsymbol{X}_A, \boldsymbol{X}_S) + \boldsymbol{\mathcal{N}}(\boldsymbol{X}_S, \boldsymbol{X}_A) + \mathcal{L}\boldsymbol{X}_A,\end{aligned} \tag{4.18}$$

where the second equation in (4.18) corresponds to the linearisation of (4.1) about the symmetric state, demonstrating that antisymmetric solutions correspond to an instability of the symmetric solutions $\boldsymbol{X}_S$. The perturbation of the symmetric equation by a constant forcing term $\boldsymbol{F}$ accounts for the splitting of the even mode pitchfork or breaking of the sign change symmetry R_e previously observed. Unlike the pitchfork bifurcation leading to mixed convection shown in figure 4.5, the pitchfork bifurcation from the conductive state to a state of even convection is not symmetric. Its branches are not related by a symmetry operation. Inspection of figure 4.2 shows that they attain different amplitudes as Ra increases.

4.3 Numerical continuation of 1-parameter bifurcations

Near the bifurcation points outlined in section 4.2, small changes of the parameter values Re_1, Ra can induce transitions between the *convection* and *rotating* solution regimes. This was demonstrated in figures 4.3 and 4.5 where bistability and hysteresis phenomena were observed, albeit for a very narrow parameter range. To understand the parameter sensitivity present in such regions, and its changes under variations of Re_1, Ra we preform numerical continuation of the bifurcation points determined for small parameter values. By doing so, we aim to understand the physical balances present in these transition regions for larger Re_1 and Ra.

Following Cliffe *et al.* (2000), we anticipate that when varying a single parameter such as Ra while keeping Re_1 fixed, a steady solution of (4.1) can have four possible bifurcations as the real part of a single eigenvalue changes sign. For a general solution state $\boldsymbol{X}$ without symmetry these are

- quadratic fold points,
- Hopf bifurcations,

and when $\boldsymbol{X}$ has $\mathcal{Z}_2$ reflection symmetry (4.15) these are

- symmetric pitchfork bifurcations,
- symmetric Hopf bifurcations.

We note that additional 1-parameter bifurcations are possible in the presence of more complex spatial symmetries such as $O(2), SO(2)$ and $O(3)$, typical of a 3D spherical shell domain (Crawford & Knobloch 1991, Cliffe *et al.* 2000). If (4.1) were not restricted to be axisymmetric one would need to consider these additional cases.

Each of these bifurcations is determined by the following augmented systems (Kuznetsov 2004). For the fold bifurcation by solving for fixed points of

$$\boldsymbol{H}(\boldsymbol{Z}) = \begin{pmatrix} \boldsymbol{\mathcal{F}}(\boldsymbol{X}, \mu) \\ A(\boldsymbol{X}, \mu)\boldsymbol{q} \\ \boldsymbol{q}_0^T \boldsymbol{q} - 1 \end{pmatrix} = 0, \quad \text{where} \quad \boldsymbol{Z} = (\boldsymbol{X}, \boldsymbol{q}, \mu) \in \mathrm{R}^{2n+1}, \tag{4.19}$$

and $A(\boldsymbol{X}, \mu) \equiv D\mathcal{F}_{\boldsymbol{X}}$ is now used to denote the Jacobian matrix. The vector $\boldsymbol{q} \in \mathbb{R}^n$ is the critical eigenvector corresponding to the eigenspace $\lambda = 0$. The system is solved using Newton Iteration which relies on the matrix

$$\boldsymbol{H}_{\boldsymbol{Z}}(\boldsymbol{Z}) = \begin{pmatrix} \boldsymbol{\mathcal{F}}_{\boldsymbol{X}} & 0_{n\times n} & \boldsymbol{\mathcal{F}}_{\mu} \\ A_{\boldsymbol{X}}\boldsymbol{q} & A & A_{\mu}\boldsymbol{q} \\ 0_{1\times n} & \boldsymbol{q}_0^T & 0 \end{pmatrix}, \tag{4.20}$$

where the action of the Hessian matrix $A_{\boldsymbol{X}}\boldsymbol{q}$ is *approximated* using a forward difference approximation

$$A_{\boldsymbol{X}}\boldsymbol{q} = \left(\frac{A(\boldsymbol{X} + \delta \frac{\boldsymbol{q}}{||\boldsymbol{q}||}, \mu) - A(\boldsymbol{X}, \mu)}{\delta} \right) ||\boldsymbol{q}|| + \mathcal{O}(\delta). \tag{4.21}$$

While central differencing or alternative schemes of higher accuracy can be used to implement this approximation, they would require additional evaluations of the Jacobian matrix. Similarly a Hopf-bifurcation is defined by fixed points of the system

$$\boldsymbol{H}(\boldsymbol{Z}) = \begin{pmatrix} \boldsymbol{\mathcal{F}}(\boldsymbol{X}, \mu) \\ A(\boldsymbol{X}, \mu)\boldsymbol{v} + \omega\boldsymbol{w} \\ A(\boldsymbol{X}, \mu)\boldsymbol{w} - \omega\boldsymbol{v} \\ \boldsymbol{v}_0^T\boldsymbol{v} + \boldsymbol{w}_0^T\boldsymbol{w} - 1 \\ \boldsymbol{w}_0^T\boldsymbol{v} - \boldsymbol{v}_0^T\boldsymbol{w} \end{pmatrix} = 0, \quad \text{where} \quad \boldsymbol{Z} = (\boldsymbol{X}, \boldsymbol{v}, \boldsymbol{w}, \mu, \omega) \in \mathrm{R}^{3n+2}, \tag{4.22}$$

where $\boldsymbol{q} = \boldsymbol{v} + \mathrm{i}\boldsymbol{w} \in \mathbb{C}^n$ is the critical complex eigenvector corresponding to the critical complex eigenspace $\lambda = \pm\mathrm{i}\omega$, and $\boldsymbol{q}_0$ is a vector that is not orthogonal $\bar{\boldsymbol{q}}^T\boldsymbol{q}_0 \neq 0$. The

system is solved using Newton Iteration which relies on the matrix

$$\boldsymbol{H}_{\boldsymbol{Z}}(\boldsymbol{Z}) = \begin{pmatrix} A & 0_{n\times n} & 0_{n\times n} & \boldsymbol{\mathcal{F}}_{\mu} & 0 \\ A_{\boldsymbol{X}}\boldsymbol{v} & A & \omega\boldsymbol{I} & A_{\mu}\boldsymbol{v} & \boldsymbol{w} \\ A_{\boldsymbol{X}}\boldsymbol{w} & -\omega\boldsymbol{I} & A & A_{\mu}\boldsymbol{w} & -\boldsymbol{v} \\ 0_{1\times n} & \boldsymbol{v}_0^T & \boldsymbol{w}_0^T & 0 & 0 \\ 0_{1\times n} & \boldsymbol{w}_0^T & -\boldsymbol{v}_0^T & 0 & 0 \end{pmatrix}, \tag{4.23}$$

where the action of the Hessian matrix $A_{\boldsymbol{X}}\boldsymbol{v}$ is computed using the forward difference approximation (4.21). The symmetric pitchfork bifurcation is determined by solving for fixed points of

$$\boldsymbol{H}(\boldsymbol{Z}) = \begin{pmatrix} \boldsymbol{\mathcal{F}}(\boldsymbol{X}_s, \mu) \\ A(\boldsymbol{X}_s, \mu)\boldsymbol{q}_A \\ \boldsymbol{q}_0^T\boldsymbol{q}_A - 1 \end{pmatrix} = 0, \quad \text{where} \quad \boldsymbol{Z} = (\boldsymbol{X}_s, \boldsymbol{q}_A, \mu) \in \mathrm{R}^{n+1}. \tag{4.24}$$

where $A(\boldsymbol{X}_s, \mu) \equiv D\mathcal{F}_{\boldsymbol{X}_s}$ is now used to denote the Jacobian matrix of the symmetric component of $\boldsymbol{X}$ and $\boldsymbol{q}_A \in \mathbb{R}^{n/2}$ is the critical antisymmetric eigenvector corresponding to the eigenspace $\lambda = 0$. The symmetric Hopf bifurcation is determined by solving for fixed points of

$$\boldsymbol{H}(\boldsymbol{Z}) = \begin{pmatrix} \boldsymbol{\mathcal{F}}(\boldsymbol{X}_s, \mu) \\ A(\boldsymbol{X}_s, \mu)\boldsymbol{v}_A + \omega\boldsymbol{w}_A \\ A(\boldsymbol{X}_s, \mu)\boldsymbol{w}_A - \omega\boldsymbol{v}_A \\ \boldsymbol{v}_0^T\boldsymbol{v}_A + \boldsymbol{w}_0^T\boldsymbol{w}_A - 1 \\ \boldsymbol{w}_0^T\boldsymbol{v}_A - \boldsymbol{v}_0^T\boldsymbol{w}_A \end{pmatrix} = 0, \quad \text{where} \quad \boldsymbol{Z} = (\boldsymbol{X}_s, \boldsymbol{v}_A, \boldsymbol{w}_A, \mu, \omega) \in \mathrm{R}^{3n/2+2}, \tag{4.25}$$

where $\boldsymbol{q}_A = \boldsymbol{v}_A + \mathrm{i}\boldsymbol{w}_A \in \mathbb{C}^{n/2}$ is the critical complex eigenvector corresponding to the critical complex eigenspace $\lambda = \pm\mathrm{i}\omega$, and $\boldsymbol{q}_0$ is a vector that is not orthogonal $\bar{\boldsymbol{q}}^T\boldsymbol{q}_0 \neq 0$.

The main difficulty in applying these methodologies to high-dimensional PDE systems arises from the linear algebra (Net & Snchez 2015). The dimension of the augmented systems (4.19) and (4.22) is a multiple of the systems solution vector. Variations of (4.19) and (4.22) formulated in terms of multiple low dimensional systems are used (Bindel *et al.* 2014), however in practical computations we found their numerical convergence to be significantly slower despite the use of preconditioning. The prevailing approach to circumvent these difficulties uses the formulation of matrix free equations which are solved using GMRES (Saad & Schultz 1986). Although matrix free methods have not be implemented for this continuation task, the discrete representation of (4.1) is typically sufficiently low in dimension due to the use of Galerkin projection and Chebyshev pseudo-spectral methods. This formulation also allows us to easily exploit the symmetry of (4.1)

when implementing systems (4.24), (4.25).

Using these techniques we now map out possible solutions in Re_1, Ra parameter space, and subsequently investigate how transitions between the *convection* and *rotating* solution regimes occur. We also highlight degenerate or co-dimension two points which can occur at isolated points along the curves defined by (4.19) to (4.25).

4.4 Flow transitions at large Ra, Re_1

In section 4.2 we observed that rotation splits the primary pitchfork bifurcation of even 2-cell flows, leading to a rotation dominated steady state u_r^+ and a convection dominated state u_r^-. Similarly, the symmetry breaking pitchfork bifurcation to an odd state of 3-cell convection switches from supercritical to subcritical at larger Pr. This leads to a bistable parameter region where for larger Pr finite amplitude perturbations may induce a transition between states. Given that we considered small values of Re_1, Ra only, we now enquire. Is bistability observed for larger values of these parameter? And is there an underlying physical mechanism which explains this behaviour? Fixing $d = 3, Pr = 10$ only variations of Re_1, Ra are now considered. In addition to facilitating numerical simulation, the restriction to wide shells ($d \geq 1$) also reduces the number of solution states.

In addition to Nu, the dimensionless torque G evaluated at either the inner or outer sphere's surface as defined by

$$G = \frac{2\pi r^3}{Re_1} \int_0^\pi \sin\theta \left[\frac{\partial u_\varphi}{\partial r} - \frac{u_\varphi}{r} \right] \sin\theta d\theta, \quad \text{where} \quad u_\varphi = \frac{\Omega_0 + \Omega}{r \sin\theta}, \tag{4.26}$$

is now used as a solution measure. Throughout this section bifurcation diagrams are presented in terms of both measures, for the purpose of illustrating that stable solutions do not necessarily maximise heat transfer or transfer of angular momentum.

Figure 4.8 shows the loci of bifurcation points in Re_1, Ra parameter space. These curves denote the stability regions for different types of steady and time-dependent solutions. For the parameter values considered it is possible to find three qualitatively different types of solutions. These are a symmetric *convection* solution u_r^- as shown in frame (b) of figure 4.4, a symmetric *rotating* solution u_r^+ as shown in frame (a) of figure 4.4 (or more clearly in figure 4.9), and an asymmetric 1-cell solution as shown in figure 4.10. Both steady and time-dependent u_r^+, 1-cell solutions are found while only steady u_r^- solutions are found.

The regions of parameter space (figure 4.8) which contain these stable solutions are:

a. 2-cell solutions u_r^+, u_r^-

b. 1-cell and 2-cell solutions u_r^-, u_r^+,

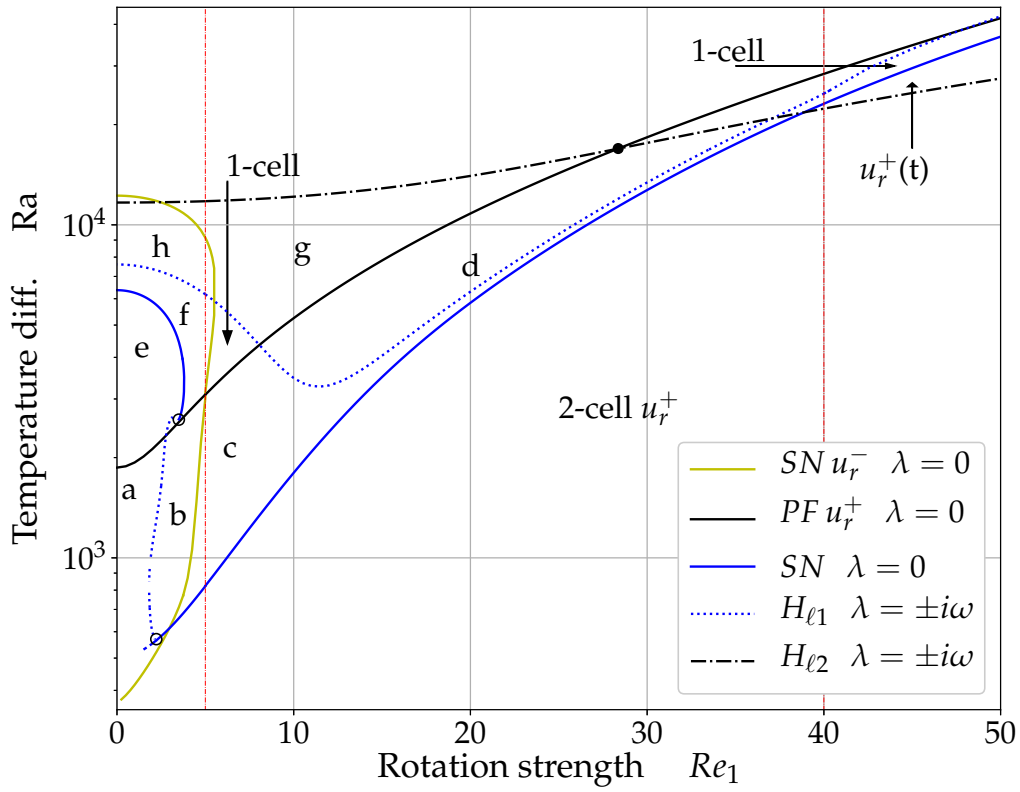


Figure 4.8: Increasing the rotation strength Re_1 stabilises the 2-cell u_r^+ solution, and leads to a bistable envelope where u_r^+ shares stability with other solutions. Bifurcation loci illustrating the stable solutions in Re_1, Ra space for $d = 3, Pr = 10$. Solid lines are used to denote saddle-node (SN) or symmetric pitchfork bifurcations (PF), chained lines symmetric Hopf bifurcations ($H_{\ell 2}$) and dotted lines Hopf bifurcations ($H_{\ell 1}$). Solid black and hollow circles denote co-dimension 2 points. Below the solid yellow, blue and chained black lines the rotation dominated 2-cell state u_r^+ is stable to all axisymmetric perturbations. At low Re_1 multiple steady solutions are bistable, while at larger Re_1 increasing Ra causes a transition to time-dependent behaviour.

c. 1-cell and 2-cell solution u_r^+,

d. time-dependent 1-cell(t) and steady 2-cell solution u_r^+,

e. 2-cell solution u_r^-,

f. 1-cell and 2-cell solution u_r^-,

g. time-dependent 1-cell(t) solution,

h. time-dependent 1-cell(t) solution and steady 2-cell solution u_r^-,

where (t) is used to indicate a time-dependent state. In addition to the 1-cell(t) solution which bifurcates from the steady 1-cell solution as it crosses the dotted blue line $H_{\ell 1}$, a time-dependent 2-cell solution $u_r^+(t)$ is also possible. This occurs when u_r^+ undergoes a symmetric Hopf bifurcation as it crosses the chained black line $H_{\ell 2}$ shown in the upper right half of figure 4.8.

The general trend illustrated by figure 4.8 is that rotation stabilises the symmetric convection solution which most resembles differential rotation. It also shows that the symmetric convection solution u_r^- is suppressed as Re_1 increases. The behaviour for each of these cases is illustrated in figure 4.4 frames (a),(b). We understand the former case u_r^+ (frame (a)) to be stable with increasing Re_1, as gradients of both Ω & T have a preference to be advected outwards at the equator.

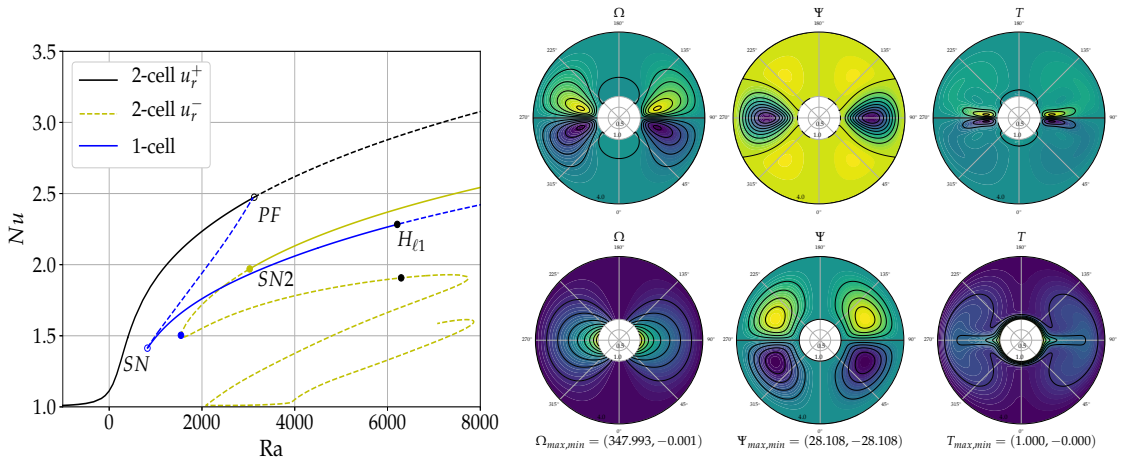
As Re_1 increases from zero the Ra for which stable asymmetric 1-cell convection can be found is reduced. For small $Re_1 \geq 1.81$ this leads to the bistability of the 1-cell and u_r^+, u_r^- solutions in region b. While in regions c,d which lie between the solid black and blue lines of figure 4.8, the u_r^+ solution is bistable with either the 1-cell or 1-cell(t) solutions. Fixing $Re_1 = 5$ and varying Ra we find that the bifurcation from u_r^+ to the 1-cell solution is subcritical, with each state connected by an unstable branch as shown in figure 4.9 frame (a). This implies that in regions b,c,d finite amplitude perturbations are required to induced a transition.

To better understand the physical mechanism responsible for transitions we examine their solutions and eigenvectors at their bifurcation points. Doing so indicates that instabilities are concentrated on either the poles or axis. In solving for the loci shown in figure 4.8 both the solutions and eigenvectors have already been determined, as the systems defined by (4.19) to (4.25) require their solution.

4.4.1 Steady bifurcations

Figure 4.9 (a) shows a cross section of figure 4.8 with fixed $Re_1 = 5$. The figure illustrates the stable and unstable solutions in terms of Nu which are found for this rotation strength and the transitions which occur as Ra is varied. For small Ra only the 2-cell solution u_r^+ is stable. Increasing Ra this solution loses stability in a symmetry breaking pitchfork bifurcation at PF and transitions to an asymmetric 1-cell state. Reducing Ra the 1-cell solution loses stability at SN and returns to the 2-cell branch u_r^+, and so this transition is hysteretic. A 2-cell u_r^- solution disconnected from the other solution branches is also possible for these parameter values. Distinct from figure 4.2 where small rotation $Re_1 = 1$ split the pitchfork bifurcation connecting the u_r^+ and u_r^- branches, the stronger rotation now results in a number of unstable rungs.

In frame (b) of figure 4.9 the steady state solution $\boldsymbol{X}_{PF}$ and its least stable eigenvector



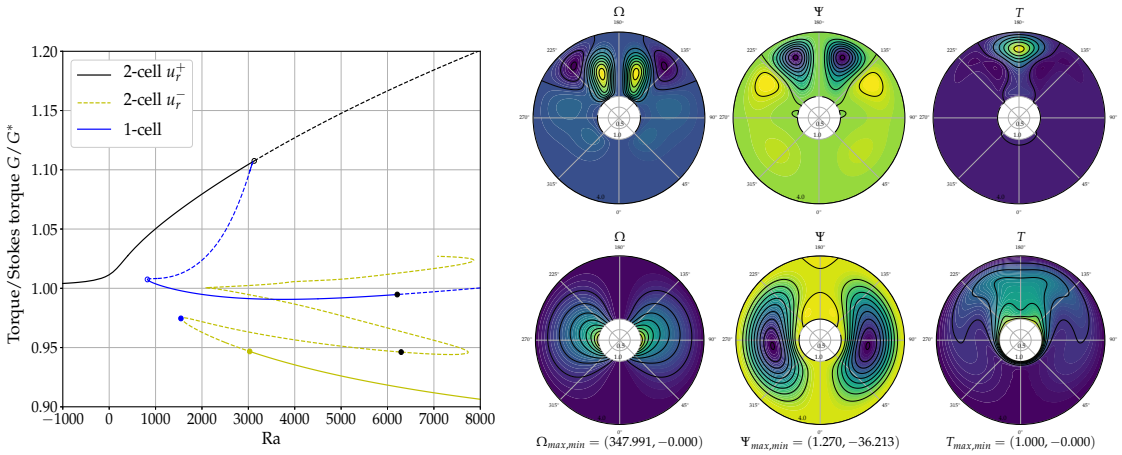
(a) Bifurcation diagram at $Re_1 = 5$. **(b)** Lower $\boldsymbol{X}_{PF}$ & upper $\boldsymbol{q}_{PF}$.

Figure 4.9: The rotating 2-cell solution u_r^+ loses stability to disturbances confined to the equator, transitioning to a state with lower heat transfer. (a) Bifurcation diagram in terms of the convective heat transfer Nu, showing the sequence of transitions as Ra is varied with fixed $Re_1 = 5$. Stable branches are shown as solid lines while unstable branches are dashed or dotted. Bifurcation points are marked by solid black dots and are annotated with their corresponding type. (b) Equilibrium solution $\boldsymbol{X}_{PF}$ bottom and leading eigenvector $\boldsymbol{q}_{PF}$ top evaluated at the symmetric pitchfork bifurcation point.

$\boldsymbol{q}_{PF}$ are shown in the lower and upper panels respectively. In this solution, the poloidal flow ψ advects gradients of Ω and T outwards at the equator. In the temperature field this motion results in two large plumes, a thin hot layer of fluid near the inner sphere's surface and a narrow jet of hot fluid drawn outwards along the equator. The least stable eigenvector $\boldsymbol{q}_{PF}$ shows that the disturbance which destabilises this flow is localized about the equator.

The physical interpretation is that as Ra increases large gradients of T accumulate in thin thermal boundary layer at the equator. Following (4.8) the radial advection of temperature gradients inside this jet must be balanced by thermal diffusion in the polar direction. For $Ra \leq PF$ the strong radial flow driven by rotation helps achieve this balance, but as Ra increases beyond the bifurcation point PF the jet widens such that diffusion acts more weakly. This results in the growth of polar gradients which destabilise the flow in a localised perturbation of the form $\boldsymbol{q}_{PF}$.

The steady equilibrium solution $\boldsymbol{X}_{SN}$ shown in frame (b) of figure 4.10 contrasts greatly with that of the 2-cell flow. Its poloidal flow ψ consists of two large cells, whose circulation is clockwise in the right half of the figure and anti-clockwise in the left half. This flow deflects the contours of Ω upwards and convects hot fluid radially outwards at the pole creating a strong thermal plume. The flow also has two small recirculation zones at its pole, in correspondence with the two smaller thermal plumes aligned either side of the



(a) Bifurcation diagram at $Re_1 = 5$. **(b)** Lower $\boldsymbol{X}_{SN}$ & upper $\boldsymbol{q}_{SN}$.

Figure 4.10: The 1-cell solution loses stability to disturbances driven by Ekman pumping (cf. figure 4.11) which are confined to the polar region. (a) Bifurcation diagram in terms of the torque G, showing the sequence of transitions as Ra is varied. (b) Equilibrium solution $\boldsymbol{X}_{SN}$ bottom and leading eigenvector $\boldsymbol{q}_{SN}$ top evaluated at the symmetric pitchfork bifurcation point. As Ra is decreased beyond the bifurcation point SN the 1-cell solution loses stability to disturbances confined to the pole and transitions to a state of higher torque.

rotation axis in the T field.

The least stable eigenvector $\boldsymbol{q}_{SN}$ shows that the disturbance which destabilises this flow is localized about the pole, particularly near the outer sphere. The ψ component of $\boldsymbol{q}_{SN}$ indicates that a cellular flow whose motion is in the opposite sense to the 1-cell flow will grow to restore the 2-cell u_r^+ solution. The growth of this disturbance is attributed to Ekman pumping driven by the inner sphere's rotation as demonstrated schematically in figure 4.11.

Near the rotation axis and the rotating sphere's surface we anticipate that the fluid flow is similar to that near a rotating disc's surface. In this configuration fluid is drawn downwards along the rotation axis until it reaches the discs surface where it is centrifuged outwards (Stewartson 1953). This behaviour is shown schematically in figure 4.11. In frame (a) the inner sphere's rotation draws cold fluid radially inwards at the rotation axis near the upper sphere, and pumps it outwards near the inner sphere. Depending on the cellular motion driven by convection, this pumping may be inhibited or enhanced. Frame (b) of figure 4.11 shows the equivalent configuration for outer sphere rotation.

At large Ra it is understood that Ekman pumping is balanced by the strong cellular flow driven by thermal convection. While rotation alters the radial velocity profile locally, it does not alter the polar velocity even near the rotation axis as shown in figure 4.12. Reducing Ra however, decreases the strength of the convective flow such that it can no

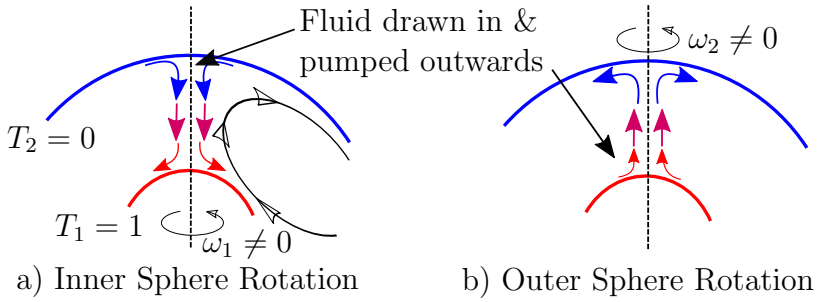
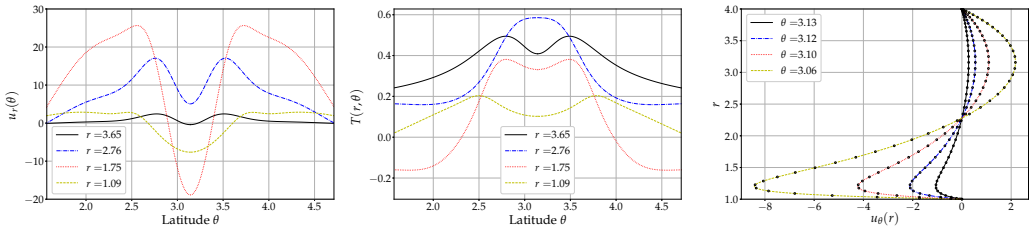


Figure 4.11: Schematic of the anticipated fluid-flow in the pole regions. Fluid is drawn along the rotation axis until it reaches the rotating spheres surface where it is then pumped outwards. (a) The inner sphere's rotation draws cooler fluid downwards which is heated as it reaches the hot sphere's surface. The cellular motion observed in figure 4.10 which opposes this motion is also indicated. (b) In the case of outer sphere rotation, hot fluid is drawn upwards and then cooled as it moves outwards along the cold sphere's surface.

longer balance the flow generated by Ekman pumping in this polar region which is in the opposite sense.

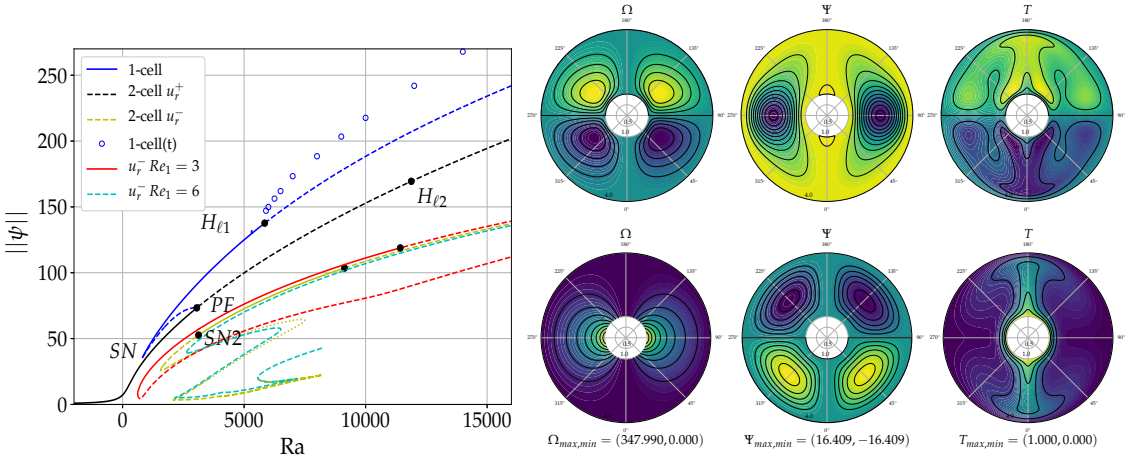
Figure 4.13 (a) shows a cross section of figure 4.8 with fixed $Re_1 = 5$. The transition of the 1-cell solution to a time dependent solution 1-cell(t) via a Hopf bifurcation denoted by $H_{\ell 1}$ as Ra is increased is indicated. The 1-cell(t) solution is available online at Movie Link, or is shown in terms of labelled frames of the temperature field in figure 4.20. The fate of the 2-cell branch u_r^- as Re_1 is increased is also shown. For $Re_1 = 3$ this branch is stable for a larger range of Ra as compared to u_r^+. Increasing Re_1 the stable portion of this branch shrinks and has disappeared for $Re_1 = 6$. An unstable branch with multiple unstable rungs is found to remain.

The lower half of frame (b) of figure 4.13 shows the symmetric flow $\boldsymbol{X}_{SN2}$ characterised by two thermal plumes, one rising towards each pole. For small Ra this flow transitions to the u_r^+ solution, while for larger Re_1 it transitions to the 1-cell solution. The disturbance $\boldsymbol{q}_{SN2}$ which induces its transition to the 1-cell state is shown in frame (b) of figure 4.13.



(a) Radial velocity $u_r(r,\theta)$. **(b)** $T(r,\theta)$ for different r. **(c)** Polar velocity $u_\theta(r,\theta)$.

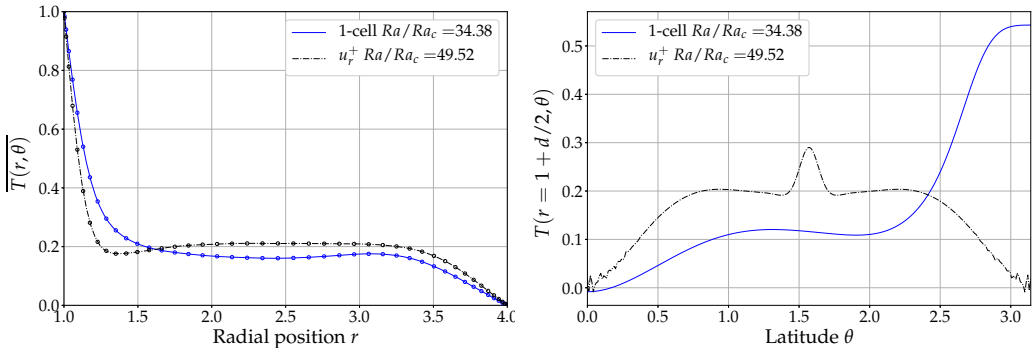
Figure 4.12: Ekman suction draws fluid radially inwards flow along the rotation axis, inhibiting the convection of hot fluid away from the inner sphere at this location. Temperature, radial velocity u_r and polar velocity u_θ profiles of the 1-cell solution for $Re_1 = 33$. (a) Near the inner and outer spheres u_r is directed inwards and becomes positive only near annulus the centre. (b) Temperature variation with latitude θ showing the development of two plumes which align about the pole. (c) The latitudinal velocity is directed towards the pole near the inner sphere ($u_\theta < 0$) and away from the pole near the outer sphere ($u_\theta > 0$).



(a) Bifurcation diagram at $Re_1 = 5$. **(b)** Lower $\boldsymbol{X}_{SN2}$ & upper $\boldsymbol{q}_{SN2}$.

Figure 4.13: Increasing the rotation strength causes the u_r^- solution to transition to the 1-cell solution, when Ra is large. For small Ra the transition is to the u_r^+ state. (a) Bifurcation diagram showing the u_r^- solution branch for different Re_1. For $Re_1 = 3$ a large portion of the branch is stable, but increasing Re_1 this stable portion is eliminated to include a number of unstable rungs. The time dependent solution 1-cell(t) is indicated by open circles. (b) Steady solution $\boldsymbol{X}_{SN2}$ and its leading eigenvector $\boldsymbol{q}_{SN2}$ for the saddle node $SN2$.

4.4.2 Stability of thermal boundary layers



(a) Latitudinally averaged temperature. **(b)** Centerline temperature profile*.

Figure 4.14: Differential rotation enhances the thermal gradients at the sphere's walls in both solutions, but stabilises the u_r^+ solution by also enhancing gradients in the thermal plumes and pole regions more effectively. (a) Latitudinally averaged $\overline{T(r,\theta)}$ and (b) centreline $T(r=1+d/2,\theta)$ profiles of the u_r^+ and 1-cell solutions for $Re_1 = 33$. *Comments on difficulties encountered resolving this solution are made at the end of this section.

To understand why the steady u_r^+ solution remains stable for larger Ra as Re_1 increases, we examine the latitudinally averaged and centreline temperature profiles of the u_r^+ and 1-cell solutions as shown in figure 4.14. Comparing these profiles we observe the u_r^+ solution achieves higher gradients at both the sphere walls and at the poles. It was shown in figures 4.9(a) and 4.10(a), that of these two solutions, the u_r^+ solution also achieves higher torque and heat transfer. Comparing the profiles in figure 4.14 with those shown in figure 3.23 (computed in the absence of rotation although at higher Ra/Ra_c), the enhancement of thermal gradients in the boundary layer regions of u_r^+ by differential rotation is apparent. It is also apparent that Ekman pumping significantly modifies the polar boundary layers observed in the non-rotating 1-cell solution's polar plume (figure 3.23).

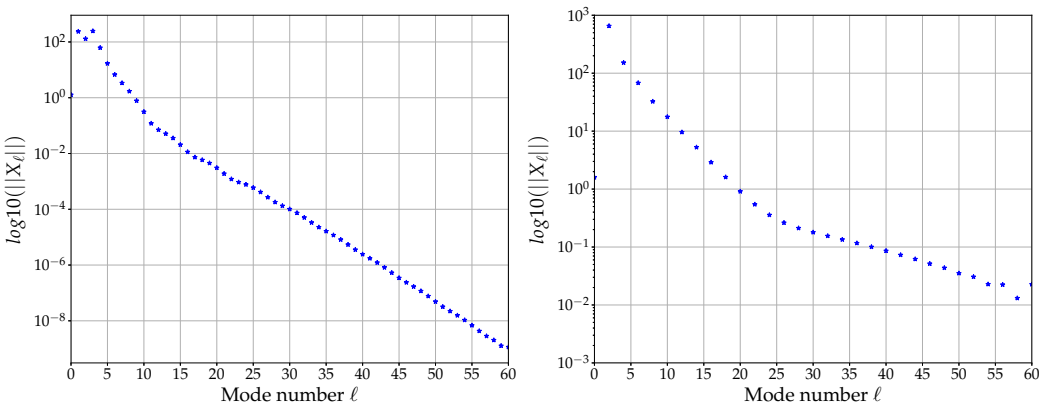
4.4.3 Transition to time-dependence

As illustrated in figure 4.8, transition from the u_r^+ solution occurs along the steady bifurcation PF for $Re_1 \lesssim 28$. While for $Re_1 \gtrsim 28$ this flow transitions to a time-dependent solution at the symmetric Hopf bifurcation $H_{\ell 2}$ resulting in an oscillation of the equatorial jet. For large Re_1 we also find that the 1-cell solution may transition to a time-dependent state 1-cell(t) as Ra is increased beyond $H_{\ell 1}$. In this section we describe these transitions and the resulting time-dependent states. Although these time-dependent solutions are likely unstable to non-axisymmetric disturbances they serve to illustrate most clearly the

non-linear dynamics of the flow with increases in the control parameters (Busse 2003). In addition, features of these flows often persist as coherent structures for more disordered configurations. For this reason we believe they are worthy of consideration.

Comments on the resolution of our spectral code

In this regime differential rotation is now strong and the 2-cell u_r^+ solution remains stable for $Ra \leq 2.2 \times 10^4$ when $Re_1 = 40$. These parameter values are also at the efficiency limit of our spectral code, which uses a Galerkin projection and therefore its numerical complexity $\sim \mathcal{O}(N_\theta^3)$, scales poorly as the required number of modes is increased.



(a) Spectrum of the 1-cell solution $\boldsymbol{X}_{H_{\ell 1}}$ **(b)** Spectrum of the 2-cell solution $\boldsymbol{X}_{H_{\ell 2}}$

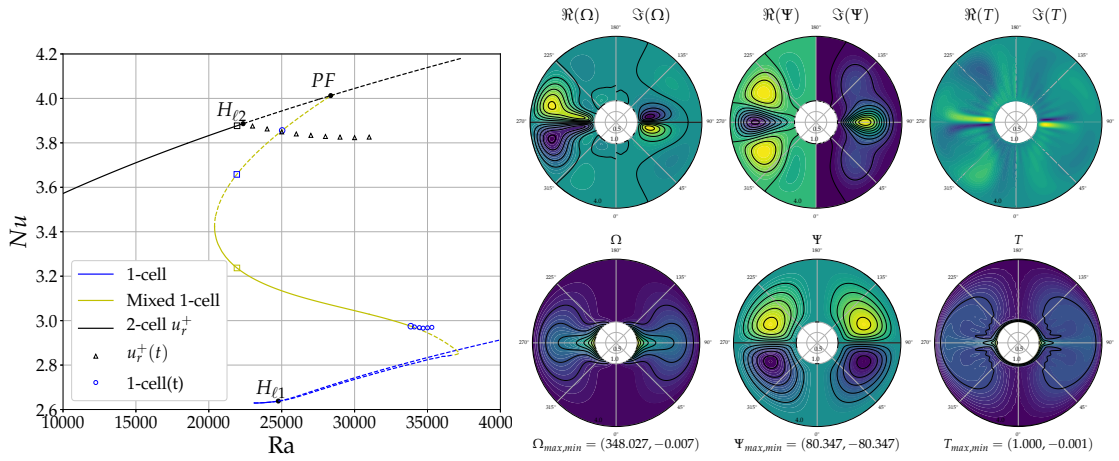
Figure 4.15: The 1-cell solution is resolved using a comparatively smaller of modes relative to the 2-cell solution. Energy spectrum of the solution vectors at $Re = 50$ using a resolution of $Nr = 50$ Chebyshev points and $N_\theta = 60$ Legendre polynomials. (a) Asymmetric 1-cell solution is adequately represented by the Galerkin projection. (b) The symmetric 2-cell requires a larger number of modes.

Figure 4.15 shows the energy spectrum of the steady state solutions evaluated at the Hopf bifurcations for $Re_1 = 50$ in figure 4.8, the largest parameter values considered in this work. Frame (a) of figure 4.15 shows the spectrum of the asymmetric 1-cell solution which is adequately represented by the Galerkin projection with minimal energy contributions from higher modes. The number of radial collocation points $N_r = 50$ has been varied to ensure the critical Rayleigh number and Hopf frequency ω_c remain within 0.25% as N_r, N_θ is increased. In frame (b), however, significant energy remains among higher modes and a larger number of polynomials is required.

The difficulties encountered in resolving this flow are attributed to the strong boundary layers present, particularly those in the neighbourhood of its thermal plume at the equator.

Expressing T as a finite sum of Legendre polynomials $P_\ell(\cos\theta)$, whose zeros concentrate near $\theta = 0, \pi$, means that while gradients in the polar regions of the 1-cell solution can be more easily resolved, those at the equator in the u_r^+ solution are more costly. Therefore while we can guarantee all results presented for asymmetric flows are numerically accurate, the small scales present in the T field of the rotation dominated 2-cell flows require additional resolution. To validate that our solutions are not artefacts of poor resolution we have also used a finite difference code.

Oscillation of the equatorial jet



(a) Bifurcation diagram at $Re_1 = 40$. **(b)** Lower $\boldsymbol{X}_{H_{\ell 2}}$ & upper $\boldsymbol{q}_{H_{\ell 2}}$.

Figure 4.16: Disturbances localized about the equator cause the transition of the 2-cell solution u_r^+ to a time-dependence state, leading to a reduction in heat transfer. (a) Increasing Ra, the u_r^+ solution loses stability via a Hopf bifurcation at $H_{\ell 2}$, transitioning to an initially time periodic state $u_r^+(t)$. Further increasing Ra, this state undergoes a global bifurcation as it intersects the unstable mixed 1-cell branch (cf. figure 4.18). (b) Equilibrium solution $\boldsymbol{X}_{H_{\ell 2}}$ bottom and top the leading eigenvector's real $\Re(\boldsymbol{q})_{H_{\ell 2}}$ and imaginary $\Im(\boldsymbol{q})_{H_{\ell 2}}$ components.

Frame (a) of figure 4.16 shows that as Ra is increased the u_r^+ solution loses stability in a symmetry breaking Hopf bifurcation at $H_{\ell 2}$. Its transition to a stable time-dependent state $u_r^+(t)$ leads to reduction in heat transfer. This was also reported by Inagaki *et al.* (2019) who computed the corresponding transition from the axisymmetric u_r^+ state to a 3D time-dependent solution. Near the Hopf bifurcation $H_{\ell 2}$, the $u_r^+(t)$ solutions time-dependence is periodic, but as Ra is increased this solution collides with the unstable mixed 1-cell branch at $Ra \approxeq 2.43 \times 10^4$. Following Knobloch *et al.* (1986) who analysed the sequence of transitions leading to chaos in a double-diffusive convection system, it is assumed that the global bifurcation which occurs at this point results in a heteroclinic

cycle. By computing the leading eigenvalues on the unsteady branch which bifurcates from PF we have verified that Šil'nikov's inequality for the existence of heteroclinic cycles is satisfied (Šil'nikov 1970). A projection of the limit cycle's behaviour near this bifurcation is shown for different Ra in figure 4.22. As this regime is at the limit of the spectral code's resolution, time-integration using finite differences indicated by hollow black triangles in figure 4.16 has also been used to compute the resulting time-periodic solution, and to verify the transition to time-dependence predicted by the spectral code.

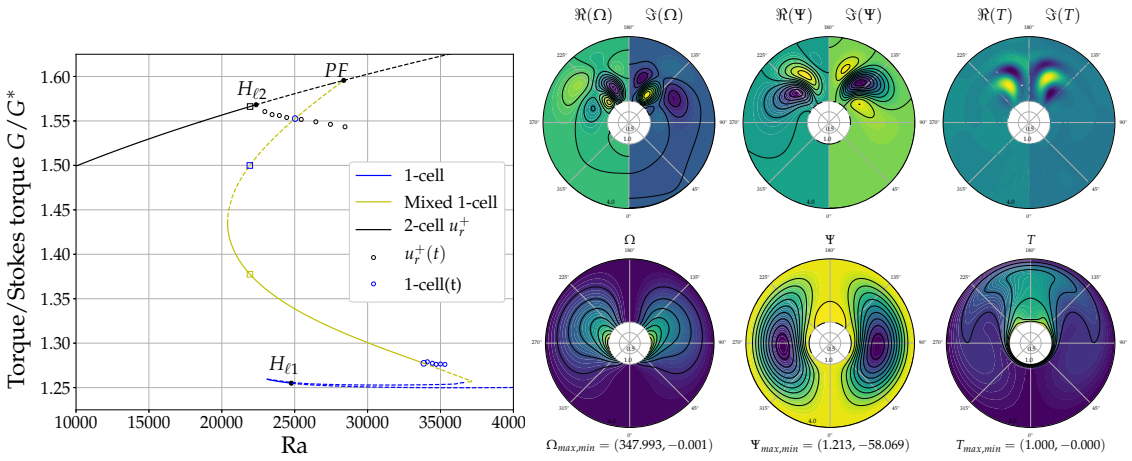
It is worth mentioning that the bifurcation curves denoted by PF and $H_{\ell 2}$ intersect at a co-dimension two $\mathcal{Z}_2$ symmetric fold-Hopf point, indicated by a solid black circle in figure 4.8. The dynamics near such points have been studied up to third order by Kuznetsov (2004) and Guckenheimer & Holmes (1983) using truncated normal forms. Although we have not obtained the normal form specific to this problem, it would be useful to do so to understand the origin of the dynamics observed in figure 4.22. As the pitchfork bifurcation PF is subcritical, higher order terms than those considered by Kuznetsov (2004) and Guckenheimer & Holmes (1983) would have to be included.

The steady solution $\boldsymbol{X}_{H_{\ell 2}}$ (frame (b) of figure 4.16) shows that both the T and Ω fields are now strongly advected by the flow ψ whose streamlines are almost parallel with the equator. The Ω field in particular has begun to deviate from its Stokes flow profile, which was observed in many of the previous 2-cell solutions. The disturbance $\boldsymbol{q}_{H_{\ell 2}}$ shown in the upper half of figure 4.16(b) indicates that an instability of thermal layer at the equator is responsible for the transition to a time-dependent state. The T and ψ components of $\boldsymbol{q}_{H_{\ell 2}}$ indicate an oscillation that will be largely back and forth across the equator, while Ω also includes a small radial component. The time-dependent solution $u_r^+(t)$ is available online at Movie Link, or is shown in terms of labelled frames of the temperature field in figure 4.19.

Oscillation of the polar plume

Also possible for a small range of Ra is the 1-cell solution which is bistable with the $u_r^+(t)$ and mixed 1-cell solutions. Increasing Ra this solution becomes initially time-periodic beyond the Hopf bifurcation $H_{\ell 1}$, but ultimately loses stability and transitions to the mixed 1-cell state (cf. figure 4.18). As the time dependent branches shown in figure 4.17 are computed by time-stepping, it was not possible to determine the unstable branch easily. We note that this task can however be performed using continuation methods which rely on deflation (Net & Snchez 2015). This technique eliminates the possibility of converging to previously determined solutions.

Increasing Ra along the stable portion of the mixed 1-cell branch, we find that for $Ra \geq 3.38 \times 10^4$, this branch loses stability in a Hopf bifurcation. The limit cycle which emerges 1-cell(t) exhibits complex time-dependent behaviour as shown in figure 4.23. Although we



(a) Bifurcation diagram at $Re_1 = 40$. **(b)** Lower $\boldsymbol{X}_{H_{\ell 1}}$ & upper $\Re(\boldsymbol{q})_{H_{\ell 1}}$.

Figure 4.17: Disturbances localized at the pole cause the 1-cell solution to transition to a time-dependence state, leading to an increase in torque and heat transfer. (a) Increasing Ra the 1-cell solution looses stability via a Hopf bifurcation at $H_{\ell 1}$ and transitions to the mixed 1-cell solution. As Ra is increased a global bifurcation occurs resulting in a limit cycle 1-cell(t) denoted by hollow blue circles. (b) Equilibrium solution $\boldsymbol{X}_{H_{\ell 1}}$ bottom and top the leading eigenvector's real $\Re(\boldsymbol{q})_{H_{\ell 1}}$ and imaginary $\Im(\boldsymbol{q})_{H_{\ell 1}}$ components.

have not investigated its behaviour, it is thought that collision of the unstable periodic solution with the unstable steady branch may play a role in its formation.

Compared with the solutions at smaller Re_1, the poloidal flow shown in figure 4.17(b) has strengthened to balance the strong differential rotation. The contours of Ω are deflected upwards strongly, and the thermal boundary layer present on the sphere's lower surface has been strengthened. On the sphere's upper surface stronger Ekman pumping, is observed to flatten the thermal plume and spread it apart. The role of Ekman pumping is also reflected in the disturbance $\boldsymbol{q}_{H_{\ell 1}}$ shown in the upper half of frame (b) figure 4.17. Contours of the disturbance ψ indicate that although the flow is unaffected at the South pole, its direction will alternate near the North pole resulting in a radial oscillation. The temperature disturbance also indicates that fluid will oscillate radially between being hot and cold at the pole. The time-dependent solution 1-cell(t) is available online at Movie Link, or is shown in terms of labelled frames of the temperature field in figure 4.21.

Connection between the unstable and stable branches

The 1-cell and u_r^+ branches are found to connect via a *mixed 1-cell* solution, as shown in yellow in figure 4.17(a). Following this branch from PF towards the 1-cell branch shown in blue, we find that the narrow equatorial jets of the u_r^+ solution are gradually deflected

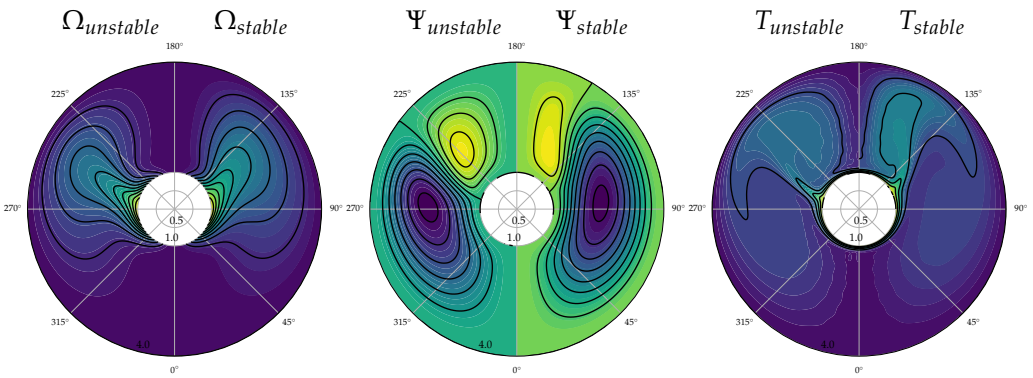


Figure 4.18: The unstable equatorial jet of the 2-cell solution (left) is deflected from the equator towards the pole. The jet moves upwards under the action of the large convection cell, until it reaches the stable mixed 1-cell state (right) where it is balanced by Ekman pumping. Transition from the 2-cell u_r^+ to the 1-cell solution for $Re_1 = 40, Ra = 2.2 \times 10^4$.

upwards towards the poles, such that a 1-cell flow is obtained upon reaching the blue 1-cell branch shown in figure 4.18. This transition is accompanied by a decrease in both convective heat transfer and torque, a reduction attributed to the decrease in surface area from which strong radial advection of hot high angular momentum fluid takes place. In the u_r^+ solution this occurs within a band about the equator, while in the 1-cell solution it is reduced to a circular patch at the pole that is comparatively of much smaller surface area.

Throughout section 4.4 we have emphasised the presence of two different types of steady flows, one that resembles 2-cell rotation termed u_r^+ the other that resembles convection termed 1-cell. This section has also served to emphasise that there are two classes of time-dependent solutions, a rotating solution with oscillations in the polar direction $u_r^+(t)$ and a convective solution with radial oscillations 1-cell(t). Figures 4.16 and 4.17 show that the bifurcation to $u_r^+(t)$ reduces both the rotating solution's convective heat transfer and torque, while the bifurcation to 1-cell(t) increases them relative to their steady state solutions.

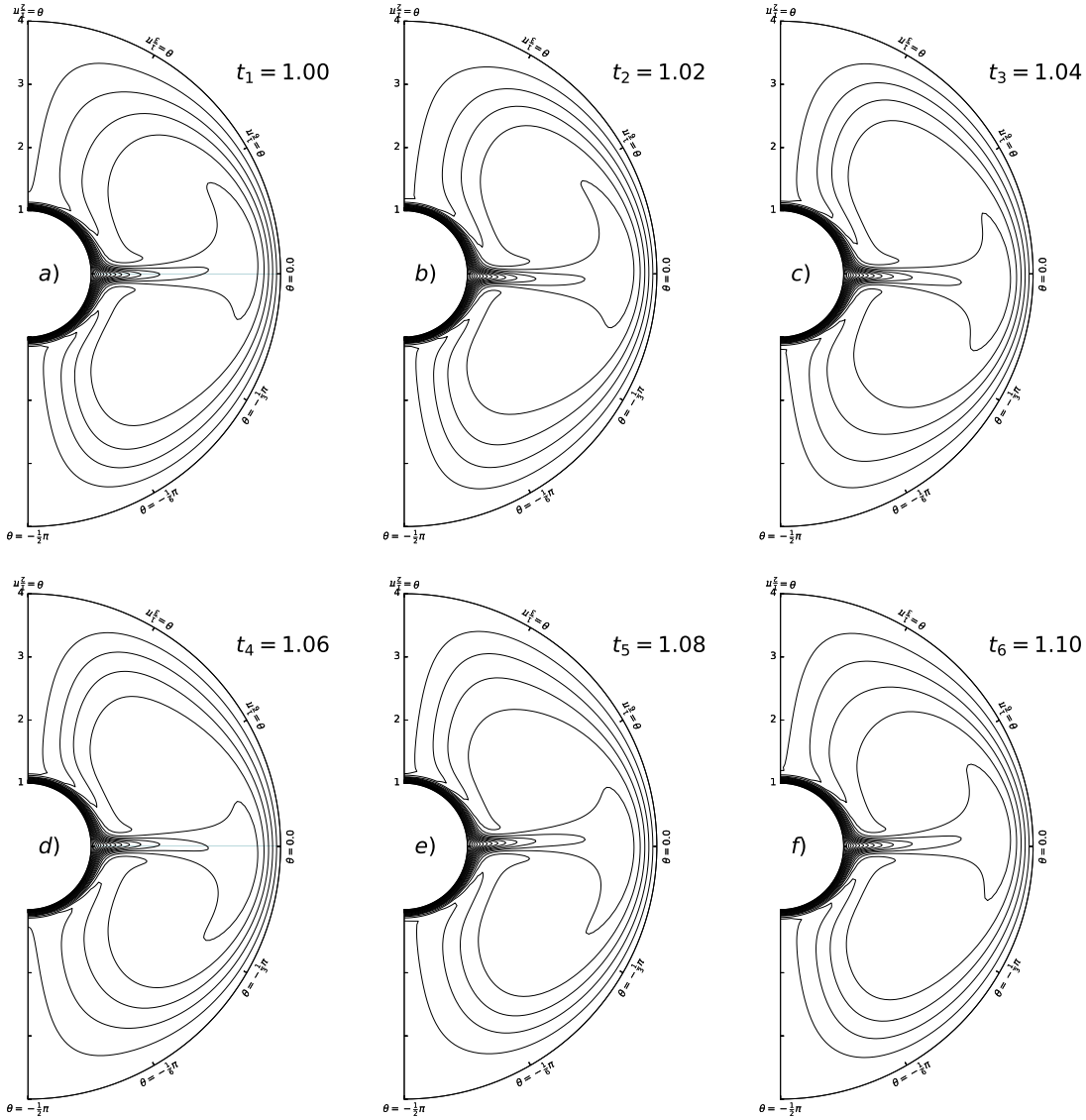


Figure 4.19: Snapshots of the temperature field demonstrating the time-periodic oscillation of the equatorial jet for $Re_1 = 40, Ra = 2.2 \times 10^4$. Frames (a) to (f) show successive snapshots evaluated over a single oscillation period. The jet which resembles a cantilever beam, extends outwards at the equator and oscillates back and forth in the polar direction. The presence of a strong thermal boundary layer is indicated by the closely bunched contours near the inner sphere.

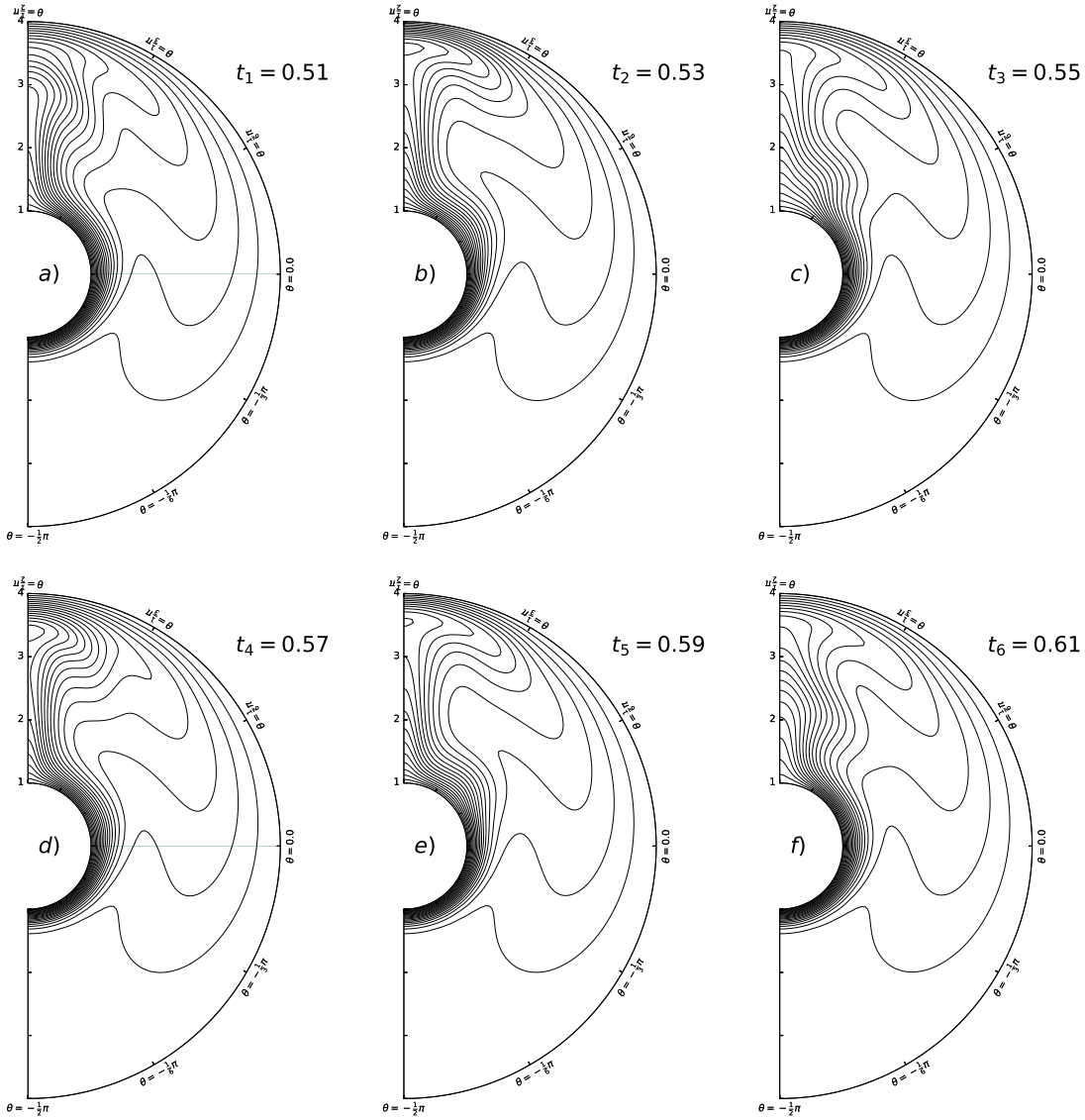


Figure 4.20: Snapshots of the temperature field demonstrating the time-periodic oscillation of the polar plume for $Re_1 = 5, Ra = 8 \times 10^3$. Frames (a) to (f) show successive snapshots evaluated over a single oscillation period. The plume which closely resembles a mushroom cloud of hot fluid travels radially outwards from the inner sphere. Upon reaching the outer sphere it is deflected in the polar direction and diffuses.

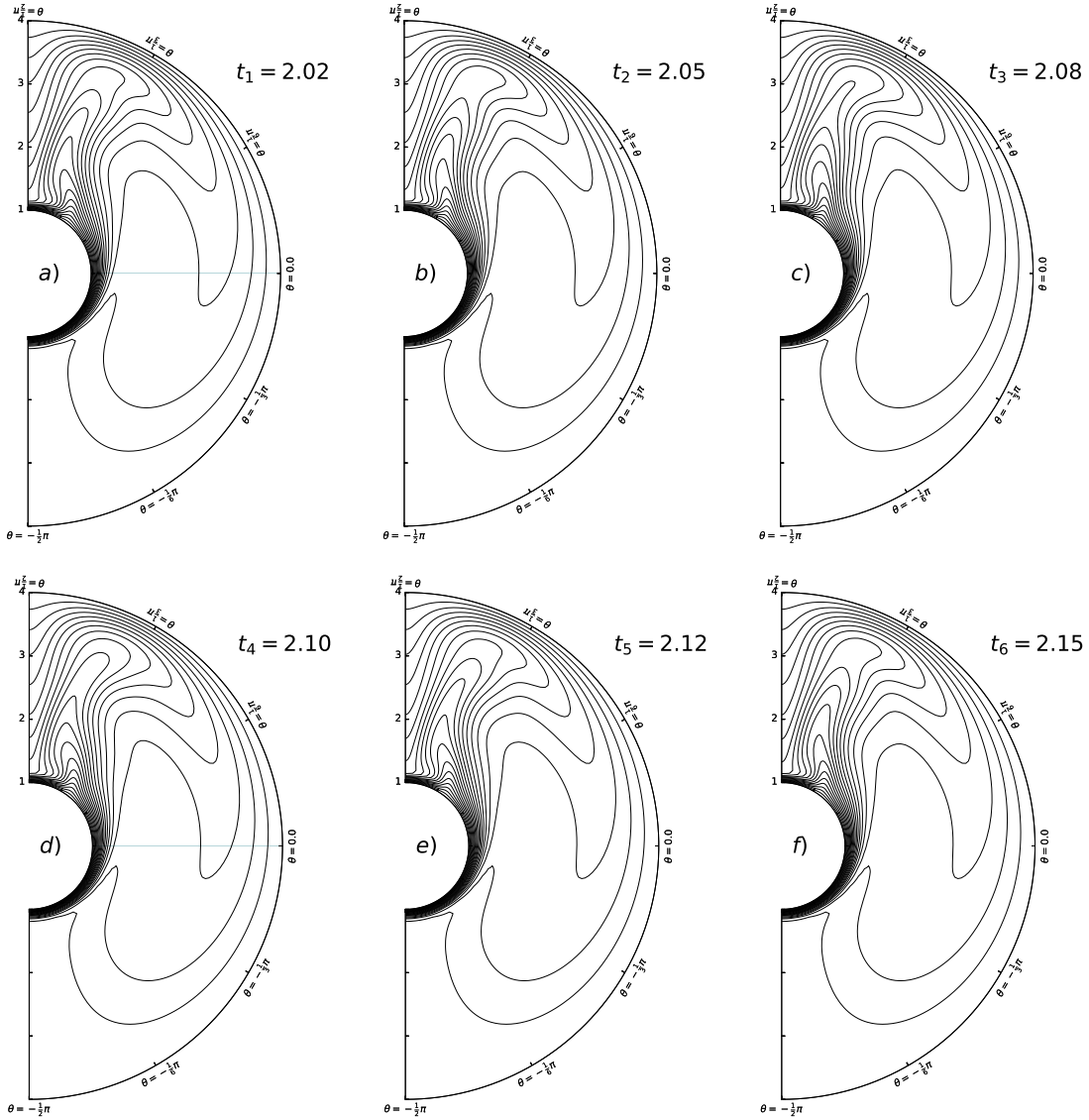
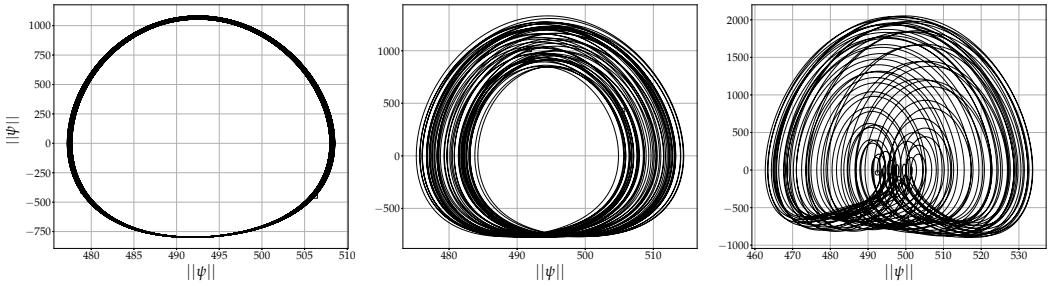
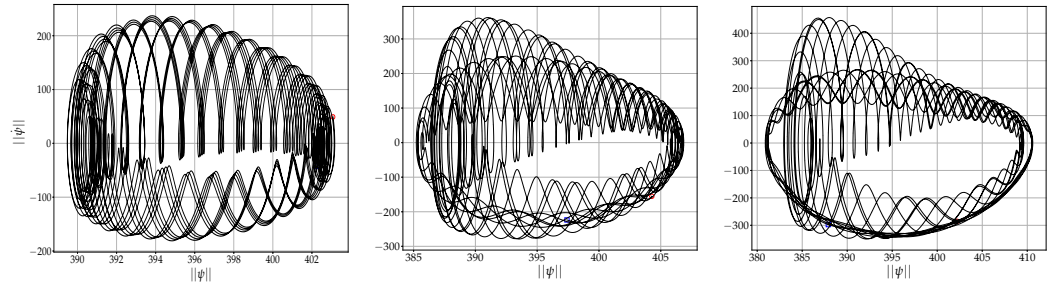


Figure 4.21: Snapshots of the temperature field demonstrating the time-periodic oscillation of the polar plume for $Re_1 = 30, Ra = 1.8 \times 10^4$. Frames (a) to (f) show successive snapshots evaluated over a single oscillation period. The narrow plume which emerges from a strong radial boundary layer is directed upwards towards the pole near the inner sphere. Near the annulus centreline the plume waves back and forth due to the influence of Ekman pumping which pushes it away form the axis and the large convection cell which forces it back towards the axis.



(a) $Ra = 28 \times 10^3$ **(b)** $Ra = 29 \times 10^3$ **(c)** $Ra = 30 \times 10^3$

Figure 4.22: Plots of the norm of the stream-function $||\psi||$ against its rate of change $||\dot{\psi}||$ for the 2-cell solution $u_r^+(t)$ at $Re_1 = 40$. As Ra is increased an initially time-periodic 2-cell solution loses stability in a global bifurcation resulting in a heteroclinic cycle, near which chaotic behaviour is found to emerge.



(a) $Ra = 34.7 \times 10^3$ **(b)** $Ra = 35 \times 10^3$ **(c)** $Ra = 35.3 \times 10^3$

Figure 4.23: Plots of the norm of the stream-function $||\psi||$ against its rate of change $||\dot{\psi}||$ for the 1-cell(t) solution at $Re_1 = 40$. As Ra is increased a steady solution loses stability in a Hopf bifurcation. This is found to give rise to chaotic behaviour near the bifurcation point. Although we have not investigated this solutions formation, it is assumed that the collision of an unstable time-periodic solution and an unstable steady branch plays a role.

5

Non-axisymmetric stability analysis

For the steady 2D solutions obtained in chapter 3 and chapter 4 to correspond to linearly stable solutions of the full three-dimensional (3D) problem, the eigenvalues corresponding to the non-axisymmetric perturbations must also be computed. This is performed by linearising (2.7), the equations corresponding to the 3D model, and verifying that all azimuthal perturbations of the following form decay

$$\boldsymbol{X}'(r,\theta,\varphi,t) = \boldsymbol{q}(r,\theta)e^{im\varphi+\lambda t}, \quad \text{where} \quad \lambda \in \mathbb{C}, \tag{5.1}$$

and the azimuthal wave number which is denoted by $m = \pm 1, \pm 2, ...$ may be of odd or even parity.

Although an axisymmetric state may initially be stable, it is likely that as we increase a control parameter such as Ra that $\Re(\lambda)$ will change sign. It was shown in chapter 4 that this crossing can happen in two ways, either $\lambda = 0$ or $\lambda = \pm \mathrm{i}\omega$, and that the type of the bifurcation which occurs depends on the solution's symmetry. Before computing the stability of these axisymmetric solutions, we first use their symmetries to briefly describe the solutions anticipated to result from their bifurcations.

In 3D, the *mixed* axisymmetric solutions solutions computed in chapter 3 and chapter 4 gain $O(2)$ symmetry-the reflections and rotations on a circle described by

$$\begin{aligned} &\text{reflections} \quad \varphi \to -\varphi: \quad \boldsymbol{X}' \to \bar{\boldsymbol{X}}', \\ &\text{rotations} \quad \varphi \to \varphi + \varphi_0: \quad \boldsymbol{X}' \to \boldsymbol{X}' e^{im\varphi_0}, \end{aligned} \tag{5.2}$$

while the even solutions now have $O(2)\times\mathcal{Z}_2$ symmetry, as they can also be reflected about the equator. Following Matthews (2003) we expect that steady-state bifurcations in the presence of $O(2)$ symmetry, will result in steady equilibria whose symmetry is determined by a subgroup of $O(2)$, which in turn is found to depend on the shell separation (Li *et al.* 2005). While for a Hopf-bifurcation in the presence of $O(2)$ symmetry, a time-dependent state with either $SO(2)$ symmetry resembling a rotating wave or Z_2 symmetry resembling a standing wave will result (Crawford & Knobloch 1991). In a study of rotating convection at both high and low Pr, Goldstein *et al.* (1993) showed that rotating waves are a direct consequence of breaking reflection symmetry and that their precession frequency may be identified with the rotation rate.

Making the substitution

$$\boldsymbol{u} = \tilde{\boldsymbol{u}} + Re_1 Pr\, \boldsymbol{u}_0(r,\theta), \quad T = \tilde{T} + T_0(r), \tag{5.3}$$

such that $\tilde{\boldsymbol{u}}, \tilde{T}$ now satisfy homogeneous boundary conditions, and using the identity

$$(\boldsymbol{u}\cdot\nabla)\boldsymbol{u} = \frac{1}{2}\nabla(\boldsymbol{u}\cdot\boldsymbol{u}) - \boldsymbol{u}\times\boldsymbol{\omega}, \tag{5.4}$$

the equations governing the 3D problem may be written as

$$\frac{1}{Pr}\left(\frac{\partial \boldsymbol{u}}{\partial t} - \boldsymbol{u}\times\boldsymbol{\omega} + \nabla p\right) = \mathrm{Ra}\, g(r)\boldsymbol{r}T + \boldsymbol{\nabla}^2\boldsymbol{u} + Re_1\big(\boldsymbol{u}_0\times\boldsymbol{\omega} + \boldsymbol{u}\times\boldsymbol{\omega}_0\big) + PrRe_1^2\,\big(\boldsymbol{u}_0\times\boldsymbol{\omega}_0\big), \tag{5.5a}$$

$$\frac{\partial T}{\partial t} + (\boldsymbol{u} + Pr\, Re_1\boldsymbol{u}_0)\cdot\nabla(T + T_0(r)) = \nabla^2 T, \qquad \boldsymbol{\nabla}\cdot\boldsymbol{u} = 0, \tag{5.5b}$$

where the tilde notation has been dropped for clarity. The ∇p term contains the pressure and other gradient like terms. In this statement of the equations, variables T and $\boldsymbol{u}$ represent the departure from the conductive base state $T_0(r)$, and the toroidal $\boldsymbol{u}_0$ base state given by

$$\boldsymbol{u}_0 = \boldsymbol{\nabla}\times\left(\frac{\Psi_0}{r}\boldsymbol{r}\right) = \big(0, 0, -(\tilde{a}r + \tilde{b}/r^2)\sin\theta\big), \quad \text{where} \quad \Psi_0 = -\Omega_0(r)P_1(\cos\theta) = -(\tilde{a}r^2 + \tilde{b}/r)P_1(\cos\theta), \tag{5.6}$$

and the constant coefficients $\tilde{a}, \tilde{b}$ are as per (2.19). Anticipating that 2D solutions of (5.5) are most likely to be stable to 3D perturbations in the limit $Pr\to\infty$, we focus on this case. For $Pr\to 0$ advection terms in the momentum equation become significant and tend

to destabilize axisymmetric solutions. Considering a range of Pr this was shown by Jones & Moore (1978) for rotating convection in a cylinder. Taking the limit $Pr \to \infty$ allows us to neglect the inertial terms appearing on the right hand side of (5.5a) provided advection terms are small and the flow is dominated by viscous forces. While this simplifies our analysis it restricts the parameter regime we may consider, as we require that $Re_1 \to 0$ such that $PrRe_1 \sim \mathcal{O}(1)$. This limit also assumes that Ra remains finite so that advective terms driven by buoyancy are also small.

The solenoidal velocity field $\boldsymbol{u}$ can be expressed in terms of its poloidal and toroidal components

$$\boldsymbol{u} = \boldsymbol{\nabla} \times \boldsymbol{\nabla} \times \left(\frac{\Phi}{r}\boldsymbol{r}\right) + \boldsymbol{\nabla} \times \left(\frac{\Psi}{r}\boldsymbol{r}\right), \tag{5.7}$$

which automatically satisfy continuity. The stream-function ψ and specific angular momentum Ω are related to the scalars Φ, Ψ by

$$\psi = -\sin\theta \frac{\partial \Phi}{\partial \theta}, \qquad \Omega = -\sin\theta \frac{\partial \Psi}{\partial \theta}. \tag{5.8}$$

Substituting (5.7) into (2.7) and operating on the momentum equation with $\boldsymbol{r} \cdot \boldsymbol{\nabla}\times$ and $\boldsymbol{r} \cdot \boldsymbol{\nabla} \times \boldsymbol{\nabla}\times$ one can express (2.7) in terms of Φ, Ψ and T only.

In the limit $Pr \to \infty, Re_1 \to 0$ this allows the problem to be written as

$$\begin{aligned}
\mathcal{L}_2 \nabla^2 (\Psi/r) &= -Re_1\, \boldsymbol{r} \cdot \nabla \times \big(\boldsymbol{u}_0 \times \boldsymbol{\omega} + \boldsymbol{u} \times \boldsymbol{\omega}_0\big), \\
\mathcal{L}_2 \nabla^2 \nabla^2 (\Phi/r) - \mathrm{Ra}\, g(r) \mathcal{L}_2 T &= Re_1\, \boldsymbol{r} \cdot \nabla \times \nabla \times \big(\boldsymbol{u}_0 \times \boldsymbol{\omega} + \boldsymbol{u} \times \boldsymbol{\omega}_0\big) + PrRe_1^2\, \boldsymbol{r} \cdot \nabla \times \nabla \times \big(\boldsymbol{u}_0 \times \boldsymbol{\omega}_0\big), \\
\big(\frac{\partial}{\partial t} - \nabla^2\big) T + \boldsymbol{u} \cdot \hat{\boldsymbol{r}} T_0' + PrRe_1 \boldsymbol{u}_0 \cdot \hat{\boldsymbol{\varphi}} \nabla T &= -\boldsymbol{u} \cdot \nabla T,
\end{aligned} \tag{5.9}$$

where the operator $\mathcal{L}_2$ is given by

$$\mathcal{L}_2 \equiv -\frac{1}{\sin\theta}\frac{\partial}{\partial\theta}\left(\sin\theta \frac{\partial}{\partial\theta}\right) - \frac{1}{\sin^2\theta}\frac{\partial^2}{\partial\varphi^2}, \qquad \mathcal{L}_2 Y_\ell^m(\theta,\varphi) = \ell(\ell+1) Y_\ell^m(\theta,\varphi). \tag{5.10}$$

The spherical harmonic of order m is defined $Y_\ell^m(\theta,\varphi) = P_\ell^m(\cos\theta) e^{im\varphi}$, with P_ℓ^m being the associated Legendre polynomials of degree ℓ and order m. The velocity $\boldsymbol{u}$ expressed in terms of its poloidal and toroidal components respectively is

$$\boldsymbol{u} = \left(\frac{\mathcal{L}_2\Phi}{r^2}, \frac{1}{r}\frac{\partial^2\Phi}{\partial r \partial\theta}, \frac{1}{r\sin\theta}\frac{\partial^2\Phi}{\partial r\partial\varphi}\right) + \left(0, \frac{1}{r\sin\theta}\frac{\partial\Psi}{\partial\varphi}, -\frac{1}{r}\frac{\partial\Psi}{\partial\theta}\right). \tag{5.11}$$

To compute the stability of an axisymmetric steady state $(\Psi, \Phi, T)^T$ we add a non-

axisymmetric perturbation $(\epsilon\Psi', \epsilon\Phi', \epsilon T')^T$ and retaining terms of $\mathcal{O}(\epsilon)$ obtain the linear system

$$\begin{aligned}
\mathcal{L}_2\nabla^2(\Psi'/r) &= -Re_1\,\boldsymbol{r}\cdot\nabla\times\big(\boldsymbol{u}_0\times\boldsymbol{\omega}'+\boldsymbol{u}'\times\boldsymbol{\omega}_0\big),\\
\mathcal{L}_2\nabla^2\nabla^2(\Phi'/r)-\mathrm{Ra}\,g(r)\mathcal{L}_2T' &= Re_1\,\boldsymbol{r}\cdot\nabla\times\nabla\times\big(\boldsymbol{u}_0\times\boldsymbol{\omega}'+\boldsymbol{u}'\times\boldsymbol{\omega}_0\big),\\
\frac{\partial T_0(r)}{\partial r}\,\frac{\mathcal{L}_2}{r^2}\Phi'-\frac{Re_1\,Pr}{r^2\sin\theta}\frac{\partial\Psi_0}{\partial\theta}\frac{\partial}{\partial\varphi}T'+\big(\lambda-\nabla^2\big)T' &= -\boldsymbol{u}'\cdot\nabla T-\boldsymbol{u}\cdot\nabla T',
\end{aligned} \tag{5.12}$$

where we have assumed the perturbation has exponential time dependency. In matrix form this system may be written as

$$\big(\lambda\mathcal{M}+\mathcal{L}\big)\boldsymbol{X}'=\begin{pmatrix}-Re_1N_{11}(\Psi_0) & -Re_1\,N_{12}(\Psi_0) & 0\\ Re_1\,N_{21}(\Psi_0) & Re_1\,N_{22}(\Psi_0) & 0\\ -N_{31}(T) & -N_{32}(T) & -N_{33}(\Phi,\Psi)\end{pmatrix}\boldsymbol{X}',\quad\text{where}\quad\boldsymbol{X}'=(\Psi',\Phi',T')^T, \tag{5.13}$$

where the matrix operators $\mathcal{M},\mathcal{L}$ are defined as

$$\mathcal{M}=\begin{pmatrix}0&0&0\\0&0&0\\0&0&1\end{pmatrix},\qquad\mathcal{L}=\begin{pmatrix}\mathcal{L}_2\nabla^2(r^{-1}) & 0 & 0\\ 0 & \mathcal{L}_2\nabla^2\nabla^2(r^{-1}) & -\mathrm{Ra}\,g(r)\mathcal{L}_2\\ 0 & \frac{\mathcal{L}_2T_0'}{r^2} & -\frac{1}{r^2\sin\theta}\frac{\partial\Psi_0}{\partial\theta}\frac{\partial}{\partial\varphi}-\nabla^2\end{pmatrix}. \tag{5.14}$$

The terms $N_{ij}(,)$ come from the linearisation of the terms $\boldsymbol{u}\cdot\boldsymbol{\nabla}\boldsymbol{u}$ and $\boldsymbol{u}\cdot\nabla T$, whose form is outlined in appendix E. To compute the growth rate $\lambda\in\mathbb{C}$ of a numerically determined axisymmetric state we use a Galerkin projection method. In this formulation the axisymmetric state is represented by a finite sum of Legendre polynomials

$$\Psi=\sum_{p=1}^{N_\theta}\Psi_p(r)P_p(\cos\theta),\quad\Phi=\sum_{p=1}^{N_\theta}\Phi_p(r)P_p(\cos\theta),\quad T=\sum_{p=0}^{N_\theta}T_p(r)P_p(\cos\theta), \tag{5.15}$$

and the perturbation by a finite sum of spherical harmonics

$$\Psi'=\sum_{\ell=m}^{N_\theta}\Psi'_{\ell m}(r)Y_\ell^m(\theta,\varphi),\quad\Phi'=\sum_{\ell=m}^{N_\theta}\Phi'_{\ell m}(r)Y_\ell^m(\theta,\varphi),\quad T'=\sum_{\ell=m}^{N_\theta}T'_{\ell m}(r)Y_\ell^m(\theta,\varphi). \tag{5.16}$$

These expansions are substituted into (5.13) and using Gaunt coefficients as outlined in appendix E, projected to obtain a system of N_θ coupled ODEs dependent on the radial coordinate r and azimuthal wavenumber m only. The radial direction is then discretized using second-order finite differences as outlined in appendix D. Given an axisymmetric state this allows the growth rate λ to be computed at different m for a range of Ra, Re_1, Pr.

We first consider the stability of even and mixed axisymmetric solutions to the thermal convection problem without rotation for small Ra and $Pr \to \infty$. These computations are repeated for different values of the separations d to outline the regions of (Ra, d) parameter space in section 3.3 where axisymmetric states are stable solutions of the 3D equations. Subsequently we consider the stability these solutions allowing for weak differential rotation.

The problem is approached in this order to emphasise that the linear convection problem is degenerate for $Ra = Ra_c, Re_1 = 0$ such that one cannot determine whether the preferred motion is axisymmetric or non-axisymmetric without considering the non-linear terms (Busse 1975). When we allow for weak rotation $Ra = Ra_c, Re_1 \neq 0$ this degeneracy is removed, however the base state becomes θ dependent and must be determined nonlinearly.

5.1 Thermal convection

The results of this computation are summarised in tables 5.1, 5.2 and have been included as neutral stability curves $\lambda(\delta, \mu, m) = 0$ in the bifurcations diagrams presented in section 3.3 figures 3.6, 3.10 and 3.13. For ease of comparison with these figures the parameters

$$\mu = (Ra - Ra_c)/Ra_c, \quad \delta = d - d_c \tag{5.17}$$

are used. As before, (d_c, Ra_c) represents the coordinates of a given degenerate point.

The results are broadly similar to those of Zebib *et al.* (1980, 1983) who considered the case of stress-free boundaries. In general our calculations indicate that just above the critical Ra_c axisymmetric solutions are unstable to some azimuthal wavenumbers, but once established at larger Ra we find that solutions stabilise. Therefore in this regime the axisymmetric flows are stable solutions of the full 3D system (2.7), although they need not be the preferred state for arbitrary initial conditions. Because of the reflectional symmetry of mixed (odd) solutions, it is only necessary to consider three solution types in tables 5.1, 5.2. An azimuthal wavenumber m is denoted by U for unstable if $\lambda > 0$, S for stable if $\lambda < 0$ and N for neutrally stable if $\lambda = 0$. The third case, a consequence of the North-South pole shift symmetry, arises when $m = 1$. It was shown by Zebib *et al.* (1980) that such a perturbation corresponds to a shift of this axis.

Degeneracy	Solution	$m=0$	$m=1$	$m=2$	$m=3$	$m=4$
$\ell=(1,2)$	$(\pm A, B)$	U	N	U	-	-
	$(0,-B)$	U	N	S	-	-
	$(0,+B)$	S	N	S if $\mu>0.5$	-	-
$\ell=(2,3)$	$(\pm A, B)$	S	N	S	S if $\mu>0.4$	-
	$(-A,0)$	S	N	U	S	-
	$(+A,0)$	S	N	U	U	-
$\ell=(3,4)$	$(\pm A, B)$	S	N	U	S	S
	$(0,-B)$	S	N	S	S if $\mu>0.1$	S if $\mu>0.19$
	$(0,+B)$	S	N	S if $\mu>0.13$	S if $\mu>0.18$	S if $\mu>0.13$

Table 5.1: Three-dimensional stability at large *Pr* and $\delta=0$ of axisymmetric solutions to azimuthal perturbations of wavenumber m at each $(\ell,\ell+1)$ degeneracy. In all cases the Ra required for 3D stability is measured from the degenerate point (d_c,Ra_c) specific to each case. The stability of solutions is denoted U = unstable for $\lambda>0$, S = stable for $\lambda<0$ or N = neutral in the special case where the $m=1$ mode is neutrally stable. Higher wavenumbers $m>4$ were found to be stable for the range of Ra considered.

5.1.1 Odd-even & even-odd interactions

The stability of solutions for different (δ,μ) is computed and the region of parameter space for which the axisymmetric solutions are stable is included in figures 3.6 and 3.10. Specifically we find that near the $\ell=(1,2)$ degenerate point, even solutions $(0,\pm B)$ are stable in regions 3 & 6 of figure 3.10, while mixed solutions $(\pm A,\ B)$ are stable in region 4 only. Near the $\ell=(2,3)$ degenerate point, even solutions $(-A,0)$ are stable only for large δ,μ, as shown in figure 3.6. Stable mixed solutions are found for $\delta<0.22$, but above this threshold are destabilized by $m=2$. Near the $\ell=(3,4)$ degenerate point, stable solutions of both even and mixed form are found. For $\delta>0$ the mixed solutions are stable, while for $\delta<0.2$ stable even mode solutions are found as shown in figure 3.10. Notably, the stability behaviour of different even solutions near the same degeneracy can vary. It was shown by Zebib *et al.* (1980, 1983) for the case of stress-free boundaries, that the heat transfer achieved by each of these solutions differs as μ is increased from the bifurcation point. Our numerical simulations identify similar behaviour for the even mode cases. Results for $\delta=0$ are summarised in table 5.1 to indicate the behaviour of different azimuthal wavenumbers.

Degeneracy	Solution	$m=0$	$m=1$	$m=2$	$m=3$	$m=4$
$\ell=(2,4)$	(A,B)	S if $\mu>0.87$	N	S if $\mu>1.01$	S if $\mu>0.45$	S
$\ell=(4,6)$	(A,B)	S if $\mu>0.42$	N	S if $\mu>0.45$	S if $\mu>0.15$	S if $\mu>0.1$

Table 5.2: Three-dimensional stability at large *Pr* and $\delta=0$ of axisymmetric solutions at even $(\ell,\ell+2)$ degeneracies to azimuthal perturbations of wavenumber m. Higher wavenumbers $m>4$ were found to be stable for the range of Ra considered.

5.1.2 Even-even interactions

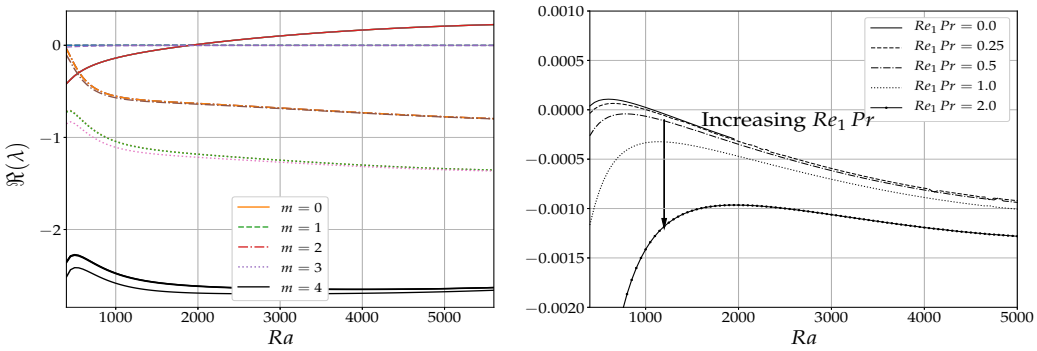
Despite the presence of linearly unstable odd modes near even-even degeneracies, stable even solutions of the full problem may also be found. Near the $\ell=(2,4)$ degeneracy solutions are stable to axisymmetric odd mode perturbations for $\mu>0.87$ and to all non-axisymmetric perturbations for $\mu>1.01$. These thresholds are however larger that those of neighbouring $\ell,\ell\pm1$ degeneracies. Near the $\ell=(4,6)$ degeneracy solutions are found to be stable above a threshold whose unstable wavenumber m varies with δ as shown in figure 3.13. Notably, the threshold for 3D stability at the $\ell=(4,6)$ degeneracy is lower than that of the $\ell=(2,4)$ case. Results for $\delta=0$ are summarised in table 5.2 to indicate the behaviour of different azimuthal wavenumbers.

5.2 Thermal convection with weak differential rotation

In chapter 4 we showed that allowing for differential rotation the convection problem (4.1) admitted two classes of solutions. Equatorially $\mathcal{Z}_2$ symmetric solutions favoured by differential rotation when *Ra* is small, and asymmetric solutions favoured by thermal convection when rotation is small. We now consider the 3D stability of both flows for the separations $d=1,1.5,3$, values where the thermal problem has a preference for solutions with 4,3 and 2 convection cells (cf. figure 3.2).

5.2.1 Symmetric even solutions

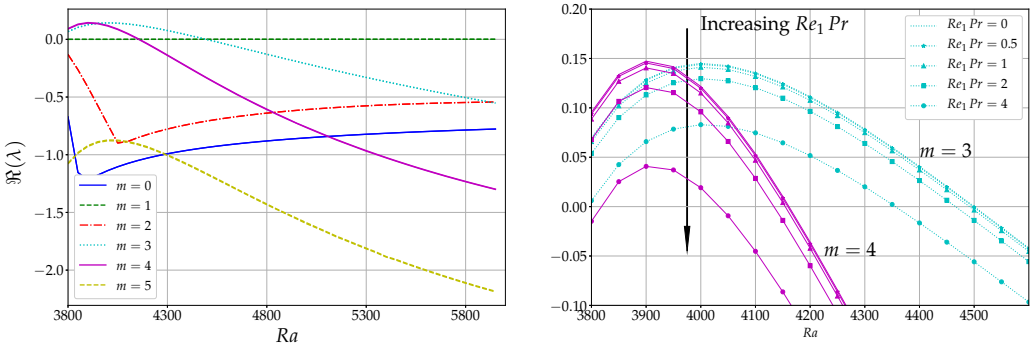
Frame (a) of figure 5.1 shows the stability of the 2-cell solution for wavenumbers $m=0\to4$ as *Ra* is varied, frame (b) the least stable wavenumber $m=1$. Frame (a) shows that for all values of *Ra*, $m=1$ is close to neutral stability, while for $Ra\geq2000$ an axisymmetric mode becomes unstable. Frame (b) shows that while $m=1$ is unstable for small *Ra*, it is stabilised as *Ra* is increased. Also indicated in this frame is the stabilising effect of



(a) Ra vs. $\Re(\lambda)$ for $m = 0 \to 4$ **(b)** Ra vs. $\Re(\lambda)$ for $m = 1$

Figure 5.1: Differential rotation stabilises the axisymmetric solution against 3D ($m = 1$) disturbances. Stability of the axisymmetric 2-cell solution u_r^+ for $d = 3$, shown in terms of the growth rate $\Re(\lambda)$ as Ra is varied. (a) High wavenumbers are strongly damped while $m = 1$ remains close to neutral. For $Ra \geq 2000$ an axisymmetric mode becomes unstable. (b) Increasing $Re_1\,Pr$ the $m = 1$ mode is stabilised.

rotation. Provided $Re_1 Pr \geq 0.5$ the $m = 1$ growth rate remains negative.



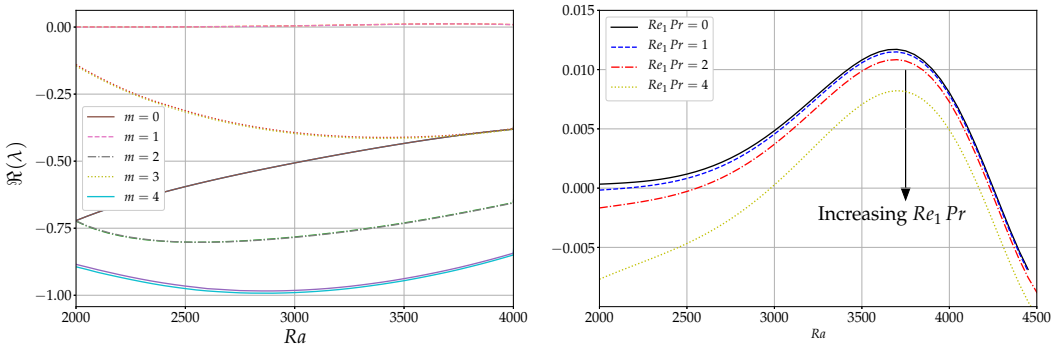
(a) Ra vs. $\Re(\lambda)$ for $m = 1 \to 5$ **(b)** Ra vs. $\Re(\lambda)$ for $m = 3, 4$

Figure 5.2: Differential rotation tends to stabilise the axisymmetric solution against 3D ($m = 3, 4$) disturbances. Stability of the symmetric 4-cell solution for $d = 1$. (a) Wavenumbers $m = 3, 4$ are unstable for small Ra but stabilised as Ra increases, while $m = 1$ remains neutrally stable. (b) Increasing $Re_1 Pr$ shows a tendency for $m = 3, 4$ to be stabilised.

Frame (a) of figure 5.2 shows the stability of the 4-cell solution for wavenumbers $m = 0 \to 5$, indicating that wavenumbers $m = 3, 4$ are unstable for small Ra, but are stabilised for larger Ra. A numerical study of the fully 3D problem by Inagaki *et al.* (2019) also found $m = 3, 4$ to be the least stable wavenumbers for $d = 1, Pr = 1$. For all values of Ra the

$m = 1$ wavenumber remains close to neutral stability. Frame (b) shows that increasing the strength of rotation also reduces the growth rate of these 3D disturbances.

5.2.2 Asymmetric mixed solutions



(a) Ra vs. $\Re(\lambda)$ for $m = 1 \to 4$ **(b)** Ra vs. $\Re(\lambda)$ for $m = 1$

Figure 5.3: Differential rotation tends to stabilise the axisymmetric solution against 3D ($m = 1$) disturbances. Stability of the asymmetric 3-cell solution for $d = 1.5$. (a) As Ra increases $m = 1$ deviates slightly from neutral stability, while all higher wave numbers remain stable. (b) Increasing $Re_1 Pr$ shows a tendency for $m = 1$ to be stabilised.

Frame (a) of figure 5.3 shows that for the 3-cell solution at $d = 1.5$, the $m = 1$ wavenumber is also the least stable. In frame (b) the stabilising effect of rotation on this mode is shown, where $\Re(\lambda)$ is reduces with increasing $Re_1 Pr$. Although this section relies on the validity of our analysis for values of $Re_1 Pr > 1$, the general trend indicates that both symmetric and asymmetric solutions are stabilised by differential rotation.

Without a fully 3D code it is not been possible to determine if a 3D solution becomes axisymmetric as the rotation strength Re_1 is increased. This behaviour has however been indicated by Inagaki *et al.* (2019) for the fixed separation $d = 1$ and $Pr = 1$. Using a 3D code they showed that for small Re_1, the Ra at which the onset convection occurs increases with Re_1, while for large $Re_1 \approxeq 500$ it is reduced. Their (Re_1, Ra) stability diagram also indicates that the axisymmetric 2-cell solution is preferred for a large range of parameter space. In addition to the results of our calculations, we believe that this provides sufficient justification for assuming that the 2-cell solution remains axisymmetric.

Although we have not computed the stability of the 1-cell solutions presented in section 4.4 to non-axisymmetric disturbances. Simple table-top experiments by Nadiga & Aurnou (2008) which demonstrate the baroclinic (density driven) instability of a cold rotating air mass in a warmer fluid, strongly suggest that this solution would become unstable to non-

axisymmetric disturbances for non-zero rotation rates. Following **?** we anticipate that the resulting state would most likely resemble a non-axisymmetric spiral. Nevertheless we believe that the instability mechanisms presented in section 4.4 are of relevance as they highlight the significance of Ekman pumping in the polar region.

6

Conclusion

Motivated by the presence of subsurface oceans in Jupiter's and Saturn's moons, we have studied a model describing thermal convection between differentially rotating spherical shells. Focusing in particular on the bistable behaviour encountered, a combination of analytical and numerical approaches have been used to present an understanding of the different physical mechanisms at play in this model. The hope is that they may help explain bistability observed in systems where transfer of both angular momentum and heat play prominent roles.

To study this model, we adopted the approach of identifying the simplest aspects of the axisymmetric model first, and then to investigate each in isolation. To this end flow driven by differential rotation was first studied (Mannix, Masters thesis). Non-rotating thermal convection was then studied by considering the linear and weakly non-linear problems analytically, and finally the full problem numerically for larger parameter values. Using the insights gained from both problems, we then numerically studied the full problem allowing for rotation of the inner sphere and thermal convection. Choosing this configuration where the outer sphere is held stationary, was justified by its likelihood to become unstable for smaller parameter values, thus facilitating the study of transitions in the system. Finally we studied the stability of the axisymmetric solutions to non-axisymmetric perturbations.

The results of the thermal convection problem highlight the influence of radial gravity and a spherical shell geometry. For narrow shell separations the problem bears strong resemblance to the planar case, while for wider shells radial asymmetry is pronounced. In the amplitude equations derived this asymmetry is highlighted by the presence of resonant

quadratic terms, while in numerical computations by differences in the radial thermal boundary layers for solutions computed at large Pr. At low Pr this asymmetry is found to influence the temporal dynamics, such that the even and odd components of time-dependent solutions oscillate in a 2:1 frequency ratio. At high Pr the stability of steady solutions is influenced by those with the most developed boundary layer structure near the poles. Whether or not bistable solutions with a different number of cells exist, is found to depend largely on the shell separation d and to a lesser extent Ra. Although the axisymmetric solutions are not stable to 3D disturbances at onset, they are found to stabilise for larger Ra.

The results of the differentially rotating problem with thermal convection at large Pr, highlight the significance of strong zonal flows, particularly near the equator and the poles. For flows with an outward jet at the equator, it is found that rotating the inner sphere, strengthens the poloidal flow and in turn the thermal boundary layers which emerge near the sphere's walls and in the plumes. This has the effect of stabilising that state of thermal convection, which most resembles the one preferred by rotation. Conversely for flows with plumes directed outwards along the rotation axis, it is found that an Ekman pumping driven by the differential rotation hinders the development of strong plumes. We find that this has the effect of destabilising the flow, eventually giving rise to a chaotic state localized at the poles.

This is the first theoretical study on a PDE model of thermal convection between differentially rotating spherical shells, which uses 2-parameter numerical continuation to identify all possible 1-parameter bifurcations of a steady axisymmetric flow. This technique is used to understand the flow regimes and transitions present in this system. While bifurcation analysis of this form has been applied more routinely to standard convection problems with a simple base state, its extension to problems where the base states must be determined nonlinearly has been much less explored. Allowing for the continuation of bifurcations, their solutions and eigenvectors, this technique is shown to be a powerful tool for understanding how bistability and hysteresis develops due to parameter changes.

A particularly novel physical feature highlighted in this model is that the bistable behaviour observed cannot be explained by assuming the flow develops to maximise the torque or maximise heat transfer. It does appear however that an understanding of this behaviour can be found by considering two critical regions in the flow: the equator and the poles. It is also of interest that while increasing the rotation strength stabilises the flow, when it does become bistable finite amplitude perturbations can induce a transition from a steady equilibrium to a chaotic state, a feature characteristic of many shear flows.

6.1 Further work

The model we have considered while providing valuable insights, is a vast simplification. In the context of the subsurface oceans of Jupiter's and Saturn's moons, a more complete model would consider: non-axisymmetric affects, rapid co-rotation, allow for time-dependent outer sphere rotation, and ideally target the parameter regimes outlined by Wilson & Kerswell (2018).

An immediate extension of the work presented in this thesis would be to investigate the configuration in which the outer sphere is rotated and the inner is held stationary, allowing for both constant and time-dependent rotation (libration). Such an investigation would help indicate how thermal convection modifies the flow's response to outer sphere libration, and would also facilitate the study of bistability in a system of non-autonomous PDEs (Langa *et al.* 2002). Currently the libration problem is better understood in the isothermal case (Aldridge & Toomre 1969). In a configuration with temperature affects included, we anticipate that *steady* rotation would stabilise the state of thermal convection with plumes directed towards the poles as shown in frame (b) of figure 4.4, and that any instabilities would also be confined to the polar region.

Previous studies of the rapidly co-rotating isothermal system, allowing for differential rotation (Hollerbach 2003, Hoff & Harlander 2019), have emphasised the importance of a free shear layer termed the Stewartson layer. This layer develops for axisymmetric flow at the inner sphere's tangent cylinder. Its stability which depends strongly on the sign of the differential rotation, is found to determine the form of the non-axisymmetric solution and how azimuthal waves precess (Hollerbach 2003, Hoff & Harlander 2019). How thermal convection will alter the formation of this shear layer, or its stability is however unknown.

Wavelength selection in spherical domains is typically studied with homogeneous boundary conditions (Busse 1975, Busse & Riahi 1982, Matthews 2003), but the problem studied in this thesis represents a case with imposed homogeneity. Performing numerical continuation in narrow shells we have found bifurcation diagrams which resemble that of homoclinic snaking Knobloch (2008, 2015), with corresponding solution states that appear to be localized. It would be interesting to investigate if an analogue of homoclinic snaking is possible in spherical domains for this problem and the related problem of double-diffusive convection. To relate any behaviour observed in these coupled PDE models to a simpler model equation such as the Swift-Hohenberg equation would also be of interest.

A

Self adjointness of the operator $\mathcal{L}$

For a vector $\boldsymbol{\phi}$ and operator $\mathcal{L}$ as outlined

$$\boldsymbol{\phi} = \begin{pmatrix} \psi(r,\theta) \\ T(r,\theta) \end{pmatrix}, \quad \mathcal{L} = \begin{pmatrix} D^2 D^2 & Ra_c g(r) \sin\theta \frac{\partial}{\partial \theta} \\ -\frac{T_0'}{r} \frac{1}{\sin\theta} \frac{\partial}{\partial \theta} & \hat{D}^2 \end{pmatrix}, \tag{A.1}$$

an inner product may be found such that

$$\langle \boldsymbol{\phi}^+, \mathcal{L}\boldsymbol{\phi} \rangle = \langle \mathcal{L}\boldsymbol{\phi}^+, \boldsymbol{\phi} \rangle. \tag{A.2}$$

Operators D^2 and $\hat{D}^2$ are defined as

$$D^2 = \frac{\partial^2}{\partial r^2} + \frac{\sin\theta}{r^2} \frac{\partial}{\partial \theta} \left(\frac{1}{\sin\theta} \frac{\partial}{\partial \theta} \right), \quad \hat{D}^2 = \frac{\partial^2}{\partial r^2} + \frac{1}{r^2 \sin\theta} \frac{\partial}{\partial \theta} \left(\sin\theta \frac{\partial}{\partial \theta} \right). \tag{A.3}$$

Assuming homogeneous boundary conditions (4.3) a sufficient condition for this system to be self-adjoint requires that the functional form of the temperature gradient and gravity field $g(r)$ satisfy

$$\frac{d}{dr} \left(\frac{g(r) r}{T_0'} \right) = 0. \tag{A.4}$$

The relevant inner product or volume integral is defined as

$$\left\langle \begin{pmatrix} \frac{A_T\psi^+(r,\theta)}{Ra_c r^2\sin^2\theta} \\ \frac{T^+(r,\theta)}{r^2} \end{pmatrix}, \begin{pmatrix} D^2D^2 & Ra_c g(r)\sin\theta\frac{\partial}{\partial\theta} \\ -\frac{T_0'}{r}\frac{1}{\sin\theta}\frac{\partial}{\partial\theta} & \hat{D}^2 \end{pmatrix} \begin{pmatrix} \psi(r,\theta) \\ T(r,\theta) \end{pmatrix} \right\rangle = \langle \boldsymbol{\phi}^+, \mathcal{L}\boldsymbol{\phi} \rangle, \tag{A.5}$$

where the additional factors included are chosen to satisfy (A.2). Provided $T_0'/r = A_T g(r)$ this can be expanded as a volume integral with $g(r)$ factorised so that one obtains

$$\int_\theta \int_r \left\{ \frac{A_T\psi^+}{Ra_c r^2\sin^2\theta} D^2D^2\psi + \frac{A_T g(r)}{r^2}\big(\psi^+\frac{1}{\sin\theta}\frac{\partial T}{\partial\theta} - T^+\frac{1}{\sin\theta}\frac{\partial\psi}{\partial\theta}\big) + \frac{T^+}{r^2}\hat{D}^2T \right\} r^2\sin\theta dr d\theta \tag{A.6}$$

As the Stokes operator D^2 and the operator $\hat{D}^2$ may be related to the Laplacian (which for homogeneous boundary conditions is self-adjoint) using

$$\frac{1}{r\sin\theta}D^2\psi = \big(\nabla^2 - \frac{1}{r^2\sin^2\theta}\big)\frac{\psi}{r\sin\theta}, \qquad \frac{1}{r}\hat{D}^2T = \nabla^2\frac{T}{r}, \tag{A.7}$$

the first and fourth term of (A.6) automatically satisfy (A.2). Considering the second and third terms, we multiply through by factors $r^2\sin^2\theta$ to yield

$$\int_r \int_\theta A_T g(r)\big(\psi^+\frac{\partial T}{\partial\theta} - T^+\frac{\partial\psi}{\partial\theta}\big) dr d\theta. \tag{A.8}$$

Integrating by parts with respect to θ we obtain

$$\int_r A_T g(r)\left\{ \psi^+T|_{\theta=0,\pi} - \int_\theta T\frac{\partial\psi^+}{\partial\theta}d\theta - T^+\psi|_{\theta=0,\pi} + \int_\theta \frac{\partial T^+}{\partial\theta}\psi d\theta \right\} dr. \tag{A.9}$$

Applying the boundary conditions at $\theta = 0, \pi$ terms outside the integral vanish yielding the desired result. Factorising $r^2\sin\theta$ terms from this expression we may rewrite the expression as

$$\int_r \int_\theta \frac{A_T g(r)}{r^2}\left\{ -\frac{T}{\sin\theta}\frac{\partial\psi^+}{\partial\theta} + \frac{1}{\sin\theta}\frac{\partial T^+}{\partial\theta}\psi \right\} r^2\sin\theta dr d\theta, \tag{A.10}$$

so that these terms also satisfy (A.2).

B

Computation of amplitude equation coefficients

B.1 Simplification of $\mathcal{O}(\epsilon^2)$ terms

The right hand side of the vorticity $D^2\psi$ equation (3.30) is

$$\begin{aligned}\psi_{2f} &= Pr^{-1}\left(\sin\theta\frac{\partial\left(\psi_1, D^2\psi_1/r^2\sin^2\theta\right)}{\partial\left(\theta,r\right)}+\frac{\partial D^2\psi_1}{\partial\tau_1}\right)-\mathrm{Ra}_c\mu g(r)\sin\theta\frac{\partial T_1}{\partial\theta},\\ T_{2f} &= \frac{1}{r\sin\theta}\frac{\partial\left(\psi_1,T_1/r\right)}{\partial(\theta,r)}+\frac{\partial T_1}{\partial\tau_1}.\end{aligned} \tag{B.1}$$

This yields coefficients for the time derivatives $\dot{A}, \dot{B}$ as

$$\begin{aligned}\tilde{a}_0 &= \frac{A_T}{PrRa_c}\left(\int_{r=1}^{1+d_c}\psi_1^\ell(r)D_\ell^2\psi_1^\ell(r)dr\right)\left(\int_{\theta=0}^{\pi}\frac{G_\ell(\theta)G_\ell(\theta)}{\sin\theta}d\theta\right)+\left(\frac{2}{2\ell+1}\right)\left(\int_{r=1}^{1+d_c}T_1^\ell(r)T_1^\ell(r)dr\right),\\ \tilde{b}_0 &= \frac{A_T}{PrRa_c}\left(\int_{r=1}^{1+d_c}\psi_1^m(r)D_m^2\psi_1^m(r)dr\right)\left(\int_{\theta=0}^{\pi}\frac{G_m(\theta)G_m(\theta)}{\sin\theta}d\theta\right)+\left(\frac{2}{2m+1}\right)\left(\int_{r=1}^{1+d_c}T_1^m(r)T_1^m(r)dr\right),\end{aligned} \tag{B.2}$$

where it is apparent that depending on the limit of Pr chosen either temperature or mo-

mentum will dominate. Coefficients of the terms proportional to $\mu A, \mu B$ are independent of Pr and given by

$$\begin{aligned}\tilde{a}_1 &= \frac{A_T}{Ra_c}\left(\int_{r=1}^{1+d_c} \psi_1^\ell(r) D_\ell^2 D_\ell^2 \psi_1^\ell(r) dr\right)\left(\int_{\theta=0}^{\pi} \frac{G_\ell(\theta)G_\ell(\theta)}{\sin\theta} d\theta\right),\\ \tilde{b}_1 &= \frac{A_T}{Ra_c}\left(\int_{r=1}^{1+d_c} \psi_1^m(r) D_m^2 D_m^2 \psi_1^m(r) dr\right)\left(\int_{\theta=0}^{\pi} \frac{G_m(\theta)G_m(\theta)}{\sin\theta} d\theta\right).\end{aligned} \tag{B.3}$$

Finally coefficients proportional to $\delta A, \delta B$ also independent of Pr are given by

$$\begin{aligned}\tilde{a}_2 &= \frac{-A_T}{Ra_c}\left(\int_{\theta=0}^{\pi} \frac{G_\ell(\theta)G_\ell(\theta)}{\sin\theta} d\theta\right)\left(\frac{\partial^2 \psi_1^\ell(r)}{\partial r^2} D_\ell^2 \psi_1^\ell(r)\Big|_{r=1+d_c}\right) + \left(\frac{2}{2\ell+1}\right)\left(\frac{\partial T_1^\ell(r)}{\partial r}\right)^2\Big|_{r=1+d_c},\\ \tilde{b}_2 &= \frac{-A_T}{Ra_c}\left(\int_{\theta=0}^{\pi} \frac{G_m(\theta)G_m(\theta)}{\sin\theta} d\theta\right)\left(\frac{\partial^2 \psi_1^m(r)}{\partial r^2} D_m^2 \psi_1^m(r)\Big|_{r=1+d_c}\right) + \left(\frac{2}{2m+1}\right)\left(\frac{\partial T_1^m(r)}{\partial r}\right)^2\Big|_{r=1+d_c}.\end{aligned} \tag{B.4}$$

We now consider terms proportional to A^2, AB, B^2 outlining both their coefficients and solution. Explicit expressions for ψ_1 are inserted subject to the following index notation

$$\begin{aligned}\psi_1 &= \sum_{k=1}^{N}\sum_{j=1}^{6}\sum_{i=0}^{1} A_{kji} r^{a_{kji}} G_k(\theta)\chi_i, \quad A_{kji}, a_{kji} \in \mathbb{C},\\ D^2\psi_1 &= \sum_{y=1}^{N}\sum_{z=1}^{6}\sum_{x=0}^{1} \mathcal{A}_{yzx} r^{a_{yzx}-2} G_y(\theta)\chi_x, \quad \mathcal{A}_{yzx}, a_{yzx} \in \mathbb{C},\\ \mathcal{A}_{yzx} &= [a_{yzx}(a_{yzx}-1) - y(y+1)]A_{yzx},\end{aligned} \tag{B.5}$$

where each of the above series contains the full solution of ψ_1 and the operator D^2 has been applied to obtain the modified coefficient $\mathcal{A}_{yzx}$. In all cases the summation index N may be taken as

$$N = 2m + 1, \tag{B.6}$$

where m is the larger of the two mode numbers. Mode amplitudes (functions of time) are now contained in the array χ defined as

$$\chi_i = [\mathbf{A}, \mathbf{B}], \tag{B.7}$$

a convention adopted to facilitate ease of manipulation. Collecting terms within the Jaco-

bian, and by the use of large sigma implying the summation over all indicies one obtains

$$\psi_{2f} = \sum r^{-5}\Big\{ -\chi_i\chi_x\Big(k(k+1)A_{kji}r^{a_{kji}}P_k\Big)\Big([a_{yzx}-4]\mathcal{A}_{yzx}r^{a_{yzx}}G_y\Big)+ \\ \chi_x\chi_i\Big([y(y+1)P_y+\frac{2\cos\theta G_y}{\sin^2\theta}]\mathcal{A}_{yzx}r^{a_{yzx}}\Big)\Big(a_{kji}A_{kji}r^{a_{kji}}G_k\Big)\Big\}. \quad \text{(B.8)}$$

Terms from this expression are gathered to isolate radial functions

$$\begin{aligned} F_1(r) &= \sum A_{kji}[a_{yzx}-4]\mathcal{A}_{yzx}r^{a_{kji}+a_{yzx}-5} = \sum A1_{kji,yzx}r^{a1_{kji,yzx}-5}, \\ F_2(r) &= \sum \mathcal{A}_{yzx}a_{kji}A_{kji}r^{a_{yzx}+a_{kji}-5} = \sum A2_{kji,yzx}r^{a2_{kji,yzx}-5}, \end{aligned} \quad \text{(B.9)}$$

and corresponding expressions for polar θ terms are gathered to yield (where $\eta = n-1$, & $\alpha = 1.5$)

$$\begin{aligned} \beta_1^n &= \frac{\eta!(\eta+\alpha)[\Gamma(\alpha)]^2}{\pi 2^{(1-2\alpha)}\Gamma(\eta+2\alpha)}\int_0^\pi \big\{-k(k+1)P_kG_y\big\}\frac{G_n}{\sin\theta}d\theta, \\ \beta_2^n &= \frac{\eta!(\eta+\alpha)[\Gamma(\alpha)]^2}{\pi 2^{(1-2\alpha)}\Gamma(\eta+2\alpha)}\int_0^\pi \big\{[y(y+1)P_y+\frac{2\cos\theta G_y}{\sin^2\theta}]G_k\big\}\frac{G_n}{\sin\theta}d\theta. \end{aligned} \quad \text{(B.10)}$$

Integration of polar terms is preformed symbolically, but does suffer from diminishing accuracy as $\ell \gg 1$ due to the increased number of coefficients. Combining these terms one obtains

$$J() = \sum \chi_i\chi_x\big\{[\beta_1^nA1_{kji,yzx}r^{a1_{kji,yzx}}]+[\beta_2^nA2_{kji,yzx}r^{a2_{kji,yzx}}]\big\}r^{-5}, G_n(\theta) \quad \text{(B.11)}$$

where simplification in terms amplitudes $\mathbf{A}^2, \mathbf{AB}, \mathbf{B}^2$ are then obtained by evaluating products of the following vectors $\chi_i\chi_x$

$$\mathbf{A}^2 = \chi_i[0]\chi_x[0],\ \mathbf{AB} = \chi_i[0]\chi_x[1]+\chi_i[1]\chi_x[0],\ \mathbf{B}^2 = \chi_i[1]\chi_x[1]. \quad \text{(B.12)}$$

Final simplifications permits expression

$$\psi_{2f} = \sum_{k=1}^{N}\sum_{j=1}^{36}\sum_{i=1}^{3}\chi_iH_{kji}r^{a_{kji}-5}G_k(\theta). \quad \text{(B.13)}$$

The nonlinear component of the right hand side of the temperature T equation (3.30) is

$$\frac{1}{r\sin\theta}\frac{\partial\big(\psi_1, T_1/r\big)}{\partial(\theta, r\big)}. \tag{B.14}$$

Inserting the explicit expressions for ψ_1, T_1, subject to the following index notation

$$\begin{aligned}
\psi_1 &= \sum_{k=1}^{N}\sum_{j=1}^{6}\sum_{i=0}^{1} A_{kji} r^{a_{kji}} G_k(\theta)\chi_i, \quad A_{kji}, a_{kji} \in \mathbb{C}, \\
T_1/r &= \sum_{y=1}^{N}\sum_{z=1}^{6}\sum_{x=0}^{1} B_{yzx} r^{a_{yzx}-2} P_y(\cos\theta)\chi_x, \quad B_{yzx}, a_{yzx} \in \mathbb{C}, \\
B_{yzx} &= \frac{1}{Ra_c}[a_{yzx}(a_{yzx}-1) - y(y+1)][(a_{yzx}-2)(a_{yzx}-3) - y(y+1)]A_{yzx},
\end{aligned} \tag{B.15}$$

where each of the above series contains products of the linear solution of ψ_1 and T_1/r. Note in this expression a $(-)$ has been absorbed in B_{yzx}. Collecting terms after expansion one obtains

$$\begin{aligned}
T_{2f} = \sum_{k,j,i,y,z,x} r^{-4}\Bigg\{ &\Big(k(k+1)A_{kji} r^{a_{kji}} P_k\chi_i\Big)\Big([a_{yzx}-2]B_{yzx} r^{a_{yzx}} P_y\chi_x\Big), \\
&+ \Big(\frac{G_y}{\sin^2\theta} B_{yzx} r^{a_{yzx}}\chi_x\Big)\Big(a_{kji}A_{kji} r^{a_{kji}} G_k\chi_i\Big)\Bigg\},
\end{aligned} \tag{B.16}$$

where terms from this expression are gathered to isolate radial functions

$$\begin{aligned}
G_1(r) &= \sum A_{kji}[a_{yzx}-2]B_{yzx} r^{a_{kji}+a_{yzx}-4} = \sum B1_{kji,yzx} r^{a1_{kji,yzx}-4}, \\
G_2(r) &= \sum B_{yzx}a_{kji}A_{kji} r^{a_{yzx}+a_{kji}-4} = \sum B2_{kji,yzx} r^{b2_{kji,yzx}-4},
\end{aligned} \tag{B.17}$$

and corresponding expression for polar θ terms are gathered to yield (where $\eta = n - 1$, & $\alpha = 1.5$)

$$\begin{aligned}
\alpha_1^n &= \frac{2n+1}{2}\int_0^\pi \big\{k(k+1)P_kP_y\big\}P_n\sin\theta d\theta, \\
\alpha_2^n &= \frac{2n+1}{2}\int_0^\pi \big\{\frac{G_yG_k}{\sin^2\theta}\big\}P_n\sin\theta d\theta.
\end{aligned} \tag{B.18}$$

The jacobian term may then be concisely expressed in terms of the following series

$$J() = \sum_{k,j,i,y,z,x} \chi_i \chi_x \left[\alpha_1^n B1_{kji,yzx} r^{a1_{kji,yzx}} + \alpha_2^n B2_{kji,yzx} r^{a2_{kji,yzx}}\right] r^{-4} P_n(\cos\theta). \quad \text{(B.19)}$$

Combining these terms we may express the solution

$$T_{2f} = \sum_{k}^{2m+1} \sum_{j=1}^{36} \sum_{i=1}^{3} \chi_i F_{kji} r^{a_{kji}-4} P_k(\cos\theta). \quad \text{(B.20)}$$

Using these simplified expressions for T_{2f} and ψ_{2f} one can write the quadratic coefficients proportional to A as

$$\begin{aligned}
\tilde{\alpha}_1 &= \frac{A_T}{PrRa_c}\Big(\int_{r=1}^{1+d_c} \psi_1^\ell(r) \sum_{i=1}^{36} H_{\ell j0} r^{a_{\ell j0}-5} dr\Big)\gamma_\ell + \Big(\frac{2}{2\ell+1}\Big)\Big(\int_{r=1}^{1+d_c} T_1^\ell(r) \sum_{i=1}^{36} F_{\ell j0} r^{a_{\ell j0}-4} dr\Big), \\
\tilde{\alpha}_2 &= \frac{A_T}{PrRa_c}\Big(\int_{r=1}^{1+d_c} \psi_1^\ell(r) \sum_{i=1}^{36} H_{\ell j1} r^{a_{\ell j1}-5} dr\Big)\gamma_\ell + \Big(\frac{2}{2\ell+1}\Big)\Big(\int_{r=1}^{1+d_c} T_1^\ell(r) \sum_{i=1}^{36} F_{\ell j1} r^{a_{\ell j1}-4} dr\Big), \\
\tilde{\alpha}_3 &= \frac{A_T}{PrRa_c}\Big(\int_{r=1}^{1+d_c} \psi_1^\ell(r) \sum_{i=1}^{36} H_{\ell j2} r^{a_{\ell j2}-5} dr\Big)\gamma_\ell + \Big(\frac{2}{2\ell+1}\Big)\Big(\int_{r=1}^{1+d_c} T_1^\ell(r) \sum_{i=1}^{36} F_{\ell j2} r^{a_{\ell j2}-4} dr\Big),
\end{aligned} \quad \text{(B.21)}$$

and similarly the coefficients for B may be wrote as

$$\begin{aligned}
\tilde{\beta}_1 &= \frac{A_T}{PrRa_c}\Big(\int_{r=1}^{1+d_c} \psi_1^m(r) \sum_{i=1}^{36} H_{mj0} r^{a_{mj0}-5} dr\Big)\gamma_m + \Big(\frac{2}{2m+1}\Big)\Big(\int_{r=1}^{1+d_c} T_1^m(r) \sum_{i=1}^{36} F_{mj0} r^{a_{mj0}-4} dr\Big), \\
\tilde{\beta}_2 &= \frac{A_T}{PrRa_c}\Big(\int_{r=1}^{1+d_c} \psi_1^m(r) \sum_{i=1}^{36} H_{mj1} r^{a_{mj1}-5} dr\Big)\gamma_m + \Big(\frac{2}{2m+1}\Big)\Big(\int_{r=1}^{1+d_c} T_1^m(r) \sum_{i=1}^{36} F_{mj1} r^{a_{mj1}-4} dr\Big), \\
\tilde{\beta}_3 &= \frac{A_T}{PrRa_c}\Big(\int_{r=1}^{1+d_c} \psi_1^m(r) \sum_{i=1}^{36} H_{mj2} r^{a_{mj2}-5} dr\Big)\gamma_m + \Big(\frac{2}{2m+1}\Big)\Big(\int_{r=1}^{1+d_c} T_1^m(r) \sum_{i=1}^{36} F_{mj2} r^{a_{mj2}-4} dr\Big),
\end{aligned} \quad \text{(B.22)}$$

where the polar integrals denoted by

$$\gamma_\ell = \Big(\int_{\theta=0}^{\pi} \frac{G_\ell(\theta) G_\ell(\theta)}{\sin\theta} d\theta\Big), \qquad \gamma_m = \Big(\int_{\theta=0}^{\pi} \frac{G_m(\theta) G_m(\theta)}{\sin\theta} d\theta\Big). \quad \text{(B.23)}$$

With the right hand side terms evaluated concisely, the particular (*inhomogeneous*) solu-

tions for $\psi_2(r,\theta), T_2(r,\theta)$ proportional to A^2, AB, B^2 are obtained as

$$\begin{aligned}\psi_2(r,\theta,t) &= \sum_{k=1}^{N}\sum_{j=1}^{36}\sum_{i=2}^{4}\chi_i A_{kji} r^{a_{kji}-1} G_k(\theta), \quad A_{kji}, a_{kji} \in \mathbb{C},\\ T_2(r,\theta,t) &= \sum_{k=0}^{N}\sum_{j=1}^{36}\sum_{i=2}^{4}\chi_i B_{kji} r^{a_{kji}-2} P_k(\cos\theta), \quad B_{kji}, a_{kji} \in \mathbb{C},\end{aligned} \tag{B.24}$$

where coefficients A_{kji} & B_{kji} are obtained by solving the system

$$\sum_{k=0}^{N}\sum_{j=1}^{36}\sum_{i=0}^{3}\begin{pmatrix} a_{kji}^{00} & Ra_c \\ A_T[k(k+1)] & a_{kji}^{11}\end{pmatrix}\begin{pmatrix} A_{kji} \\ B_{kji}\end{pmatrix} = \begin{pmatrix} Pr^{-1}E_{kji} \\ F_{kji}\end{pmatrix}, \tag{B.25}$$

where

$$\begin{aligned}a_{kji}^{00} &= [(a_{kji}-3)(a_{kji}-4) - k(k+1)][(a_{kji}-1)(a_{kji}-2) - k(k+1)],\\ a_{kji}^{11} &= [(a_{kji}-2)(a_{kji}-3) - k(k+1)],\end{aligned} \tag{B.26}$$

and $A_T = -(1+d)/d$ or $\frac{r_{in}r_{out}}{r_{in}-r_{out}}$ is a constant pertaining to the temperature gradient. Noteworthy is that series coefficients now depend on Pr. Similarly for the terms proportional to $\dot{A}, \dot{B}$ particular (*inhomogeneous*) solutions for $\psi_2(r,\theta), T_2(r,\theta)$ are obtained as

$$\begin{aligned}\psi_2(r,\theta,t) &= \sum_{k=\ell,m}\sum_{j=1}^{6}\sum_{i=0}^{1}\chi_i A_{kji} r^{a_{kji}+2} G_k(\theta), \quad A_{kji}, a_{kji} \in \mathbb{C},\\ T_2(r,\theta,t) &= \sum_{k=\ell,m}\sum_{j=1}^{36}\sum_{i=0}^{1}\chi_i B_{kji} r^{a_{kji}+1} P_k(\cos\theta), \quad B_{kji}, a_{kji} \in \mathbb{C},\end{aligned} \tag{B.27}$$

where coefficients A_{kji} & B_{kji} are obtained by solving the system

$$\sum_{k=0}^{N}\sum_{j=1}^{36}\sum_{i=0}^{3}\begin{pmatrix} a_{kji}^{00} & Ra_c \\ A_T[k(k+1)] & a_{kji}^{11}\end{pmatrix}\begin{pmatrix} A_{kji} \\ B_{kji}\end{pmatrix} = \begin{pmatrix} Pr^{-1}E_{kji} \\ F_{kji}\end{pmatrix}, \tag{B.28}$$

where

$$\begin{aligned}a_{kji}^{00} &= [(a_{kji}+2)(a_{kji}+1) - k(k+1)][a_{kji}(a_{kji}-1) - k(k+1)],\\ a_{kji}^{11} &= [(a_{kji}+1)a_{kji} - k(k+1)].\end{aligned} \tag{B.29}$$

Finally a homogeneous solution must be added to satisfy the associated boundary conditions. This is achieved by adding functions of the form

$$\begin{aligned}
\psi(r,\theta,t) &= \sum_{k=1}^{N}\sum_{j=1}^{6}\sum_{i=0}^{3}\chi_i A^h_{kji} r^{a^h_{kji}} G_k(\theta),\\
T(r,\theta,t) &= \sum_{k=0}^{N}\sum_{j=1}^{6}\sum_{i=0}^{3}\alpha_{kji} A^h_{kji} r^{a^h_{kji}-1} P_k(\cos\theta),\\
\alpha_{kji} &= -\frac{1}{Ra_c}[(a_{kji}-3)(a_{kji}-4)-k(k+1)][(a_{kji}-1)(a_{kji}-2)-k(k+1)].
\end{aligned} \tag{B.30}$$

Applying the 6 boundary condutions for each polynomial mode k and amplitude of the vector χ_i results in the following system $A\boldsymbol{x} = B\boldsymbol{\chi} = \boldsymbol{b}$ for terms A^h_{jkm}, B^h_{jkm}, the superscripts h, ih being used to indicate homogeneous and inhomogeneous respectively

$$\sum_{k=1}^{2m+1}\sum_{i=0}^{3}\Big(\ldots\ldots\Big)\begin{pmatrix} A^h_{k1i}\\ A^h_{k2i}\\ A^h_{k3i}\\ A^h_{k4i}\\ A^h_{k5i}\\ A^h_{k6i}\end{pmatrix} = \sum_{j=1}^{36}\begin{pmatrix} -\psi_2^{ih}|_{r=1}\\ -\psi_2^{ih}|_{r=1+d}\\ -\partial_r\psi_2^{ih}|_{r=1}\\ -\partial_r\psi_2^{ih}|_{r=1+d}\\ -T_2^{ih}|_{r=1}\\ -T_2^{ih}|_{r=1+d}\end{pmatrix}. \tag{B.31}$$

While this system may be solved easily for $k \neq \ell, m$, for $k = \ell, m$ the matrix A is singular and $\boldsymbol{b}$ is not orthogonal to the null space $A\boldsymbol{x}_0 = 0$. A solvability condition must be applied to remove resonant terms present which cannot be solved for. We first calculate the null space $\boldsymbol{x}_0$ and adjoint null space $\boldsymbol{y}_0$ by solving

$$A\boldsymbol{x}_0 = 0, \quad A^\dagger \boldsymbol{y}_0 = 0, \quad \text{where} \quad \langle \bar{\boldsymbol{y}}_0^T, \boldsymbol{x}_0\rangle = \sum_{i=0}^{n} \bar{y}_0^i x_0^i = 1, \quad \text{where} \quad y_0^i, x_0^i \in \mathbb{C} \tag{B.32}$$

where $A^\dagger$ represents the conjugate transpose or hermitian of the matrix A. The solvability condition is then applied to remove the resonant component of $\boldsymbol{b}$ by subtraction

$$\boldsymbol{b} = \boldsymbol{b} - \langle \bar{\boldsymbol{y}}_0^T, \boldsymbol{b}\rangle \boldsymbol{x}_0. \tag{B.33}$$

As the matrix A is singular, the solution space must be restricted to $\mathbb{C}^n \setminus \{\boldsymbol{x}_0\}$. To do so we solve the *bordered system* which is invertible

$$\begin{pmatrix} A & \boldsymbol{x}_0\\ \bar{\boldsymbol{y}}_0^T & 0\end{pmatrix}\begin{pmatrix}\boldsymbol{x}\\ \mu\end{pmatrix} = \begin{pmatrix}\boldsymbol{b}\\ 0\end{pmatrix}, \quad \text{where} \quad \mu \in \mathbb{R}. \tag{B.34}$$

Solving by this method however demands that the solvability condition is later substituted, as this step has altered the form of $\boldsymbol{b}$ for the purpose of applying boundary conditions only. The case $k = 0$ represents a special case and requires different treatment. By virtue of $G_0(\cos\theta) = 0$, ψ must everywhere be zero and only the homogeneous temperature boundary conditions must be satisfied using

$$T(r,t)_{k=0} = c_0 + c_1 r + T^{ih}(r,\theta,t)|_{r=1,1+d} = 0. \tag{B.35}$$

A general solution for ψ_2, T_2 are thus obtained as

$$\begin{aligned}
\psi_2(r,\theta,t) &= \sum_{i=0}^{4} \chi_i \sum_{k=1}^{N} \left\{ \sum_{j=1}^{6} A_{kji}^{h} r^{a_{kji}^{h}+1} + \sum_{j=1}^{36} A_{kji}^{ih} r^{a_{kji}^{ih}} \right\} r^{-1} G_k(\theta), \quad A_{kji}, a_{kji} \in \mathbb{C}, \\
T_2(r,\theta,t) &= \sum_{i=0}^{4} \chi_i \sum_{k=1}^{N} \left\{ \sum_{j=1}^{6} \alpha_{kji} A_{kji}^{h} r^{a_{kji}^{h}+1} + \sum_{j=1}^{36} B_{kji}^{ih} r^{a_{kji}^{ih}} \right\} r^{-2} P_k(\cos\theta), \quad B_{kji} \in \mathbb{C},
\end{aligned} \tag{B.36}$$

where the vector $\chi_i \in \mathbb{R}$ contains the mode amplitudes

$$\chi_i = [\dot{\boldsymbol{A}}, \dot{\boldsymbol{B}}, \boldsymbol{A}^2, \boldsymbol{AB}, \boldsymbol{B}^2]. \tag{B.37}$$

Additional amplitudes $\boldsymbol{C}, \boldsymbol{D}$ corresponding to aribitrary multiples of ϕ_1 can also be included in this solution. It may be shown however that their contribution integrates to zero.

B.2 Simplification of $\mathcal{O}(\epsilon^3)$ terms

The right hand of the vorticity equation termed ψ_{3f} may be expressed as

$$\psi_{3f} = -\mu \,\mathrm{Ra_c}\, g(r)\frac{\partial T_1}{\partial \theta}\sin\theta + Pr^{-1}\bigg(\sin\theta\frac{\partial\big(\psi_1+\psi_2, \frac{D^2(\psi_1+\psi_2)}{r^2\sin^2\theta}\big)}{\partial(\theta,r)} + \frac{\partial D^2\psi_1}{\partial\tau_2} + \frac{\partial D^2\psi_2}{\partial\tau_1}\bigg), \tag{B.38}$$

where it may be noted that the jacobian involving $\psi_1+\psi_2$ contains additional terms not of $\mathcal{O}(\epsilon^3)$, this expression is however chosen for brevity. Explicit expressions for ψ_1, ψ_2 & T_1 are inserted subject to the following index convention

$$\begin{aligned}
\psi_1+\psi_2 &= \sum_{k=1}^{N}\sum_{j=1}^{48}\sum_{i=0}^{6} A_{kji} r^{a_{kji}-1} G_k(\theta)\chi_i, \quad A_{kji}, a_{kji} \in \mathbb{C}, \\
D^2(\psi_1+\psi_2) &= \sum_{y=1}^{N}\sum_{z=1}^{48}\sum_{x=0}^{6} \mathcal{A}_{yzx} r^{a_{yzx}-3} G_y(\theta)\chi_x, \quad \mathcal{A}_{yzx}, a_{yzx} \in \mathbb{C}, \\
\mathcal{A}_{yzx} &= [(a_{yzx}-1)(a_{yzx}-2) - y(y+1)]A_{yzx}, \qquad T_1 = \sum_i A_i r^{z_i},
\end{aligned} \tag{B.39}$$

where each of the above series contains the full solution of $\psi_1+\psi_2$, summed for all amplitudes and modes $N = 2m+1$, where m is the larger of the two modes . In addition the operator D^2 has also been applied resulting in the modified coefficient $\mathcal{A}$. Amplitude coefficients are now contained in the array χ, which contains terms at both orders $\mathcal{O}(\epsilon)$ and (ϵ^2)

$$\chi_i = [\boldsymbol{A}, \boldsymbol{B}, \dot{\boldsymbol{A}}, \dot{\boldsymbol{B}}, \boldsymbol{A}^2, \boldsymbol{AB}, \boldsymbol{B}^2], \tag{B.40}$$

and the structure of each of the above solution arrays is as follows

$$\sum_{y=1}^{N}\sum_{j=1}^{48}\sum_{i=0}^{6} A_{kji} r^{a_{kji}-1} = r^{-1}\big(\underbrace{A_{1\to6} r^{a_{1\to6}+1}}_{\text{linear solution } \psi_1} + \underbrace{A^h_{7\to12} r^{a^h_{7\to12}+1}}_{\text{homogeneous solution } \psi_2} + \underbrace{A^{ih}_{13\to48} r^{a^{ih}_{13\to48}}}_{\text{inhomogeneous solution } \psi_2}\big), \tag{B.41}$$

This convention is used as it combines expressions into a single array facilitating ease of manipulation. Collecting terms only of order $\mathcal{O}(\epsilon^3)$ one obtains

$$\psi_{3f} = -\mu\mathbf{Ra}_c r^{-3}\big\{\mathbf{A}f_\ell(r)G_\ell(\theta) + \mathbf{B}f_m(r)G_m(\theta)\big\} + Pr^{-1}\bigg(\big\{\dot{\boldsymbol{A}}(\tau_2)G_\ell D^2F_\ell + \dot{\boldsymbol{B}}(\tau_2)G_m D^2F_m\big\} + J_\psi()\bigg), \tag{B.42}$$

the dependence on τ_2 exclusively arising from the coefficinets proportional to τ_1 all being

zero. where the Jacobian term expressed explicity is (*summations are omitted for brevity*):

$$J_\psi() = \sum_{k,j,i,y,z,x} r^{-7}\Big\{ -\chi_i\chi_x\Big(k(k+1)A_{kji}r^{a_{kji}}P_k\Big)\Big([a_{yzx}-5]\mathcal{A}_{yzx}r^{a_{yzx}}G_y\Big)+ \\ \chi_x\chi_i\Big([y(y+1)P_y+\frac{2\cos\theta G_y}{\sin^2\theta}]\mathcal{A}_{yzx}r^{a_{yzx}}\Big)\Big([a_{kji}-1]A_{kji}r^{a_{kji}}G_k\Big)\Big\}, \quad \text{(B.43)}$$

terms are gathered to obtain radial functions

$$\begin{aligned} F_1(r) &= \sum A_{kji}[a_{yzx}-5]\mathcal{A}_{yzx}r^{a_{kji}+a_{yzx}-7} = \sum A1_{kji,yzx}r^{a1_{kji,yzx}}, \\ F_2(r) &= \sum \mathcal{A}_{yzx}[a_{kji}-1]A_{kji}r^{a_{yzx}+a_{kji}-7} = \sum A2_{kji,yzx}r^{a2_{kji,yzx}}, \end{aligned} \quad \text{(B.44)}$$

corresponding expressions for polar θ terms are gathered to yield (where $\eta = n-1,\ \&\ \alpha = 1.5$)

$$\begin{aligned} \beta_1^n &= \frac{\eta!(\eta+\alpha)[\Gamma(\alpha)]^2}{\pi 2^{(1-2\alpha)}\Gamma(\eta+2\alpha)}\int_0^\pi \big\{-k(k+1)P_kG_y\big\}\frac{G_n}{\sin\theta}d\theta, \\ \beta_2^n &= \frac{\eta!(\eta+\alpha)[\Gamma(\alpha)]^2}{\pi 2^{(1-2\alpha)}\Gamma(\eta+2\alpha)}\int_0^\pi \big\{[y(y+1)P_y+\frac{2\cos\theta G_y}{\sin^2\theta}]G_k\big\}\frac{G_n}{\sin\theta}d\theta, \end{aligned} \quad \text{(B.45)}$$

when integrated symbolically the process may be accelerated by noting that when $(k+y)\%2 = 0$ and $n\%2! = 0$ the coefficent is apriori known to be zero. Combining these terms one obtains

$$J_\psi() = \sum_{k,j,i,y,z,x} \chi_i\chi_x\Big\{\beta_1^n A1_{kji,yzx}r^{a1_{kji,yzx}} + \beta_2^n A2_{kji,yzx}r^{a2_{kji,yzx}}\Big\}G_n(\theta), \quad \text{(B.46)}$$

where simplification in terms amplitudes $\mathbf{AB}^2, \mathbf{A}^2\mathbf{B}, \mathbf{A}^3, \mathbf{B}^3$ are then obtained by evaluating products of the following vectors $\chi_i\chi_x$.

$$\begin{aligned} \boldsymbol{A}\dot{\boldsymbol{A}} &= \chi_i[0]\chi_x[2] + \chi_i[2]\chi_x[0]\big(\dots\big) \\ \boldsymbol{B}\dot{\boldsymbol{A}} &= \chi_i[1]\chi_x[2] + \chi_i[2]\chi_x[1]\big(\dots\big) \\ \boldsymbol{A}\dot{\boldsymbol{B}} &= \chi_i[0]\chi_x[3] + \chi_i[3]\chi_x[0]\big(\dots\big) \\ \boldsymbol{B}\dot{\boldsymbol{B}} &= \chi_i[1]\chi_x[3] + \chi_i[3]\chi_x[1]\big(\dots\big) \\ \mathbf{A}^2\mathbf{B} &= \chi_i[4]\chi_x[1] + \chi_i[1]\chi_x[4] + \chi_i[0]\chi_x[5] + \chi_i[5]\chi_x[0]\big(\dots\big) \\ \mathbf{AB}^2 &= \chi_i[6]\chi_x[0] + \chi_i[0]\chi_x[6] + \chi_i[1]\chi_x[5] + \chi_i[5]\chi_x[1]\big(\dots\big) \\ \mathbf{A}^3 &= \chi_i[0]\chi_x[4] + \chi_i[4]\chi_x[0]\big(\dots\big), \qquad \mathbf{B}^3 = \chi_i[1]\chi_x[6] + \chi_i[6]\chi_x[1]\big(\dots\big) \end{aligned} \quad \text{(B.47)}$$

The right hand side of the temperature equation termed T_{3f} is

$$T_{3f} = \frac{1}{r\sin\theta}\frac{\partial(\psi_1+\psi_2,(T_1+T_2)r^{-1})}{\partial(\theta,r)} + \frac{\partial T_1}{\partial\tau_2} + \frac{\partial T_2}{\partial\tau_1}, \tag{B.48}$$

where as previously outlined additional terms, not $\mathcal{O}(\epsilon^3)$ are also present, but the expression is chosen for brevity of expression. Inserting ψ_1, ψ_2 & T_1, T_2 subject to the following index convention

$$\begin{aligned}\psi_1+\psi_2 &= \sum_{k=1}^{N}\sum_{j=1}^{48}\sum_{i=0}^{6} A_{kji} r^{a_{kji}-1} G_k(\theta)\chi_i, \quad A_{kji}, a_{kji} \in \mathbb{C},\\ (T_1+T_2)r^{-1} &= \sum_{y=1}^{N}\sum_{z=1}^{48}\sum_{x=0}^{6} B_{yzx} r^{a_{yzx}-3} P_y(\cos\theta)\chi_x, \quad B_{yzx}, a_{yzx} \in \mathbb{C},\end{aligned} \tag{B.49}$$

and the structure of each of the temperature solution is as follows

$$\sum_{k=0}^{N}\sum_{j=1}^{48}\sum_{i=0}^{5} B_{kji} r^{a_{kji}-3} = r^{-3}\big(\underbrace{B_{1\to 6} r^{a_{1\to 6}+1}}_{\text{linear solution } T_1} + \underbrace{B^h_{7\to 12} r^{a^h_{7\to 12}+1}}_{\text{homogeneous solution } T_2} + \underbrace{B^{ih}_{13\to 48} r^{a^{ih}_{13\to 48}}}_{\text{inhomogeneous solution } T_2}\big), \tag{B.50}$$

explicit expressions for ψ_1, T_1, ψ_2, T_2 are substituted and after simplification we obtain

$$T_{3f} = \dot{\boldsymbol{A}}(\tau_2) f_\ell(r) P_\ell(\cos\theta) + \dot{\boldsymbol{B}}(\tau_2) f_m(r) P_m(\cos\theta) + J(\ldots), \tag{B.51}$$

where the jacobian term expanded is

$$\begin{aligned}J_T() = \sum_{k,j,i,y,z,x} \Big\{ &\Big(-k(k+1) A_{kji} r^{a_{kji}-2} P_k \chi_i \Big)\Big([a_{yzx}-3] B_{yzx} r^{a_{yzx}-4} P_y \chi_x \Big)\\ &- \Big(\frac{G_y}{\sin^2\theta} B_{yzx} r^{a_{yzx}-4} \chi_x \Big)\Big([a_{kji}-1] A_{kji} r^{a_{kji}-2} G_k \chi_i \Big)\Big\}.\end{aligned} \tag{B.52}$$

Expressing in terms of radial and polar functions

$$\begin{aligned}G_1(r) &= \sum A_{kji}[a_{yzx}-3] B_{yzx} r^{a_{kji}+a_{yzx}-6} = \sum B1_{kji,yzx} r^{a1_{kji,yzx}},\\ G_2(r) &= \sum B_{yzx}[a_{kji}-1] A_{kji} r^{a_{yzx}+a_{kji}-6} = \sum B2_{kji,yzx} r^{b2_{kji,yzx}},\end{aligned} \tag{B.53}$$

with inner products for the polar terms are defined

$$\begin{aligned}\alpha_1^n &= \frac{2n+1}{2}\int_0^\pi \big\{ -k(k+1)P_kP_y\big\}P_n\sin\theta d\theta,\\ \alpha_2^n &= \frac{2n+1}{2}\int_0^\pi \big\{\frac{-G_yG_k}{\sin^2\theta}\big\}P_n\sin\theta d\theta,\end{aligned} \tag{B.54}$$

where it must be noted that the $len(\alpha_1^n) > len(\alpha_2^n)$ due to the presence of $T \sim f(r)P_0(\cos\theta)$ being admissable, such that associated terms as for example

$$\frac{1}{r\sin\theta}\frac{\partial\psi}{\partial\theta}\frac{\partial T/r}{\partial r}, \tag{B.55}$$

are non-zero. The jacobian term may then be concisely expressed in terms of the following series

$$J_T() = \sum_{k,j,i,y,z,x}\chi_i\chi_x\Big\{\alpha_1^n B1_{kji,yzx}r^{a1_{kji,yzx}} + \alpha_2^n B2_{kji,yzx}r^{a2_{kji,yzx}}\Big\}P_n(\cos\theta), \tag{B.56}$$

collecting terms corresponding to all amplitudes one may write the vector $\mathcal{F}_3 = [\psi_{3f}, T_{3f}]^T$ as

$$\begin{aligned}\psi_{3f} &= -\mu\mathbf{Ra}_c r^{-3}\big\{\mathbf{A}G_\ell H_\ell + \mathbf{B}G_mH_m\big\} + Pr^{-1}\Big(\big\{\dot{\mathbf{A}}D^2F_\ell G_\ell + \dot{\mathbf{B}}D^2F_mG_m\big\} + J_\psi(\ldots)\Big),\\ T_{3f} &= \dot{\mathbf{A}}P_\ell H_\ell + \dot{\mathbf{B}}P_mH_m + J_T(\ldots),\end{aligned} \tag{B.57}$$

to account for the variation at the outer boundary however an additional term must be added to each equation. The modified boundary conditions at $\mathcal{O}(\epsilon^3)$ are

$$\begin{aligned}&b.c's \quad \psi_3(r,\theta,t) = 0,\ \psi_3'(r,\theta,t) = 0,\ T_3(r,\theta,t) = 0 \quad \text{at} \quad r = 1,\\ &b.c's \quad \psi_3(r,\theta,t) + \delta\psi_1'(r,\theta,t) = 0,\ \psi_3'(r,\theta,t) + \delta\psi_1''(r,\theta,t) = 0,\ \delta T_1'(r,\theta,t) + T_3(r,\theta,t) = 0 \quad \text{at} \quad r = 1+d,\end{aligned} \tag{B.58}$$

where it may be noted that ψ_1, T_1 are proportional to amplitudes $\boldsymbol{A}(\tau_2)$ & $\boldsymbol{B}(\tau_2)$ only, and the inhomogeneos diffusion problem to be solved is

$$\mathcal{L}\phi_3 = -\delta\mathcal{L}\phi_1 + \mathcal{F}_3. \tag{B.59}$$

C

Axisymmetric finite-difference code

In this formulation we express the full equations as

$$Pr^{-1}\left(\frac{\partial \xi}{\partial t} - \mathcal{J}(\psi,\xi) - N_1(\Omega,\Omega)\right) = -\mathrm{Ra}\, g(r) r \frac{\partial T}{\partial \theta}\sin\theta + D^2\xi, \tag{C.1a}$$

$$\frac{\partial T}{\partial t} + J(\psi,T) = \nabla^2 T, \tag{C.1b}$$

$$\frac{\partial \Omega}{\partial t} + J(\psi,\Omega) = PrD^2\Omega, \tag{C.1c}$$

$$\xi = -D^2\psi, \tag{C.1d}$$

where

$$J(f,g) = \frac{1}{r^2\sin\theta}\frac{\partial(f,g)}{\partial(\theta,r)}, \quad \mathcal{J}(f,g) = \sin\theta\frac{\partial(f,g/(r^2\sin^2\theta))}{\partial(\theta,r)}, \tag{C.2}$$

and

$$N_1(f,g) = \frac{2f}{r^2\sin\theta}\big(\cot\theta\frac{\partial g}{\partial r} - \frac{1}{r}\frac{\partial g}{\partial \theta}\big). \tag{C.3}$$

Defining the indices i, j to be the location of the $i^{th} \in [0, N_r]$ radial and $j^{th} \in [0, N_\theta]$ polar grid-point, we use second order finite differences in both spatial directions. The time discretisation uses Crank-Nicoloson and forward Euler schemes for the linear and nonlinear terms respectively. Denoting the value at the current time-step by superscript

ξ^n and at the next step by ξ^{n+1}, all interior grid points are updated according to

$$Pr^{-1}\left(\frac{\xi_{i,j}^{n+1}-\xi_{i,j}^{n}}{\Delta t}-\mathcal{J}(\psi_{i,j}^{n},\xi_{i,j}^{n})-N_1(\Omega_{i,j}^{n},\Omega_{i,j}^{n})\right)=-\mathrm{Ra}\,g(r_i)r_i\frac{\partial T_{i,j}}{\partial\theta}\sin\theta_j+\frac{1}{2}(D^2\xi_{i,j}^{n+1}+D^2\xi_{i,j}^{n}), \tag{C.4a}$$

$$\frac{T_{i,j}^{n+1}-T_{i,j}^{n}}{\Delta t}+J(\psi_{i,j}^{n},T_{i,j}^{n})=\frac{1}{2}(\nabla^2T_{i,j}^{n+1}+\nabla^2T_{i,j}^{n}), \tag{C.4b}$$

$$\frac{\Omega_{i,j}^{n+1}-\Omega_{i,j}^{n}}{\Delta t}+J(\psi_{i,j}^{n},\Omega_{i,j}^{n})=\frac{Pr}{2}(D^2\Omega_{i,j}^{n+1}+D^2\Omega_{i,j}^{n}), \tag{C.4c}$$

and the stream-function is updated by inverting the Poisson equation

$$\xi_{i,j}^{n+1}=-D^2\psi_{i,j}^{n+1}. \tag{C.5}$$

The discretised linear operators ∇^2, D^2 have a sparse penta-diagonal structure. They are thus stored as sparse matrices and operated with using sparse linear algebra routines. At the sphere's boundaries we enforce that the grid points

$$\begin{aligned}&T_{0,j}=1,\quad T_{N_r,j}=0,\\&\Omega_{0,j}=PrRe_1\sin\theta_j^2,\quad \Omega_{N_r,j}=PrRe_2\sin\theta_j^2,\end{aligned} \tag{C.6}$$

for each time-step. We must we must enforce the Dirichlet and Neumann boundary conditions $\psi=\psi'=0$ at the sphere's boundaries. The Dirichlet boundary condition is implemented in solving (C.5), while the Neumann boundary condition is applied to solve for

$$\xi=-\frac{\partial^2\psi}{\partial r^2},\quad \text{at}\quad r=1,1+d. \tag{C.7}$$

Using a forward difference approximation into the domain at each boundary gives

$$\xi_{0,j}=-\frac{2\psi_{1,j}}{\Delta r^2},\quad \xi_{N_r,j}=-\frac{2\psi_{N_r-1,j}}{\Delta r^2}. \tag{C.8}$$

Numerical stability is enforced by satisfying, the CFL condition and r-diffusion number at each time-step

$$\begin{aligned}&CFL=\left(\frac{|u_r|\Delta t}{\Delta r}+\frac{|u_\theta|\Delta t}{r\Delta\theta}\right)\leq 1,\\&\frac{Pr\Delta t}{\Delta r^2}\leq 1/2,\qquad \frac{Pr\Delta t}{(r\Delta\theta)^2}\leq 1/2.\end{aligned} \tag{C.9}$$

C.1 Code validation

Code validation is performed by demonstrating that the numerical approximation convergences with second order error to the true solution. Evaluating solutions for different grid sizes $N_r \times N_\theta$, we assume that the error of the numerical approximation compared with a true solution behaves as

$$\epsilon = |\psi_{anal} - \psi_{num}| \approxeq A\Delta t + B\Delta r^2 + C\Delta\theta^2, \tag{C.10}$$

where

$$|\psi_{anal} - \psi_{num}| = \left(\sum_i^{N_r \times N_\theta} (\psi^i_{anal} - \psi^i_{num})^p \right)^{1/p}, \tag{C.11}$$

$$A\Delta t + B\Delta r^2 + C\Delta\theta^2 = \left(\sum_i^{N_r \times N_\theta} (A_i\Delta t + B_i\Delta r^2 + C_i\Delta\theta^2)^p \right)^{1/p}, \tag{C.12}$$

defines the L^p norm such that ϵ represents the sum of the error at all grid points. In convergence tests we set $\Delta r \approxeq \Delta\theta$ such that

$$\epsilon = |\psi_{anal} - \psi_{num}| \approxeq A\Delta t + (B + C)\Delta r^2 \equiv A\Delta t + \hat{B}\Delta r^2. \tag{C.13}$$

To ensure that the temporal error is comparable between runs for different grid sizes, we adjust Δt such that $r = Pr\Delta t/(\Delta r^2)$ remains constant. By obtaining two error measures for different grid sizes we can evaluate the unknown exponent γ in the relation

$$\epsilon = |\psi_{anal} - \psi_{num}| \approxeq A\Delta t + \hat{B}\Delta r^\gamma. \tag{C.14}$$

Assuming the temporal error $A\Delta t$ remains constant between different runs, each denoted by the subscripts $1, 2$, one make take the logarithm of (C.14) giving

$$\ln(\epsilon_1) \approxeq \ln(A\Delta t) + \gamma \ln(\hat{B}_1\Delta r_1), \qquad \ln(\epsilon_2) \approxeq \ln(A\Delta t) + \gamma \ln(\hat{B}_2\Delta r_2). \tag{C.15}$$

Combining these expressions yields an estimation of the exponent

$$\gamma \approxeq \ln(\epsilon_1/\epsilon_2)/\ln(\hat{B}_1\Delta r_1/\hat{B}_2\Delta r_2). \tag{C.16}$$

To evaluate its anticipated value, we assume the constants A_i, B_i are independent of their grid-points such that

$$\left(\sum_{i}^{N_r \times N_\theta} (A_i \delta t + B_i \delta r^2)^p\right)^{1/p} \approxeq \left(\Delta r^{-2}(A\delta t + B\delta r^2)^p\right)^{1/p} \approxeq const \Delta r^{-2} + B\Delta r^{\frac{-2+2p}{p}}, \tag{C.17}$$

which depending on the chosen norm gives the following convergence rates

$$L^1 \quad \gamma \approxeq 0, \quad L^2 \quad \gamma \approxeq 1, \quad L^\infty \quad \gamma \approxeq 2. \tag{C.18}$$

In the absence of an analytical solution to (C.1), we define the following functions

$$\begin{aligned} \psi(r,\theta) &= \sin(k(r_1 - r)) \sin(k(r_2 - r)) \sin\theta \frac{\partial P_\ell(\cos\theta)}{\partial \theta}, \\ T(r,\theta) &= \cos(k/2(r_1 - r)), \\ \Omega(r,\theta) &= (\tilde{a} r^2 + \tilde{b}/r) \sin^2\theta, \\ \xi(r,\theta) &= D_\ell^2 \psi(r,\theta), \quad \text{where} \quad k = \pi/(d), \end{aligned} \tag{C.19}$$

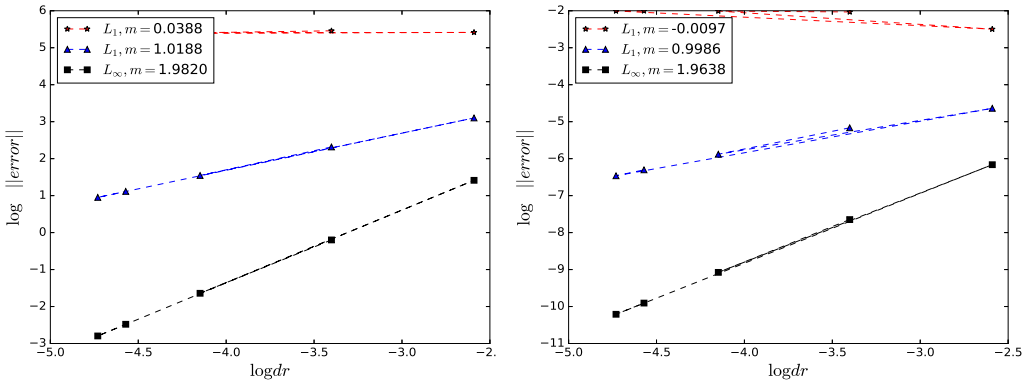
to satisfy the boundary conditions exactly. When substituted into (C.1) however, a remainder term is obtained. This remainder is determined analytically and added as a forcing to (C.1), such that (C.19) become exact solutions. A caveat of this validation method, is that (C.19) may be unstable, such that a time dependent code will not converge.

Setting the annulus width $d = 0.3$ and choosing $Pr = 1, Ra = 1, Re = 1$, the following grid-sizes and time-steps are chosen.

Test	N_r	N_θ	Δt
1)	5	54	1e-05
2)	10	105	
3)	20	209	
4)	30	314	
5)	35	366	

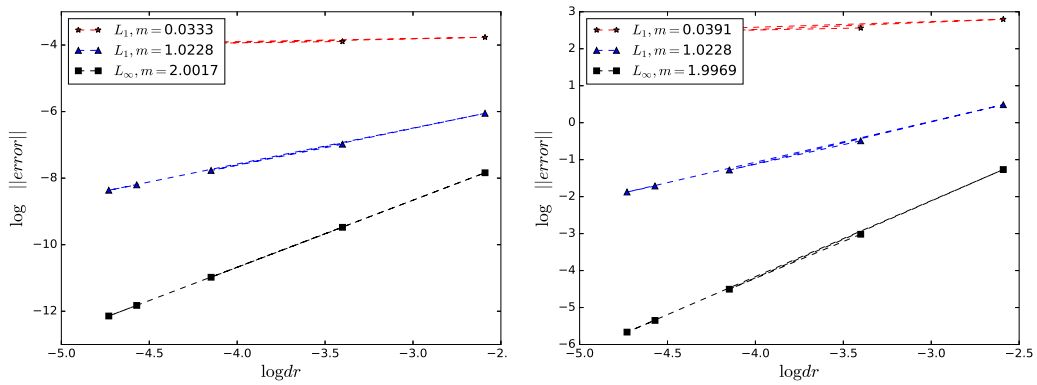
Table C.1: Set of grid-sizes chosen for code validation. The value of N_θ is adjusted such that $\Delta_r \approxeq \Delta_\theta$ in each test.

Figures C.1, C.2 demonstrate the convergence rates anticipated by (C.18) for each field variable.



(a) $||\xi_{num} - \xi_{anal}||$ vs. N_r. **(b)** $||T_{num} - T_{anal}||$ vs. N_r.

Figure C.1: Both the vorticity ξ and temperature field T converge to their true solution as the grid-size N_r is increased. This is also reflected in their exponents shown in the upper right corners. In this figure m, dr are used in place of $\gamma, \Delta r$.



(a) $||\Omega_{num} - \Omega_{anal}||$ vs. N_r. **(b)** $||\psi_{num} - \psi_{anal}||$ vs. N_r.

Figure C.2: Both the specific angular momentum Ω and stream function fields ψ converge to their true solution as the grid-size N_r is increased. This is also reflected in their exponents shown in the upper right corners. In this figure m, dr are used in place of $\gamma, \Delta r$.

D

Axisymmetric spectral code

To calculate equilibrium states $\boldsymbol{X}_0$ and eigenvectors $\boldsymbol{X}'$ a spectral method is used. The solutions θ dependency is expanded in terms of Legendre $P_\ell(\cos\theta)$ for T and Gegenbauer polynomials $G_\ell(\theta)$ for ψ, Ω up to degree N_θ, thus satisfying the symmetry conditions at $\theta = 0, \pi$ exactly. To treat the solutions radial dependency a Chebyshev psuedo-spectral method and finite-difference stencil are outlined.

The state vector is defined as

$$\boldsymbol{X} = \begin{pmatrix} \psi \\ T \\ \Omega \end{pmatrix} = \sum_{\ell=0}^{N_\theta} \begin{pmatrix} \psi_\ell(r,t) G_\ell(\theta) \\ T_\ell(r,t) P_\ell(\cos\theta) \\ \Omega_\ell(r,t) G_\ell(\theta) \end{pmatrix}, \tag{D.1}$$

such that $\boldsymbol{X}$ contains $3 \times N_\theta \times N_r$ elements. The projection onto this basis, requires that we define the following normalization conditions. Representing nonlinear products of the polynomials as an arbitrary function $f(\theta)$, we may express series of Legendre polynomials as

$$f(\theta) = \sum_{\ell=0}^{N_\theta} \alpha_\ell P_\ell(\cos\theta), \quad \alpha_\ell = \frac{2\ell+1}{2} \int_0^\pi f(\theta) P_\ell(\cos\theta) \sin\theta \, d\theta \tag{D.2}$$

and equivalently Gegenbauer polynomials as

$$G_\ell(\theta) = -\sin^2\theta C_{\ell-1}^{(\alpha=3/2)}(\cos\theta) = \sin\theta \frac{d}{d\theta} P_\ell(\cos\theta) \tag{D.3a}$$

$$f(\theta) = \sum_{\ell=0}^{N_\theta} \beta_\ell G_\ell(\theta), \quad \beta_\ell = \tilde{C}(\ell) \int_0^\pi \frac{G_\ell(\theta) f(\theta)}{\sin\theta} d\theta \tag{D.3b}$$

where $\tilde{C}(\ell)$ is a normalising constant given by

$$\tilde{C}(\ell) = \frac{\eta!(\eta+\alpha)[\Gamma(\alpha)]^2}{\pi 2^{(1-2\alpha)}\Gamma(\eta+2\alpha)}, \quad \text{where} \quad \eta = \ell - 1,\ \alpha = 1.5, \tag{D.4}$$

and Γ is the gamma function. Substituting the state vector into the full equations and projecting onto a finite sum of N_θ basis functions we obtain the Galerkin projection of the full equations given by

$$\mathcal{M}\frac{\partial \boldsymbol{X}}{\partial t} = \mathcal{N}(\boldsymbol{X}, \boldsymbol{X}) + \mathcal{L}\boldsymbol{X} + \boldsymbol{F}. \tag{D.5}$$

where the components of the vector $\boldsymbol{X}$ are now

$$\boldsymbol{X} = \begin{pmatrix} \psi_{\ell=0}(r,t) \\ T_{\ell=0}(r,t) \\ \Omega_{\ell=0}(r,t) \\ \vdots \\ \psi_{\ell=N_\theta}(r,t) \\ T_{\ell=N_\theta}(r,t) \\ \Omega_{\ell=N_\theta}(r,t) \end{pmatrix}. \tag{D.6}$$

The corresponding matrix operator $\mathcal{M}$ is now given by

$$\mathcal{M} = \begin{pmatrix} M_{\ell=0} & \cdots & 0 \\ \vdots & \ddots & \vdots \\ 0 & \cdots & M_{N_\theta} \end{pmatrix}, \quad \text{where} \quad M_\ell = \begin{pmatrix} D_\ell^2 & 0 & 0 \\ 0 & \mathbb{I} & 0 \\ 0 & 0 & \mathbb{I} \end{pmatrix}, \tag{D.7}$$

and similarly the right-hand side matrix $\mathcal{L}$ is given by

$$\mathcal{L} = \begin{pmatrix} L_{\ell=0,m=0} & \cdots & 0 \\ \vdots & \ddots & \vdots \\ 0 & \cdots & L_{N_\theta N_\theta} \end{pmatrix}, \quad \text{where} \quad L_{\ell m} = \begin{pmatrix} Pr\, D_\ell^2 D_\ell^2 & Pr\,\mathrm{Ra}\, g(r) & Re_1\, PrN\Psi\Omega(\Omega_0)_{\ell m} \\ \ell(\ell+1)\frac{T_0'(r)}{r^2} & \nabla_\ell^2 & 0 \\ Re_1\, PrN\Omega(\Omega_0)_{\ell m} & 0 & Pr\, D_\ell^2 \end{pmatrix}, \tag{D.8}$$

where the terms $N\Psi\Omega(\Omega_0)_\ell, N\Omega(\Omega_0)_\ell$ arise from the interaction with the base state $\Omega_0(r,\theta)$ and are outlined subsequent sections. Notably these terms will populate off-

diagonal entries in $\mathcal{L}$. The forcing vector $\boldsymbol{F}$ is given by

$$F_{\ell=2} = Pr^2\left(-\frac{2\tilde{a}\tilde{b}}{r^2}-\frac{2\tilde{b}^2}{r^5}\right)G_{\ell=2}(\theta), \quad \tilde{a} = -\frac{Re_2(1+d)-Re_1}{(1+d)^3-1}, \qquad \tilde{b} = -\frac{(1+d)[Re_1(1+d)^2-Re_2]}{(1+d)^3-1}, \tag{D.9}$$

where $\tilde{a}, \tilde{b}$ are as per (2.19). We first outline the use of finite differences and subsequently the Chebyshev collocation methods to treat the radial dependency.

D.1 Finite difference method

D.1.1 Linear terms

Using a stencil of N_r equispaced grid-points we obtain the representation

$$\boldsymbol{X} = \begin{pmatrix} X_{\ell=0} \\ \vdots \\ X_{\ell=N_\theta} \end{pmatrix}, \quad \text{where} \quad X_\ell = \left(\psi_\ell^{i=1}\dots\psi_\ell^{i=N_r-2}\; T_\ell^{i=1}\dots T_\ell^{i=N_r-2}\; \Omega_\ell^{i=1}\dots\Omega_\ell^{i=N_r-2}\right)^T, \tag{D.10}$$

and each superscript i corresponds to the location of a radial grid point, with $r_{i=0} = 1$ representing the shell's inner boundary. The finite difference representation of the boundary conditions is given by

$$\begin{aligned} &\psi_\ell^0 = \psi_\ell^{N_r-1} = 0, \\ &\frac{d\psi_\ell^0}{dr} = 0, \; \frac{d\psi_\ell^{N_r-1}}{dr} = 0, \\ &T_\ell^0 = T_\ell^{N_r-1} = 0, \\ &\Omega_\ell^0 = \Omega_\ell^{N_r-1} = 0. \end{aligned} \tag{D.11}$$

In defining (D.35) we have omitted the grid points $i = 0, i = N_r - 1$ to enforce the Dirichlet boundary conditions at the annulus boundaries. Specifying each of the operators in this manner also helps to avoid the calculation of spurious eigenvalues when conducting stability analysis. As can be seen in (D.12), specifying $\psi^i = 0$ or $\psi^{N_r-1} = 0$ would imply that any λ_i is a solution of

$$\begin{pmatrix} 1 & \cdots & \cdots & \cdots & 0 \\ \left(\frac{-2}{\Delta r^2} - \frac{l(l+1)}{r_{i=1}^2}\right) & \frac{1}{\Delta r^2} & 0 & \cdots & 0 \\ \vdots & \ddots & \ddots & \ddots & \vdots \\ 0 & \cdots & \cdots & \cdots & 1 \end{pmatrix} \begin{pmatrix} \psi_\ell^{i=0} \\ \psi_\ell^{i=1} \\ \vdots \\ \psi_\ell^{i=N_r-1} \end{pmatrix} = \begin{pmatrix} 0 \\ \vdots \\ \vdots \\ 0 \end{pmatrix} \lambda_i \mathbb{I}. \tag{D.12}$$

The second order matrix operators D_ℓ^2, ∇_ℓ^2 are given by

$$\begin{aligned} D_\ell^2 \psi_\ell &= \frac{\partial^2 \psi_\ell}{\partial r^2} - \frac{\ell(\ell+1)}{r^2}\psi_\ell, \\ \nabla_\ell^2 \psi_\ell &= \frac{\partial^2 \psi_\ell}{\partial r^2} + \frac{2}{r}\frac{\partial \psi_\ell}{\partial r} - \frac{\ell(\ell+1)}{r^2}\psi_\ell, \end{aligned} \tag{D.13}$$

and their discretization in matrix form by

$$D_\ell^2 = \begin{pmatrix} \left(\frac{-2}{\Delta r^2} - \frac{l(l+1)}{r_{i=1}^2}\right) & \frac{1}{\Delta r^2} & 0 & \cdots & 0 \\ \frac{1}{\Delta r^2} & \left(\frac{-2}{\Delta r^2} - \frac{l(l+1)}{r_{i=2}^2}\right) & \frac{1}{\Delta r^2} & \cdots & 0 \\ \vdots & \ddots & \ddots & \ddots & \vdots \\ 0 & \cdots & \frac{1}{\Delta r^2} & \left(\frac{-2}{\Delta r^2} - \frac{l(l+1)}{r_{i=N_r-3}^2}\right) & \frac{1}{\Delta r^2} \\ 0 & \cdots & 0 & \frac{1}{\Delta r^2} & \left(\frac{-2}{\Delta r^2} - \frac{l(l+1)}{r_{i=N_r-2}^2}\right) \end{pmatrix}, \tag{D.14}$$

,

$$\nabla_\ell^2 = \begin{pmatrix} \left(\frac{-2}{\Delta r^2} - \frac{l(l+1)}{r_{i=1}^2}\right) & \left(\frac{1}{\Delta r^2} + \frac{1}{r_{i=1}\Delta r}\right) & 0 & \cdots & 0 \\ \left(\frac{1}{\Delta r^2} - \frac{1}{r_{i=2}\Delta r}\right) & \left(\frac{-2}{\Delta r^2} - \frac{l(l+1)}{r_{i=2}^2}\right) & \left(\frac{1}{\Delta r^2} + \frac{1}{r_{i=2}\Delta r}\right) & \cdots & 0 \\ \vdots & \ddots & \ddots & \ddots & \vdots \\ 0 & \cdots & \left(\frac{1}{\Delta r^2} - \frac{1}{r_{i=N_r-3}\Delta r}\right) & \left(\frac{-2}{\Delta r^2} - \frac{l(l+1)}{r_{i=N_r-3}^2}\right) & \left(\frac{1}{\Delta r^2} + \frac{1}{r_{i=N_r-3}\Delta r}\right) \\ 0 & \cdots & 0 & \left(\frac{1}{\Delta r^2} - \frac{1}{r_{i=N_r-2}\Delta r}\right) & \left(\frac{-2}{\Delta r^2} - \frac{l(l+1)}{r_{i=N_r-2}^2}\right) \end{pmatrix}. \tag{D.15}$$

In addition to the Dirichlet boundary condition the Neumann boundary condition on ψ must also be enforced in the discretizations of $D_\ell^2 D_\ell^2$ and D_ℓ^3, operators which arise in the vorticity equation. These are given by

$$
\begin{aligned}
D_\ell^3\psi_\ell &= \frac{\partial^3\psi_\ell}{\partial r^3} - \frac{2}{r}\frac{\partial^2\psi_\ell}{\partial r^2} - \frac{\ell(\ell+1)}{r^2}\frac{\partial\psi_\ell}{\partial r} + \frac{4\ell(\ell+1)}{r^3}\psi_\ell, \\
D_\ell^2 D_\ell^2\psi_\ell &= \frac{\partial^4\psi_\ell}{\partial r^4} - \frac{2\ell(\ell+1)}{r^2}\frac{\partial^2\psi_\ell}{\partial r^2} + \frac{4\ell(\ell+1)}{r^3}\frac{\partial\psi_\ell}{\partial r} + \frac{\big([\ell(\ell+1)]^2 - 6\ell(\ell+1)\big)}{r^4}\psi_\ell.
\end{aligned}
\tag{D.16}
$$

The matrix operator D_ℓ^3 is given by the stencil

$$
D_\ell^3\psi_\ell^i = a\psi_\ell^{i-2} + b\psi_\ell^{i-1} + c\psi_\ell^i + d\psi_\ell^{i+1} + e\psi_\ell^{i+2} \tag{D.17}
$$

where the coefficients are given by

$$
a = -\frac{1}{2\Delta r^3}, \quad b = \frac{\ell(\ell+1)}{r_i^2 2\Delta r} - \frac{2}{r_i\Delta r^2} + \frac{1}{\Delta r^3}, \quad c = \frac{4\ell(\ell+1)}{r_i^3} + \frac{4}{r_i\Delta r^2}, \quad d = -\frac{\ell(\ell+1)}{r_i^2 2\Delta r} - \frac{2}{r_i\Delta r^2} - \frac{1}{\Delta r^3}, \quad e = \frac{1}{2\Delta r^3}. \tag{D.18}
$$

Similarly the matrix operator $D_\ell^2 D_\ell^2$ is given by the stencil

$$
D_\ell^2 D_\ell^2\psi_\ell^i = a\psi_\ell^{i-2} + b\psi_\ell^{i-1} + c\psi_\ell^i + d\psi_\ell^{i+1} + e\psi_\ell^{i+2} \tag{D.19}
$$

with corresponding coefficients

$$
\begin{aligned}
&a = e = \frac{1}{\Delta r^4}, \quad b = \frac{-4}{\Delta r^4} - \frac{2l(l+1)}{r_i^2\Delta r^2} - \frac{2l(l+1)}{r_i^3\Delta r} \\
&c = \frac{6}{\Delta r^4} + \frac{4l(l+1)}{r_i^2\Delta r^2} - \frac{l(l+1)\big(6 - l(l+1)\big)}{r_i^4}, \quad d = \frac{-4}{\Delta r^4} - \frac{2l(l+1)}{r_i^2\Delta r^2} + \frac{2l(l+1)}{r_i^3\Delta r}.
\end{aligned}
\tag{D.20}
$$

In addition to applying the Dirichlet boundary conditions as previous, the derivatives must vanish at the boundaries. This is achieved by introducing ghost nodes ψ_ℓ^{-1}, $\psi_\ell^{N_r}$ and setting the derivative as approximated by central difference to be zero as follows. The ghost nodes allow the function to be made symmetric at the boundary forcing the derivative to be zero as follows

$$
\frac{d\psi^0}{dr} = \frac{\psi_\ell^{-1} - \psi_\ell^1}{2\Delta r} = 0, \quad \frac{d\psi^{N_r-1}}{dr} = \frac{\psi_\ell^{N_r-2} - \psi_\ell^{N_r}}{2\Delta r} = 0, \tag{D.21}
$$

For both operators this yields a matrix of the form

$$\begin{pmatrix} (c+a) & d & e & 0 & 0 & \cdots & 0 \\ b & c & d & e & 0 & \cdots & 0 \\ a & b & c & d & e & \cdots & 0 \\ \vdots & \ddots & \ddots & \ddots & & \cdots & \vdots \\ 0 & \cdots & a & b & c & d & e \\ 0 & 0 & \cdots & a & b & c & d \\ 0 & \cdots & 0 & 0 & a & b & (c+e) \end{pmatrix}. \tag{D.22}$$

D.1.2 Non-linear terms

The quadratic nonlinearity $\mathcal{N}(\boldsymbol{X}, \boldsymbol{X})$ is treated by writing it as an linear operator $\mathcal{N}(\boldsymbol{X})$ acting on a vector $\boldsymbol{X}'$. This procedure is chosen as it allows the resulting linear matrix to be used for time-stepping, linear stability and steady state solving routines. In state space representation this yields

$$\mathcal{N}(\boldsymbol{X})\boldsymbol{X}' = \sum_{\ell=0}^{N_\theta} \mathcal{N}(\boldsymbol{X})_{\ell m} \boldsymbol{X}'_m, \tag{D.23}$$

where the matrix $\mathcal{N}(\boldsymbol{X})_{\ell m}$ is defined by

$$\mathcal{N}(\boldsymbol{X})_{\ell m} = \begin{pmatrix} N_{00} & \cdots & N_{0N_\theta} \\ \vdots & \ddots & \vdots \\ 0 & \cdots & N_{N_\theta N_\theta} \end{pmatrix}, \quad \text{where} \quad N_{\ell m} = \begin{pmatrix} N\Psi(\psi_\ell)_{\ell m} & 0 & N\Psi\Omega(\Omega_\ell)_{\ell m} \\ 0 & NT(\psi_\ell)_{\ell m} & 0 \\ 0 & 0 & N\Omega(\psi_\ell)_{\ell m} \end{pmatrix}. \tag{D.24}$$

The submatrices contained each of dimension $(Nr-2 \times Nr-2)$ are given by

$$\begin{aligned} N\Psi(\psi_\ell) &= \left[\frac{a\psi(\ell,m)}{r^2}\right]\left[\psi_\ell\right]\left[D^3_m\right] + \left[\frac{b\psi(\ell,m)}{2\Delta r\, r^2}\right]\left[\mathcal{D}\psi_\ell\right]\left[D^2_m\right], \\ N\Psi\Omega(\Omega_\ell) &= \left[\frac{a\psi\Omega(\ell,m)}{2\Delta r\, r^2}\right]\left[\Omega_\ell\right]\left[\mathcal{D}\right] + \left[\frac{b\psi(\ell,m)}{r^3}\right]\left[\Omega_\ell\right], \\ NT(\psi_\ell) &= \left[\frac{aT(\ell,m)}{2\Delta r\, r^2}\right]\left[\psi_\ell\right]\left[\mathcal{D}\right] + \left[\frac{bT(\ell,m)}{2\Delta r\, r^2}\right]\left[\mathcal{D}\psi_\ell\right], \\ N\Omega(\psi_\ell) &= \left[\frac{a\Omega(\ell,m)}{2\Delta r\, r^2}\right]\left[\psi_\ell\right]\left[\mathcal{D}\right] + \left[\frac{b\Omega(\ell,m)}{2\Delta r\, r^2}\right]\left[\mathcal{D}\psi_\ell\right], \end{aligned} \tag{D.25}$$

where D^3_ℓ, D^2_ℓ are given by (D.22), (D.14), the differentitaion matrix $\mathcal{D}$ is given by

$$\mathcal{D} = \begin{pmatrix} 0 & 1 & \cdots & \cdots & 0 \\ -1 & 0 & 1 & \cdots & 0 \\ 0 & \ddots & \ddots & \ddots & 0 \\ 0 & 0 & 0 & -1 & 0 \end{pmatrix}, \tag{D.26}$$

and the coefficients depending on indicies ℓ, m are given by the integrals (D.49), (D.50), (D.51). Similarly the matrix corresponding to $\mathcal{N}(\boldsymbol{X}', \boldsymbol{X})$ is defined by

$$\mathcal{N}(\boldsymbol{X}', \boldsymbol{X}) = \sum_{m=0}^{N_\theta} \mathcal{N}(\boldsymbol{X})_{m\ell} \boldsymbol{X}'_\ell, \tag{D.27}$$

with matrix entries given by

$$\mathcal{N}(\boldsymbol{X})_{m\ell} = \begin{pmatrix} N_{m\ell} & \cdots & N_{0N_\theta} \\ \vdots & \ddots & \vdots \\ 0 & \cdots & N_{N_\theta N_\theta} \end{pmatrix}, \quad \text{where} \quad N_{m\ell} = \begin{pmatrix} N\Psi(\psi_m)_{m\ell} & 0 & N\Psi\Omega(\Omega_m)_{m\ell} \\ NT(T_m)_{m\ell} & 0 & 0 \\ N\Omega(\Omega_m)_{m\ell} & 0 & 0 \end{pmatrix}. \tag{D.28}$$

The submatrices contained each of dimension $(Nr - 2 \times Nr - 2)$ are given by

$$\begin{aligned} N\Psi(\psi_m) &= \left[\frac{a\psi(\ell,m)}{r^2}\right]\left[D_m^3\psi_m\right] + \left[\frac{b\psi(\ell,m)}{2\Delta r\, r^2}\right]\left[D_m^2\psi_m\right]\left[\mathcal{D}\right], \\ N\Psi\Omega(\Omega_m) &= \left[\frac{a\psi\Omega(\ell,m)}{2\Delta r\, r^2}\right]\left[\mathcal{D}\Omega_m\right] + \left[\frac{b\psi(\ell,m)}{r^3}\right]\left[\Omega_m\right], \\ NT(\psi_m) &= \left[\frac{aT(\ell,m)}{2\Delta r\, r^2}\right]\left[\mathcal{D}T_m\right] + \left[\frac{bT(\ell,m)}{2\Delta r\, r^2}\right]\left[T_m\right]\left[\mathcal{D}\right], \\ N\Omega(\psi_m) &= \left[\frac{a\Omega(\ell,m)}{2\Delta r\, r^2}\right]\left[\mathcal{D}\Omega_m\right] + \left[\frac{b\Omega(\ell,m)}{2\Delta r\, r^2}\right]\left[\Omega_m\right]\left[\mathcal{D}\right], \end{aligned} \tag{D.29}$$

and the coefficients depending on indices ℓ, m are given by the integrals (D.49), (D.50), (D.51). Distinct from operators $\mathcal{M}, \mathcal{L}$, the operator $\mathcal{N}$ is dense as the block matrices $N_{\ell m}$ are present at almost all (ℓ, m) indices, for solutions lacking equatorial symmetry. This arises from the expression of nonlinear products in θ as a linear superposition of modes when projecting onto a basis of Legendre or Gegenbauer polynomials.

D.2 Pseudo-spectral method

The Chebyshev points are defined by

$$x_j = \cos(j\pi/N), \quad j = 0, 1, .., N, \tag{D.30}$$

and the mapping form the interval $[-1, 1]$ to $[r_i, r_o]$ is given by

$$r_j = \frac{r_o + r_i}{2} + \frac{r_o - r_i}{2} x_j. \tag{D.31}$$

In contrast to the equidistant finite difference grid, these collocation points cluster near the sphere's boundaries as required. Using these points we now solve for the values of a grid function f evaluated at these collocation points. Following Trefethen (2000) we introduce the unique polynomial $p(r_j)$ of degree $\leq N$ with $f_j = p(r_j)$, $0 \leq j \leq N$. Provided that all r_j are distinct, the unique interpolant of degree N is defined by

$$p_j(x) = \frac{1}{a_j} \prod_{k=0, k\neq j}^{N} (x - x_k), \qquad a_j(x) = \frac{1}{a_j} \prod_{k=0, k\neq j}^{N} (x_j - x_k). \tag{D.32}$$

To obtain the differentiation matrix $\mathcal{D}$ we take the logarithm of (D.32) and differentiate to obtain

$$p_j'(x) = p_j(x) \sum_{k=0, k\neq j}^{N} (x - x_k)^{-1}. \tag{D.33}$$

Using this relation the entries of $\mathcal{D}$ are defined

$$\mathcal{D}_{ij} = \frac{a_i}{a_j(x_i - x_j)}, \qquad \mathcal{D}_{ij} = \sum_{k=0, k\neq j}^{N} (x_i - x_j)^{-1} \tag{D.34}$$

Higher derivatives of order ν are obtained by taking powers of $\mathcal{D}$. An alternative method for computing the derivatives of a grid function makes use of fast Fourier transform (Trefethen 2000). The numerical complexity of this method scales as $\mathcal{O}(N \log N)$ and is preferable for large vectors.

D.2.1 Linear terms

As in the previous section, we treat all θ dependent terms using a Galerkin projection to yield a system of N_θ coupled ODEs each denoted by a subscript ℓ. The resulting ODE system is then discretized using a Chebyshev-collocation method. Denoting the grid functions $\psi_\ell^j, T_\ell^j, \Omega_\ell^j$ represented at N collocation points, the corresponding state vector is given by

$$\boldsymbol{X} = \begin{pmatrix} X_{\ell=0} \\ \vdots \\ X_{\ell=N_\theta} \end{pmatrix}, \quad \text{where} \quad X_\ell = \left(\psi_\ell^{j=1} \dots \psi_\ell^{j=N-1}\ T_\ell^{j=1} \dots T_\ell^{j=N-1}\ \Omega_\ell^{j=1} \dots \Omega_\ell^{j=N-1}\right)^T. \tag{D.35}$$

Choosing an eigenbasis of the governing equations the Galerkin projection automatically enforces the boundary conditions in θ, while in the radial direction we must implement the Dirichlet and Neumann boundary conditions

$$\frac{d\psi_\ell}{dr} = \psi_\ell = T_\ell = \Omega_\ell = 0, \quad \text{for} r = r_i, r_o. \tag{D.36}$$

The Dirichlet boundary conditions are enforced by omitting the collocation points $j = 0, j = N_r - 1$, such that we only solve for the interior points defined as per (D.35). When implemented for the second order linear operators this yields

$$\begin{aligned} \nabla_\ell^2 &= \mathcal{D}^2 + \mathrm{diag}\big(\frac{2}{r_j}\big)\mathcal{D} - \mathrm{diag}\big(\frac{\ell(\ell+1)}{r_j^2}\big), \\ D_\ell^2 &= \mathcal{D}^2 - \mathrm{diag}\big(\frac{\ell(\ell+1)}{r_j^2}\big), \end{aligned} \tag{D.37}$$

where $j = 1, \dots, Nr-1$ and $\mathcal{D} \in \mathbb{D}^{Nr-1 \times Nr-1}$. Both the Neumann and Dirichlet boundary conditions must be enforced on the higher order operators appearing in the fourth order vorticity equation given by (D.16). To implement these conditions we redefine our grid function using the relation

$$f(r) = (r^2 + br + c)q(r), \quad b = -(r_i + r_o), c = r_i r_o, \tag{D.38}$$

a polynomial of degree $\leq N + 2$ which satisfies $f(r) = f'(r) = 0$ at $r = r_i, r_o$. Taking four differentiations we obtain

$$
\begin{aligned}
f'(r) &= (2r+b)q(r) + (r^2+br+c)q'(r),\\
f''(r) &= 2q(r) + 2(2r+b)q'(r) + (r^2+br+c)q''(r),\\
f'''(r) &= 6q'(r) + 3(2r+b)q''(r) + (r^2+br+c)q'''(r),\\
f''''(r) &= 12q''(r) + 4(2r+b)q'''(r) + (r^2+br+c)q''''(r).
\end{aligned}
\tag{D.39}
$$

To implement the spectral differentiation in matrix form we define q to be the unique polynomial of degree $\leq N$ with $f(r_i) = f(r_o) = 0$ and $q(r_j) = v_j/(r_j^2 + br_j + c)$ for the interior points $j = 1, ..., Nr-1$. In terms of matrices, we represent the derivative of order $q^\nu(r)$ by $\mathcal{D}^\nu$ and omit the first and last rows and columns of $\mathcal{D}^\nu$ to enforce the Dirichlet boundary conditions. For the third and fourth order derivatives we obtain

$$
\begin{aligned}
\tilde{D}^3 \equiv \frac{\partial^3 \psi_\ell}{\partial r^3} &= \Big[6\mathcal{D} + 3(2r_j+b)\mathcal{D}^2 + (r_j^2+br_j+c)\mathcal{D}^3\Big] \times \mathrm{diag}\bigg(\frac{1}{(r_j^2+br_j+c)}\bigg),\\
\tilde{D}^4 \equiv \frac{\partial^4 \psi_\ell}{\partial r^4} &= \Big[12\mathcal{D}^2 + 4(2r_j+b)\mathcal{D}^3 + (r_j^2+br_j+c)\mathcal{D}^4\Big] \times \mathrm{diag}\bigg(\frac{1}{(r_j^2+br_j+c)}\bigg),
\end{aligned}
\tag{D.40}
$$

where $j = 1, .., Nr-1$ and $\mathcal{D} \in \mathbb{D}^{Nr-1 \times Nr-1}$. Substituting these relations into (D.16), we obtain these operators in matrix form

$$
D_\ell^3 = \tilde{D}^3 - \mathrm{diag}\big(\frac{2}{r_j}\big)\mathcal{D}^2 - \mathrm{diag}\big(\frac{\ell(\ell+1)}{r_j^2}\big)\mathcal{D} + \mathrm{diag}\big(\frac{4\ell(\ell+1)}{r_j^3}\big), \tag{D.41}
$$

$$
D_\ell^2 D_\ell^2 \psi_\ell = \tilde{D}^4 - \mathrm{diag}\big(\frac{2\ell(\ell+1)}{r_j^2}\big)\mathcal{D}^2 + \mathrm{diag}\big(\frac{4\ell(\ell+1)}{r_j^3}\big)\mathcal{D} + \mathrm{diag}\big(\frac{\big([\ell(\ell+1)]^2 - 6\ell(\ell+1)\big)}{r_j^4}\big). \tag{D.42}
$$

D.2.2 Non-linear terms

The quadratic nonlinearity $\mathcal{N}(\boldsymbol{X}, \boldsymbol{X})$ is treated by writing it as an linear operator $\mathcal{N}(\boldsymbol{X})$ acting on an unknown vector $\boldsymbol{X}'$. This procedure is chosen as it allows the resulting linear matrix to be use for time-stepping, linear stability and steady state solving routines. In state space representation this yields

$$
\mathcal{N}(\boldsymbol{X})\boldsymbol{X}' = \sum_{\ell=0}^{N_\theta} \mathcal{N}(\boldsymbol{X})_{\ell m} \boldsymbol{X}'_m, \tag{D.43}
$$

where the matrix $\mathcal{N}(\boldsymbol{X})_{\ell m}$ is defined by

$$\mathcal{N}(\boldsymbol{X})_{\ell m} = \begin{pmatrix} N_{00} & \cdots & N_{0N_\theta} \\ \vdots & \ddots & \vdots \\ 0 & \cdots & N_{N_\theta N_\theta} \end{pmatrix}, \quad \text{where} \quad N_{\ell m} = \begin{pmatrix} N\Psi(\psi_\ell)_{\ell m} & 0 & N\Psi\Omega(\Omega_\ell)_{\ell m} \\ 0 & NT(\psi_\ell)_{\ell m} & 0 \\ 0 & 0 & N\Omega(\psi_\ell)_{\ell m} \end{pmatrix}. \tag{D.44}$$

The submatrices contained each of dimension $(Nr-1 \times Nr-1)$ are given by

$$\begin{aligned} N\Psi(\psi_\ell) &= \left[\frac{a\psi(\ell,m)}{r^2}\right]\left[\psi_\ell\right]\left[D_m^3\right] + \left[\frac{b\psi(\ell,m)}{r^2}\right]\left[\mathcal{D}\psi_\ell\right]\left[D_m^2\right], \\ N\Psi\Omega(\Omega_\ell) &= \left[\frac{a\psi\Omega(\ell,m)}{r^2}\right]\left[\Omega_\ell\right]\left[\mathcal{D}\right] + \left[\frac{b\psi(\ell,m)}{r^3}\right]\left[\Omega_\ell\right], \\ NT(\psi_\ell) &= \left[\frac{aT(\ell,m)}{r^2}\right]\left[\psi_\ell\right]\left[\mathcal{D}\right] + \left[\frac{bT(\ell,m)}{r^2}\right]\left[\mathcal{D}\psi_\ell\right], \\ N\Omega(\psi_\ell) &= \left[\frac{a\Omega(\ell,m)}{r^2}\right]\left[\psi_\ell\right]\left[\mathcal{D}\right] + \left[\frac{b\Omega(\ell,m)}{r^2}\right]\left[\mathcal{D}\psi_\ell\right], \end{aligned} \tag{D.45}$$

where D_ℓ^3, D_ℓ^2 are given by (D.37), (D.41) and the coefficients depending on indicies ℓ, m are given by the integrals (D.49), (D.50), (D.51). Similarly the matrix corresponding to $\mathcal{N}(\boldsymbol{X}', \boldsymbol{X})$ is defined by

$$\mathcal{N}(\boldsymbol{X}', \boldsymbol{X}) = \sum_{m=0}^{N_\theta} \mathcal{N}(\boldsymbol{X})_{m\ell} \boldsymbol{X}'_\ell, \tag{D.46}$$

with matrix entries given by

$$\mathcal{N}(\boldsymbol{X})_{m\ell} = \begin{pmatrix} N_{m\ell} & \cdots & N_{0N_\theta} \\ \vdots & \ddots & \vdots \\ 0 & \cdots & N_{N_\theta N_\theta} \end{pmatrix}, \quad \text{where} \quad N_{m\ell} = \begin{pmatrix} N\Psi(\psi_m)_{m\ell} & 0 & N\Psi\Omega(\Omega_m)_{m\ell} \\ NT(T_m)_{m\ell} & 0 & 0 \\ N\Omega(\Omega_m)_{m\ell} & 0 & 0 \end{pmatrix}. \tag{D.47}$$

The sub-matrices contained each of dimension $(Nr-1 \times Nr-1)$ are given by

$$
\begin{aligned}
N\Psi(\psi_m) &= \left[\frac{a\psi(\ell,m)}{r^2}\right]\left[D_m^3\psi_m\right] + \left[\frac{b\psi(\ell,m)}{r^2}\right]\left[D_m^2\psi_m\right]\left[\mathcal{D}\right], \\
N\Psi\Omega(\Omega_m) &= \left[\frac{a\psi\Omega(\ell,m)}{r^2}\right]\left[\mathcal{D}\Omega_m\right] + \left[\frac{b\psi(\ell,m)}{r^3}\right]\left[\Omega_m\right], \\
NT(\psi_m) &= \left[\frac{aT(\ell,m)}{r^2}\right]\left[\mathcal{D}T_m\right] + \left[\frac{bT(\ell,m)}{2r^2}\right]\left[T_m\right]\left[\mathcal{D}\right], \\
N\Omega(\psi_m) &= \left[\frac{a\Omega(\ell,m)}{r^2}\right]\left[\mathcal{D}\Omega_m\right] + \left[\frac{b\Omega(\ell,m)}{r^2}\right]\left[\Omega_m\right]\left[\mathcal{D}\right],
\end{aligned}
\tag{D.48}
$$

and the coefficients depending on indices ℓ, m are given by the integrals (D.49), (D.50), (D.51). Distinct from operators $\mathcal{M}, \mathcal{L}$, the operator $\mathcal{N}$ is dense as the block matrices $N_{\ell m}$ are present at almost all (ℓ, m) indices. This arises from the expression of nonlinear products in θ as a linear superposition of modes when projecting onto a basis of Legendre or Gegenbauer polynomials.

D.3 Galerkin projection

The nonlinear terms involve products of θ dependent terms and require integrals for their product to summation transform. These integrals depend on the order of the polynomials (ℓ, m) substituted and the order of the equation n. The integrals for terms arising in the temperature equation are

$$
\begin{aligned}
aT(\ell,m,n) &= \frac{2n+1}{2}\int_0^\pi \left\{\ell(\ell+1)P_\ell P_m\right\}P_n \sin\theta d\theta, \\
bT(\ell,m,n) &= \frac{2n+1}{2}\int_0^\pi \left\{\frac{G_\ell G_m}{\sin^2\theta}\right\}P_n \sin\theta d\theta,
\end{aligned}
\tag{D.49}
$$

the specific angular momentum integrals are

$$
\begin{aligned}
a\Omega(\ell,m,n) &= \frac{\eta!(\eta+\alpha)[\Gamma(\alpha)]^2}{\pi 2^{(1-2\alpha)}\Gamma(\eta+2\alpha)}\int_0^\pi \left\{\ell(\ell+1)P_\ell G_m\right\}\frac{G_n}{\sin\theta}d\theta, \\
b\Omega(\ell,m,n) &= \frac{\eta!(\eta+\alpha)[\Gamma(\alpha)]^2}{\pi 2^{(1-2\alpha)}\Gamma(\eta+2\alpha)}\int_0^\pi \left\{-m(m+1)P_m G_\ell\right\}\frac{G_n}{\sin\theta}d\theta,
\end{aligned}
\tag{D.50}
$$

and the integrals for the vorticity equation are

$$
\begin{aligned}
a\Psi(\ell,m,n) &= \frac{\eta!(\eta+\alpha)[\Gamma(\alpha)]^2}{\pi 2^{(1-2\alpha)}\Gamma(\eta+2\alpha)}\int_0^\pi \big\{\ell(\ell+1)P_\ell G_m\big\}\frac{G_n}{\sin\theta}d\theta,\\
b\Psi(\ell,m,n) &= \frac{\eta!(\eta+\alpha)[\Gamma(\alpha)]^2}{\pi 2^{(1-2\alpha)}\Gamma(\eta+2\alpha)}\int_0^\pi \big\{-[m(m+1)P_m+\frac{2\cos\theta G_m}{\sin^2\theta}]G_\ell\big\}\frac{G_n}{\sin\theta}d\theta,\\
a\Psi\Omega(\ell,m,n) &= \frac{\eta!(\eta+\alpha)[\Gamma(\alpha)]^2}{\pi 2^{(1-2\alpha)}\Gamma(\eta+2\alpha)}\int_0^\pi -2\big\{\frac{\cos\theta}{\sin^2\theta}G_m G_\ell\big\}\frac{G_n}{\sin\theta}d\theta,\\
b\Psi\Omega(\ell,m,n) &= \frac{\eta!(\eta+\alpha)[\Gamma(\alpha)]^2}{\pi 2^{(1-2\alpha)}\Gamma(\eta+2\alpha)}\int_0^\pi -2\big\{m(m+1)P_m G_\ell\big\}\frac{G_n}{\sin\theta}d\theta,
\end{aligned}
\tag{D.51}
$$

where in each case ($\eta = n-1,\ \&\ \alpha = 1.5$). All integrals are evaluated using Weigner-3j notation, outlined in appendix E.

D.4 Validation of numerical code

We validate that the projection of the state vector $\boldsymbol{X}$ is correct, and that all matrices are discretised correctly, that is to an $\mathcal{O}(\Delta r^2)$ accuracy in space. Here we assume that a sufficient number of orthogonal polynomials have been used in the solution representation. This is ascertained by increasing N_θ until the solution norm $||\boldsymbol{X}||$ approaches machine precision. Steady states are solved according to a Newton-Iteration scheme

$$\mathcal{F}(\boldsymbol{X}^n) + \mathcal{D}\mathcal{F}|_{\boldsymbol{X}^n}(\boldsymbol{X}^{n+1} - \boldsymbol{X}^n) = 0. \tag{D.52}$$

To demonstrate second order spatial convergence we solve for a known solution $\bar{\boldsymbol{X}}$ and compare this with a numerical solution $\boldsymbol{X}_{num}$ as the radial grid spacing $\Delta r = d/N_r$ is varied. This task is facilitated by the following procedure. If correctly discretised the numerical of a steady solution at each grid point is given by its difference from the true solution

$$\delta^i = |\bar{\boldsymbol{X}}^i - \boldsymbol{X}^i_{num}| \approxeq A_i \Delta r^2, \tag{D.53}$$

where δ^i represents the absolute error at the i^{th} radial grid point. For the sum of all grid points this is defined by the L^p norm

$$\delta = \big(\sum_{i=1}^{N_r} |\bar{\boldsymbol{X}}^i - \boldsymbol{X}^i_{num}|^p\big)^{1/p} \approxeq \big(\sum_{i=1}^{N_r} A_i \Delta r^{2p}\big)^{1/p} \approxeq A\Delta r^{\frac{-1+2p}{p}}, \tag{D.54}$$

where we have made use of the fact that $N = d/\Delta r$. We can therefore anticipate the

following convergence rates to be

$$L^1 \to \gamma \approxeq 1, \quad L^2 \to \gamma \approxeq 3/2, \quad L^\infty \to \gamma \approxeq 2. \tag{D.55}$$

To verify these relations we define an unknown exponent γ as

$$\delta^i = |\bar{\boldsymbol{X}}^i - \boldsymbol{X}^i_{num}| \approxeq A\Delta r^\gamma. \tag{D.56}$$

Calculating the error for different values of Δr we obtain estimates on γ. Considering two different grid spacings Δr_1 and Δr_2, and taking the natural logarithm of (D.56) we obtain

$$\ln(\delta_1) = \gamma \ln(A\Delta r_1), \quad \ln(\delta_2) = \gamma \ln(A\Delta r_2), \tag{D.57}$$

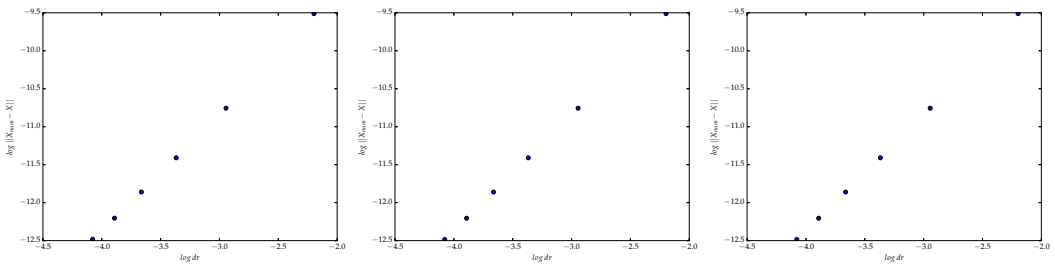
whose difference of this expression yields the following expression for γ

$$\gamma \approxeq \ln(\delta r_1/\delta r_2)/\ln(\Delta r_1/\Delta r_2). \tag{D.58}$$

Following this procedure for multiple values of Δr validates the converge of the numerical solution to the true solution as $\Delta r \to 0$. In the absence of fully coupled analytical solutions to (2.21), we prescribe an analytical solution satisfying the respective boundary conditions

$$\bar{\boldsymbol{X}} = \begin{pmatrix} \sin(\frac{2\pi}{d}(r_1 - r))\sin(\frac{2\pi}{d}(r_2 - r))\sin\theta\partial_\theta P_3(\cos\theta) \\ \sin(\frac{2\pi}{d}(r_1 - r))\sin(\frac{2\pi}{d}(r_2 - r))P_3(\cos\theta) \\ \sin(\frac{2\pi}{d}(r_1 - r))\sin(\frac{2\pi}{d}(r_2 - r))\sin\theta\partial_\theta P_3(\cos\theta) \end{pmatrix}, \tag{D.59}$$

and substituting this solution into the right hand side of (2.21) obtain an analytically derived forcing vector $\boldsymbol{G}$, which is added to the right hand side such that (D.59) becomes a solution of the forced problem. Fixing the separation $d = 1$, the remaining parameter values are chosen as $\mathrm{Ra} = 1, Re_1 = 1, Re_2 = -1$. We then solve the solution error (D.56) for $N_r = \{10, 20, 30, 40, 50, 60\}$ and three values of Prandtl number $Pr = \{0.01, 1, 10\}$.



(a) $Pr = 0.01$ **(b)** $Pr = 1$ **(c)** $Pr = 10$

Figure D.1: Convergence of the steady-state solver to the known solution as measured using the L^2 norm. By decreasing the radial grid space dr the exponent $\gamma \to 1.5$ as anticipated.

E

3D STABILITY NUMERICAL SOLUTION METHOD

The temperature terms simplify to yield

$$\boldsymbol{u}' \cdot \nabla T = \frac{\partial T}{\partial r}\frac{L_2\Phi'}{r^2} + \frac{1}{r^2}\frac{\partial T}{\partial \theta}\frac{\partial^2 \Phi'}{\partial r \partial \theta} + \frac{1}{r^2 \sin\theta}\frac{\partial T}{\partial \theta}\frac{\partial \Psi'}{\partial \varphi}, \tag{E.1}$$

$$\boldsymbol{u} \cdot \nabla T' = N_{33}(\Phi, \Psi)T' = \frac{L_2\Phi}{r^2}\frac{\partial T'}{\partial r} + \frac{1}{r^2}\frac{\partial^2 \Phi}{\partial r \partial \theta}\frac{\partial T'}{\partial \theta} - \frac{1}{r^2 \sin\theta}\frac{\partial \Psi}{\partial \theta}\frac{\partial T'}{\partial \varphi}. \tag{E.2}$$

These can be grouped as

$$N_{31}(T)\Psi' = \frac{1}{r^2 \sin\theta}\frac{\partial T}{\partial \theta}\frac{\partial \Psi'}{\partial \varphi}, \tag{E.3}$$

$$N_{32}(T)\Phi' = \frac{L_2\Phi'}{r^2}\frac{\partial T}{\partial r} + \frac{1}{r^2}\frac{\partial T}{\partial \theta}\frac{\partial^2 \Phi'}{\partial r \partial \theta}, \tag{E.4}$$

and substituting the series expansions (5.15), (5.16) one obtains

$$N_{31}(T)\Psi' = \mathrm{i}\sum_{p,l,n}^{N_\theta} w_3(l,p,n,m)\frac{m\,T_p}{r^2}\Psi'_{lm}, \tag{E.5}$$

$$N_{32}(T)\Phi' = \sum_{p,l,n}^{N_\theta} w_1(l,p,n,m)\frac{l(l+1)}{r^2}\frac{\partial T_p}{\partial r}\Phi'_{lm} + w_2(l,p,n,m)\frac{T_p}{r^2}\frac{\partial \Phi'_{lm}}{\partial r}, \tag{E.6}$$

for terms linearised about T, and similarly one obtains

$$N_{33}(\Phi,\Psi)T' = \sum_{p,l,n}^{N_\theta} w_1(l,p,n,m)\frac{p(p+1)\Phi_p}{r^2}\frac{\partial T'_{lm}}{\partial r} + w_2(l,p,n,m)\frac{1}{r^2}\frac{\partial \Phi_p}{\partial r}T'_{lm} - im\, w_3(l,p,n,m)\frac{\Psi_p}{r^2}T'_{lm}, \tag{E.7}$$

for the terms linearised about Φ, Ψ. The θ dependent coefficients present in these terms can be integrated exactly using Gaunt coefficients. This is achieved by use of the following three integrals w_1, w_2, w_3 which are functions of indices (l,p,n,m).

$$\begin{aligned} w_1(l,p,n,m) &= \int_0^\pi P_l^m\, P_p\, P_n^m \sin\theta d\theta, \\ w_2(l,p,n,m) &= \int_0^\pi \frac{\partial P_l^m}{\partial \theta}\frac{\partial P_p}{\partial \theta}\, P_n^m \sin\theta d\theta, \\ w_3(l,p,n,m) &= \int_0^\pi \frac{P_l^m}{\sin\theta}\frac{\partial P_p}{\partial \theta}\, P_n^m \sin\theta d\theta. \end{aligned} \tag{E.8}$$

The product to sum formula for obtaining coefficients of the associated Legendre polynomials are given by

$$w_1(l,p,n,m,q,s) = \int_0^\pi P_\ell^m P_p P_n^s \sin\theta\, d\theta, \quad \text{where} \quad \int_0^\pi P_\ell^m P_n^s \sin\theta d\theta = \frac{2}{2n+1}\frac{(n+s)!}{(n-s)!}\delta_{n,\ell}\delta_{m,s}. \tag{E.9}$$

Using the following formula to evaluate products of associated Legendre polynomials

$$\int_0^\pi P_\ell^m P_p^q P_n^s \sin\theta d\theta = 2(-1)^s \begin{pmatrix} \ell & p & n \\ 0 & 0 & 0 \end{pmatrix}\begin{pmatrix} \ell & p & n \\ m & q & -s \end{pmatrix}\sqrt{\frac{(\ell+m)!}{(\ell-m)!}\frac{(p+q)!}{(p-q)!}\frac{(n+s)!}{(n-s)!}}, \tag{E.10}$$

one may write

$$w_1(l,p,n,m,q,s) = (2n+1)(-1)^s \begin{pmatrix} \ell & p & n \\ 0 & 0 & 0 \end{pmatrix}\begin{pmatrix} \ell & p & n \\ m & q & -s \end{pmatrix}\sqrt{\frac{(\ell+m)!}{(\ell-m)!}\frac{(p+q)!}{(p-q)!}\frac{(n-s)!}{(n+s)!}}, \tag{E.11}$$

where the square of factorial terms is a consequence of the chosen normalization. To

simplify the second integral

$$w_2(l,p,n,m,q,s) = \int_0^\pi \frac{\partial P_\ell^m}{\partial\theta}\frac{\partial P_p^q}{\partial\theta} P_n^s \sin\theta\, d\theta, \tag{E.12}$$

we expand its derivatives as follows

$$\int_0^\pi \frac{\partial P_\ell^m}{\partial\theta}\frac{\partial P_p^q}{\partial\theta} P_n^s \sin\theta\, d\theta = \frac{1}{4}\int_0^\pi \big[-(\ell+m)(\ell-m+1)P_\ell^{m-1}P_p^{q+1} - (p+q)(p-q+1)P_\ell^{m+1}P_p^{q-1}\big] P_n^s \sin\theta d\theta, \tag{E.13}$$

and using Gaunt's formula one may write

$$w_2(l,p,n,m,q,s) = (2n+1)(-1)^s \left(\frac{-(b+c)}{4}\right)\sqrt{\frac{(\ell+m)!}{(\ell-m)!}\frac{(p+q)!}{(p-q)!}\frac{(n-s)!}{(n+s)!}}, \tag{E.14}$$

where

$$b = \begin{pmatrix} \ell & p & n \\ 0 & 0 & 0 \end{pmatrix}\begin{pmatrix} \ell & p & n \\ m-1 & q+1 & -s \end{pmatrix}\sqrt{(\ell+m)(\ell-m+1)}\sqrt{(p-q)(p+q+1)}, \tag{E.15}$$

$$c = \begin{pmatrix} \ell & p & n \\ 0 & 0 & 0 \end{pmatrix}\begin{pmatrix} \ell & p & n \\ m+1 & q-1 & -s \end{pmatrix}\sqrt{(p+q)(p-q+1)}\sqrt{(\ell-m)(\ell+m+1)}. \tag{E.16}$$

To simplify the third integral

$$w_3(l,p,n,m,q,s) = \int_0^\pi \frac{P_\ell^m}{\sin\theta}\frac{\partial P_p^q}{\partial\theta} P_n^s \sin\theta\, d\theta = \int_{-1}^1 -\frac{\partial P_p^q}{\partial x} P_\ell^m P_n^s\, dx, \tag{E.17}$$

we set $q=0$ and use the identity

$$\frac{\partial P_p^{q=0}}{\partial x} = \frac{(p^4-2p^3-p^2+2p)P_{p-1}^{-2} + P_{p-1}^2 + 2(p^2+p)P_{p-1}}{4}. \tag{E.18}$$

Substituting (E.18) into (E.17) and expanding its right hand side as follows we obtain

$$w_3(l,p,n,m,q=0,s) = -\frac{1}{4}\int_0^\pi \big[\left(p^4-2\,p^3-p^2+2\,p\right)P_{p-1}^{-2} + P_{p-1}^2 + \left(2\,p^2+2\,p\right)P_{p-1}\big] P_l^m P_n^s \sin\theta d\theta, \tag{E.19}$$

which is computed using Gaunt's formula, such that one may write

$$w_3(l,p,n,m,q=0,s) = (2n+1)(-1)^s \left(\frac{-(a+b+c)}{4}\right) \sqrt{\frac{(\ell+m)!}{(\ell-m)!}\frac{(p+q)!}{(p-q)!}\frac{(n-s)!}{(n+s)!}}, \tag{E.20}$$

where

$$\begin{aligned}
a &= \begin{pmatrix} \ell & p-1 & n \\ 0 & 0 & 0 \end{pmatrix} \begin{pmatrix} \ell & p-1 & n \\ m & -2 & -s \end{pmatrix} \left(p^4 - 2\,p^3 - p^2 + 2\,p\right), \\
b &= \begin{pmatrix} \ell & p-1 & n \\ 0 & 0 & 0 \end{pmatrix} \begin{pmatrix} \ell & p-1 & n \\ m & 2 & -s \end{pmatrix}, \\
c &= \begin{pmatrix} \ell & p-1 & n \\ 0 & 0 & 0 \end{pmatrix} \begin{pmatrix} \ell & p-1 & n \\ m & 0 & -s \end{pmatrix} 2(p^2+p).
\end{aligned} \tag{E.21}$$

The toroidal terms maybe simplified to yield

$$\begin{aligned}
N_{11}(\Psi_0)\Psi' &= \sum_{l,n}^{N_\theta} \mathrm{i}\,\alpha_1(l,m,n)\frac{\Psi_0(r)}{r^3}\Psi'_{lm}, \\
N_{12}(\Psi_0)\Phi' &= \sum_{l,n}^{N_\theta} \alpha_2(l,m,n)\left(\frac{1}{r^3}\frac{\partial\Psi_0(r)}{\partial r}\right)\Phi'_{lm} + \alpha_3(l,m,n)\frac{\Psi_0(r)}{r^3}\frac{\partial\Phi'_{lm}}{\partial r},
\end{aligned} \tag{E.22}$$

where

$$\begin{aligned}
\alpha_1(l,m,n) &= m(l^2+l-2)\delta_{l,n}, \\
\alpha_2(l,m,n) &= \frac{l(l+1)(l+2)(l-m+1)}{(2l+1)}\delta_{l+1,n} - \frac{l(l+1)(l-1)(l+m)}{(2l+1)}\delta_{l-1,n}, \\
\alpha_3(l,m,n) &= -2\left(\frac{l(l+2)(l-m+1)}{(2l+1)}\right)\delta_{l+1,n} - 2\left(\frac{(l-1)(l+1)(l+m)}{(2l+1)}\right)\delta_{l-1,n}.
\end{aligned} \tag{E.23}$$

Similarly the poloidal terms simplify to yield

$$N_{21}(\Psi_0)\Psi' = \sum_{l,n}^{N_\theta} \left(\alpha_3(l,m,n)\frac{1}{r^3}\frac{\partial\Psi_0(r)}{\partial r} + \beta_2(l,m,n)\,\frac{\Psi_0(r)}{r^4}\right)\Psi'_{lm} + \alpha_3(l,m,n)\frac{\Psi_0(r)}{r^3}\frac{\partial\Psi'_{lm}}{\partial r}, \tag{E.24}$$

where

$$\beta_2(l,m,n) = -2\left(\frac{(l+1)(l-1)^2(l+m)}{2l+1}\right)\delta_{l-1,n} + 2\left(\frac{l(l+2)^2(l-m+1)}{2l+1}\right)\delta_{l+1,n}, \tag{E.25}$$

$$N_{22}(\Psi_0)\Phi' = \mathrm{i}\sum_{l,n}^{N_\theta}\gamma_1\left(r^2\partial_r^2\Psi_0(r) - 2r\partial_r\Psi_0(r) + l(l+1)\Psi_0(r)\right)\frac{\Phi'_{lm}}{r^5} + \left(r\partial_r\Psi_0(r) - 2\Psi_0(r)\right)\frac{\gamma_3}{r^4}\frac{\partial\Phi'_{lm}}{\partial r} + \gamma_4\frac{\Psi_0(r)}{r^3}\frac{\partial^2\Phi'_{lm}}{\partial r^2} \tag{E.26}$$

$$\begin{aligned}\gamma_1(l,m,n) &= ml(l+1)\,\delta_{l,n},,\\ \gamma_3(l,m,n) &= 2m\,\delta_{l,n},\\ \gamma_4(l,m,n) &= -(l^2+l-2)m\,\delta_{l,n}.\end{aligned} \tag{E.27}$$

In each case to simplify integrals with factors of $xP_l^m(x)$ appearing the following relation is used

$$xP_l^m(x) = \frac{1}{2l+1}\left((l-m+1)P_{l+1}^m(x) + (l+m)P_{l-1}^m(x)\right). \tag{E.28}$$

References

Aldridge, Keith D., & Toomre, Alar. 1969. Axisymmetric inertial oscillations of a fluid in a rotating spherical container. *Journal of Fluid Mechanics*, **37**(2), 307323.

Araki, K., Mizushima, J., & Yanase, S. 1994. Thermal Instability of a Fluid in a Spherical Shell with Thin Layer Approximation Analysis. *Journal of the Physical Society of Japan*, **63**(6), 2123–2132.

Araki, K., Yanase, S., & Mizushima, J. 1996. Symmetry Breaking by Differential Rotation and Saddle-Node Bifurcation of the Thermal Convection in a Spherical Shell. *Journal of the Physical Society of Japan*, **65**(12), 3862–3870.

Aurnou, Jonathan, Heimpel, Moritz, & Wicht, Johannes. 2007. The effects of vigorous mixing in a convective model of zonal flow on the ice giants. *Icarus*, **190**(1), 110 – 126.

Batchelor, G. K. 1956. On steady laminar flow with closed streamlines at large Reynolds number. *Journal of Fluid Mechanics*, **1**(2), 177190.

Beltrame, P., & Chossat, P. 2015. Onset of intermittent octahedral patterns in spherical Bnard convection. *European Journal of Mechanics - B/Fluids*, **50**, 156 – 174.

Bercovici, D., Schubert, G., & Glatzmaier, G.A. 1989. Three-Dimensional Spherical Models of Convection in the Earth's Mantle. *Science*, **244**(4907), 950–955.

Bindel, D., Friedman, M., Govaerts, W., Hughes, J., & Kuznetsov, Yu.A. 2014. Numerical computation of bifurcations in large equilibrium systems in matlab. *Journal of Computational and Applied Mathematics*, **261**, 232 – 248.

Bodenschatz, E., Pesch, W., & Ahlers, G. 2000. Recent Developments in Rayleigh-Bnard Convection. *Annual Review of Fluid Mechanics*, **32**(1), 709–778.

Bühler, K. 1990. Symmetric and asymmetric Taylor vortex flow in spherical gaps. *Acta Mechanica*, **81**(1), 3–38.

Busse, F. H., & Riahi, H. 1982. Patterns of convection in spherical shells. Part 2. *Journal of Fluid Mechanics*, **123**, 283301.

Busse, F.H. 1975. Patterns of convection in spherical shells. *Journal of Fluid Mechanics*, **72**(1), 67–85.

Busse, F.H. 2003. The Sequence-Of-Bifurcations Approach Towards Understanding Turbulent Fluid Flow. *Suveys in Geophysics*, April, 269–288.

Chan, T. 1984. Newton-Like Pseudo-Arclength Methods for Computing Simple Turning Points. *SIAM Journal on Scientific and Statistical Computing*, **5**(1), 135–148.

Chandrasekhar, S. 1961. *Hydrodynamic and hydromagnetic stability*. International Series of Monographs on Physics, no. 1. Oxford: Clarendon.

Childress, S., & Soward, A. M. 1989. Scalar transport and alpha-effect for a family of cat's-eye flows. *Journal of Fluid Mechanics*, **205**, 99133.

Chossat, P. 1978. Bifurcation and Stability of Convective Flows in a Rotating or not Rotating Spherical Shell. *SIAM J. Appl. Math.*, **37**(3), 624–647.

Chossat, P. 2001. The bifurcation of heteroclinic cycles in systems of hydrodynamical type. *Journal of Continuous Discrete and Impulsive Systems Series A*, **8**(4a), 575–590.

Chossat, P., & Stewart, C. A. 1992. Spherical Symmetry-Breaking Bifurcations and Thermal Convection in the Earth's Mantle. *Pages 11–42 of:* Yuen, David A. (ed), *Chaotic Processes in the Geological Sciences*. New York, NY: Springer US.

Cliffe, K. A., Spence, A., & Tavener, S. J. 2000. The numerical analysis of bifurcation problems with application to fluid mechanics. *Acta Numerica*, **9**, 39131.

Crawford, J. D., & Knobloch, E. 1991. Symmetry and Symmetry-Breaking Bifurcations in Fluid Dynamics. *Annual Review of Fluid Mechanics*, **23**(1), 341–387.

Ermentrout, B. 2002. *Simulating, Analyzing, and Animating Dynamical Systems: A Guide to XPPAUT for Researchers and Students*. SIAM.

Favier, Benjamin, Guervilly, Cline, & Knobloch, Edgar. 2019. Subcritical turbulent condensate in rapidly rotating RayleighBnard convection. *Journal of Fluid Mechanics*, **864**, R1.

Feudel, F., Bergemann, K., Tuckerman, L.S., Egbers, C., Futterer, B., Gellert, M., & Hollerbach, R. 2011. Convection patterns in a spherical fluid shell. *Phys. Rev. E*, **83**(Apr), 046304.

Friedrich, R., & Haken, H. 1986. Static, wavelike, and chaotic thermal convection in spherical geometries. *Phys. Rev. A*, **34**(Sep), 2100–2120.

Futterer, B., Egbers, C., Dahley, N., Koch, S., & Jehring, L. 2010. First identification of sub- and supercritical convection patterns from GeoFlow, the geophysical flow simulation experiment integrated in Fluid Science Laboratory. *Acta Astronautica*, **66**(1), 193 – 200.

Gastine, T., Yadav, R. K., Morin, J., Reiners, A., & Wicht, J. 2013. From solar-like to antisolar differential rotation in cool stars. *Monthly Notices of the Royal Astronomical Society: Letters*, **438**(1), L76–L80.

Gastine, Thomas, Wicht, Johannes, & Aurnou, Jonathan M. 2015. Turbulent RayleighBnard convection in spherical shells. *Journal of Fluid Mechanics*, **778**, 721764.

Gettling, A.V. 1998. *Rayleigh-Bnard Convection: Structures and Dynamics*. Advanced Series in Nonlinear Dynamics, vol. 11. World Scientific.

Goldstein, H. F., Knobloch, E., Mercader, I., & Net, M. 1993. Convection in a rotating cylinder. Part 1 Linear theory for moderate Prandtl numbers. *Journal of Fluid Mechanics*, **248**, 583604.

Golubitsky, M., & Schaeffer, D. 1985. *Singularities and Groups in Bifurcation Theory*. Applied Mathematical Sciences, vol. 1. Springer.

Gough, D. O. 1969. The Anelastic Approximation for Thermal Convection. *Journal of the Atmospheric Sciences*, **26**(3), 448–456.

Guckenheimer, J., & Holmes, P. 1983. *Nonlinear Oscillations, Dynamical Systems, and Bifurcations of Vector Fields*. Springer.

Hansen, Candice J., Esposito, L., Stewart, A. I. F., Colwell, J., Hendrix, A., Pryor, W., Shemansky, D., & West, R. 2006. Enceladus' Water Vapor Plume. *Science*, **311**(5766), 1422–1425.

Heimpel, Moritz, & Aurnou, Jonathan M. 2012. Convective Bursts and the Coupling of Saturn's Equatorial Storms and Interior Rotation. *The Astrophysical Journal*, **746**(1), 51.

Hoff, Michael, & Harlander, Uwe. 2019. Stewartson-layer instability in a wide-gap spherical Couette experiment: Rossby number dependence. *Journal of Fluid Mechanics*, **878**, 522543.

Hollerbach, R. 2003. Instabilities of the Stewartson layer Part 1. The dependence on the sign of *Ro*. *Journal of Fluid Mechanics*, **492**, 289302.

Hollerbach, R., Junk, M., & Egbers, C. 2006. Non-axisymmetric instabilities in basic state spherical Couette flow. *Fluid Dynamics Research*, **38**(4), 257–273.

Howett, C. J. A., Spencer, J. R., Pearl, J., & Segura, M. 2011. High heat flow from Enceladus' south polar region measured using 10600 cm1 Cassini/CIRS data. *Journal of Geophysical Research: Planets*, **116**(E3).

Hoyle, R. 2006. *Pattern Formation An Introduction to Methods.* Cambridge University Press.

H.W. Muller, M.Lucke, M.Kamps. 1992. Transversal convection pattens in horizontal shear flow. *Physical Review A*, **45**(6), 3714–3726.

Inagaki, T., Itano, T., & Sugihara-Seki, M. 2019. Numerical study on the axisymmetric state in spherical Couette flow under unstable thermal stratification. *Acta Mechanica*, **230**(10), 3499–3509.

Jones, C.A., & Moore, D.R. 1978. The stability of axisymmetric convection. *Geophysical & Astrophysical Fluid Dynamics*, **11**(1), 245–270.

Joseph, Daniel D., & Carmi, Shlomo. 1966. Subcritical convective instability Part 2. Spherical shells. *Journal of Fluid Mechanics*, **26**(4), 769–777.

Junk, M., & Egbers, C. 2000. Isothermal spherical Couette flow. *Pages 215–233 of:* Egbers, Christoph, & Pfister, Gerd (eds), *Physics of Rotating Fluids.* Berlin, Heidelberg: Springer Berlin Heidelberg.

Kelly, R.E. 1994. The Onset and Development of Thermal Convection in Fully Developed Shear Flows. Advances in Applied Mechanics, vol. 31. Elsevier.

Kidachi, H. 1982. Side Wall Effect on the Pattern Formation of the Rayleigh-Bnard Convection. *Progress of Theoretical Physics*, **68**(1), 49–63.

King, Eric M., Soderlund, Krista M., Christensen, Ulrich R., Wicht, Johannes, & Aurnou, Jonathan M. 2010. Convective heat transfer in planetary dynamo models. *Geochemistry, Geophysics, Geosystems*, **11**(6).

Knobloch, E. 2008. Spatially localized structures in dissipative systems: open problems. *Nonlinearity*, **21**(4), T45–T60.

Knobloch, E. 2015. Spatial Localization in Dissipative Systems. *Annual Review of Condensed Matter Physics*, **6**(1), 325–359.

Knobloch, E., Moore, D.R., Toomre, J., & Weiss, N.O. 1986. Transitions to chaos in two-dimensional double-diffusive convection. *Journal of Fluid Mechanics*, **166**, 409448.

Kuznetsov, Yuri A. 2004. *Elements of Applied Bifurcation Theory.* Applied Mathematical Science, vol. 112. Springer.

Langa, José A, Robinson, James C, & Suárez, Antonio. 2002. Stability, instability, and bifurcation phenomena in non-autonomous differential equations. *Nonlinearity*, **15**(3), 887–903.

Lewis, G. M., & Langford, W. F. 2008. Hysteresis in a Rotating Differentially Heated Spherical Shell of Boussinesq Fluid. *Siam Journal of Applied Dynamical Systems*, **7**(4), 14211444.

Li, L., P.Zhang, Liao, X., & Zhang, K. 2005. Multiplicity of nonlinear thermal convection in a spherical shell. *Phys. Rev. E*, **71**(Jan), 016301.

Loukopoulos, V. C. 2004. Taylor vortices in annular heated spherical flow at medium and large aspect ratios. *Physics of fluids*, **17**.

Mamun, C.K., & Tuckerman, L.S. 1995. Asymmetry and Hopf bifurcation in spherical Couette flow. *Physics of Fluids*, **7**(1), 80–91.

Mannix, P. M., & Mestel, A. J. 2019. Weakly nonlinear mode interactions in spherical Rayleigh-Bénard convection. *Journal of Fluid Mechanics*, **874**, 359390.

Marcus, P.S., & Tuckerman, L. S. 1987a. Simulation of flow between concentric rotating spheres. Part 1. Steady states. *Journal of Fluid Mechanics*, **185**(12), 1–30.

Marcus, P.S., & Tuckerman, L. S. 1987b. Simulation of flow between concentric rotating spheres. Part 2. Transitions. *Journal of Fluid Mechanics*, **185**(12), 31–65.

Matthews, P. C. 2003. Pattern formation on a sphere. *Phys. Rev. E*, **67**(Mar), 036206.

Moore, D. R., & Weiss, N. O. 1973. Two-dimensional Rayleigh-Benard convection. *Journal of Fluid Mechanics*, **58**(2), 289312.

Müller, H. W., Tveitereid, M., & Trainoff, S. 1993. Rayleigh-Bénard problem with imposed weak through-flow: Two coupled Ginzburg-Landau equations. *Phys. Rev. E*, **48**(Jul), 263–272.

Munson, B. R., & Joseph, D. D. 1971a. Viscous incompressible flow between concentric rotating spheres. Part 1. Basic flow. *Journal of Fluid Mechanics*, **49**(2), 289303.

Munson, B. R., & Joseph, D. D. 1971b. Viscous incompressible flow between concentric rotating spheres. Part 2. Hydrodynamic stability. *Journal of Fluid Mechanics*, **49**(9), 305–318.

Nadiga, B. T., & Aurnou, J. M. 2008. A Tabletop Demonstration of Atmospheric Dynamics: Baroclinic Instability. *Oceanography*, **21**(4), 196–201.

Net, M., & Snchez, J. 2015. Continuation of Bifurcations of Periodic Orbits for Large-Scale Systems. *SIAM Journal on Applied Dynamical Systems*, **14**(2), 674–698.

Nimmo, F., & Pappalardo, R. T. 2016. Ocean worlds in the outer solar system. *Journal of Geophysical Research: Planets*, **121**(8), 1378–1399.

Noir, J., Hemmerlin, F., Wicht, J., Baca, S.M., & Aurnou, J.M. 2009. An experimental and numerical study of librationally driven flow in planetary cores and subsurface oceans. *Physics of the Earth and Planetary Interiors*, **173**(1), 141 – 152.

Noir, J., Cbron, D., Bars, M. Le, Sauret, A., & Aurnou, J.M. 2012. Experimental study of libration-driven zonal flows in non-axisymmetric containers. *Physics of the Earth and Planetary Interiors*, **204-205**, 1 – 10.

Peale, S.J. 2003. Tidally Induced Volcanism. *Celestial Mechanics and Dynamical Astronomy*, **87**(1), 129–155.

Peale, Stanton J, Cassen, P, & Reynolds, Ray T. 1979. Melting of Io by tidal dissipation. *Science*, **203**(4383), 892–894.

Proctor, M.R.E., & Jones, C.A. 1988. The interaction of two spatially resonant patterns in thermal convection. Part 1. Exact 1:2 resonance. *Journal of Fluid Mechanics*, **188**, 301335.

Proudman, Ian. 1956. The almost-rigid rotation of viscous fluid between concentric spheres. *Journal of Fluid Mechanics*, **1**(11), 505–516.

Proudman, Joseph, & Lamb, Horace. 1916. On the motion of solids in a liquid possessing vorticity. *Proceedings of the Royal Society of London. Series A, Containing Papers of a Mathematical and Physical Character*, **92**(642), 408–424.

Ravelet, Florent, Marié, Louis, Chiffaudel, Arnaud, & Daviaud, Fran çois. 2004. Multistability and Memory Effect in a Highly Turbulent Flow: Experimental Evidence for a Global Bifurcation. *Phys. Rev. Lett.*, **93**(Oct), 164501.

Rayleigh. 1916. On convection currents in a horizontal layer of fluid, when the higher temperature is on the under side. *Philosophical Magazine*, **32**(192), 529–546.

Read, Peter L. 2009. Rotating convection on the edge. *Nature*, **457**(January), 270–271.

Rovira-Navarro, Marc, Rieutord, Michel, Gerkema, Theo, Maas, Leo R.M., van der Wal, Wouter, & Vermeersen, Bert. 2019. Do tidally-generated inertial waves heat the subsurface oceans of Europa and Enceladus? *Icarus*, **321**, 126 – 140.

Saad, Youcef., & Schultz, Martin H. 1986. GMRES: A Generalized Minimal Residual Algorithm for Solving Nonsymmetric Linear Systems. *SIAM Journal on Scientific and Statistical Computing*, **7**(3), 856–869.

Saur, Joachim, Duling, Stefan, Roth, Lorenz, Jia, Xianzhe, Strobel, Darrell F., Feldman, Paul D., Christensen, Ulrich R., Retherford, Kurt D., McGrath, Melissa A., Musacchio, Fabrizio, Wennmacher, Alexandre, Neubauer, Fritz M., Simon, Sven, & Hartkorn,

Oliver. 2015. The search for a subsurface ocean in Ganymede with Hubble Space Telescope observations of its auroral ovals. *Journal of Geophysical Research: Space Physics*, **120**(3), 1715–1737.

Schmid, Peter J. 2007. Nonmodal Stability Theory. *Annual Review of Fluid Mechanics*, **39**(1), 129–162.

Schubert, G., Stevenson, D.J., & Ellsworth, K. 1981. Internal structures of the Galilean satellites. *Icarus*, **47**(1), 46 – 59.

Showman, Adam P., & Malhotra, Renu. 1997. Tidal Evolution into the Laplace Resonance and the Resurfacing of Ganymede. *Icarus*, **127**(1), 93 – 111.

Shtern, Vladimir, & Hussain, Fazle. 1999. Collapse, symmetry breaking, and hysteresis in swirling flows. *Annual Review of Fluid Mechanics*, **31**(1), 537–566.

Šil'nikov, L P. 1970. A Contribution to the problem of the structure of an extended neighborhood of a rough equilibrium state of saddle-foucs type. *Mathematics of the USSR-Sbornik*, **10**(1), 91–102.

Simitev, R. D., & Busse, F. H. 2009. Bistability and hysteresis of dipolar dynamos generated by turbulent convection in rotating spherical shells. *EPL (Europhysics Letters)*, **85**(1), 19001.

Spencer, J. R., Pearl, J. C., Segura, M., Flasar, F. M., Mamoutkine, A., Romani, P., Buratti, B. J., Hendrix, A. R., Spilker, L. J., & Lopes, R. M. C. 2006. Cassini Encounters Enceladus: Background and the Discovery of a South Polar Hot Spot. *Science*, **311**(5766), 1401–1405.

Spencer, John Ronald, Barr, Amy C., Esposito, Larry W., Helfenstein, P, Ingersoll, Andrew P., Jaumann, Ralf, McKay, Christopher P, Nimmo, Francis, Porco, Carolyn C., & Waite, J Hunter. 2009. 22 . Enceladus : An Active Cryovolcanic Satellite.

Spiegel, E. A., & Weiss, N. O. 1982. Magnetic buoyancy and the Boussinesq approximation. *Geophysical & Astrophysical Fluid Dynamics*, **22**(3-4), 219–234.

Sreenivasan, K. R., Bershadskii, A., & Niemela, J. J. 2002. Mean wind and its reversal in thermal convection. *Phys. Rev. E*, **65**(May), 056306.

Stewartson, K. 1953. On the flow between two rotating coaxial disks. *Mathematical Proceedings of the Cambridge Philosophical Society*, **49**(2), 333341.

Subramanian, Priya, Brausch, Oliver, Daniels, Karen E., Bodenschatz, Eberhard, Schneider, Tobias M., & Pesch, Werner. 2016. Spatio-temporal patterns in inclined layer-convection. *Journal of Fluid Mechanics*, **794**, 719745.

Taylor, Geoffrey Ingram. 1923. Stability of a viscous liquid contained between two rotating cylinders. *Proceedings of the Royal Society of London. Series A, Containing Papers of a Mathematical and Physical Character*, **102**(718), 541–542.

Travnikov, Vadim, Zaussinger, Florian, Beltrame, Philippe, & Egbers, Christoph. 2017. Influence of the temperature-dependent viscosity on convective flow in the radial force field. *Phys. Rev. E*, **96**(Aug), 023108.

Trefethen, Llyod N. 2000. *Spectral Methods in Matlab*. SIAM.

Turcotte, D. L., & Oxburgh, E. R. 1967. Finite amplitude convective cells and continental drift. *Journal of Fluid Mechanics*, **28**(1), 2942.

Turner, J S. 1974. Double-Diffusive Phenomena. *Annual Review of Fluid Mechanics*, **6**(1), 37–54.

Tyler, Robert H. 2008. Strong ocean tidal flow and heating on moons of the outer planets. *Nature*, **456**, 770–772.

Uecker, Hannes, Wetzel, Daniel, & Rademacher, Jens D. M. 2014. pde2path - A Matlab Package for Continuation and Bifurcation in 2D Elliptic Systems. *Numerical Mathematics: Theory, Methods and Applications*, **7**(1), 58106.

Wilson, Alec, & Kerswell, Rich R. 2018. Can libration maintain Enceladus's ocean? *Earth and Planetary Science Letters*, **500**, 41 – 46.

Wimmer, Manfred. 1976. Experiments on a viscous fluid flow between concentric rotating spheres. *Journal of Fluid Mechanics*, **78**(2), 317335.

Wimmer, Manfred. 1981. Experiments on the stability of viscous flow between two concentric rotating spheres. *Journal of Fluid Mechanics*, **103**, 117131.

Yanase, Shinichiro, Mizushima, Jiro, & Araki, Keisuke. 1995. Multiple Solutions for a Flow between Two Concentric Spheres with Different Temperatures and Their Stability. *Journal of the Physical Society of Japan*, **64**(7), 2433–2443.

Young, R.E. 1974. Finite-amplitude thermal convection in a spherical shell. *Journal of Fluid Mechanics*, **63**(4), 695–721.

Zebib, A., Schubert, G., & Straus, J.M. 1980. Infinite Prandtl number thermal convection in a spherical shell. *Journal of Fluid Mechanics*, **97**(2), 257277.

Zebib, A., Schubert, G., Dein, J. L., & Paliwal, R. C. 1983. Character and stability of axisymmetric thermal convection in spheres and spherical shells. *Geophysical & Astrophysical Fluid Dynamics*, **23**(1), 1–42.

Zhang, Keke, & Liao, Xinhao. 2017. *Theory and Modeling of Rotating Fluids, Convection, Intertial Waves and Precession.* Cambridge Monographs on Mechanics. Cambridge.

Zimmerman, Daniel S., Triana, Santiago Andrs, & Lathrop, D. P. 2011. Bi-stability in turbulent, rotating spherical Couette flow. *Physics of Fluids*, **23**(6), 065104.